

School of Science
Department of Physics and Astronomy 'Augusto Righi'
Master Degree in Physics

**Spectral distortions of the cosmic
microwave background and
small-scale gravitational waves as new
windows on the Early Universe**

Supervisor:

Prof. Roberto Balbinot

Co-supervisors:

Dr. Fabio Finelli

Dr. Matteo Braglia

Dr. Daniela Paoletti

Submitted by:

Matteo Tagliazucchi

To my friend Giulio R.

ACKNOWLEDGMENTS

At the end of this journey, I think some acknowledgments are due. First of all, I want to thank my supervisor Prof. Roberto Balbinot for raising my interest in general relativity and cosmology and for all the useful advice he gave me. I would also like to extend my deepest gratitude to Dr. Fabio Finelli for welcoming me to INAF-OAS, for allowing me to move the first steps in the research world, for his priceless support to this work and for continuously suggesting new stimulating ideas. I am deeply indebted to Dr. Matteo Braglia for his incredible contribution to this thesis, for being always available to answer my questions - also those outside the scope of this elaborate - and for teaching me so many things in the clearest possible way. Without Matteo, this work would definitely not have been possible. I also wish to thank extensively Dr. Daniela Paoletti for the support with CLASS, MONTEPYTHON, OAS cluster and all the useful comments on the manuscript. Special thanks to Matteo Lucca and Jens Chluba for clarifying my doubts about spectral distortions and their implementation in CLASS and MONTEPYTHON.

This journey would not have been the same without all the friends, too many to be listed without forgetting anyone, I met at the University during these years. Thanks to all of you I spent the best, though demanding, years of my life so far. Of course, I must thank also my friends in Pavullo for always being there and for sharing unforgettable memories.

The most important acknowledgment goes to my family. Thank you for always supporting my choices and for giving me the opportunity to do what I want. Finally, I wish to thank Morgana, for everything.

Abstract

In this thesis, we explore constraints that can be put on the primordial power spectrum of curvature perturbations beyond the scales probed by anisotropies of the cosmic microwave background and galaxy surveys. We exploit present and future measurements of CMB spectral distortions, and their synergy with CMB anisotropies, as well existing and future upper limits on the stochastic background of gravitational waves. We derive for the first time phenomenological templates that fit small-scale bumps in the primordial power spectrum generated in multi-field models of inflation. By using such templates, we study for the first time imprints of primordial peaks on anisotropies and spectral distortions of the cosmic microwave background and we investigate their contribution to the stochastic background of gravitational waves. Through a Monte Carlo Markov Chain analysis, we infer for the first time the constraints on the amplitude, the width and the location of such bumps using Planck and FIRAS data. We also forecast how a future spectrometer like PIXIE could improve FIRAS constraints. The results derived in this thesis have implications for the possibility of primordial black holes from inflation.

CONTENTS

INTRODUCTION	3
CHAPTER I. THE HOT BIG-BANG MODEL	5
1 Preliminaries	5
1.1 General Relativity	5
1.2 Cosmological Principle	6
2 Background Cosmology	8
2.1 Kinematics	9
2.2 Dynamics	13
3 Brief Thermal History of the Universe	18
3.1 The Primordial Plasma	18
3.2 Recombination and the Cosmic Microwave Background	24
CHAPTER II. CMB SPECTRAL DISTORTIONS	29
4 Formulation of the thermalization problem	29
4.1 Black body radiation	29
4.2 Beyond thermal equilibrium	30
4.3 Photon Boltzmann equation	34
5 Spectral distortions characteristics	39
5.1 Shapes	39
5.2 Amplitudes	43
5.3 Green's function of the thermalization problem	45
6 Some causes of CMB spectral distortions	48
6.1 Heating mechanisms in Λ CDM model	49
6.2 Heating mechanisms in exotic scenarios	50
CHAPTER III. INFLATION	52
7 The Standard Inflationary Universe	52
7.1 The problems of the Hot-Big Bang Model	52
7.2 Single Field Inflation	58
8 Quantum Fluctuations during Inflation	61
8.1 Cosmological Perturbations	61
8.2 Scalar Fluctuations	67
8.3 Tensor Fluctuations	75
8.4 Short catalog of inflationary models	78
CHAPTER IV. CMB ANISOTROPIES, SILK DAMPING SPECTRAL DISTORTIONS AND SCALAR-INDUCED GRAVITATIONAL WAVES	83
9 Anisotropies of the cosmic microwave background	83

9.1	Photons Boltzmann equation in a perturbed Universe	83
9.2	CMB angular power spectra	86
10	Silk damping spectral distortions	92
10.1	Superposition of black bodies	93
10.2	Dissipation of primordial acoustic waves	95
11	Primordial gravitational waves	97
11.1	Gravitational waves from inflation	98
11.2	Scalar induced gravitational waves	99
CHAPTER V. SMALL-SCALE PRIMORDIAL FEATURES		105
12	Primordial black holes formation from large overdensities	105
13	Small-scale features in two-field models of inflation	107
13.1	Two-stage inflation	108
13.2	Hybrid inflation α -attractors	111
14	Phenomenological templates	114
14.1	Modified log-normal bump	114
14.2	Smoothly broken power law bump	115
14.3	Oscillating bump	116
15	Impact on observables	117
15.1	Modified log-normal template	119
15.2	Smoothly broken power law template	123
15.3	Oscillating bump template	127
CHAPTER VI. CONSTRAINTS ON THE PRIMORDIAL POWER SPECTRUM FROM THE CMB		131
16	Methodology	131
16.1	Basics of Bayesian inference	131
16.2	CMB likelihoods	133
16.3	Semi-analytical constraints	135
17	Results	136
17.1	FIRAS and Planck constraints	136
17.2	Forecast for PIXIE	140
18	Discussion	143
CONCLUSIONS		145
APPENDIX A. COSMOLOGICAL PERTURBATIONS		147
BIBLIOGRAPHY		149

INTRODUCTION

The pioneering COBE/FIRAS mission in the early 1990s proved that the cosmic microwave background (CMB) has a nearly perfect black body intensity spectrum [1] and determined its temperature. On top of such a nearly uniform and isotropic spectrum, the CMB displays very tiny anisotropies of order of $\delta T/T_0 \sim 10^{-5}$, generated by inhomogeneities in the photon-baryon plasma before photon decoupling. The initial conditions for these anisotropies are set by inflation, a stage of accelerated expansion before the onset of the Hot Big Bang evolution. During such stage, quantum vacuum fluctuations were stretched outside the Hubble radius, where they became classical. Therefore, CMB anisotropies can constrain the shape of the primordial power spectrum (PPS) set by inflation. In particular, the simplest models of Slow-Roll (SR) inflation produce a near scale invariant PPS, which is in good agreement with the latest measurements of CMB anisotropies by Planck [2] and data from Large Scale Structure (LSS) surveys. However, such experiments only constrain very large cosmological scales in the range $k \in [10^{-4}, 1]\text{Mpc}^{-1}$. Upcoming CMB experiments, as the ground-based Simons Observatory [3] and CMB-S4 [4], complemented by the space mission LiteBIRD [5], will map the CMB sky with improved precision and resolution, but will hardly extend the probed scales beyond 1Mpc^{-1} . It is therefore interesting to explore other cosmological or astrophysical observables to test Inflation beyond the $\log(10^4) \sim 9$ e-folds probed by CMB and galaxy surveys. Indeed, the PPS at smaller scales is poorly known and only indirect and very model dependent constraints exist.

There are however observables that can probe the PPS at smaller scales, such as the Lyman- α lines and 21 cm intensity mapping, CMB spectral distortions (SDs) and a stochastic gravitational wave background. In this thesis we concentrate on the last two cases. SDs are tiny departures of the CMB frequency spectrum from the black body shape and they are a unique and independent way to study cosmology in the range $[10^{-1}, 10^{-4}]\text{Mpc}^{-1}$. There are several SDs signals predicted by the standard ΛCDM cosmological model and so a precise measurement of the CMB frequency spectrum will test this model at scales never probed before. For this reason, SDs are a target for experimental efforts from ground, such as TMS [6] and COSMO [7], up to space concepts as PIXIE [8], Pristine [9], Fossil [10] and the one described to answer the ESA call Voyage 2050 [11]. A particular mechanism that generates SDs is the Silk damping effect [12], i.e. the diffusion of photons from hotter to colder regions of the primordial plasma. Such superposition of black bodies at different temperatures smooths the temperature fluctuations of the CMB, in turn damping its anisotropies at small scales, and generating SDs, since it creates a black body with a temperature larger than the average plus some distortion terms. SDs due to Silk damping depend on the pattern of CMB temperature fluctuations and so on the PPS.

At small scales the PPS could deviate from the nearly scale invariant law tightly constrained by CMB and LSS. In particular, several models of inflation predict a significant amplification of power at such scales. Furthermore, large primordial overdensities can collapse into primordial black holes (PBHs) upon horizon re-entry during the radiation dominated era. PBHs have recently seen a surge of interest after they were proposed as an explanation (see Refs. [13, 14, 15]) for the LIGO first detection of a merger of two black holes of about 30 solar masses [16]. Even if the latest O3 catalog of the LIGO/VIRGO/KAGRA collaboration [17] suggests that a population of PBHs, if existing, must be subdominant and cannot constitute the whole abundance of cold dark matter, their existence can still have interesting astrophysical and cosmological implications. The standard mechanism to seed PBHs formation requires the amplification of the PPS of about 7 orders of magnitude with respect to its value measured by Planck [18] at large scales. This motivates the exploration of a large amplification of power at small scales and its imprints on cosmological observables. As many models of inflation generically predict a transient amplification, i.e. a localized bump rather than a systematic amplification, we focus on such localized features in this thesis.

Specifically, we use CMB anisotropies and SDs to constrain the shape of small-scale bumps produced in multi-field models of inflation. We derive phenomenological templates that capture their shape and study their imprints on CMB observables. Another interesting consequence of large scalar overdensities is the generation of tensor perturbations at horizon re-entry, due to second order perturbation theory effects. If the bump is at scales testable by SDs, the resulting Stochastic Gravitational Wave Background (SGWB) can be tested by current and future PTA [19, 20] and even planned space-based observatories [21], provided its width is large enough. For this reason, we also study the contribution of large bumps in the PPS to the SGWB.

We finally run a Monte Carlo Markov Chain (MCMC) simulation to infer how current SDs data from FIRAS constrains the PPS. We derive the constraints on a PPS with a broad bump near to the SDs sensitivity range in order to extend the upper limits found in the literature, that are valid for peaks with no width, e.g a Dirac δ bump. We further explore how the synergy between CMB anisotropies and SDs improves such constraints and we forecast the possibility of a future spectrometer like PIXIE.

This thesis is organized as follows. In the first chapter we present the standard Hot Big-Bang Model. In the second chapter we review the physics of CMB spectral distortions. In the third chapter we discuss the problems of the Hot Big bang model, how inflation is the most elegant solution to them and a short list of the simplest inflationary models. In the fourth chapter we study the three observables, i.e. anisotropies and spectral distortions of the cosmic microwave background and scalar-induced small-scale gravitational waves, that we use for our analysis. In particular we derive their dependence on the shape of the PPS. In the fifth chapter we derive the phenomenological templates that match the theoretical predictions of some multi-field models of inflation and we show their effects on the observables aforementioned. In the last chapter we present the results of the MCMC analysis.

I

THE HOT BIG-BANG MODEL

Cosmology is the branch of physics that studies the origin and the evolution of our Universe and it is based on two main assumptions: the Universe can be treated as a four-dimensional spacetime described with the general theory of relativity and the cosmological principle holds.

In the first section we present the key ingredients of General Relativity that are used in cosmology and we introduce the cosmological principle. In the second section, we discuss the kinematic and dynamic properties of the metric describing the Universe. Since it is impossible to follow the evolution of each particle of the Universe, statistical mechanics is necessary to study how the different components of the Universe evolve. Recent observations show that the early Universe was approximately in thermal equilibrium and so equilibrium thermodynamics is sufficient to study the thermal history of the Universe. In the third section, equilibrium thermodynamics is applied to study the evolution of the different components of the Universe.

1 Preliminaries

1.1 General Relativity

The dynamics of the Universe on large scales is mostly determined by gravity. Any cosmological model requires a consistent theory of gravitation. The most accepted theory describing gravity is the General Theory of Relativity (GR), which is based on two principles: the Principle of General Relativity, which implies that the physical laws should have the same form in every frame of reference, and the Equivalence Principle, that states that it is always possible to find a locally inertial frame of reference where physical laws are those predicted by the Special Theory of Relativity. In GR framework, an event is a point of the 4-dimensional spacetime manifold labelled with some coordinates $x^\mu = (x^0, x^1, x^2, x^3, x^4) \equiv (t, x, y, z)$. Distances and vector lengths on such manifold are defined through the symmetric rank-2 metric tensor $g_{\mu\nu}(x)$. For each couple of points $(x^\mu, x^\mu + dx^\mu)$ on the manifold we define the proper distance ds or the proper time interval as $d\tau$ as

$$ds^2 = -d\tau^2 = g_{\mu\nu}(x)dx^\mu dx^\nu. \quad (1.1)$$

In this thesis we use the "mostly plus" convention and the metric signature is $(-, +, +, +)$ and we set $c = \hbar = 1$. Once the metric tensor is defined, we can find how test particles move

on the manifold. The trajectories are solutions of the so-called geodesic equations

$$\frac{d^2 x^\mu}{d\lambda^2} + \Gamma_{\sigma\rho}^\mu \frac{dx^\sigma}{d\lambda} \frac{dx^\rho}{d\lambda} = 0, \quad (1.2)$$

where λ is an affine parameter describing the curve and where the Christoffel symbols are given by

$$\Gamma_{\lambda\rho}^\mu = \frac{g^{\mu\alpha}}{2} \left(\frac{\partial g_{\lambda\alpha}}{\partial x^\rho} + \frac{\partial g_{\alpha\rho}}{\partial x^\lambda} - \frac{\partial g_{\lambda\rho}}{\partial x^\alpha} \right). \quad (1.3)$$

The metric tensor $g_{\mu\nu}$ is in general obtained by solving Einstein field equations

$$R_{\mu\nu} - \frac{1}{2} g_{\mu\nu} R - \Lambda g_{\mu\nu} = 8\pi G T_{\mu\nu}, \quad (1.4)$$

where $R_{\mu\nu}$ and R are the Ricci tensor and scalar respectively and they are defined in terms of the Riemann tensor

$$R^\rho{}_{\mu\lambda\nu} \stackrel{\text{def}}{=} \Gamma_{\mu\nu,\lambda}^\rho - \Gamma_{\mu\lambda,\nu}^\rho + \Gamma_{\mu\nu}^\kappa \Gamma_{\lambda\kappa}^\rho - \Gamma_{\mu\lambda}^\kappa \Gamma_{\nu\kappa}^\rho, \quad (1.5)$$

as

$$R_{\mu\nu} \stackrel{\text{def}}{=} R^\lambda{}_{\mu\lambda\nu}, \quad R \stackrel{\text{def}}{=} R^\mu{}_\mu. \quad (1.6)$$

By introducing the energy-momentum tensor associated with the cosmological constant Λ

$$T_{\mu\nu}^{(\Lambda)} = \frac{\Lambda}{8\pi G} g_{\mu\nu} \stackrel{\text{def}}{=} \rho_\Lambda g_{\mu\nu}, \quad (1.7)$$

and by contracting both sides by $g^{\mu\nu}$, we can write Einstein equations as

$$R_{\mu\nu} = 8\pi G \left(T_{\mu\nu}^{(tot)} - \frac{1}{2} g_{\mu\nu} T^{(tot)\lambda}{}_\lambda \right) \stackrel{\text{def}}{=} 8\pi G S_{\mu\nu}. \quad (1.8)$$

1.2 Cosmological Principle

The Cosmological Principle states that our Universe is spatially homogeneous and isotropic. To study the consequences of this principle we have to choose a coordinates system. We choose spatial coordinates x^i that have origin at the center of the Milky Way and whose directions are fixed by the lines of sight from our galaxy to some typical distant galaxies. It is believed that the Universe is filled by several monotonically decreasing scalar fields, like its proper energy density ρ . We can choose as cosmic standard coordinate time t any decreasing function of such scalar fields, say S : $t = t(S)$. Suppose that we measure in the cosmic standard coordinates system $x^\mu = (t, \mathbf{x})$ the tensors $g_{\mu\nu}(x)$ and $T_{\mu\nu}(x)$. Another set of coordinates x'^μ is equivalent to the cosmic standard one if the transformation $x^\mu \rightarrow x'^\mu$ is

an isometry or equivalently if $g_{\mu\nu}$ and $T_{\mu\nu}$ are form-invariant under such transformation:

$$g_{\mu\nu}(y) = g'_{\mu\nu}(y), \quad T_{\mu\nu}(y) = T'_{\mu\nu}(y); \quad \forall y. \quad (1.9)$$

In general, a n -parameters isometry of metric implies the existence of n independent Killing vectors, which can be obtained by considering infinitesimal transformations. All the cosmic fields have to be form-invariant, even the scalar field S used to define the standard cosmic time. The form-invariance of S at $y = x'$ and the scalars defining property $S'(x') = S(x)$ imply

$$S(t') = S'(t') \equiv S(t) \implies t' = t. \quad (1.10)$$

We conclude that all coordinates systems equivalent to the cosmic standard one must use the same standard cosmic time.

Isotropy means that all spatial directions of the Universe are equivalent. This hypothesis requires the existence of a 3-parameters family of coordinates $x'^{\mu}(x^{\mu}; \theta^i)$ equivalent to the cosmic standard one, that shares the same origin with them and that is an isometry of the metric. We can interpret θ^i as the Euler angles expressing the orientation of x'^i with respect to the x^i .

Homogeneity implies the existence of a family of 3-parameters coordinates $\bar{x}'^{\mu}(x; a)$, equivalent to the cosmic standard ones, that have the origin on some fundamental trajectory $x^i = X^i(t; a)$ - which are determined by the motion of the members of the ensemble of galaxies near the Earth and that fill up all space occupied by the ensemble of galaxies at any t - and which is an isometry of the metric. Homogeneity assumption applies only to portions of the Universe that include a large number of fundamental trajectories, for example cells with a diameter of 10^8 to 10^9 light years.

Consider a N -dimensional spacetime and a M -dimensional subspace. Let u^i be the M coordinates describing the subspace and v^a the $N - M$ ones describing the rest of the spacetime. The subspaces defined by $v^a = \text{constant}$ is said to be maximally symmetric if the metric of the whole space is invariant under a group of infinitesimal transformations

$$\begin{cases} u^i \rightarrow u'^i = u^i + \epsilon \xi^i(u, v), \\ v^a \rightarrow v'^a = v^a, \end{cases} \quad (1.11)$$

with $M(M + 1)/2$ independent Killing vectors ξ^i . In this case, the most generic metric in such spacetime is [22]

$$d\tau^2 = -g_{ab}dv^a dv^b - f(v) \left[d\mathbf{u}^2 + \frac{k(\mathbf{u} \cdot d\mathbf{u})^2}{1 - k\mathbf{u}^2} \right], \quad (1.12)$$

where $f(v)$ is positive and k can be only $-1, 0, 1$.

The Cosmological Principle implies that the metric of the Universe is invariant under the

transformations

$$\begin{cases} x^i \rightarrow x'^i = x^i + \epsilon \xi^i(t, \mathbf{x}), & i = 1, 2, 3 \\ t \rightarrow t' = t, \end{cases} \quad (1.13)$$

where the Killing vectors ξ^i are 6 (3 due to isotropy and 3 to homogeneity). We recognize the analogy $v^a \leftrightarrow t(a = 1)$, $u^i \leftrightarrow x^i(i = 3)$ and we conclude that our Universe has a maximally symmetric 3-dimensional subspace defined by the family of hypersurfaces $t = \text{constant}$ and that the most general metric describing it is

$$d\tau^2 = -g(t)dt^2 - f(t) \left[d\mathbf{x}^2 + \frac{k(\mathbf{x} \cdot d\mathbf{x})^2}{1 - k\mathbf{x}^2} \right], \quad (1.14)$$

where t is some time coordinate equivalent to the standard cosmic time and x^i the spatial ones. We introduce the new time coordinate

$$t' \stackrel{\text{def}}{=} \int dt \sqrt{-g(t)}, \quad (1.15)$$

so that the final form of the metric becomes

$$d\tau^2 = dt'^2 - a^2(t') \left[d\mathbf{x}^2 + \frac{k(\mathbf{x} \cdot d\mathbf{x})^2}{1 - k\mathbf{x}^2} \right], \quad (1.16)$$

with $a(t') = \sqrt{f(t)}$. This is the so-called Friedman-Lemaitre-Robertson-Walker (FLRW) metric. The FLRW metric has $g_{00} = -1$ and it is such that the Christoffel symbol Γ_{00}^i vanishes always. For this reason, (t, x^i) are called comoving coordinates [22]. From now on, the prime on t' will be omitted. The Cosmological Principle set constraints also on the form of the energy-momentum tensor of the cosmic matter. As aforementioned, all cosmic fields should be form-invariant, in the sense of equation (1.9), under the set of transformations (1.11), which are purely spatial transformations. As a consequence, they transform T^{00} , T^{0i} and T^{ij} as a scalar, a vector and a rank-2 tensor respectively. It is possible to prove that in this case $T^{\mu\nu}$ must be in the perfect fluid form [22]

$$T_{\mu\nu} = P g_{\mu\nu} + (P + \rho) u_\mu u_\nu, \quad \text{where } u^\mu \stackrel{\text{def}}{=} (1, 0). \quad (1.17)$$

ρ and P are the energy density and the pressure of the fluid.

2 Background Cosmology

The FLRW metric (1.16) can be written in a compact form [22]

$$ds^2 = -dt^2 + a^2(t) \gamma_{ij} dx^i dx^j, \quad (2.1)$$

where

$$\gamma_{ij} = \delta_{ij} + k \frac{x_i x_j}{1 - k(x_k x^k)}. \quad (2.2)$$

By using the conformal time

$$d\eta \stackrel{\text{def}}{=} \frac{dt}{a(t)}. \quad (2.3)$$

the FLRW metric becomes conformally equivalent to a flat spacetime:

$$ds^2 = a^2(t) \left[-d\eta^2 + \gamma_{ij} dx^i dx^j \right]. \quad (2.4)$$

The only two free parameters of the FLRW metric are $a(t)$ and k . The parameter k entering in the FLRW metric (2.1) defines three different spacetimes

$$k = \begin{cases} 0 & \text{Euclidean or flat,} \\ +1 & \text{spherical or closed,} \\ -1 & \text{hyperbolic or open,} \end{cases} \quad (2.5)$$

because $\gamma_{ij} dx^i dx^j$ becomes the three-dimensional Euclidean line element for $k = 0$ and so on. The three-dimensional curvature of the Universe is defined as ${}^3K(t) = k \cdot a^{-2}(t)$. Clearly, for $k = -1, 0$ the spacetime is infinite, while for $k = +1$ it is finite though unbounded. In this case, one defines its proper circumference ${}^3L(t) = 2\pi a(t)$ and its proper volume ${}^3V(t) = 2\pi^2 a^3(t)$. For $k = +1$, the spatial part of the Universe can be interpreted as a sphere or radius $a(t)$ embedded in a four-dimensional spacetime. Neither for $k = 0$ or $k = -1$ such interpretation is possible, but still $a(t)$ represents some scale factor that describes if the Universe is expanding, contracting or it is stationary.

2.1 Kinematics

Redshift

Particles, in absence of other non-gravitational forces, move along the geodesics of the underlying spacetime, which are the solutions of the geodesic equation

$$\frac{d^2 x^\mu}{d\lambda^2} + \Gamma_{\sigma\rho}^\mu \frac{dx^\sigma}{d\lambda} \frac{dx^\rho}{d\lambda} = 0, \quad (2.6)$$

where λ is an affine parameter describing the curve. For massive particles, the most simple choice for λ is the proper time τ . In a FLRW spacetime, the 0-th component of the geodesic equations is

$$\frac{d^2 x^0}{d\tau^2} + \Gamma_{\alpha\beta}^0 \frac{dx^\alpha}{d\tau} \frac{dx^\beta}{d\tau} = \frac{d^2 x^0}{d\tau^2} + \Gamma_{00}^0 \left(\frac{dx^0}{d\tau} \right)^2 + \Gamma_{ij}^0 \frac{dx^i}{d\tau} \frac{dx^j}{d\tau} = 0. \quad (2.7)$$

The Christoffel symbols in a FLRW Universe are

$$\begin{aligned}\Gamma_{00}^0 &= 0, & \Gamma_{0i}^0 &= 0, & \Gamma_{ij}^0 &= a(t)\dot{a}(t)\gamma_{ij}, \\ \Gamma_{00}^i &= 0, & \Gamma_{0i}^k &= \frac{\dot{a}}{a}\delta_i^k, & \Gamma_{ij}^k &= \frac{\gamma^{km}}{2}(\gamma_{im,j} + \gamma_{mj,i} - \gamma_{ij,m}),\end{aligned}\quad (2.8)$$

so that equation (2.7) reduces to

$$\frac{d^2x^0}{d\tau^2} + a(t)\dot{a}(t)\gamma_{ij}\frac{dx^i}{d\tau}\frac{dx^j}{d\tau} = 0. \quad (2.9)$$

It is better to write this equation in terms of the four-momentum, which is defined as

$$P^\mu \stackrel{\text{def}}{=} mU^\mu \equiv m\frac{dx^\mu}{d\tau} \equiv (P^0, \mathbf{P}), \quad (2.10)$$

and normalized as

$$-g_{\mu\nu}P^\mu P^\nu \equiv (P^0)^2 - a^2\gamma_{ij}P^i P^j \equiv -m^2g_{\mu\nu}\frac{dx^\mu}{d\tau}\frac{dx^\nu}{d\tau} = m^2. \quad (2.11)$$

The amplitude of the physical three-momentum p is defined by

$$p^2 \stackrel{\text{def}}{=} g_{ij}P^i P^j = a^2\gamma_{ij}P^i P^j. \quad (2.12)$$

This momentum is physical in the sense that it is the one measured in a local inertial coordinates system:

$$\eta_{\mu\nu}p^\mu p^\nu = -m^2 = g_{\mu\nu}P^\mu P^\nu, \quad (2.13)$$

where $p^\mu = (E, p^i)$. This condition implies $P^0 = E$. P^μ is the "comoving" four-momentum because it is the conjugate momentum of the comoving coordinate x^μ . In the case of a flat Universe, $\gamma_{ij} = \delta_{ij}$, the physical three-momentum p^i is related to the comoving one P^i by a factor a . The 0-th component of the geodesic equation in terms of p is

$$\frac{dp}{dt} + \frac{\dot{a}}{a}p = 0 \implies p \propto \frac{1}{a(t)}. \quad (2.14)$$

Massless particles move along null-geodesics $d\tau = 0$ and the momentum normalization is

$$(P^0)^2 - a^2\gamma_{ij}P^i P^j = 0. \quad (2.15)$$

It follows that the amplitude of the physical three-momentum in the massless case is simply E . In the massive case we have instead

$$P^i = m\frac{dx^i}{d\tau} = m\frac{dt}{d\tau}v^i, \quad (2.16)$$

where $v^i = \dot{x}^i$. From the normalization condition $-1 = g_{\mu\nu}(\mathrm{d}x^\mu/\mathrm{d}\tau)(\mathrm{d}x^\nu/\mathrm{d}\tau)$ we have further

$$\frac{\mathrm{d}t}{\mathrm{d}\tau} \left[1 - a^2 \gamma_{ij} v^i v^j \right] = 1, \quad (2.17)$$

and so in the massive case

$$p = \sqrt{-g_{ij} P^i P^j} = \sqrt{m^2 a^2 \gamma_{ij} v^i v^j (\mathrm{d}t/\mathrm{d}\tau)^2} = \frac{mv}{\sqrt{1-v^2}}, \quad (2.18)$$

where $v^2 = -g_{ij} v^i v^j = a^2 \gamma_{ij} v^i v^j$. To sum up,

$$p = \begin{cases} E & \text{massless particle,} \\ \frac{m|\mathbf{v}|}{\sqrt{1-|\mathbf{v}|^2}} & \text{particle with mass } m. \end{cases} \quad (2.19)$$

Equation (2.14) suggests that the energy of a massless particle scales as a^{-1} . As a consequence, also the wavelength of a massless particle $\lambda = h/E = h/p$ scales with $a(t)$. In particular, a photon emitted at t_1 with wavelength λ_1 will be detected at $t_0 > t_1$ with wavelength $\lambda_0 = \lambda_1 a(t_0)/a(t_1)$. If our Universe is expanding, $a(t_0) > a(t_1)$, then photons are redshifted $\lambda_0 > \lambda_1$, while if it is contracting light is blueshifted $\lambda_0 < \lambda_1$. It is conventional to define the redshift/blueshift parameter z as

$$z \stackrel{\text{def}}{=} \frac{\lambda_0 - \lambda_1}{\lambda_1}, \quad (2.20)$$

and in a FLRW spacetime it is equal to

$$z = \frac{a(t_0)}{a(t_1)} - 1. \quad (2.21)$$

Once $a(t)$ is known, the previous equation is a sort of conversion between the redshift and the cosmic time. Sometimes, cosmologists normalize $a(t)$ so that it is equal to one at the present day t_0 : $a(t_0) = 1$.

Distances

The proper distance is defined as the distance between two events measured in the frame of reference where they occur simultaneously:

$$s(t) \stackrel{\text{def}}{=} \int \mathrm{d}s|_{\mathrm{d}t=0} \stackrel{\text{def}}{=} \int \sqrt{-\mathrm{d}\tau^2}|_{\mathrm{d}t=0} = \int \sqrt{g_{\mu\nu} \mathrm{d}x^\mu \mathrm{d}x^\nu}|_{\mathrm{d}t=0} = \int \sqrt{g_{ij} \mathrm{d}x^i \mathrm{d}x^j}. \quad (2.22)$$

In a FLRW Universe it is conventionally computed in polar coordinates

$$\mathrm{d}s^2 = -\mathrm{d}\tau^2 = -\mathrm{d}t^2 + a^2(t) \left[\frac{\mathrm{d}r^2}{1-kr^2} + r^2(\mathrm{d}\theta^2 + \sin^2\theta \mathrm{d}\phi^2) \right]. \quad (2.23)$$

If the two events occur at $r = 0$ and $r = r_1$ with fixed angles θ and ϕ , s is given by:

$$s(t) = \int \sqrt{g_{\mu\nu} dx^\mu dx^\nu} \Big|_{dt=d\theta=d\phi=0} = \int_0^{r_1} \sqrt{g_{rr}} dr = a(t) \times \begin{cases} \sin^{-1} r_1 & k = +1 \\ \sinh^{-1} r_1 & k = -1 \\ r_1 & k = 0 \end{cases} \quad (2.24)$$

Another type of distance that can be defined in the FLRW Universe is the comoving, or coordinate, distance χ :

$$d\chi^2 \stackrel{\text{def}}{=} \gamma_{ij} dx^i dx^j \quad (2.25)$$

In polar coordinates and with $d\theta = d\phi = 0$, χ is equal to

$$\chi \equiv \int_0^{r_1} \frac{\sqrt{g_{rr}}}{a(t)} dr = \frac{s(t)}{a(t)}. \quad (2.26)$$

χ is the distance between two events as measured by a comoving observer that does not feel the expansion/contraction of the Universe. The comoving distance is equal to the change in conformal time: $\Delta\chi = \Delta\eta$.

Horizons

A consequence of the constancy of the speed of light is that not all events are in causal contact. In particular, only time-like or null-like separated events ($d\tau^2 \geq 0$ or $ds^2 \leq 0$) are causally connected. The boundaries of the causally connected region are set by the condition for photon propagation $d\tau = 0$. In a FLRW Universe, this condition corresponds to:

$$\int \frac{dt}{a(t)} = \int \sqrt{\gamma_{ij} dx^i dx^j}. \quad (2.27)$$

If the photon is radially emitted at $(t = 0, r_H)$ and the comoving observer is placed at $(t, r = 0)$, then r_H has to satisfy

$$\int_0^t \frac{dt}{a(t)} = \frac{1}{a(t_0)} \int_0^{r_H} \sqrt{g_{rr}} dr. \quad (2.28)$$

for the photon to reach the observer. The proper distance to the horizon is

$$s_H(t) = a(t) \int_0^t \frac{dt}{a(t)} \equiv a(t) \int_0^a \frac{da}{a^2 H(a)} \equiv a(t) \int_0^{r_H} \frac{dr}{\sqrt{1 - kr^2}}, \quad (2.29)$$

where it was assumed that $a(0) = 0$. $s_H(t)$ is called particle horizon and it sets the boundaries between the visible Universe and the regions from which light signals have not reached us.

By using equation (2.24), one can write the particle horizon as

$$s_H(t) = a(t) \times \begin{cases} \sin^{-1} r_H & k = +1, \\ \sinh^{-1} r_H & k = -1, \\ r_H & k = 0. \end{cases} \quad (2.30)$$

The particle horizon should not be confused with the Hubble radius $1/H(t)$, which represents the distance traveled by particles during one expansion time. The Hubble radius is a different way to know whether two particles are causally connected or not. If they are separated by a proper distance larger than $1/H(t)$ at time t , they cannot be causally connected at that time. The difference between the particle horizon and Hubble radius is the following. Particles separated by a proper distance larger than $s_H(t)$ have never been in causal contact, while if they are separated by a distance larger than $H^{-1}(t)$ then they cannot communicate at t .

The comoving particle horizon is instead defined as

$$r_H(t) \stackrel{\text{def}}{=} \int_0^t \frac{dt}{a(t)} = \int_0^a \frac{da}{a^2 H(a)} = \int_0^a d \ln(a) \frac{1}{aH(a)}, \quad (2.31)$$

where $(aH)^{-1}$ is the comoving Hubble radius. r_H can be obtained by inverting equation (2.30):

$$r_H = \begin{cases} \sin^{-1} \left(\int_0^t \frac{dt}{a(t)} \right) & k = +1, \\ \sinh^{-1} \left(\int_0^t \frac{dt}{a(t)} \right) & k = -1, \\ \left(\int_0^t \frac{dt}{a(t)} \right) & k = 0. \end{cases} \quad (2.32)$$

The physical meaning of the comoving particle horizon r_H is that particles separated by comoving distances larger than r_H do not talk to each other. On the other hand, if at some time t two particles were separated by a comoving distance larger than $(aH)^{-1}$ then they cannot communicate at that time.

2.2 Dynamics

One of the main goals of cosmological theories is to describe the evolution of the Universe, that is to find how the scale factor $a(t)$ evolves. The evolution of the scale factor is determined by Einstein field equations:

In a FLRW spacetime with $\Lambda = 0$, the components of the Ricci tensor are given by [22]

$$\begin{aligned} R_{00} &= 3 \frac{\ddot{a}}{a}, \\ R_{0i} &= 0, \\ R_{ij} &= - \left[2k + 2\dot{a}^2 + a(t)\ddot{a} \right] a^2 \gamma_{ij}, \end{aligned} \quad (2.33)$$

while the source term takes the form

$$S_{\mu\nu} = T_{\mu\nu} - \frac{1}{2}g_{\mu\nu}T_{\lambda}^{\lambda} = \frac{1}{2}(\rho - P)g_{\mu\nu} + (P + \rho)u_{\mu}u_{\nu}, \quad (2.34)$$

where u_{μ} is given in equation (1.17). The components of $S_{\mu\nu}$ are

$$S_{00} = \frac{1}{2}(\rho + 3P), \quad (2.35a)$$

$$S_{0i} = 0, \quad (2.35b)$$

$$S_{ij} = \frac{1}{2}(\rho - P)a^4\gamma_{ij}, \quad (2.35c)$$

and so Einstein equations read

$$(00)\text{-component :} \quad 3\ddot{a} = -4\pi G(\rho + 3P)a, \quad (2.36a)$$

$$(0i)\text{-components :} \quad 0 = 0, \quad (2.36b)$$

$$(ij)\text{-components :} \quad a\ddot{a} + 2\dot{a}^2 + 2k = 4\pi G(\rho - P)a^2. \quad (2.36c)$$

These equations can be combined into a single equation, the so-called Friedmann equation:

$$\dot{a}^2 + k = \frac{8\pi G}{3}\rho a^2. \quad (2.37)$$

Furthermore, the energy momentum tensor $T_{\mu\nu}$ has to satisfy the continuity equation $T_{;\nu}^{\mu\nu} = 0$. In a FLRW spacetime the $\mu = i$ components of the continuity equation are trivially satisfied, while the $\mu = 0$ one gives

$$\frac{d\rho}{dt} + 3\frac{\dot{a}}{a}(\rho + P) = 0. \quad (2.38)$$

To close the system it is necessary to specify an equation of state $P = P(\rho)$.

However, it is possible to find some characteristics of the scale factor $a(t)$ even without specifying an equation of state. For example, the time-time component of Einstein equations (2.36) suggests that as long as $\rho + 3P$ is positive, the quantity \ddot{a}/a is negative. Present observations measure redshift or equivalently $\dot{a}/a > 0$ - see equation (2.21) - and by definition $a(t_0) > 0$.

Then, as long as $\rho + 3P$ is positive, $a(t)$ versus t must be a concave downward curve and must have reached $a(t^*) = 0$ at some time t^* in the past. This instant of time is set equal to zero by definition and is called Big-Bang singularity.

Our Universe is expanding and the expansion is described by the temporal evolution of the scale factor $a(t)$. The rate of expansion is measured by the so-called Hubble parameter

$$H(t) \stackrel{\text{def}}{=} \frac{\dot{a}(t)}{a(t)}, \quad (2.39)$$

which can be defined also in conformal time

$$\mathcal{H}(\eta) \stackrel{\text{def}}{=} \frac{a'(\eta)}{a(\eta)} \equiv aH, \quad (2.40)$$

where the prime indicates a derivative with respect to the conformal time. Recent experiments try to measure the Hubble parameter today H_0 (Hubble constant)[†]. The Hubble rate is determined by the Friedmann equation, which can be written directly as an equation for H :

$$\frac{k}{H^2 a^2} = \frac{8\pi G}{3H^2} \rho - 1 \stackrel{\text{def}}{=} \Omega - 1 \quad \text{or} \quad H^2 = \frac{8\pi G}{3} \rho - \frac{k}{a^2}, \quad (2.41)$$

where Ω is the ratio between the total density of the Universe ρ and the critical density defined as

$$\Omega = \frac{\rho}{\rho_c} \quad \text{with} \quad \rho_c \stackrel{\text{def}}{=} \frac{3}{8\pi G} H^2. \quad (2.42)$$

Equation (2.41) determines the geometry of the Universe. Indeed, since $H^2 a^2 > 0$, there is a correspondence between the value of k and the sign of $\Omega - 1$: if $k = -1, 0, +1$ then $\Omega - 1$ negative, zero or positive respectively. To solve the Friedmann equation, an equation of state has to be specified. All the equations of state can be written as

$$P = w\rho. \quad (2.43)$$

The most simple choice is a time-independent w . Given this generic equation of state, equation (2.38) gives

$$\rho \propto a^{-3(1+w)} \implies \rho = \rho_0 \left(\frac{a}{a_0} \right)^{-3(1+w)}. \quad (2.44)$$

The Universe is not filled by one single fluid. In the standard cosmological model, the three sources that fill the Universe are:

- Matter: particles that have a pressure negligible with respect to the energy density. Examples are baryons, leptons and dark matter. In the matter case $w = 0$ and $\rho_m \propto a^{-3}$.
- Radiation: particles that are ultrarelativistic/massless Their equation of state is given by $P = (1/3)\rho$ or $w = 1/3$ Then $\rho_r \propto a^{-4}$. Examples are photons, neutrinos and gravitons (if they exist).
- Dark energy. Radiation and matter are not sufficient to describe the present-day Universe evolution, which is dominated by an unknown source, called dark energy, which satisfies the equation of state $P = -\rho$. In this case $w = -1$ and the energy density remains constant during the evolution of the Universe: $\rho_\Lambda \propto a^0$.

This model is called Λ CDM model because it includes cold dark matter and dark energy (Λ). In figure 1, we present the behavior of the energy density for the three different sources.

[†] from now on the subscript 0 means that the considered quantity is evaluated at the present day.

In general, the total energy density of the Universe is the sum of the contributions coming

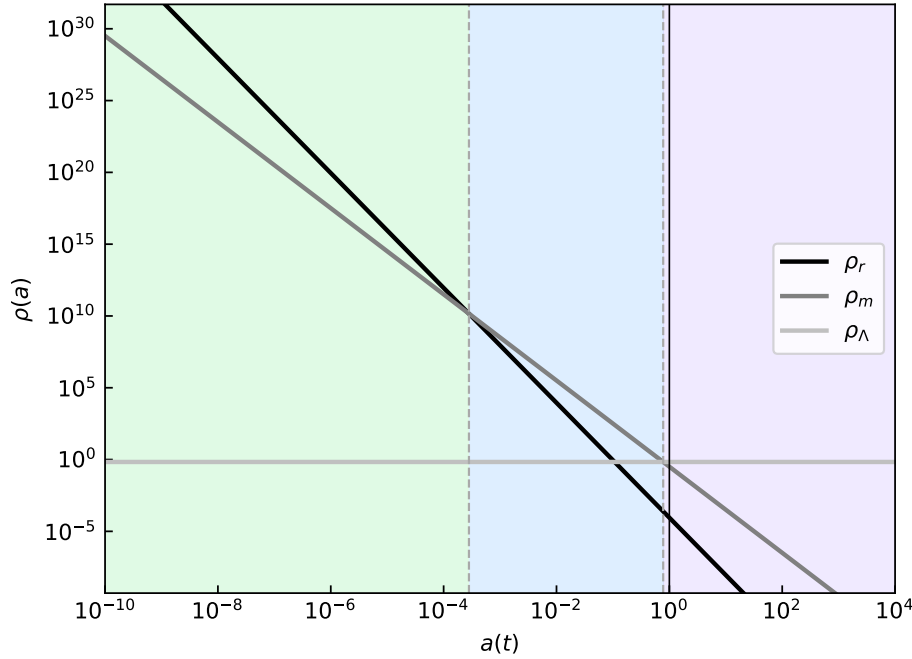


Fig. 1 – Behavior of the energy density for radiation, matter and dark energy in log-log scale. These lines are drawn by considering the present day abundances of matter, radiation and dark energy [18]: $\Omega_{r,0} = 8.99 \times 10^{-5}$, $\Omega_{m,0} = 0.32$, $\Omega_{\Lambda,0} = 0.68$. The curvature density is neglected since $|\Omega_{k,0}| < 0.005$. The green region on the left represents the radiation-dominated era. A dashed grey vertical line separates such region from the matter-dominated era (blue area). The purple region is instead the dark-energy-dominated epoch. The matter-radiation equivalence occurs when $\rho_m = \rho_r$, i.e. at $a(t) = a_{\text{eq}}(t_{\text{eq}}) = a_0 \Omega_{r,0} / \Omega_{m,0} \approx 2.9 \times 10^{-4}$, where the convention $a_0 = 1$ was assumed. The corresponding redshift is $z_{\text{eq}} = 1/a_{\text{eq}} - 1 \approx 3500$. Similarly, the transition from the matter-dominated Universe to the dark-energy-dominated one happens at $a_{m\Lambda}(t_{m\Lambda}) = a_0 (\Omega_{m,0} / \Omega_{\Lambda,0})^{1/3} \approx 0.77$ or $z_{m\Lambda} \approx 0.3$. The solid black vertical line centered on $a(t) = a_0 = 1$ indicates the present day.

from each source:

$$\Omega = \Omega_m + \Omega_r + \Omega_{\Lambda}. \quad (2.45)$$

Figure 1 suggests that at early times, when $a(t)$ was small, the energy density of the Universe was dominated by radiation, while at later times the main contribution to the total ρ came from matter. Finally, today the Universe is dominated by dark energy. The cosmic time when the energy density of the radiation was equal to those of the matter is called equivalence time t_{eq} . Well before and after the equivalence, the Universe can be considered as dominated by a single component, which is radiation for $t < t_{\text{eq}}$ or matter for $t > t_{\text{eq}}$. Around the equivalence we should treat the Universe as a two-components fluid. This is true also during the transition from the matter-dominated era to the dark-energy one.

Taking into account all the possible matter sources, the Friedmann equation (2.41) becomes:

$$H^2(a) = \sum_w \frac{8\pi G}{3} \rho_0^{(w)} \left(\frac{a}{a_0}\right)^{-3(1+w)} - \frac{k}{a^2}, \quad (2.46)$$

where \sum_w runs over all the possible values of w and where $\rho_0^{(w)}$ is the present-day value of

the energy density of the source parametrized by w . The previous equation in terms of the parameters Ω_w introduced in equation (2.42) is

$$H^2(a) = H_0^2 \left[\sum_w \Omega_{w,0} \left(\frac{a}{a_0} \right)^{-3(1+w)} + \Omega_{k,0} \left(\frac{a}{a_0} \right)^{-2} \right], \quad (2.47)$$

where we introduced a curvature density parameter $\Omega_{k,0} \stackrel{\text{def}}{=} -k/(a_0 H_0)^2$. The Hubble parameter as a function of the redshift is

$$H^2(z) = H_0^2 \left[\sum_w \Omega_{w,0} (1+z)^{3(1+w)} + \Omega_{k,0} (1+z)^2 \right]. \quad (2.48)$$

In a flat radiation-dominated Universe, i.e. $\Omega_m = \Omega_\Lambda = \Omega_k = 0$ and so $\Omega_r = 1$, the solution of the Friedmann equation is simply given by

$$H(a) \equiv \frac{\dot{a}}{a} = H_0 \left(\frac{a_0}{a} \right)^2 \implies a(t) = a_0 \sqrt{2H_0} \sqrt{t} \propto t^{1/2}, \quad (2.49)$$

while in the matter-dominated case it is

$$H(a) \equiv \frac{\dot{a}}{a} = H_0 \left(\frac{a_0}{a} \right)^{3/2} \implies a(t) = a_0 \left(\frac{3}{2} H_0 \right)^{2/3} t^{2/3} \propto t^{2/3}. \quad (2.50)$$

Finally, in a vacuum-energy-dominated Universe, $a(t)$ is given by

$$H(a) \equiv \frac{\dot{a}}{a} = H_0 \implies a(t) = e^{H_0 t} \propto e^t. \quad (2.51)$$

The equation describing the acceleration of the Universe is the (00) - Einstein equation (2.36), which in terms of the Hubble parameter (2.39) can be written as

$$\frac{dH}{dt} = \frac{\ddot{a}}{a} - \frac{\dot{a}^2}{a^2} \equiv -\frac{4\pi G}{3}(\rho + 3P) - H^2 \stackrel{\text{def}}{=} -H^2(1+q), \quad (2.52)$$

where we defined the so-called deceleration parameter

$$q \stackrel{\text{def}}{=} -\frac{\ddot{a}}{H^2 a} \equiv \frac{4\pi G}{3H^2}(\rho + 3P). \quad (2.53)$$

Its present-day value is given by

$$q_0 = \frac{1}{2} \sum_w (1+3w) \Omega_{w,0} \equiv \frac{1}{2} (\Omega_{m,0} + \Omega_{r,0} + \Omega_{\Lambda,0}). \quad (2.54)$$

Recent observations suggest $q_0 < 0$ implying that the Universe is accelerating.

3 Brief Thermal History of the Universe

The standard cosmological model which is nowadays favored by many cosmological data (although with some cracks due to re-known tensions) is based on the fact that when $a(t) = 0$, all the energy and the matter of the Universe were compressed in a really small region. At that time, the energy scale of the Universe, or equivalently its temperature, was really high. As the Universe expanded, the temperature dropped down, as it happens for example in an adiabatic expansion, and the energy got diluted. The story of the Universe is then a cooling history that can be studied using some concepts of statistical mechanics and thermodynamics. In this section, we study the evolution of cosmic sources with thermodynamics.

3.1 The Primordial Plasma

The first phases of the hot Big Bang model depend on the particle interaction laws, which are well known up to few hundred GeV. Under this energy scale, particle fundamental interactions are described by the so-called Standard Model.

At $t = 0$ the scale factor was zero and all the matter and energy of the universe were confined in a tiny region at a temperature larger than the Planck mass (10^{19}GeV). Above the TeV scale there are many ways to extend the Standard Model and so there is a huge uncertainty on the Universe matter content in the very first instants after the Big Bang. As the Universe expanded, the temperature of the Universe decreased until the scale of the Standard Model of particles is reached. From that instant, the physics of the Early Universe can be studied pretty accurately.

Equilibrium Thermodynamics

In the Early Universe, the interactions between the particles were so fast and efficient that all the particles were kept in local thermal equilibrium in a sort of 'primordial plasma' [†].

Each component of the primordial plasma can be treated as a diluted, weakly-interacting gas of particles with g degrees of freedom. For this kind of gas, one can define its number density n , energy density ρ and pressure p in terms of the phase space distribution $f(x, p)$, which tells how many particles there are in a given volume of the phase space at t .

Since the Universe evolved from a small hot and really dense point, one may ask in which epochs the phase-space description of the primordial plasma is possible. Presumably, this is possible as long as the de Broglie wavelength $\lambda = \hbar/p$ of the particles is small compared to the size of the Universe [23]. If T is the temperature of the Universe, then $\lambda \approx 1/T$. In a radiation-dominated Universe, the size of the Universe is roughly M_{pl}/T^2 , where $M_{pl} = (8\pi G)^{-1/2}$ is the reduced Planck mass in natural units. So, the phase-space description is valid as $T < M_{pl}$, which is almost always except near the Big Bang singularity.

[†] The empirical proof of the thermal equilibrium of the primordial plasma of particles lies in the spectrum of the relic photons that are detected today, as it will be explained in subsection 3.2.

To rigorously introduce f , consider a spacelike surface $d\sigma$, whose normal vector dS_μ is defined so that

$$dS_\mu = (a^3(t)dx dy dz, 0, 0, 0). \quad (3.1)$$

The phase space distribution of a given species in the primordial plasma $f(x, P)$ is defined so that the number of world-lines that penetrate $d\sigma$ is given by

$$dN = -f(x, P)P^\mu dS_\mu 2\delta^{(+)}(P^2 + m^2)d^4Pa^3, \quad (3.2)$$

where $P^2 \stackrel{\text{def}}{=} g_{\mu\nu}P^\mu P^\nu \equiv -(P^0)^2 + a^2\gamma_{ij}P^i P^j$ as usual. The quantity $\delta^{(+)}(P^2 + m^2)$ is defined by the relation

$$\begin{aligned} \delta(-(P^0)^2 + a^2\gamma_{ij}P^i P^j + m^2) &= \frac{\delta\left(P^0 - \sqrt{a^2\gamma_{ij}P^i P^j + m^2}\right) + \delta\left(P^0 + \sqrt{a^2\gamma_{ij}P^i P^j + m^2}\right)}{2P^0} = \\ &\stackrel{\text{def}}{=} \delta^{(+)}(P^2 + m^2) + \delta^{(-)}(P^2 + m^2). \end{aligned} \quad (3.3)$$

To study a gas of weakly-interacting particles it is necessary to determine how $f(x, P)$ varies along a world-line characterized by an affine parameter λ . In absence of interactions, the equation that determines such evolution is the collision-less Boltzmann equation

$$\hat{\mathbf{L}}[f] = 0. \quad (3.4)$$

where the Liouville operator in a FLRW spacetime is:

$$\hat{\mathbf{L}}[f] = \frac{\partial f}{\partial t} - \frac{\dot{a}}{a}p^i \frac{\partial f}{\partial p^i}, \quad (3.5)$$

A derivation of the Boltzmann equation can be found in [23].

f allows to define some macroscopic quantities that characterize the gas, such as the particle current density

$$N^\mu \stackrel{\text{def}}{=} g \int \frac{d^3p}{(2\pi)^2} f \frac{p^\mu}{p^0}, \quad (3.6)$$

where g is an additional factor that takes into account the degrees of freedom of the particle species. Isotropy implies that the only non-vanishing component of N^μ is the particle number density $N^0 \equiv n$:

$$n = g \int \frac{d^3p}{(2\pi)^3} f, \quad (3.7)$$

The covariant divergence of N^μ is

$$N^\mu{}_{;\mu} = \frac{g}{a^3} \frac{\partial}{\partial t} \left(a^3 \int \frac{d^3p}{(2\pi)^3} f \right) = 3g \frac{\dot{a}}{a} \int \frac{d^3p}{(2\pi)^3} f + g \frac{\dot{a}}{a} \int \frac{d^3p}{(2\pi)^3} p_i \frac{\partial f}{\partial p_i} + g \int \frac{d^3p}{(2\pi)^3} \hat{\mathbf{L}}[f]. \quad (3.8)$$

By integrating by parts and dropping boundary terms, the previous equation reduces to

$$\frac{1}{a^3} \frac{\partial(a^3 n)}{\partial t} = \int \frac{d^3 p}{(2\pi)^3} \hat{\mathbf{L}}[f](p). \quad (3.9)$$

In the collision-less case equation (3.4) holds and the conservation of the particle number density becomes

$$\frac{1}{a^3} \frac{\partial(a^3 n)}{\partial t} = 0 \longrightarrow n \propto a^{-3}. \quad (3.10)$$

The energy momentum-tensor of the gas is defined as

$$T^{\mu\nu} = g \int \frac{d^3 p}{(2\pi)^3} \frac{p^\mu p^\nu}{p^0} f(p), \quad (3.11)$$

and the energy density is given by

$$T^{00} = g \int \frac{d^3 p}{(2\pi)^3} p^0 f(p) = g \int \frac{d^3 p}{(2\pi)^3} E(p) f(p) \stackrel{\text{def}}{=} \rho. \quad (3.12)$$

In an isotropic Universe, T^{ij} does not depend on the direction and T^{ij} can be integrated along the direction to obtain the pressure of the gas

$$T^{ij} = \frac{g^{ij}}{3} \int \frac{d^3 p}{(2\pi)^3} \stackrel{\text{def}}{=} g^{ij} P. \quad (3.13)$$

To sum up, the number density, the energy density and the pressure of a weakly-interacting gas of particles can be expressed also in terms of the energy of the particle

$$n = g \int \frac{d^3 p}{(2\pi)^3} f(p) = g \int \frac{d^3 p}{(2\pi)^3} f(p), \quad (3.14a)$$

$$\rho = \frac{g}{g} \int \frac{d^3 p}{(2\pi)^3} f(p) E(p) = g \int \frac{d^3 p}{(2\pi)^3} f(p) E(p), \quad (3.14b)$$

$$P = g \int \frac{d^3 p}{(2\pi)^3} f(p) \frac{p^2}{3E(p)} = g \int \frac{d^3 p}{(2\pi)^3} f(p) \frac{p^2}{3E(p)}, \quad (3.14c)$$

where $E(p) = p^2 + m^2$.

A particle species is in thermodynamic equilibrium if its distribution function f_{eq} is a solution of the collision-less equation

$$\hat{\mathbf{L}}[f_{eq}] = 0. \quad (3.15)$$

It is possible to show [23] that in a FLRW Universe there is no solution to this equation, basically because the FLRW metric does not have a timelike Killing vector. There are only two limiting cases in which an equilibrium distribution exists: when $m \rightarrow 0$ (ultra-relativistic gas) and when $m \rightarrow \infty$ (non-relativistic gas). However, if the interactions between particles

were faster than the expansion of the Universe, particles had enough time to set a state of local thermal equilibrium. The basic rule to determine if a particle species was in thermal equilibrium with the primordial plasma is to compare the Hubble rate H with the interaction efficiency

$$\Gamma \stackrel{\text{def}}{=} n\sigma|v|, \quad (3.16)$$

where n is the density of the target particle species and $\sigma|v|$ the cross section times the relative velocity properly averaged. As long as $\Gamma > H$, the interactions are occurring rapidly enough to maintain the local thermal equilibrium. When $\Gamma < H$, the interactions are 'frozen', in the sense that they are negligible compared to the Universe expansion, and the particle species decouples from the plasma. The temperature at which $\Gamma = H$ is called 'freeze-out' temperature. These little departures from thermal equilibrium are fundamental to explain the present structure of the Universe. Indeed, if the Universe would have been always in thermal equilibrium, it will be filled with a plasma of particles and there will be no complex structures like galaxies, stars, planets and us. A careful treatment of non-equilibrium processes requires the inclusion of interactions between particles in the Boltzmann equation.

The form of the phase space distribution is known both for fermions (+) and bosons (−) when they are in thermal equilibrium within the primordial plasma:

$$f(t, p) = \left[\exp\left(\frac{E(p) - \mu}{T}\right) \pm 1 \right]^{-1}. \quad (3.17)$$

The phase space distribution is determined by the temperature T and the chemical potential μ of the considered gas. In an expanding Universe, the temperature evolves with time and so $f(t, p)$ depends implicitly on t . The chemical potential describes the response of a system to a change in particle number and it can be temperature dependent. In the non-relativistic limit ($T \ll m$), both fermionic and bosonic phase space distributions reduce to the Maxwell-Boltzmann one

$$f(t, p) = \exp\left(-\frac{E(p) - \mu}{T}\right). \quad (3.18)$$

Each particle species has its distribution function f_i that depends on (m_i, T_i, μ_i) . Species in thermal equilibrium share the same temperature T and so they differ only because of their different masses and/or chemical potentials.

By inserting equation (3.17) into (3.14), we find implicit relations between ρ , n , P and the temperature T . In the relativistic limit $T \gg m$ and for $T \gg \mu$ these relations are

$$n = \begin{cases} (\zeta(3)/\pi^2)gT^3, & \text{bosons} \\ (3/4)(\zeta(3)/\pi^2)gT^3, & \text{fermions} \end{cases} \quad (3.19a)$$

$$\rho = \begin{cases} (\pi^2/30)gT^4, & \text{bosons} \\ (7/8)\pi^2/30)gT^4, & \text{fermions} \end{cases} \quad (3.19b)$$

$$P = \rho/3, \quad (3.19c)$$

where $\zeta(x)$ is the Riemann zeta function:

$$\zeta(s) \stackrel{\text{def}}{=} \frac{1}{\Gamma(s)} \int_0^\infty dx \frac{x^{s-1}}{e^x - 1} \quad \text{where} \quad \Gamma(s) \stackrel{\text{def}}{=} \int_0^\infty dx x^{s-1} e^{-x}. \quad (3.20)$$

In the non-relativistic case these relations are instead:

$$n = g \left(\frac{mT}{2\pi} \right)^{3/2} \exp[-(m - \mu)/T], \quad (3.21a)$$

$$\rho = mn, \quad (3.21b)$$

$$p = nT \ll \rho. \quad (3.21c)$$

At early times chemical potentials of all particles were much smaller than the shared temperature [24]. Then, the total energy density and pressure of a collection of different species in thermal equilibrium at temperature T were [25]

$$\rho_t = T^4 \sum_{i=\text{all species}} \left(\frac{T_i}{T} \right)^4 \frac{g_i}{2\pi^2} \int_{x_i}^\infty du \frac{u^2 (u^2 - x_i^2)^{1/2}}{\exp(u - y_i) \pm 1}, \quad (3.22a)$$

$$P_t = T^4 \sum_{i=\text{all species}} \left(\frac{T_i}{T} \right)^4 \frac{g_i}{6\pi^2} \int_{x_i}^\infty du \frac{(u^2 - x_i^2)^{3/2}}{\exp(u - y_i) \pm 1}, \quad (3.22b)$$

where $x_i \stackrel{\text{def}}{=} m_i/T$, $y_i \stackrel{\text{def}}{=} \mu_i/T$. However, the energy density and pressure of a non-relativistic species are exponentially smaller than that of a relativistic one. This is evident from the comparison of equations (3.19a) and (3.21). So, a good approximation is to include only the relativistic species in the previous summations:

$$\rho_t = \frac{\pi^2}{30} g_* T^4 \equiv \rho_R, \quad (3.23a)$$

$$P_t = \rho_t/3 \equiv p_R, \quad (3.23b)$$

where g_* is the effective number of degrees of freedom

$$g_* \stackrel{\text{def}}{=} \sum_{i=\text{bosons}} g_i \left(\frac{T_i}{T} \right)^4 + \frac{7}{8} \sum_{j=\text{fermions}} g_j \left(\frac{T_j}{T} \right)^4. \quad (3.24)$$

The factor (7/8) comes from equation (3.19a) and relates to the different contribution to ρ of relativistic fermions with respect to bosons. When all particles are in thermal equilibrium, i.e. $T_i = T, \forall i$, g_* is determined only by the type of particles present in the plasma. When a particle species decouples from the Plasma, the effective number of degrees of freedom changes.

In the early Universe all the Standard Model particles and antiparticles - with all the

possible flavors - were present and in thermal equilibrium and so

$$g_* = g_\gamma + 3g_{W^\pm, Z_0} + 8g_g + g_H + \frac{7}{8}(6g_l + 36g_q + 6g_\nu) = 106.75. \quad (3.25)$$

As the energy decreased, some particle species became non-relativistic and they annihilated. The first particle species to annihilate was the top quark because it is the heaviest. This happened at $T \approx (1/6)m_t \approx 30\text{Gev}^\dagger$. After the top quark annihilation, the effective number of degrees of freedom became $g_* = 106.75 - (7/8) * 6 * g_q = 96.25$. Next, Higgs and other gauge bosons annihilated (at $T \approx 10\text{GeV}$) and so $g_* = 86.25$. Later on, the bottom and charm quark and the tau leptons annihilated and g_* turned into 61.75. Before the strange quarks had time to annihilate, the QCD phase transition occurred ($T_{qh} \approx 200\text{MeV}$) in which the remaining quarks in the plasma combined into hadrons, including protons, neutrons and pions. All of these particles, except the pions (which carry $g_\pi = 1$), are non-relativistic at a temperature below T_{qh} and so they should not be included in the computation of g_* , which thus dropped down to $g_* = 17.25$. After the QCD phase transition, pions and muons annihilated and $g_* = 10.75$.

Temperature of decoupled species

We now derive the evolution of the temperature of a particle species that decouples from the plasma. Consider a massless particle species, initially in local thermal equilibrium, that decouples from the thermal bath at time t_D when the temperature is T_D and the scale factor is $a(t_D) = a_D$. The phase space distribution at decoupling is given in (3.17) with $T = T_D$ and $\mu = 0$ for simplicity. After the decoupling, the momentum - and so the energy - of each massless particle is redshifted: $E(t) = E(t_D)(a_D/a(t))$. The number density of the massless species goes instead as $n \propto a^{-3}$ after the decoupling. Thus, the phase space distribution is the same of a species in local thermal equilibrium, but with a redshifted temperature $T(t) = T_D a_D/a(t)$. For a non-relativistic massive particle species the temperature is like a^{-2} - not a^{-1} - because the energy $E = |\mathbf{p}|^2/2m$ and not $E = |\mathbf{p}|$ as in the massless case. In the massive case, also the chemical potential has to vary like $\mu(t) = m + (\mu_D - m)T(t)/T_D$ in order to have $n \propto a^{-3}$. To sum up

$$T(t) = \begin{cases} T_D \left(\frac{a_D}{a(t)} \right)^1 \propto (1+z) & \text{decoupled massless species,} & (3.26a) \\ T_D \left(\frac{a_D}{a(t)} \right)^2 \propto (1+z)^2 & \text{decoupled massive species.} & (3.26b) \end{cases}$$

[†] the 1/6 factor takes into account that the transition from the relativistic to the non-relativistic behavior is not instantaneous.

3.2 Recombination and the Cosmic Microwave Background

Three minutes after the Big Bang the lightest nuclei of the known atoms - hydrogen and helium - formed. As long as the temperature is above 1 eV, the plasma is made of electrons, positrons, photons and the lightest nuclei in thermal equilibrium. In particular, photons are kept in thermal equilibrium mainly via Compton scattering with the electrons. The few hydrogen atoms produced in this period are rapidly destroyed by energetic photons. However, when $T < 0.3\text{eV}$, electrons and nuclei can combine permanently in hydrogen and helium atoms. This is the so-called recombination. As atoms form, the fraction of free electrons decreases and the Compton scattering becomes less efficient and photons decouple from the plasma. Relic photons form the cosmic microwave background.

Recombination

When a generic $1 + 2 \leftrightarrow 3 + 4$ reaction is in chemical equilibrium, the chemical potentials of the species involved satisfy the condition $\mu_1 + \mu_2 \leftrightarrow \mu_3 + \mu_4$. Furthermore, when the number of a given particle species is not conserved, its chemical potential vanishes. In the $e^- + p \leftrightarrow H + \gamma$ reaction, the chemical potentials satisfy

$$\mu_e + \mu_p = \mu_H, \quad (3.27)$$

because photon number is not conserved [26]. This is valid only in full thermal equilibrium, thus neglecting recombination into excited states of hydrogen. A more refined treatment of recombination needs to consider the helium fraction and the multi-level atomic structure of hydrogen. This requires non-equilibrium thermodynamics and usually it is done numerically. However, a roughly correct treatment of recombination can be still done with equilibrium thermodynamics. In thermal equilibrium at $T < 0.3\text{eV}$, electrons, protons and hydrogen atoms are non-relativistic and their number densities are given by equation (3.21). The Universe is electrically neutral, $n_e = n_p$, and chemical potentials satisfy $n_e + n_p = n_H$. Thus:

$$\frac{n_e^2}{n_H} = \frac{n_e n_p}{n_H} = \frac{g_e g_p}{g_H} \left(\frac{m_e m_p T}{m_H 2\pi} \right)^{3/2} \exp\left(-\frac{m_e + m_p - m_H}{T}\right). \quad (3.28)$$

The degrees of freedom are $g_e = g_p = 2$, $g_H = 4$ and m_p is roughly equal to m_H . The quantity $m_e + m_p - m_H \stackrel{\text{def}}{=} \Delta = 13.6\text{eV}$ is the binding energy of the hydrogen. The previous equation is equivalent to

$$\frac{n_e^2}{n_H} = \left(\frac{m_e T}{2\pi} \right)^{3/2} e^{-\Delta/T}. \quad (3.29)$$

It is convenient to introduce the free electron fraction

$$X_e \stackrel{\text{def}}{=} \frac{n_e}{n_p + n_H} \equiv \frac{n_e}{n_e + n_H}. \quad (3.30)$$

A full ionized Universe has $X_e = 1$, while a Universe with no free electrons at all has $X_e = 0$. We write

$$\frac{X_e^2}{1 - X_e} = \frac{n_e^2}{(n_H + n_p - n_e)(n_p + n_H)} \equiv \frac{n_e^2}{n_H(n_p + n_H)}, \quad (3.31)$$

where $n_p + n_H = n_b$ is the baryon density. Furthermore, $n_b = \eta n_\gamma$, where $\eta \approx 5.5 \times 10^{-10}$ is the baryon-to-photon ratio. By using equation (3.29), we can write

$$\frac{X_e^2}{1 - X_e} = \frac{1}{\eta n_\gamma} \frac{n_e^2}{n_H} = \frac{1}{\eta n_\gamma} \left(\frac{m_e T}{2\pi} \right)^{3/2} e^{-\Delta/T}. \quad (3.32)$$

By using the expression for the number of density of photons in thermal equilibrium (3.19a), we can write the previous as

$$\frac{X_e^2}{1 - X_e} = \frac{\pi^2}{2\eta\zeta(3)} \left(\frac{m_e}{2\pi T} \right)^{3/2} e^{-\Delta/T}. \quad (3.33)$$

This is the Saha equation. Notice that for $T \sim \Delta$, the right hand side of the Saha equation is of order 10^{15} and the equation can be satisfied only for X_e very close to 1, that is when all hydrogen is ionized. The time of recombination is conventionally defined as the moment when $X_e = 0.5$. This is possible only when $T \ll \Delta$. Saha equation is not exact, but it is valid only in the hypothesis that recombination proceeded in full thermal equilibrium. This cannot be true since as long as X_e falls, also the rate of the interaction between electrons and photons drops and thermodynamic equilibrium is difficult to maintain [27]. To follow the free electron fraction accurately, non-equilibrium thermodynamics is necessary and this will be done in section 4.2.

The Saha equation allows making a good estimation of the recombination temperature, which is $T_{\text{rec}} = 0.335\text{eV}$. The corresponding redshift can be computed by assuming that shortly after T_{rec} photons decouple from the plasma and from that moment their temperature evolves as a^{-1} . Then, we can project backward in time the present day photon temperature $T_0 = 2.72548\text{K}$ [28] until recombination: $T_{\text{rec}} = T_0(1 + z_{\text{rec}})$. This gives $z_{\text{rec}} = 1425$.

The end of recombination is defined as the moment when the free electron fraction is the 10%. The Saha equation is not able to find the corresponding redshift because it fails as X_e drops down. It is still possible to estimate the end of recombination by comparing the interaction efficiency of the reaction $e^- + p \leftrightarrow H + \gamma$, which is [26]

$$\begin{aligned} \Gamma_R &= n_p \sigma_R |v| = X_e \left(\frac{0.75 n_b}{n_\gamma} \right) n_\gamma \sigma_R |v| = \\ &\approx X_e \left(\frac{0.75 n_b}{n_\gamma} \right) n_\gamma 4.7 \times 10^{-24} \left(\frac{T}{1\text{eV}} \right)^{-1/2} \text{cm}^2 = \\ &\approx 2.1 \times 10^{-10} \text{cm}^{-1} \left(\frac{T}{1\text{eV}} \right)^{7/4} e^{-\Delta/2T} (\Omega_b h^2)^{1/2}, \end{aligned} \quad (3.34)$$

where Ω_b is the ratio between the density of baryons and the critical one, with the Hubble

rate, that can be obtained from equation (2.46) by assuming a matter-dominated flat universe

$$H^2 = \frac{8\pi G}{3}\rho = \frac{8\pi G}{3}\rho_0 \left(\frac{a_0}{a}\right)^3 = \frac{8\pi G}{3}\Omega_m\rho_c(t_0) \left(\frac{T}{T_0}\right)^3. \quad (3.35)$$

The recombination freeze out temperature T_g is defined as $\Gamma_R(T_g) = H(T_g)$ and it is obtained from

$$\left(\frac{T_g}{1\text{eV}}\right)^{1/4} e^{-\Delta/2T_g} \approx 1.4 \times 10^{-13} \left(\frac{\Omega_m}{\Omega_b}\right)^{1/2}. \quad (3.36)$$

From [18] one has $\Omega_m \approx 6.4\Omega_b$ and thus $T_g \approx 0.24\text{eV}$. The corresponding redshift is $z_g \approx 1010$.

Photon Decoupling

The main interaction that keeps photons in equilibrium with the plasma is Compton scattering with electrons, whose interaction efficiency is given by $\Gamma_\gamma \approx n_e\sigma_T$ (photons have $|v| = 1$), where $\sigma_T = (8\pi/3)\alpha^2 m_e^{-2} \approx 2 \times 10^{-3}\text{MeV}^{-2}$ is the Thomson cross section. This interaction efficiency depends on the temperature since n_e does. Indeed, by using $n_e = X_e n_b = X_e \eta n_\gamma$ and equation (3.19a) for n_γ we can write

$$\Gamma_\gamma(T) = \sigma_T X_e(T) \eta \frac{2\zeta(3)}{\pi^2} T^3. \quad (3.37)$$

The photon decoupling temperature is

$$X_e(T_{\text{dec}}) T_{\text{dec}}^{3/2} = \frac{\pi^2}{2\zeta(3)\eta\sigma_T} \sqrt{\frac{8\pi G\Omega_m\rho(t_0)}{3T_0^3}} \implies T_{\text{dec}} \approx 0.25\text{eV}. \quad (3.38)$$

This temperature corresponds to the redshift $z_{\text{dec}} \approx 1100$. So, photon decoupling occurs during recombination.

This redshift is also called 'last scattering surface'. This definition is related to the one of optical depth. In general, light emitted with intensity I_0 , travelling in a medium, will be observed at distance \mathbf{r} with intensity $I(\mathbf{r}) = I_0 e^{-\tau(\mathbf{r})}$. The function τ is called optical depth of the medium: if $\tau \ll 1$ the medium is transparent or optically thin, while if $\tau \gg 1$ the medium is said to be optically thick. In cosmology, the Thomson scattering between electrons and photons is a sort of medium and we can define the Thomson optical depth

$$\tau(t) = \int_t^{t_0} dt' \Gamma_\gamma(t') = \int_t^{t_0} dt' \sigma_T n_e(t'). \quad (3.39)$$

$e^{-\tau(t)}$ is the probability for a photon to not scatter between t and t_0 . Then, the probability for a photon to scatter for the last time between t and $t + dt$ is

$$\frac{d}{dt} (1 - e^{-\tau(t)}) dt = e^{-\tau(t)} \frac{d\tau(t)}{dt} dt = \sigma_T n_e(t) e^{-\tau(t)} \stackrel{\text{def}}{=} g(t) dt. \quad (3.40)$$

$g(t)$ is called visibility function and it is the probability density of last scatter between t and $t + dt$. In redshift space such probability is expressed as

$$g(z)dz = g(t(z))\frac{dt}{dz}dz = \frac{\sigma_T n_e(z)e^{-\tau(z)}}{(1+z)H(z)}dz, \quad (3.41)$$

where the relation between t and z

$$t \equiv \int dt' \equiv \int_0^a \frac{da}{\dot{a}} \equiv \int_0^a \frac{da}{aH(a)} \equiv \int_{(1+z)^{-1}}^\infty \frac{dz}{(1+z)H(z)}. \quad (3.42)$$

was used. The last scattering redshift z_{ls} corresponds to the maximum of the function $g(z)$: at this redshift photons have the highest probability to scatter for the last time.

Reionization

In the hypothesis that $X_e = 1$ always, equation (3.38) suggests that photons still could decouple from the plasma due to the expansion of the Universe. In this case, the decoupling redshift z'_{dec} is given by

$$1 + z'_{\text{dec}} = T_0^{-1} \left(\frac{\pi^2}{2\zeta(3)\eta\sigma_T} \sqrt{\frac{8\pi G\Omega_m\rho(t_0)}{3T_0^3}} \right)^{2/3}. \quad (3.43)$$

Current observations show that at $z_{\text{reio}} \approx 6$ the Universe was reionized. If the Universe was reionized at very early times before z'_{dec} , the observables linked to CMB would be dramatically affected. Since $z_{\text{reio}} \ll z'_{\text{dec}}$, the alteration is slight.

CMB spectrum

If photons were in local thermal equilibrium at decoupling, their present phase space distribution is expected to have a black body shape (see equation (3.26) and the discussion above it). A measure of such distribution would be able to prove if the primordial plasma was really in local thermal equilibrium.

Actually, the phase space distribution is not observable, but we measure the CMB spectral intensity $u(\nu)$, which is the flux of energy per unit of volume and per unit of frequency [†]:

$$u(\nu) \stackrel{\text{def}}{=} \frac{\partial\rho(h\nu)}{\partial\nu} \implies \rho = \int_0^\infty d\nu u(\nu). \quad (3.44)$$

By using equations (3.14),(3.17) and the fact that photons satisfy $E(p) = c|p| = h\nu$, we find

$$\rho(\nu) = \frac{g}{h^3} \int d^3p \frac{E(p)}{\exp\left(\frac{E(p)}{k_B T_0}\right) - 1} = \frac{4\pi gh}{c^3} \int_0^\infty d\nu \frac{\nu^3}{\exp\left(\frac{h\nu}{k_B T_0}\right) - 1}. \quad (3.45)$$

[†] only for this computation the standard units are temporarily restored

We performed an integration over the solid angle. Since photons have $g = 2$, one gets

$$u(\nu) = \frac{8\pi h}{c^3} \frac{\nu^3}{\exp\left(\frac{h\nu}{k_B T_0}\right) - 1}. \quad (3.46)$$

The intensity, or spectral radiance, is defined as

$$I(\nu) = \frac{c}{4\pi} u(\nu) \equiv \frac{2h}{c^2} \frac{\nu^3}{\exp\left(\frac{h\nu}{k_B T_0}\right) - 1}. \quad (3.47)$$

In figure 2 we plot the data measured by the COBE/FIRAS mission and the theoretical prediction of the black body intensity (3.46) at temperature [28]

$$T_0 = (2.72548 \pm 0.00057)\text{K}. \quad (3.48)$$

The data agree with the black body prediction. Deviations from a pure black body spectrum

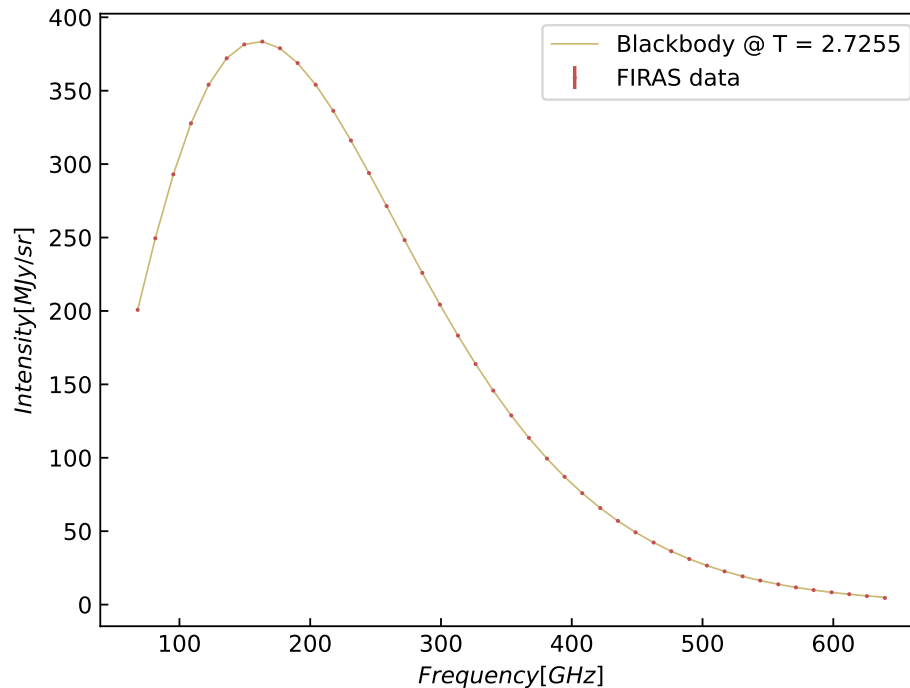


Fig. 2 – CMB intensity spectrum as measured by COBE/Firas mission [28]. The solid represents the theoretical prediction for a blackbody at temperature T_0 given by (3.48). Error bars are not visible since their order of magnitude is kJy sr^{-1} .

are parametrized with two adimensional parameters μ and y . These parameters are strictly constrained by the FIRAS mission [1]:

$$|\mu| < 9 \times 10^{-5}, \quad |y| < 1.5 \times 10^{-5}. \quad (3.49)$$

II

CMB SPECTRAL DISTORTIONS

The early Universe was in thermal equilibrium because the CMB spectrum has an almost perfect black body shape. However, even in the standard cosmological model, we expect deviations from the black body shape, called spectral distortions (SDs). There are mainly two types of SDs, whose (adimensional) amplitudes are usually written as μ and y . The latest measurement of the CMB spectrum is due to the COBE/FIRAS mission in the early 90's, which did not detect any deviations from the black body shape and set tight constraints on μ and y (3.49). Every cosmological model has to satisfy these constraints.

With present-day technology, a future space-based spectrometer, like Pixie [8] or the one proposed to answer the ESA Voyage 2050 call [11], could improve by three orders of magnitude the constraints on μ and y . This could be a crucial test for the Λ CDM model because it predicts SDs of the order of 10^{-8} . Furthermore, Λ CDM SDs are generated at small scales, where this model has never been tested before. CMB SDs can also constrain exotic scenarios, such as primordial black hole evaporation or annihilating dark matter.

Most of the work made in this thesis was devoted to understanding the physics behind CMB SDs, how they are generated and how they can be used to test different cosmological models. In this chapter, we present a review of SDs physics. In the first section, the thermalization problem, which tries to understand how CMB reacts to deviations from thermal equilibrium, is introduced. In the second section, we describe the characteristics of SDs. Finally, in the last section of the chapter, we list some causes of SDs. To be more precise, a particular source of SDs, which provide the case of interest for this thesis, will be examined in depth in chapter IV.

4 Formulation of the thermalization problem

4.1 Black body radiation

When the temperature of the Universe was between m_e and the recombination temperature T_{rec} , the primordial plasma contained mainly photons and electrons/positrons that interacted mostly via Compton scattering (CS), $e + \gamma \rightarrow e + \gamma$, double Compton scattering (DCS), $e + \gamma \rightarrow e + 2\gamma$, and Bremsstrahlung (BR), $e + X \rightarrow e + X + \gamma$, where X is an atomic nucleus, usually a helium-4 or hydrogen nucleus. In particular, CS is a process that redistributes photons/electrons in energy while DCS and BR are photons-number-changing interactions. As long as these three interactions were efficient, they were able to smooth out

any departure from thermal equilibrium in the photons-electrons/positrons bath. This effect is called thermalization of the CMB.

To understand naively how thermalization works, forget for a while about the Universe and consider a box with a hole filled with electrons and photons in thermal equilibrium. Since photons are in thermal equilibrium, their intensity spectrum will have the shape of a Planckian spectrum. Imagine now heating one side of the box for a small time. In this time interval, photons that hit the hot wall of the box heated up. Equivalently, we can say that there is an energy-release in the photons-electrons bath that causes a departure from thermal equilibrium and thus a distortion of the photons black body spectrum. However, thanks to the Compton scattering between electrons and high energetic photons, most of the injected energy is redistributed among electrons and lower energetic photons. If there are too many energetic photons, number changing processes, like the BR or DCS, transform these photons in lower energy one until the black body shape is restored. Of course, due to the conservation of energy, the temperature of the black body increases, so that the final spectrum is still Planckian but with an increased temperature.

When CS, DCS and BR stop being efficient, energy releases do not simply translate into a temperature shift of the Planckian spectrum. Indeed, if the box expands, as the Universe does, the interactions become less efficient because the mean free path between electrons and photons increases. As a consequence, energy releases could not be fully thermalized causing the so-called SDs of the photons spectrum.

4.2 Beyond thermal equilibrium

To formalize the thermalization problem, it is necessary to include collisions in the context of the Boltzmann equation and to follow the evolution of the photon phase space distributions.

When collisions are not negligible, the collision-less Boltzmann equation (3.4) is modified as

$$\hat{\mathbf{L}}[f] = \mathbf{C}[f], \quad (4.1)$$

where \mathbf{C} is the collision operator and includes all the interactions between the considered species and all the other ones. Its form depends on the specific interactions considered. In the case of thermal equilibrium, both sides of the Boltzmann equation are zero. By integrating the Boltzmann equation over $g d^3 p / (2\pi)^3$ and by using equation (3.9), we get

$$\frac{dn}{dt} + 3Hn = \frac{g}{(2\pi)^3} \int d^3 p \mathbf{C}[f]. \quad (4.2)$$

Consider for example a species ψ that undergoes to the process $\psi + a + b + \dots \longleftrightarrow i + j + \dots$. The integrated collision operator in this case is

$$\begin{aligned} \frac{g}{(2\pi)^3} \int d^3 p_\psi \mathbf{C}[f_\psi] &= \int d\Pi_\psi d\Pi_a d\Pi_b \dots d\Pi_i d\Pi_j \dots \times \\ &\times (2\pi)^4 \delta^4(p_\psi + p_a + p_b \dots - p_i - p_j \dots) \times \end{aligned}$$

$$\begin{aligned} & \times \left[|\mathcal{M}|_{i+j+\dots \rightarrow \psi+a+b+\dots}^2 f_i f_j \dots (1 \pm f_a)(1 \pm f_b) \dots (1 \pm f_\psi) \right. \\ & \left. - |\mathcal{M}|_{\psi+a+b+\dots \rightarrow i+j+\dots}^2 f_a f_b \dots f_\psi (1 \pm f_i)(1 \pm f_j) \dots \right], \end{aligned} \quad (4.3)$$

where $+$ ($-$) applies for bosons (fermions) and where the phase space volume element is defined as

$$d\Pi = \frac{g}{(2\pi)^3} \frac{d^3 p}{2E}. \quad (4.4)$$

We then identify the collision operator $\mathcal{C}[f_\psi]$ as

$$\begin{aligned} \mathcal{C}[f_\psi] &= \frac{1}{2E_\psi} \int d\Pi_a d\Pi_b \dots d\Pi_i d\Pi_j \dots \times \\ & \times (2\pi)^4 \delta^4(p_\psi + p_a + p_b \dots - p_i - p_j \dots) \times \\ & \times \left[|\mathcal{M}|_{i+j+\dots \rightarrow \psi+a+b+\dots}^2 f_i f_j \dots (1 \pm f_a)(1 \pm f_b) \dots (1 \pm f_\psi) \right. \\ & \left. - |\mathcal{M}|_{\psi+a+b+\dots \rightarrow i+j+\dots}^2 f_a f_b \dots f_\psi (1 \pm f_i)(1 \pm f_j) \dots \right]. \end{aligned} \quad (4.5)$$

The 4-dimensional delta function ensures momentum conservation, while $|\mathcal{M}|_{\psi+a+b+\dots \rightarrow i+j+\dots}^2$ is the module squared matrix element for the process $\psi + a + b + \dots \rightarrow i + j + \dots$ averaged over initial and final spin states. \mathcal{M} includes also an appropriate symmetry factor. The first term in the squared brackets of $\mathcal{C}[f_\psi]$ represents the production of ψ particles while the second one represents their destruction.

In the primordial plasma there were more than one particle species, say n . The evolution of each species is determined by a set of n Boltzmann equations coupled via the collision operators C_i . This set of integral-partial differential equations is difficult to be solved and to simplify calculations it is common to consider equilibrium distributions for those species that rapidly interact with the other ones. We also assume CP invariance so that the previous system becomes $|\mathcal{M}|_{\psi+a+b+\dots \rightarrow i+j+\dots}^2 = |\mathcal{M}|_{i+j+\dots \rightarrow \psi+a+b+\dots}^2 \stackrel{\text{def}}{=} |\mathcal{M}|^2$ and thus

$$\begin{aligned} \mathcal{C}[f_\psi] &= \frac{1}{2E_\psi} \int d\Pi_a d\Pi_b \dots d\Pi_i d\Pi_j \dots \times \\ & \times (2\pi)^4 \delta^4(p_\psi + p_a + p_b \dots - p_i - p_j \dots) |\mathcal{M}|^2 \times \\ & \times [f_i f_j \dots (1 \pm f_a)(1 \pm f_b) \dots (1 \pm f_\psi) \\ & - f_a f_b \dots f_\psi (1 \pm f_i)(1 \pm f_j) \dots]. \end{aligned} \quad (4.6)$$

When the temperature of the system is smaller than $E - \mu$, it is possible to use the Maxwell-Boltzmann distribution instead of the Fermi-Dirac or Bose-Einstein ones. This gives $1 \pm f \approx 1$ and so $[f_i f_j \dots - f_a f_b \dots f_\psi]$.

In the case of a $1 + 2 \leftrightarrow 3 + 4$ process, the Boltzmann equation for the species "1" is

$$\begin{aligned} \dot{n}_1 + 3Hn_1 &= \int d\Pi_1 d\Pi_2 d\Pi_3 d\Pi_4 (2\pi)^4 \delta^4(p_1 + p_2 - p_3 - p_4) |\mathcal{M}|^2 \times \\ & \times [f_3 f_4 (1 \pm f_1)(1 \pm f_2) - f_1 f_2 (1 \pm f_3)(1 \pm f_4)]. \end{aligned} \quad (4.7)$$

Notice that the left-hand side of the previous equation is nothing but $a^{-3} d(n_\psi a^3)/dt$ and clearly in absence of interaction - $|\mathcal{M}| = 0$ - the solution is $n_\psi \propto a^{-3}$ as expected. By considering systems at temperatures smaller than $E - \mu$, the squared brackets on the left hand side are equal to

$$[f_3 f_4 (1 \pm f_1)(1 \pm f_2) - f_1 f_2 (1 \pm f_3)(1 \pm f_4)] = e^{-(E_1+E_2)/T} [e^{(\mu_3+\mu_4)T} - e^{(\mu_1+\mu_2)T}], \quad (4.8)$$

where we used the energy conservation $E_1 + E_2 = E_3 + E_4$ condition. The number densities n_i are linked to μ_i through

$$n_i = g_i e^{\mu_i/T} \int \frac{d^3 p}{(2\pi)^3} e^{-E_i/T} \quad (4.9)$$

so that equation (4.8) becomes

$$[f_3 f_4 (1 \pm f_1)(1 \pm f_2) - f_1 f_2 (1 \pm f_3)(1 \pm f_4)] = e^{-(E_1+E_2)/T} \left[\frac{n_3 n_4}{n_3^{(0)} n_4^{(0)}} - \frac{n_1 n_2}{n_1^{(0)} n_2^{(0)}} \right], \quad (4.10)$$

where $n_i^{(0)}$ is n_i in the case of $\mu_i = 0$. Defined the thermally averaged cross section $\langle \sigma v \rangle$ as

$$\langle \sigma v \rangle = \frac{1}{n_1^{(0)} n_2^{(0)}} \int d\Pi_1 d\Pi_2 d\Pi_3 d\Pi_4 (2\pi)^2 \delta^4(p_1 + p_2 - p_3 - p_4) |\mathcal{M}|^2 e^{-(E_1+E_2)/T}, \quad (4.11)$$

we can finally write the Boltzmann equation (4.7) as

$$\dot{n}_1 + 3H n_1 = \langle \sigma v \rangle n_1^{(0)} n_2^{(0)} \left[\frac{n_3 n_4}{n_3^{(0)} n_4^{(0)}} - \frac{n_1 n_2}{n_1^{(0)} n_2^{(0)}} \right]. \quad (4.12)$$

The order of the left hand side of the previous equation is $H n_1$ while the right hand side is of order $\langle \sigma v \rangle n_1 n_2$. The right hand side dominates the left one as long as $\langle \sigma v \rangle n_2 \gg H$. In this case, the only way to keep thermal equilibrium is that all the terms on the right hand side cancel. For large interactions the equilibrium can be achieved if the following condition is satisfied

$$\frac{n_3 n_4}{n_3^{(0)} n_4^{(0)}} = \frac{n_1 n_2}{n_1^{(0)} n_2^{(0)}}. \quad (4.13)$$

This is nothing but the Saha equation found when studying recombination as a consequence of chemical equilibrium (see equation (3.33)).

The Boltzmann equation formalism can be applied to prove the rule that states that particles are kept in thermal equilibrium in the plasma as long as $\Gamma \gg H$. Consider the new variable

$$Y \stackrel{\text{def}}{=} n/s, \quad (4.14)$$

where s is the entropy density that, given a set of species in thermal equilibrium, is equal to

$s = \sum_i(\rho_i + p_i)/T$. The Boltzmann equation (4.12) can be rewritten as

$$\frac{d \ln Y_1}{d \ln a} = -\frac{\Gamma_1}{H} \left[1 - \left(\frac{Y_1^{(0)} Y_2^{(0)}}{Y_3^{(0)} Y_4^{(0)}} \right) \frac{Y_3 Y_4}{Y_1 Y_2} \right], \quad (4.15)$$

where

$$\Gamma_1 \stackrel{\text{def}}{=} n_2 \langle \sigma v \rangle \quad (4.16)$$

is the interaction efficiency. The bracket in front of Γ_1 describes the deviation from thermal equilibrium. Since the Universe expansion can be considered as adiabatic, the entropy density remains constant: $s \propto a^{-3}$. When thermal equilibrium is satisfied the number of particles scales as a^{-3} and thus Y remains constant. Given that $\Gamma_1 \gg H$, if $Y_1 \gg Y_1^{(0)}$ and $Y_i \gg Y_i^{(0)}$ for $i = 2, 3, 4$, the right hand side of (4.15) is negative and there will be a destruction of particles of type "1" to decrease Y_1 towards $Y_1^{(0)}$. Vice versa, for $Y_1 \ll Y_1^{(0)}$ there will be a production of particles "1" to have $Y_1 \rightarrow Y_1^{(0)}$. When the interaction efficiency drops down the Hubble parameter, $\Gamma_1 \ll H$, the right hand side of equation (4.15) is approximately zero and thus the comoving density Y_1 approaches a constant relic density which survived until the present day.

Recombination revisited

We can now give a more precise treatment of recombination. The Boltzmann equation (4.12) in the case of the $e^- + p \leftrightarrow H + \gamma$ process is

$$\frac{1}{a^3} \frac{d(a^3 n_e)}{dt} = n_e^{(0)} n_p^{(0)} \langle \sigma v \rangle \left(\frac{n_H}{n_H^{(0)}} - \frac{n_e^2}{n_e^{(0)} n_p^{(0)}} \right), \quad (4.17)$$

provided that $n_e = n_p$ and $n_\gamma = n_\gamma^{(0)}$. By introducing X_e and using equation (3.32), the previous relation turns into

$$\frac{dX_e}{dt} = \left[(1 - X_e)\beta - X_e^2 n_b \alpha^{(2)} \right], \quad (4.18)$$

where

$$\alpha^{(2)} \stackrel{\text{def}}{=} \langle \sigma v \rangle \quad \beta = \alpha^{(2)} \left(\frac{m_e T}{2\pi} \right)^{3/2} e^{-\Delta/T}. \quad (4.19)$$

The superscript ⁽²⁾ in the recombination rate α indicates recombination to Hydrogen first excited state ($n = 2$). Recombination to the ground state ($n = 0$) has a zero net effect because it produces high energy photons able to immediately ionize a neutral atom.

Recombination can proceed only via the capture to one of the excited states of hydrogen. $\alpha^{(2)}$ is approximately [27]

$$\alpha^{(2)} = 9.78 \frac{\alpha^2}{m_e^2} \left(\frac{\Delta}{T} \right)^{1/2} \ln \left(\frac{\Delta}{T} \right). \quad (4.20)$$

The detailed evolution of X_e is determined by integrating numerically equation (4.18). The comparison between numerical results and Saha approximated ones is shown in figure 3. The figure suggests that Saha equation estimates the redshift z_{rec} for which $X_e = 0.5$ ($z_{\text{rec}} = 1353$) well. However, it overestimates the redshift for which $X_e = 0.1$, which is correctly computed with the full Boltzmann equation $z'_{\text{rec}} = 1070$. This value is almost the same as the recombination freeze out redshift obtained in equation (3.36).

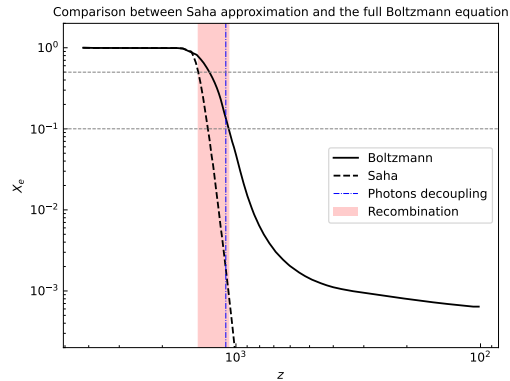


Fig. 3 – Comparison of the free electrons fraction predicted by the Saha and Boltzmann equations (3.33), (4.18).

4.3 Photon Boltzmann equation

The thermalization problem consists in following the photon phase space distribution evolution in presence of energy release. The evolution is determined by the photon Boltzmann equation, in which electrons and positrons are involved. We assume that electrons and positrons have a thermal distribution but their temperature T_e can be different from the photons one $T_z = T_0(1 + z)$.

The collision operator appearing in the full Boltzmann equation (4.1) is the sum of the contributions coming from CS, BR and DCS interactions

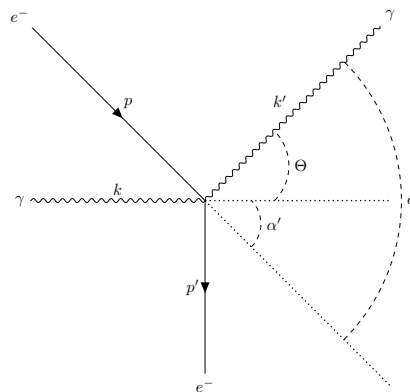
$$\mathbf{C}[f] = \mathbf{C}[f]|_{\text{CS}} + \mathbf{C}[f]|_{\text{DC}} + \mathbf{C}[f]|_{\text{BR}} + \mathbf{C}[f]|_{\text{S}}, \quad (4.21)$$

where $\mathbf{C}[f]|_{\text{S}}$ represents an energy release source term.

Compton Scattering

The Compton scattering is schematized as

$$e^-(p) + \gamma(k) \longleftrightarrow e^-(p') + \gamma(k')$$



The associated collision operator is fully derived in [29] and the result is the famous Kompaneets equation

$$\left. \frac{\partial f}{\partial \tau} \right|_{\text{CS}} \approx \frac{\theta_e}{x_e^2} \frac{\partial}{\partial x_e} \left(x_e^4 \left[\frac{\partial f}{\partial x_e} + f(1+f) \right] \right) \equiv \frac{\theta_e}{x_e^2} \frac{\partial}{\partial x} \left(x^4 \left[\frac{\partial f}{\partial x} + \frac{T_z}{T_e} f(1+f) \right] \right), \quad (4.22)$$

where τ is the Thomson optical depth

$$\Delta \tau = \sigma_{\text{T}} N_e \Delta t, \quad (4.23)$$

and

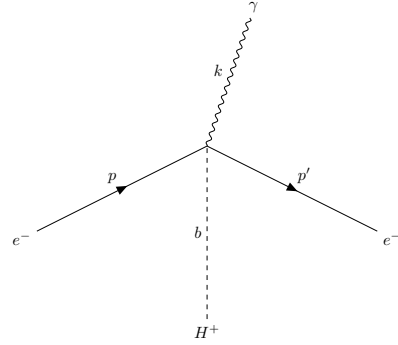
$$x \stackrel{\text{def}}{=} \nu / (k_B T), \quad x_e \stackrel{\text{def}}{=} \nu / (k_B T_e), \quad \theta_e \stackrel{\text{def}}{=} k_B T_e / m_e, \quad (4.24)$$

We used the approximation $T_e \approx T_z$ in the second equality.

Bremsstrahlung

Thermal Bremsstrahlung is the radiative correction to Coulomb scattering with a changing photons number. It can be schematized as

$$e^-(p) + H^+(h) \longleftrightarrow e^-(p') + H^+(h') + \gamma(k)$$



Actually, H^+ can be a generic gas of N ions with charge Ze^+ . b is the impact parameter and it is the closest distance between the passing electron and H^+ . The BR collision operator is [29]

$$\left. \frac{\partial f}{\partial \tau} \right|_{\text{BR}} \approx \frac{K_{\text{BR}} e^{-x_e}}{x_e^3} [1 - f(e^{x_e} - 1)], \quad (4.25a)$$

$$K_{\text{BR}} \stackrel{\text{def}}{=} \frac{\alpha}{2\pi} \frac{\lambda_e^3}{\sqrt{6\pi\theta_e^{7/2}}} \sum_i Z_i^2 N_i \overline{g_{\text{ff}}}(Z_i, T_e, \nu) \approx 1.4 \times 10^{-6} \left[\frac{\overline{g_{\text{ff}}}}{3.00} \right] \left[\frac{\Omega_b h^2}{0.022} \right] (1+z)^{-1/2}. \quad (4.25b)$$

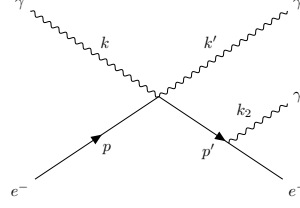
where $\lambda_e = 1/m_e \approx 2.43 \times 10^{-10}$ cm is the Compton wavelength and $\alpha = 2\pi e^2 = 1/137$ the fine-structure constant. In the previous equation we introduced the thermally averaged Gaunt factor that can be numerically approximated as [29]:

$$\overline{g_{\text{ff}}}(x_e) \approx \begin{cases} \frac{\sqrt{3}}{\pi} \ln \left(\frac{2.25}{x_e} \right), & \text{for } x_e \leq 0.37 \\ 1, & \text{otherwise} \end{cases} \quad (4.26)$$

Double Compton scattering

DCS can be interpreted as the radiative correction to Compton scattering

$$e^-(p) + \gamma(k) \longleftrightarrow e^-(p') + \gamma(k') + \gamma(k_2)$$



By assuming that $\gamma(k_2)$ is a soft photon, i.e. with $nu_2 \ll \nu \sim \nu'$, and that $\nu \ll m_e$, DCS collision operator has a form similar to the BR one:

$$\left. \frac{\partial f}{\partial \tau} \right|_{\text{DCS}} \approx \frac{K_{\text{DCS}}}{x^3} [1 - f(e^{x_e} - 1)] \quad (4.27a)$$

$$K_{\text{DCS}} \stackrel{\text{def}}{=} g_{\text{DCS}} \frac{4\alpha}{3\pi} \theta_\gamma^2 \int dx x^4 f(x) [1 + f(x)] \approx 1.7 \times 10^{-20} g_{\text{DCS}} (1 + z)^2. \quad (4.27b)$$

where [30]:

$$g_{\text{DCS}} \approx \frac{1 + \frac{3}{2}x + \frac{29}{24}x^2 + \frac{11}{16}x^3 + \frac{5}{12}x^4}{1 + 19.739\theta_\gamma - 5.5797\theta_e}. \quad (4.28)$$

Final equation and time-scales

We can now write the full Boltzmann equation for photons. We change the physical momentum p into the adimensional frequency x in the Boltzmann equation to absorb the $-Hp\partial_\rho f$ term present in the Liouville operator. We further compute the derivatives with respect to the Thomson time, $d\tau = \sigma_T N_e dt$. The final equation is

$$\begin{aligned} \frac{\partial f}{\partial \tau} \approx \frac{\theta_e}{x^2} \frac{\partial}{\partial x} x^4 \left[\frac{\partial}{\partial x} f + \frac{T_z}{T_e} f(1 + f) \right] + \frac{K_{\text{BR}} e^{-x_e}}{x_e^3} [1 - f(e^{x_e} - 1)] \\ + \frac{K_{\text{DCS}} e^{-2x}}{x^3} [1 - f(e^{x_e} - 1)] + S(\tau, x), \end{aligned} \quad (4.29)$$

where

$$K_{\text{BR}} = \frac{\alpha}{2\pi} \frac{\lambda_e^3}{\sqrt{6\pi}\theta_e^{7/2}} \sum_i Z_i^2 N_i \bar{g}_{\text{ff}}(Z_i, T_e, T_z, x_e), \quad (4.30a)$$

$$K_{\text{DCS}} = \frac{4\alpha}{3\pi} \theta_\gamma^2 g_{\text{DCS}}(T_e, T_z, x) \int dx x^4 f(x) [1 + f(x)], \quad (4.30b)$$

$$\bar{g}_{\text{ff}}(x_e) \approx \begin{cases} \frac{\sqrt{3}}{\pi} \ln\left(\frac{2.25}{x_e}\right), & \text{for } x_e \leq 0.37 \\ 1, & \text{otherwise} \end{cases} \quad (4.30c)$$

$$g_{\text{DCS}} \approx \frac{1 + \frac{3}{2}x + \frac{29}{24}x^2 + \frac{11}{16}x^3 + \frac{5}{12}x^4}{1 + 19.739\theta_\gamma - 5.5797\theta_e}. \quad (4.30d)$$

To numerically solve this equation it is necessary to follow the evolution of the electron temperature T_e in presence of energy injections, which is [30]

$$\frac{d\rho_e}{d\tau} \stackrel{\text{def}}{=} \frac{dT_e/T_z}{d\tau} = \frac{t_T \dot{Q}}{\alpha_h \theta_\gamma} + \frac{4\tilde{\rho}_\gamma}{\alpha_h} [\rho_e^{eq} - \rho_e] - \frac{4\tilde{\rho}_\gamma}{\alpha_h} \mathcal{H}_{\text{DCS,BR}}(\rho_e) - H t_T \rho_e, \quad (4.31)$$

where T_e is the matter temperature. We introduced the heat capacity of the medium

$$\alpha_h = \frac{3}{2}[N_e + N_H + N_{He}] \equiv \frac{3}{2}N_H[1 + f_{He} + X_e], \quad (4.32)$$

the energy injection rate \dot{Q} , the energy density of the photon field in units of the electron mass $\tilde{\rho}_e = \rho_\gamma/m_e$ and where $\rho_e^{eq} = T_e^{eq}/T_z$. We also introduced the BR/CDS heating integrals

$$\mathcal{H}_{\text{DCS,BR}} = \frac{1}{4\mathcal{G}_3\theta_z} \int dx [1 - f(x)(e^{x_e} - 1)] \times K_{\text{DCS,BR}}(x, \theta_z, \theta_e), \quad (4.33)$$

where

$$\mathcal{G}_3 = \int dx x^3 f(x). \quad (4.34)$$

The Compton scattering time-scale is defined as

$$\left. \frac{\partial \rho_\gamma}{\partial t} \right|_{\text{CS}} \propto \frac{1}{t_{\text{CS}}} \rho_\gamma, \quad (4.35)$$

or analogously

$$\left. \frac{\partial \rho_\gamma}{\partial \tau} \right|_{\text{CS}} \propto \frac{t_T}{t_{\text{CS}}} \rho_\gamma. \quad (4.36)$$

It represents the typical time interval during which electrons transfer energy to photons. In case of $T_e = T_z$, it is equal to

$$t_{e\gamma} = \frac{t_T}{4\theta_e} \approx 1.2 \times 10^{29} (1+z)^{-4} \text{s}, \quad (4.37)$$

where $t_T \stackrel{\text{def}}{=} (\sigma_T N_e)^{-1}$ is the Thomson rate. By comparing this rate with the Hubble one, one finds that Comptonization becomes inefficient at

$$z_K \approx 5 \times 10^4. \quad (4.38)$$

The time-scale on which BR emission and absorption bring the photons field distribution in thermal equilibrium with electrons is

$$\left. \frac{\partial f}{\partial \tau} \right|_{\text{BR}} \propto \frac{t_T}{t_{\text{BR}}} f, \quad (4.39)$$

and at any frequency x_e it is given by

$$t_{\text{BR}} = \frac{t_{\text{T}} x_e^3}{K_{\text{BR}}(1 - e^{-x_e})} \approx 1.4 \times 10^{-6} \left[\frac{\overline{g_{\text{ff}}}}{3.00} \right] \left[\frac{\Omega_b h^2}{0.022} \right] \frac{x_e^3}{1 - e^{-x_e}} (1 + z)^{-5/2}. \quad (4.40)$$

The BR time-scale depends not only on the redshift as in CS case but also on the (adimensional) frequency x_e . In particular, BR is particularly efficient at high redshift or at low frequencies.

The typical time-scale for the double Compton scattering is

$$t_{\text{DCS}} = \frac{t_{\text{T}} x^3 e^{2x}}{K_{\text{DCS}}(e^{x_e} - 1)}, \quad (4.41)$$

and as in the BR case it depends on the frequency. By assuming $x_e = x$, we have that for $z \gtrsim 10^3$

$$K_{\text{BR}} = 1.4 \times 10^6 \left[\frac{\overline{g_{\text{ff}}}}{3.0} \right] \left[\frac{\Omega_b h^2}{0.022} \right] (1 + z)^{-1/2}, \quad (4.42a)$$

$$K_{\text{DCS}} = 1.7 \times 10^{-20} (1 + z)^2. \quad (4.42b)$$

BR and DCS are comparable at

$$z_{\text{DCS,BR}} = 3.7 \times 10^5 \left(\left[\frac{\overline{g_{\text{ff}}}}{3.0} \right] \left[\frac{\Omega_b h^2}{0.022} \right] \right)^{2/5}. \quad (4.43)$$

At $z > z_{\text{DCS,BR}}$, DCS is more efficient than BR while at lower redshift BR dominates. Both BR and DCS are efficient at $z \gtrsim 2 \times 10^6$.

To sum up, the relevant redshifts are

1. $z_{\text{th}} \approx 2 \times 10^6$ both BR and DCS become inefficient for high energy photons. They are however efficient for soft photons.
2. $z_{\text{K}} \equiv z_{\mu y} \approx 5 \times 10^4$, Compton scattering becomes inefficient.

For $z > z_{\text{th}}$ all the collision processes are efficient and energy injections occurring above z_{th} are fully thermalized leading to a simple temperature shift (g) of the black body spectrum. As the Universe expands, these processes become inefficient and energy releases cannot be fully thermalized generating SDs. At early times, for $z_{\text{K}} < z < z_{\text{th}}$, BR and DCS are not efficient anymore and the number of photons is almost frozen. However, CS is still efficient and can restore the equilibrium after an energy release. Since CS does not change the number of photons, the resulting spectrum will be a Bose-Einstein distribution, characterized by a frequency-dependent chemical potential $\mu(x)$. These are the so-called chemical potential, or μ -type, CMB SDs. At late times $z < z_{\text{K}}$ also Compton scattering becomes inefficient and thus energy injections may produce the so-called Compton y -distortions. The transition from the μ -era to the y -one is not instantaneous but gradual. During the transition from the

μ - to the y -era, not all CMB SDs can be simply parametrized as a $\mu + y$ distortion, but there is a small residual (r -type) distortion that contains information on the time-dependence of the energy release [31].

5 Spectral distortions characteristics

In this section we analyze SDs characteristics. We also present the linearized thermalization problem and its Green's function solution which allows a fast and precise computation of SDs. The Green's function method is particularly important because it is the one numerically implemented in the Einstein-Boltzmann solver CLASS [32], [33], [34].

5.1 Shapes

To model the shape of spectra distortions, we split the photon phase space distribution $f(t, x)$ as

$$f(t, x) = B(x) + \Delta f(t, x), \quad (5.1)$$

where $B(x)$ is the phase space distribution of a black body at the temperature T_z : $B(x) = [e^x - 1]^{-1}$. $\Delta f(t, x)$ represents the SDs. This separation allows to include SDs due to deviation of the radiation temperature T_γ from the simple $T_z \propto (1 + z)$ law. In this case, the distortion has the shape of a black body but with a different temperature. This type of spectral distortion is called temperature shift. Since temperature shifts are really hard to be observed, as it will be soon shown, keeping them separated from other SDs is crucial for the forecast of future experiments.

When $f(t, x)$ has not a simple black body shape, the definition of temperature is not unique. In this thesis, the photon temperature T_γ is the one of a black body that would share the same number density of the distorted photon phase space distribution.

Temperature shift

For $z < z_{\text{th}} \approx 2 \times 10^6$, all energy injections are thermalized and the photon phase space distribution at first order is

$$f(x) = B(p/T_\gamma) = B\left(\frac{x}{1 + \Delta T/T_z}\right) \approx B(x) - x \frac{\partial B(x)}{\partial x} \frac{\Delta T}{T_z} \stackrel{\text{def}}{=} B(x) + G(x) \frac{\Delta T}{T_z}, \quad (5.2)$$

where $\Delta T = T_\gamma - T_z \ll T_z$. The shift of the phase space distribution is

$$\Delta f(x) = G(x) \frac{\Delta T}{T_z}. \quad (5.3)$$

G represents the shape of a temperature shift and it is equal to

$$G(x) \stackrel{\text{def}}{=} -x \frac{\partial B(x)}{\partial x} = \frac{x e^x}{(e^x - 1)^2}. \quad (5.4)$$

The difference of the chosen reference temperature $T_0 = T_z(z = 0)$ with the true one $T_\gamma(z = 0)$ determines the amplitude of the temperature shift. In practice it is always possible to readjust the reference temperature to coincide with the observed one. For this reason, it is hard to detect temperature shifts.

Chemical potential distortion

For $z_K < z < z_{\text{th}}$, CS is very efficient and so $C[f]|_{\text{CS}} = 0$. The Kompaneets equation (4.22) gives

$$\frac{\theta_e}{x^2} \frac{\partial}{\partial x} \left(x^4 \left[\frac{\partial f}{\partial x} + \frac{T_z}{T_e} f(1 + f) \right] \right) = 0. \quad (5.5)$$

This equation is satisfied as long as f is a solution of the equation

$$\left[\frac{\partial f}{\partial x} + \frac{T_z}{T_e} f(1 + f) \right] = 0. \quad (5.6)$$

The physically relevant solution to this equation is a Bose-Einstein distribution

$$f(x) = \frac{1}{e^{\tilde{x} + C} - 1}, \quad \text{where } \tilde{x} = x T_z / T_e, \quad (5.7)$$

and where C is an integration constant representing the chemical potential. When DCS and BR scatterings are efficient, C must vanish because the photon number is not conserved, otherwise a μ -type spectral distortion is created. \tilde{x} can be replaced with x because their difference is a simple temperature shift and it is not relevant for μ -distortions. By defining C with μ_0 , the shape of this type distortions can be easily found in the limit of a small μ_0 :

$$f(x) = B(x + \mu_0) = \frac{1}{e^{x + \mu_0} - 1} \approx B(x) - \mu_0 \frac{G(x)}{x} + O(\mu_0^2). \quad (5.8)$$

The naive definition of the μ -type shape would be

$$\tilde{M}(x) = -\frac{G(x)}{x}, \quad (5.9)$$

but this is not correct since this type of distortion does not conserve the number of photons as it should. Indeed, the definition of \tilde{M} can be seen as a temperature shift plus a pure μ -distortions [34]. The shape of the pure μ -distortion is then obtained by subtracting to \tilde{M} the temperature shift contribution:

$$M(x) = \tilde{M}(x) - \alpha_\mu G(x) = -G(x) \left(\frac{1}{x} - \alpha_\mu \right), \quad (5.10)$$

where α_μ is an integration constant obtained by imposing that μ -type distortions conserve photon number, i.e.

$$\Delta n = \int d^3p \delta f(t, p) \equiv 4\pi T_z^3 \int dx x^2 \Delta f(x) = 0. \quad (5.11)$$

We can easily check that

$$\int dx x^2 M(x) = \int (-x + \alpha_\mu x^2) G(x) = -G_1 + \alpha_\mu G_2 = 0, \quad (5.12)$$

where $G_k \stackrel{\text{def}}{=} \int dx x^k G(x) = (k+1)! \zeta(k+1)$. Therefore

$$\alpha_\mu = G_1/G_2 \approx \frac{1}{3} \frac{\zeta(2)}{\zeta(3)} \approx 0.4561. \quad (5.13)$$

In the end, the μ -distortion shape is

$$M(x) = G(x) \left[0.4561 - \frac{1}{x} \right], \quad (5.14)$$

and we can write

$$\Delta f(x) = \mu M(x). \quad (5.15)$$

A positive amplitude μ implies that there are fewer photons than in a black body at temperature T_e , while $\mu < 0$ means that there are more photons. $\mu > 0$ is achieved by an energy injection, while $\mu < 0$ is caused by an energy extraction. If $\mu = 0$ the photon field is in full thermal equilibrium with electrons and it has a black body shape.

Compton distortion

A Compton, or y -type, distortion occurs for $z < z_K$ when CS still takes place but it is not very efficient. To find its shape and amplitude, we have to solve the Kompaneets equation when it does not reach the equilibrium solution:

$$\frac{\Delta f}{\Delta \tau} \approx \frac{T_e}{m_e} \frac{1}{x^2} \frac{\partial}{\partial x} \left(x^4 \left[\frac{\partial B(x)}{\partial x} + \frac{T_z}{T_e} B(x)(1 + B(x)) \right] \right) = \frac{T_z - T_e}{m_e} \frac{1}{x^2} \frac{\partial}{\partial x} (x^3 G(x)), \quad (5.16)$$

where it was assumed that the photon field started with a black body distribution. The shift Δf is then

$$\Delta f(x) \approx \Delta \tau \frac{T_e - T_z}{m_e} \left[\frac{1}{x^2} \frac{\partial}{\partial x} (x^3 G(x)) \right] \stackrel{\text{def}}{=} y Y(x), \quad (5.17)$$

where the y -type shape is determined by

$$Y(x) = -\frac{1}{x^2} \frac{\partial}{\partial x} (x^3 G(x)) = G(x) \left[x \frac{e^x + 1}{e^x - 1} - 4 \right]. \quad (5.18)$$

The photon number is already conserved by a y -distortions:

$$\Delta n \propto \int dx x^2 Y(x) = 0. \quad (5.19)$$

The amplitude of y -type distortions is determined by the Compton parameter

$$y \stackrel{\text{def}}{=} \int_0^\tau d\tau' \frac{k_B}{m_e} (T_e - T_z) = \int_0^t dt \frac{k_B}{m_e} (T_e - T_z) \sigma_T N_e, \quad (5.20)$$

which depends on the number of scattering (via τ) and on the net energy exchange $\Delta\nu/\nu \approx 4(\theta_e - \theta_\gamma)$. If electron and photon temperatures are equal, the Compton parameter vanishes. On the other hand, a positive y indicates that a Comptonization occurred: the overall energy was transferred from electrons to photons. Vice versa, if $y < 0$ there was an energy transfer from photons to electrons.

The inefficiency of CS is not the only way to produce a y -type SD. Indeed, by expanding temperature shift (5.2) at second order one finds

$$\begin{aligned} B\left(\frac{x}{1 + \frac{\Delta T}{T_z}}\right) &\equiv F\left(\frac{\Delta T}{T_z}\right) \approx \\ &\approx F(0) + F'(0) \frac{\Delta T}{T_z} + \frac{1}{2} F''(0) \left(\frac{\Delta T}{T_z}\right)^2 + \dots = \\ &= B(x) + \frac{x e^x}{(e^x - 1)^2} \frac{\Delta T}{T_z} + \frac{1}{2} \frac{x e^x}{(e^x - 1)^2} \left[x \frac{e^x + 1}{e^x - 1} - 2 \right] \left(\frac{\Delta T}{T_z}\right)^2 + \dots \equiv \\ &\equiv B(x) + G(x) \left[\frac{\Delta T}{T_z} + \left(\frac{\Delta T}{T_z}\right)^2 \right] + \frac{1}{2} Y(x) \left(\frac{\Delta T}{T_z}\right)^2 + \dots \end{aligned} \quad (5.21)$$

It is important to include the second-order contribution of temperature shifts because it can add to the total y -type amplitude a term up to around 2×10^{-8} , which is not negligible since it is above the target sensitivity of future experiments [8],[11]. Terms of order g^3 are instead negligible since they are of order 10^{-12} .

Actually, $B(x)$, $G(x)$, $M(x)$ and $Y(x)$ are the shapes at the level of the phase space distribution. To translate them in terms of the spectral radiance intensity, it is necessary to multiply them by $\mathcal{N}x^3$, where $\mathcal{N} = 2(k_B T_0)^3$. We plot the SDs shapes compared to the CMB black-body spectrum detected by FIRAS in figure 4. Notice that we plotted SDs for large amplitudes in order to highlight the different shapes, but FIRAS set very tight constraints on these parameters.

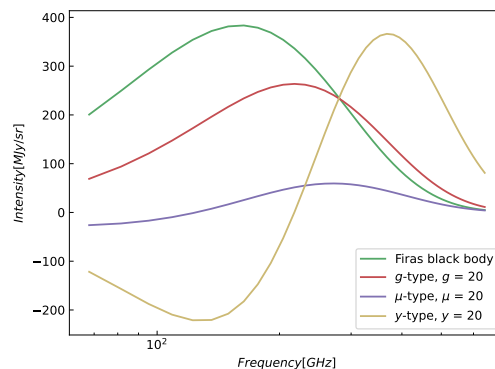


Fig. 4 – SDs shapes compared to CMB black body spectrum.

5.2 Amplitudes

At this stage, the disturbed spectral radiance spectrum of the CMB is written as

$$I(x) = I_0(x) + \Delta I(x) = I_0(x) + \Delta I_T(x) + \Delta I_\mu(x) + \Delta I_y(x), \quad (5.22)$$

where $I_0 = \mathcal{N}x^3 B(x)$ is the black body intensity and

$$\Delta I_T(x) = \mathcal{N}x^3 [g(1+g)G(x) + (g^2/2)Y(x)] \quad (5.23a)$$

$$\Delta I_\mu(x) + \Delta I_y(x) = \mathcal{N}x^3 [B(x)\mu M(x) + yY(x)]. \quad (5.23b)$$

We recall that the shapes are given by

$$\begin{aligned} B(x) &= \frac{1}{e^x - 1}, & G(x) &= \frac{xe^x}{(e^x - 1)^2}, \\ Y(x) &= G(x) \left[x \frac{e^x + 1}{e^x - 1} - 4 \right], & M(x) &= G(x) \left[0.4561 - \frac{1}{x} \right]. \end{aligned} \quad (5.24)$$

The amplitudes μ and y can be roughly computed as follows. Consider the case in which a μ distortion is completely generated by an energy release occurring only in the μ -era. Then:

$$\left. \frac{\Delta\rho_\gamma}{\rho_\gamma} \right|_\mu = \frac{\int dx x^3 \Delta f(x)}{\int dx x^3 B(x)} = \frac{\int dx x^3 \mu M(x)}{\int dx x^3 B(x)} = \frac{\mu}{1.401} \implies \mu = 1.401 \left. \frac{\Delta\rho_\gamma}{\rho_\gamma} \right|_\mu. \quad (5.25)$$

Similarly, for the y -type case one finds

$$\left. \frac{\Delta\rho_\gamma}{\rho_\gamma} \right|_y = \frac{\int dx x^3 \Delta f(x)}{\int dx x^3 B(x)} = \frac{\int dx x^3 y Y(x)}{\int dx x^3 B(x)} = 4y \implies y = \frac{1}{4} \left. \frac{\Delta\rho_\gamma}{\rho_\gamma} \right|_y. \quad (5.26)$$

These are the 0-th order expressions for μ and y .

Also photon injections create SDs. In general, the correct treatment of photon injections requires the solution of the full Boltzmann equation, which can be only performed numerically with a tool such as COSMOTHERM [35]. If the injected photons are highly energetic, they can be treated as a pure energy release [36]. More discussion about photon injections can be found in [37]. For this thesis, only energy-releases are relevant. We want to derive a generic expression for the amplitudes. We define the the effective heating rate \dot{Q} as

$$\dot{Q} \stackrel{\text{def}}{=} \int d^3p EC[f] = \frac{\partial\rho_\gamma}{\partial t} + 4\pi H\rho_\gamma, \quad (5.27)$$

where the second equality holds thank to the Boltzmann equation (4.1). We can rewrite the previous equation as

$$\frac{\partial(a^4\rho_\gamma)}{\partial t} = a^4\dot{Q}. \quad (5.28)$$

The general solution of this equation is the sum of a homogeneous solution and a particular

one: $\rho_\gamma = \rho_0 + \Delta\rho_\gamma$. The particular solution can be easily found as

$$\frac{\Delta\rho_\gamma}{\rho_\gamma} = \int_0^\infty dt' \frac{\dot{Q}}{\rho_\gamma(t)} \equiv \int_z^\infty dz \frac{\dot{Q}}{(1+z)H\rho_\gamma(t)} \equiv \int dz \frac{dQ/dz}{\rho_\gamma}. \quad (5.29)$$

This is the total energy release. We can decompose it into a sum of different contributions to SDs:

$$\frac{\Delta\rho_\gamma}{\rho_\gamma} \Big|_{tot} \equiv \int \frac{dQ/dz}{\rho_\gamma} \equiv \frac{\Delta\rho_\gamma}{\rho_\gamma} \Big|_T + \frac{\Delta\rho_\gamma}{\rho_\gamma} \Big|_\mu + \frac{\Delta\rho_\gamma}{\rho_\gamma} \Big|_y + \frac{\Delta\rho_\gamma}{\rho_\gamma} \Big|_r. \quad (5.30)$$

Therefore, the expression for a generic spectral distortion amplitude a is

$$a = C_a \frac{\Delta\rho_\gamma}{\rho_\gamma} \Big|_a \equiv C_a \int dz \frac{dQ/dz}{\rho_\gamma} \mathcal{J}_a(z), \quad (5.31)$$

where C_a is a normalization factor, that was already computed for μ - and y -distortions: $C_\mu = 1.401$, $C_y = 1/4$. In the temperature shift case, it is given by

$$\frac{\Delta\rho_\gamma}{\rho_\gamma} \Big|_g = \frac{\int dx x^3 g G(x)}{\int dx x^3 B(x)} = 4g \equiv g/C_g \implies C_g = 1/4. \quad (5.32)$$

The distortions visibility functions $\mathcal{J}_a(z)$ determine how much of the injected energy contributes to a as a function of the redshift. At the 0-th order, the visibility functions are Heaviside step functions $\Theta_H(x)$:

$$\mathcal{J}_g(z) = \Theta_H(z - z_t h), \quad (5.33a)$$

$$\mathcal{J}_\mu(z) = \Theta_H(z_{th} - z) \Theta_H(z - z_K), \quad (5.33b)$$

$$\mathcal{J}_y(z) = \Theta_H(z_K - z). \quad (5.33c)$$

The 0-th order expressions were found by making two assumptions. The first was to neglect photon production in the μ -era due to BR and DCS. By relaxing this hypothesis, one has that μ is non constant anymore, but it is both time and frequency dependent [38]. This dependence is usually decomposed as [39]

$$\mu(t, x) = \mu_0(t) e^{-x_c(t)/x}, \quad (5.34)$$

where $x_c(t)$ is the critical frequency of the BR and DCS processes, usually of order 10^{-3} , and where μ_0 obeys the differential equation

$$\frac{d\mu_0}{d\tau} = 1.401 \frac{\dot{Q}}{\rho_\gamma} - \gamma_N \frac{T_\gamma x_c \mu_0}{m_e}, \quad (5.35)$$

with $\gamma_N \stackrel{\text{def}}{=} (4/3)(1.401/G_2)$. This equation says that the chemical potential is exponentially

decaying and the decay time is roughly

$$\tau_\mu(z) \approx \gamma_N \int d\tau \frac{T_\gamma x_c}{m_e} \approx (z/z_{\text{th}})^{5/2}. \quad (5.36)$$

This defines a more precise visibility function for μ -distortions:

$$\mathcal{J}_\mu(z) \stackrel{\text{def}}{=} e^{-\tau_\mu(z)} \Theta_H(z - z_K) \approx \exp\left(- (z/z_{\text{th}})^{5/2}\right) \Theta_H(z - z_K). \quad (5.37)$$

The new set of visibility functions is then

$$\mathcal{J}_g(z) = 1 - \exp\left(- (z/z_{\text{th}})^{5/2}\right) \Theta_H(z - z_K), \quad (5.38a)$$

$$\mathcal{J}_\mu(z) = \exp\left(- (z/z_{\text{th}})^{5/2}\right) \Theta_H(z - z_K), \quad (5.38b)$$

$$\mathcal{J}_y(z) = \Theta_H(z_K - z). \quad (5.38c)$$

The second approximation is that the transition from the μ - to the y -era occurs instantaneously at $z = z_K$. A more refined treatment of SDs requires a gradual transition. This has been studied in [40] by using the full Green's function of the thermalization problem. The result, valid at each redshift, is

$$\mathcal{J}_g(z) = 1 - \exp\left(- (z/z_{\text{th}})^{5/2}\right), \quad (5.39a)$$

$$\mathcal{J}_\mu(z) = \left\{ 1 - \exp\left[- \left(\frac{1+z}{5.8 \times 10^4}\right)^{1.88}\right] \right\} \exp\left(- (z/z_{\text{th}})^{5/2}\right), \quad (5.39b)$$

$$\mathcal{J}_y(z) = \left[1 + \left(\frac{1+z}{6.0 \times 10^4}\right)^{2.58} \right]. \quad (5.39c)$$

Notice that the visibility functions do not add up to unity. This means that the total injected energy is not fully stored in g -, μ - and y -distortions. The missing energy can be found in residual distortions, which will be introduced in the next subsection. To ensure energy conservation while neglecting residual distortions, it is possible to redefine $\mathcal{J}_\mu = [1 - \mathcal{J}_y] \exp\left[- (z/z_{\text{th}})^{5/2}\right]$, as suggested in [41].

5.3 Green's function of the thermalization problem

Current constraints on μ and y (3.49) set an upper bound on the amplitude of energy release in the Early Universe $\Delta\rho_\gamma/\rho_\gamma < 6 \times 10^{-5}$. Since this value is small, the thermalization problem can be linearized and solved by using a Green's function approach, as suggested in [40].

Given a linear differential equation with a differential operator \mathcal{D} , $\mathcal{D}y(x) = f(x)$, its solution can be always written as $y(x) = \int dx' f(x') G(x, x')$, where the Green's function $G(x, x')$ is the particular solution of the equation $\mathcal{D}G(x, x') = \delta(x - x')$. Notice that $G(x, x')$ does not depend on $f(x)$.

In the SDs case the Green's function of the thermalization problem is the solution of the equation $\mathcal{D}G_{\text{th}}(x, x') = \delta(x - x')$, where \mathcal{D} represents all the possible interactions. The Green's function property for which it does not depend on $f(x)$ implies that G_{th} solves the thermalization problem for arbitrary heating histories. This is true only as long as the thermalization problem is a linear differential equation and this is verified only at first order in the distortions of the photon phase space distribution. Therefore, we exclude the second-order contribution in g . We can then write the total distortion term as

$$\Delta I_{\text{tot}}(x) = gG(x) + \mu M(x) + yY(x). \quad (5.40)$$

ΔI is easily computed once we know G_{th} and the heating history

$$\Delta I_{\text{tot}}(x, z) = \int dz' G_{\text{th}}(x, z, z') \frac{dQ(z')/dz'}{\rho_{\gamma}(z')}. \quad (5.41)$$

The Green's function G_{th} was numerically computed in [40] by following the evolution of the full photon phase space distribution with COSMOTHERM

$$\frac{d(Q/\rho_{\gamma})}{dz} \approx \frac{\Delta\rho_{\gamma,h}}{\rho_{\gamma,h}} \frac{\exp(-(z - z_h)^2/(2\sigma_z^2))}{\sqrt{2\pi\sigma_z^2}}, \quad (5.42)$$

where $\sigma_z \approx 0.01$ and $\Delta\rho_{\gamma,h}/\rho_{\gamma,h} \approx 10^{-6}$.

At very early times, when the thermalization process is efficient, the Green's function has the shape of a temperature shift $G_{\text{th}} \propto \mathcal{N}x^3G(x)$. Later, photon production by DCS and BR at low frequencies becomes less efficient while CS is still very fast and distortions have a μ -type shape. Finally, in the regime for $z \ll z_K$, SDs will have the shape of y -distortions. The form of the Green's function can be found at all redshifts by inserting equation (5.31) into (5.41) and comparing the result with equation (5.40):

$$G_{\text{th}}(x, z') = (1/4)G(x)\mathcal{J}_g(z') + (1/4)Y(x)\mathcal{J}_y(z') + 1.401M(x)\mathcal{J}_{\mu}(z'). \quad (5.43)$$

To ensure energy conservation we should add a term $\Delta I_R(x)$, that represents the so-called residual distortions, to equation (5.40). Residual distortions provide a tool to investigate the time and frequency dependence of the energy release. Therefore, we write

$$\Delta I_{\text{tot}}(x, z) = \int dz' G_{\text{th}}(x, z, z') \frac{dQ(z')/dz'}{\rho_{\gamma}(z')} + R(x, z'), \quad R(x, z') = \epsilon R(x), \quad (5.44)$$

where

$$\epsilon = \int dz' C_{\epsilon} \frac{dQ(z')/dz'}{\rho_{\gamma}(z')} \mathcal{J}_r(z'), \quad (5.45)$$

with $\mathcal{J}_r(z') = 1 - \mathcal{J}_g(z') - \mathcal{J}_{\mu}(z') - \mathcal{J}_y(z')$ and C_{ϵ} is a normalization constant. Numerically it is simpler to compute directly $R(x, z')$ from the full Green's functions, which now has the

form

$$G_{\text{th}}(x, z') = (1/4)G(x)\mathcal{J}_g(z') + (1/4)Y(x)\mathcal{J}_y(z') + 1.401M(x)\mathcal{J}_\mu(z') + R(x, z'). \quad (5.46)$$

The visibility functions $\mathcal{J}_a(z')$ are numerically computed by least-squares fitting the numerical Green's function with the shapes $\{G(x), Y(x), M(x)\}$ appearing in the analytic expression (5.46). $\mathcal{J}_a(z')$ are then the branching ratios and $R(x, z')$ the residual of G_{th} . Numerically, it is better to discretize in frequency space all the quantities involved $\mathbf{A} = A(\nu_i)$ and replace the least-squares fitting with the Grams-Schmidt orthogonalization. Let \mathbf{G} , \mathbf{Y} , \mathbf{M} be an orthonormal basis of distortion shapes and

$$\mathbf{e}_g = \mathbf{G}_\perp/|\mathbf{G}_\perp|, \quad \mathbf{e}_\mu = \mathbf{M}_\perp/|\mathbf{M}_\perp|, \quad \mathbf{e}_y = \mathbf{Y}/|\mathbf{Y}|, \quad (5.47)$$

the corresponding basis vector. The perpendicular components are defined as

$$\mathbf{M}_\perp = \mathbf{M} - M_y\mathbf{e}_y, \quad \mathbf{G}_\perp = \mathbf{G} - G_y\mathbf{e}_y - G_\mu\mathbf{e}_\mu, \quad (5.48)$$

with $M_y = \mathbf{M} \cdot \mathbf{e}_y$ and so on. The discretized Green's function is

$$\mathbf{G}_{\text{th}}(z) = (1/4)\mathbf{G}\mathcal{J}_g(z) + (1/4)\mathbf{Y}\mathcal{J}_y(z) + 1.401\mathbf{M}\mathcal{J}_\mu(z) + \mathbf{R}(z), \quad (5.49)$$

where the branching ratios are computed as

$$\mathcal{J}_g(z) = (\mathbf{e}_g \cdot \mathbf{G}_{\text{th}}(z))/(\mathbf{G}_\perp), \quad (5.50a)$$

$$\mathcal{J}_\mu(z) = (\mathbf{e}_\mu \cdot \mathbf{G}_{\text{th}}(z) - G_\mu\mathcal{J}_g(z))/|\mathbf{M}_\perp|, \quad (5.50b)$$

$$\mathcal{J}_y(z) = (\mathbf{e}_y \cdot \mathbf{G}_{\text{th}}(z) - M_y\mathcal{J}_\mu(z) - G_y\mathcal{J}_g(z))/|\mathbf{Y}|, \quad (5.50c)$$

$$\mathcal{J}_R(z) = 1 - \mathcal{J}_g(z) - \mathcal{J}_y(z) - \mathcal{J}_\mu(z), \quad (5.50d)$$

and where the residual $\mathbf{R}(z)$ is given by the difference between the full Green's function and the sum of the \mathbf{G} , \mathbf{M} , \mathbf{Y} shapes weighted by the branching ratios.

Principal Components Analysis

The principal components analysis is useful to understand the physical origin of residual distortions. It consists in decomposing $\mathbf{R}(z)$ into shapes $\mathbf{S}^{(k)}$ and amplitudes μ_k :

$$\Delta I_i^R = \sum_\alpha \hat{R}_{i\alpha} dQ_\alpha, \quad (5.51)$$

where i refers to the frequency ν_i , α to the redshift z_α and where we defined $\hat{R}_{i\alpha} = R(x_i, z_\alpha)\Delta \ln(z_\alpha)$ and $dQ_\alpha = [(dQ/d \ln z)/(\rho_\gamma)]|_{z_\alpha}$. As argued in [41], the shapes $\mathbf{S}^{(k)}$ are defined so that the signal to noise ratio (SNR) of a given experiment is maximum. The SNR of a given experiment is quantified from the Fisher-information matrix, which in the

diagonal-noise-covariance case is a symmetric matrix given by

$$\mathcal{F}_{\alpha\beta} = \sum_i \frac{1}{\delta I_{\text{noise}}^2(\nu_i)} \frac{\partial \Delta I_i^R}{\partial dQ_\alpha} \frac{\partial \Delta I_i^R}{\partial dQ_\beta} = \sum_i \frac{\hat{R}_{i\alpha} \hat{R}_{i\beta}}{\delta I_{\text{noise}}(\nu_i)^2}. \quad (5.52)$$

The amplitudes μ_k and the shapes $\mathbf{S}^{(k)}$ are computed from the orthonormal eigenvectors $E_\alpha^{(k)}$ of \mathcal{F} :

$$\mu_k = \sum_\alpha E_\alpha^{(k)} dQ_\alpha, \quad \mathbf{S}^{(k)} = \sum_\alpha E_\alpha^{(k)} \hat{\mathbf{R}}_\alpha. \quad (5.53)$$

Hence, residual distortions are

$$\Delta \mathbf{I}^R \approx \sum_k \mu_k \mathbf{S}^{(k)}. \quad (5.54)$$

With a similar approach one can compute the ϵ parameters of equation (5.45):

$$\epsilon = \sum_k C_S^{(k)} \mu_k \quad (5.55)$$

where $C_S^{(k)} = \sum_i S^{(k)}(x_i) \Delta x_i / \sum_i B(x_i) \Delta x_i$ represent the normalization C_ϵ .

In the end, SDs computed with the Green's function machinery are detector dependent. Indeed, to compute the branching ratio it is necessary to discretize all quantities in frequency space, which is naturally binned once the detector specifications $\{\nu_{\min}, \nu_{\max}, \Delta\nu_c\}$ are known. Furthermore, to compute the shapes and to decompose the residual distortions with the principal components analysis it is necessary to know the detector noise $\delta I_{\text{noise}}(\nu_i)$. This method is the one implemented in CLASS and it provides a fast and precise tool to compute CMB SDs due to energy release.

6 Some causes of CMB spectral distortions

We now discuss the heating rate \dot{Q} , which is the last missing ingredient to compute SDs amplitudes. First, it is necessary to distinguish between injected and deposited energy. The injected energy is the energy released in the intergalactic medium. The deposited energy in the intergalactic medium is instead the fraction of injected energy that affects the medium after the radiative transfer and the electron cooling. The energy can be deposited in various deposition channels c . The deposition function $f_c(z)$ quantifies the injected energy that is deposited in the channel c at redshift z . $f_c(z)$ can be further decomposed into an injection efficiency function $f_{\text{eff}}(z)$ times a deposition fraction $\chi_c(z)$. f_{eff} determines how much injected energy is deposited regardless of the form and usually depends on the emitting process and the characteristics of the Universe. Moreover, f_{eff} may not be simply the electromagnetically released energy f_{em} since electromagnetically particles can lose energy through redshifting or secondary processes before depositing energy into the medium: $f_{\text{eff}} = f_{\text{em}}(1 - f_{\text{loss}})$. f_{loss} is particularly important during Dark Ages. The on-the-spot approximation assumes that the deposition occurs instantaneously and so $f_{\text{loss}} = 0$. A more detailed calculation can be

performed numerically with tools such as DARKHISTORY[42].

The deposition fraction is normalized over all the deposition channels $\sum_c \chi_c(z) = 1$. The deposited energy in the channel c is given by the injected energy times the deposition function:

$$\left. \frac{dE}{dt dV} \right|_{\text{dep},c} = \left. \frac{dE}{dt dV} \right|_{\text{inj},c} f_c \equiv \left. \frac{dE}{dt dV} \right|_{\text{inj},c} f_{\text{eff}} \chi_c \stackrel{\text{def}}{=} \dot{Q} \chi_c. \quad (6.1)$$

For computing SDs, the only interesting channel is the one that corresponds to the heating of the photon field and intergalactic medium. In CLASS there are several models implemented to approximate the deposition fraction χ_c .

Energy injections can heat up photons or baryons. In both cases, SDs could be produced. Even when no energy is injected, the photon field spectrum could deviate from the black body shape. This occurs for example when the energy is internally redistributed between photons and baryons. Examples are provided by the adiabatic cooling of electrons and baryons and the dissipation of acoustic waves. In general, the total heating rate \dot{Q} can be split as

$$\dot{Q} = \left. \frac{dE}{dt dV} \right|_{\text{dep},h} + \dot{Q}_{\text{non-inj}} = \dot{Q} \chi_h + \dot{Q}_{\text{non-inj}}, \quad (6.2)$$

where the first term represents the heating generated by a direct injection of energy (h stands for 'heating' channel), while the second one is due to an internal redistribution of energy.

6.1 Heating mechanisms in Λ CDM model

Dissipation of acoustic waves and adiabatic cooling of baryons are two processes of energy re-distribution predicted by the standard cosmological Λ CDM model. Here, only the second process is briefly discussed. Acoustic waves dissipation will be discussed in-depth in section 10. Other examples of standard mechanisms generating SDs are the cosmological recombination radiation, CMB multipoles and reionization.

Adiabatic cooling

Temperature of non-relativistic matter scales as $T_m \propto (1+z)^2$, while photon temperature changes roughly as $T_\gamma \propto (1+z)$. Due to the tight coupling between photons and baryons at high redshifts, matter continuously extracts energy from photons to maintain $T_m \approx T_\gamma$. The cooling rate associated with this process is [34]:

$$\dot{Q}_{\text{non-inj}} = -H \alpha_h T_\gamma, \quad (6.3)$$

where α_h is the intergalactic medium heat capacity (4.32).

Cosmological recombination radiation

The cosmological recombination radiation represents the emission and absorption of photons due to the recombination of H and He. The relevant redshift interval for the transition $\text{HII} \rightarrow \text{HI}$ is $500 < z < 2000$, while for $\text{HeII} \rightarrow \text{HeI}$ is $1600 < z < 3500$ and $5000 < z < 8000$ for $\text{HeIII} \rightarrow \text{HeII}$. The cosmological recombination radiation can be precisely computed with COSMOREC[43] and COSMOSPEC[44]. Its total contribution to SDs is small $\Delta I_{\text{tot}} \approx 0.01 - 1 \text{ Jy sr}^{-1}$, but it can be reached with futuristic spectrometers [11].

CMB multipoles

COBE/FIRAS measured a difference of 3.381(7) mK between the all-sky averaged temperature and the dipole one. This difference is caused by the relative motion of the Earth with respect of the CMB rest frame (Doppler effect). Then, the all-sky averaged temperature T_{ref} does not correspond to the intrinsic temperature $T_{\gamma}(z=0) \approx T_0 \equiv T_z(z=0)$ and this induces a temperature shift distortion, that at second order is

$$I(x, \theta) - I_{\text{ref}}(x) = \epsilon(\theta) [1 + \epsilon(\theta)] G(x) + [\epsilon(\theta)^2/2] Y(x), \quad (6.4)$$

where $\epsilon(\theta) = \Delta T/T_{\text{ref}}$ and $\Delta T = T(\cos \theta) - T_{\text{ref}}$. $T(\cos \theta)$ is the Doppler-shifted dipole temperature

$$T(\cos \theta) = \frac{T_0}{\gamma[1 - \beta \cos \theta]}. \quad (6.5)$$

β and γ are the usual relativistic velocity and Lorentz factor. T_{ref} can be computed as

$$T_{\text{ref}} = \frac{1}{4\pi} \int_0^{2\pi} d\phi \int_0^{\pi} d\theta \sin \theta T(\cos \theta) = \frac{1}{2} \int_{-1}^1 d \cos \theta T(\cos \theta) = \frac{T_0}{2\gamma\beta} \ln \left(\frac{1 + \beta}{1 - \beta} \right). \quad (6.6)$$

Reionization

The y -distortions are created both at early- and late times (for $z < 5 \times 10^4$). Reionization and structure formation are examples of late-time processes that create y -distortions. Reionization contributes to SDs with the so-called Sunyaev-Zeldovich (SZ) effect, which describes the interactions between photons and the free electrons through inverse Compton scattering. Such an effect is present also in galaxy clusters where free electrons are hot due to the galactic dynamics and CS might occur, creating SDs. The total y contribution is roughly [45]:

$$\Delta I_{\text{reio}}(x) = \mathcal{N} x^3 y_{\text{SZ}} Y(x) \quad \text{where} \quad y_{\text{SZ}} \approx 1.77 \times 10^{-6} \quad (6.7)$$

6.2 Heating mechanisms in exotic scenarios

There are also exotic processes that create SDs, which can then be used to study exotic scenarios beyond the standard model, such as dark matter annihilation, decaying or interacting

with other particles, and Primordial Black Holes accretion or evaporation.

Dark matter annihilation

If a dark matter candidate χ with mass M_χ annihilates, it injects energy in the primordial plasma with an effective heating rate given by

$$\dot{Q} = \rho_{\text{cdm}}^2 f_{\text{frac}} f_{\text{eff}} \frac{\langle \sigma v \rangle v}{M_\chi} \stackrel{\text{def}}{=} \rho_{\text{cdm}}^2 p_{\text{ann}}. \quad (6.8)$$

f_{frac} is the fraction of annihilating dark matter with respect to total dark matter content, while $\langle \sigma v \rangle$ is the annihilation cross section. f_{eff} is the same parameters comparing in equation (6.1).

Dark matter decay

A dark matter particle χ that decays with a given lifetime τ_χ injects energy with an effective heating rate given by

$$\dot{Q} = \rho_{\text{cdm}} f_{\text{frac}} f_{\text{eff}} \Gamma_\chi e^{-\Gamma_\chi t}, \quad (6.9)$$

where $\Gamma_\chi = 1/\tau_\chi$ is the decay width of χ .

Primordial Black Holes evaporation and accretion

Primordial Black Holes are subjected to Hawking evaporation which causes their mass to decrease as [34]:

$$\frac{dM}{dt} = -5.34 \frac{\text{g}}{\text{sec}} \times \mathcal{F}(M) M^{-2}, \quad (6.10)$$

where $\mathcal{F}(M)$ is the number of effective species in the Hawking radiation. The energy injection rate was computed in [46] and it is equal to

$$\dot{Q} = \rho_{\text{cdm}} f_{\text{frac}} f_{\text{eff}} \frac{\dot{M}}{M}, \quad (6.11)$$

Another mechanism that is able to modify the mass of a Primordial Black Hole is the accretion of matter into it. This could also modify the thermal history of the Universe. Furthermore, the accreting matter could heat up, ionize and hence radiate high-energy photons that distort the CMB black body spectrum. Before recombination, the accretion is assumed to be spherical and this does not produce an appreciable level of SDs.

III

INFLATION

The Hot Big-Bang model as explained in chapter I is not perfect and indeed it presents some problems. The most accepted solution to these problems predicts the existence of a very early phase of exponential expansion of the Universe, called inflation. There are different models of inflation, but in the most simple one the rapid expansion is driven by a single scalar field coupled to gravity, called inflaton, whose dynamics determines the Universe evolution during inflation. Quantum fluctuations in the inflaton field during inflation seed the formation of inhomogeneities in the Early Universe and therefore of CMB temperature anisotropies.

In this chapter, a brief review of inflation is presented. In the first section, the Hot Big-Bang problems and the standard inflationary solution are described. In the second section, quantum fluctuations of the inflaton field are discussed.

7 The Standard Inflationary Universe

7.1 The problems of the Hot-Big Bang Model

The Hot-Big bang model has mainly three problems.

Flatness

Present measurements show that the curvature parameter $\Omega_k = -k/\dot{a}^2$ is smaller than unity. In the matter-dominated era, the expansion factor increased as $t^{2/3}$ (2.50) and also Ω_k grew as $t^{2/3}$. In order to have $|\Omega_{k,0}| < 1$, Ω_k should have been of order 10^{-4} at the equivalence. At earlier times, in the radiation-dominated epoch, $a \propto t^{1/2}$ and $\Omega_k \propto t$. To have $|\Omega_k(t_{eq})| \approx 10^{-4}$, it is necessary that $|\Omega_k|$ was roughly 10^{-16} at time of electron-positron annihilation. Near $t = 0$, $|\Omega_k|$ was even smaller. We conclude that the very early Universe was basically flat. This is not a paradox, but physicists want to try to explain why Ω_k has to be extremely fine tuned to zero in the past. A possible explanation is that before the radiation-dominated era, where $a \propto t^{1/2}$, there was an earlier period - inflation - when the energy density of the Universe was dominated by vacuum energy and H remained constant. This implies that $\Omega_k = -k/(H^2 a^2)$ has varied as a^{-2} making it vanishing at the end of inflation. A de Sitter phase, where $a(t)$ grows exponentially[†] is a possible model of inflation.

[†] An early phase of exponential expansion was proposed in 1979 by Starobinsky, which noted that quantum corrections to general relativity lead to a solution of the Einstein equations with an effective cosmological constant, which is equivalent to a de Sitter expansion. See: A.A. Starobinsky. "Spectrum of relict gravitational radiation and the early state of the universe". In: *Soviet Journal of Experimental and Theoretical Physics*

In general, one defines the number of e -foldings during inflation as

$$\mathcal{N} \stackrel{\text{def}}{=} \int_{a(t_i)}^{a(t_f)} d \ln(a) = \int_{t_i}^{t_f} dt H. \quad (7.1)$$

In the case of an exponential expansion the scale factor varies as

$$a(t) = a(t_i) \exp(H_I(t - t_i)) \equiv a(t_f) \exp(-H_I(t_f - t)). \quad (7.2)$$

with $H = H_I = \text{constant}$ and \mathcal{N} is equal to $H_I(t_f - t_i)$. An exponential expansion phase solves the flatness problem in the following way. Suppose that Ω_k was larger than 1 at the beginning of inflation. During inflation, the curvature parameter decreased as $e^{-2\mathcal{N}}$:

$$|\Omega_{k,0}| = e^{-2\mathcal{N}} \left(\frac{a(t_f)H_I}{a_0H_0} \right)^2. \quad (7.3)$$

Given a proper \mathcal{N} , Ω_k can be arbitrary small at the end of inflation:

$$e^{\mathcal{N}} > \frac{a(t_f)H_I}{a_0H_0}, \quad (7.4)$$

To have $|\Omega_k| \approx 10^{-16}$ at the time of e^\pm annihilation or $|\Omega_{k,0}| < 1$, \mathcal{N} should be larger than 62 [47]. To compute this number Weinberg assumed that the end of inflation coincided with the beginning of the radiation-dominated era (denoted with the subscript 1), i.e. $a(t_f)H_I = a_1H_1$. Inflation is not the only explanation for the flatness problem. The most simple hypothesis is that $k = 0$ now and always.

The de Sitter phase is not the only way to solve the flatness problem. To make Ω_k small, it is sufficient to impose that the comoving Hubble radius $(aH)^{-1}$ shrinks during inflation

$$\frac{d}{dt}(aH)^{-1} < 0, \quad (7.5)$$

In a Universe filled by a single-component fluid with constant equation of state $w = P/\rho = \text{constant}$, the comoving Hubble radius is given by

$$(aH)^{-1} = H_0^{-1} a^{\frac{1}{2}(1+3w)}. \quad (7.6)$$

This condition is satisfied by non-ordinary sources that violates the strong energy condition (SEC) $w > 1/3$, that is that have negative pressure. An example is the vacuum energy ($w = -1$). The negative pressure condition can be formulated also as:

(i) *Accelerated expansion.*

$$\frac{d}{dt}(aH)^{-1} = -\frac{\ddot{a}}{\dot{a}^2} < 0 \implies \ddot{a} > 0 \quad (7.7)$$

(ii) *Slowly-varying Hubble parameters.*

$$\frac{d}{dt}(aH)^{-1} = -\frac{\dot{a}H + a\dot{H}}{(aH)^2} = -\frac{1 - \epsilon}{a} < 0 \implies \epsilon \stackrel{\text{def}}{=} -\frac{\dot{H}}{H^2} < 1. \quad (7.8)$$

ϵ is the so-called slowly-varying Hubble parameter. Since $d\mathcal{N} = Hdt$, the condition $\epsilon < 1$ is equivalent to require that the change of the Hubble parameter per e -fold ($d\mathcal{N}$) is small. If $\epsilon = 0$, inflation is said to be perfect and the spacetime during inflation is the de Sitter one: $a(t) = e^{Ht}$, where $H = \partial_t \ln(a) = \text{constant}$. Inflation has to end and so a perfect de Sitter phase is not admitted. For a small but non-zero ϵ , the de Sitter metric is still a good approximation for the inflationary background and we refer to inflation as a quasi-de Sitter period.

The fact that \mathcal{N} should be sufficiently large in order to solve the flatness problem means that inflation should have lasted enough time, i.e. ϵ must have been less than 1 for a sufficiently large number of e -folds or of comoving Hubble times. This condition is measured by a second parameter

$$\tilde{\eta} \stackrel{\text{def}}{=} \frac{d \ln(\epsilon)}{d\mathcal{N}} = \frac{\dot{\epsilon}}{H\epsilon}. \quad (7.9)$$

$\tilde{\eta}^\dagger$ is the second slowly-varying Hubble parameter. For $\tilde{\eta} < 1$, the fractional change of ϵ per Hubble time is small and inflation persists.

For later convenience, equation (7.6) can be written in terms of the first slowly rolling Hubble parameter

$$a \propto \eta^{1+b}, \quad \text{with} \quad b = \frac{1 - 3w}{1 + 3w}. \quad (7.10)$$

$b = 0$ corresponds to a radiation-dominated Universe ($w = 1/3$), while $b < 0$ indicates a fluid that violates the SEC condition.

There can be higher order slowly-rolling Hubble parameters. In literature, these are defined as

$$\epsilon_0 \stackrel{\text{def}}{=} \frac{H_{\text{in}}}{H}, \quad \epsilon_{i+1} \stackrel{\text{def}}{=} \frac{\dot{\epsilon}_i}{H\epsilon_i} \equiv \frac{1}{H} \frac{d\epsilon_i}{d\mathcal{N}} \quad \text{for } i = 0, 1, 2, \dots, \quad (7.11)$$

where H_{in} is some initial value of H during inflation. In particular, $\epsilon_1 \equiv \epsilon$ and $\epsilon_2 \equiv \tilde{\eta}$. Notice also that the first slowly-rolling Hubble parameter is related to the equation of state as

$$\epsilon_1 = \frac{3}{2}(1 + w). \quad (7.12)$$

To sum up, inflation solves the flatness problem if the following conditions are satisfied

$$\epsilon_1 = -\frac{\dot{H}}{H^2} < 1, \quad \epsilon_2 = \frac{\dot{\epsilon}}{H\epsilon} < 1. \quad (7.13)$$

[†] The $\tilde{\eta}$ is used to distinguish this parameter from the conformal time.

Horizon

CMB looks almost the same from every directions. This is possible only if the entire Universe was in casual contact at the last scattering surface. In this case, atomic interactions smoothed out all temperature fluctuations. However, it is not possible for the entire Universe to be in causal contact due to the existence of the proper particle horizon (2.29). The particle proper horizon at the time of last scattering was

$$s_H(t_{\text{ls}}) = a(t_{\text{ls}}) \int_0^{t_{\text{ls}}} \frac{dt}{a(t)} = a(t_{\text{ls}}) \int_0^{a(t_{\text{ls}})} \frac{da}{a^2 H(a)}, \quad (7.14)$$

where equation (2.46) and the condition $a(0) = 0$ were used. By using equation (2.47) and the variable $x = a/a_0 = (1+z)^{-1}$, the previous integral becomes

$$s_H(z_{\text{ls}}) = \frac{1}{H_0(1+z_{\text{ls}})} \int_0^{(1+z_{\text{ls}})^{-1}} \frac{dx}{x^2 \sqrt{[\sum_w \Omega_{w,0} (x)^{-3(1+w)} + \Omega_{k,0} (x)^{-2}]}}. \quad (7.15)$$

At this redshift the Universe can be treated as filled only by matter and with zero curvature. Therefore, the previous integral gives

$$s_H(z_{\text{ls}}) = \frac{1}{H_0(1+z_{\text{ls}})} \int_0^{(1+z_{\text{ls}})^{-1}} \frac{dx}{x^2 \sqrt{x^{-3}}} = \frac{2}{H_0(1+z_{\text{ls}})^{3/2}} \propto \frac{1}{H_0(1+z_{\text{ls}})^{3/2}}. \quad (7.16)$$

To easily compare the horizon at last scattering with observations, it is useful to convert it in an angular distance. To define the angular diameter distance, consider a source placed at $(t = t_1, r = r_1)$ with proper diameter D that emits two photons detected later at $(t = t_0, r = 0)$. It is always possible to find a coordinates system where the center of the source is at $\theta = 0$ and the light travels from its edges towards the observer defining a cone with half-angle $\theta = \delta/2$. The edges of the source are at fixed angle ϕ , cosmic time t_1 and radial coordinate r_1 . From the FLRW metric (2.23) it is easy to compute the proper diameter:

$$s \equiv D = \int \sqrt{g_{\mu\nu} dx^\mu dx^\nu} \Big|_{dt=dr=d\phi=0} = a(t_1) r_1 \int_{-\delta/2}^{\delta/2} d\theta = a(t_1) r_1 \delta. \quad (7.17)$$

The angular distance is then defined as

$$d_A \stackrel{\text{def}}{=} \frac{D}{\delta} = a(t_1) r_1 \equiv \frac{a(t_0) r_1}{1+z_1}, \quad (7.18)$$

To compute d_A at last scattering it is necessary to compute the radial coordinate distance at the last scattering surface r_{ls} . Since, CMB is made up by photons one can use the condition $d\tau = 0$ to compute r_{ls} as a function of t_{ls} (or z_{ls}). The result is the same of equation (2.32), but with different labels. In a flat Universe with $z_{\text{ls}} \approx 1100 \gg 1$, the result is $r_{\text{ls}} \approx (a_0 H_0)^{-1}$.

The angular diameter distance at the last scattering surface is then

$$d_A(z_{\text{ls}}) = \frac{a_0 r_{\text{ls}}}{1 + z_{\text{ls}}} \propto \frac{1}{H_0(1 + z_{\text{ls}})}. \quad (7.19)$$

Finally, the horizon at last scattering now subtends an angle of order

$$\theta_{\text{hor}} = \frac{s_H(z_{\text{ls}})}{d_A(z_{\text{ls}})} \propto (1 + z_{\text{ls}})^{-1/2} = 1.6^\circ. \quad (7.20)$$

Thus, only the portions of sky that are now separated by an angle smaller than 1.6° were in causal contact at last scattering. So, Compton scattering was able to smooth the temperature fluctuations only in the regions of the Universe that are now inside an angle of 1.6° . The large-scale ($\theta > 7^\circ$) isotropy of the CMB is a problem that cannot be explained using the standard Hot-Big Bang model.

The inflationary solution solves the horizon problem in the following way. During the inflationary expansion, the proper particle horizon at last scattering changed as

$$s_H(t_{\text{ls}}) = a(t_{\text{ls}}) \int_{t_i}^{t_{\text{ls}}} \frac{dt}{a(t)}, \quad (7.21)$$

By accepting that this integral is much larger than the contribution coming from the time interval $[t_{\text{ls}}, t_f]$, we can change the upper extreme of the previous integral into t_f . Then, by inserting equation (7.2) in the previous integral, we get

$$d_H(t_{\text{ls}}) = \frac{a(t_{\text{ls}})}{a(t_f)} \int_{t_i}^{t_f} dt \exp(H_I(t_f - t)) = \frac{a(t_{\text{ls}})}{a(t_f)H_I} [\exp(\mathcal{N}) - 1]. \quad (7.22)$$

Since it is necessary to have $e^{\mathcal{N}}$ large, the -1 can be neglected. The angular diameter distance did not change and it is still given by equation (7.19), where $(1 + z_{\text{ls}})^{-1} \equiv a_0/a_{\text{ls}}$. CMB isotropy on large scales is mathematically translated to the condition $d_H(t_{\text{ls}}) > d_A(t_{\text{ls}})$ or equivalently

$$e^{\mathcal{N}} > \frac{a(t_f)H_I}{a_0H_0}. \quad (7.23)$$

This is the same condition required to solve the flatness problem. To sum up, the accelerated inflationary expansion allows those regions that in the standard cosmological evolution are not in causal contact to be causally connected near the physical singularity. Figure 5 shows schematically the horizon problem and its solution.

The horizon problem can be described also by comparing a physical scale λ with the Hubble radius H^{-1} (see figure 6). Suppose that λ is the distance at last scattering between two photons detected today. The horizon problem means that such distance was larger than the Hubble radius at last scattering.

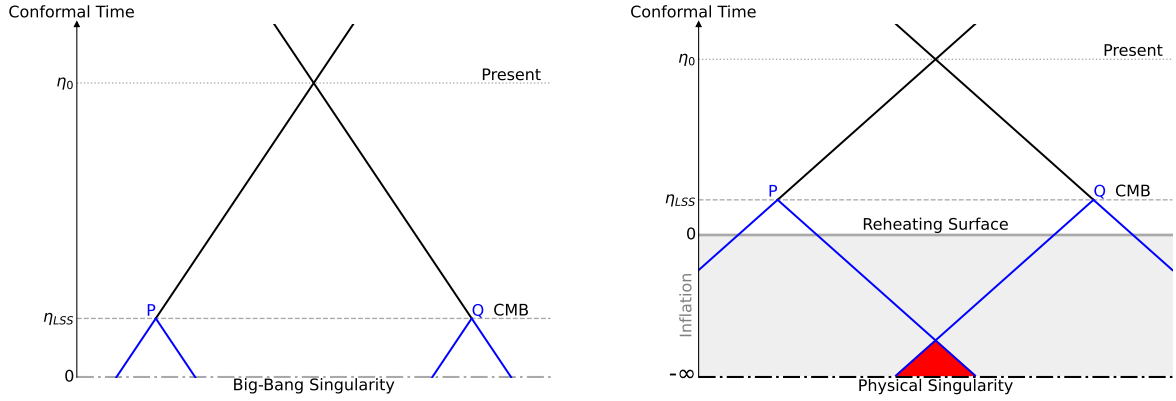


Fig. 5 – Schematic representation of the horizon problem (left) and of the corresponding inflationary solution (right). The black lines are the past light cone from the present back to the last scattering surface. P and Q represent the two furthest points of the last scattering surface that we can see now. In the standard Hot-Big-Bang model, the (blue) light cones drawn from these points never intersect. The inflationary solution "adds more conformal time" before the last scattering surface so that P and Q have the chance to get in causal contact (red region). During inflation (slightly grey region), the conformal time is negative. The singularity of the standard Big-Bang model is replaced by the reheating surface, which represents the transition from inflation to the standard Big-Bang model. The physical singularity is now at $\eta = -\infty$.

However, to explain why these photons look so similar, it is necessary that they were in causal contact at last scattering. In a matter-dominated or radiation-dominated universe any physical distance λ starts below the Hubble radius and crosses it only once since $\lambda \propto a^1$, while $H^{-1} \propto a^2$ (RD) or $H^{-1} \propto a^{3/2}$ (MD). So, only when $\lambda = H^{-1}$ the two particles separated by λ are in causal contact. In the standard Hot Big-Bang model, λ crosses the Hubble radius H^{-1} after the last scattering.

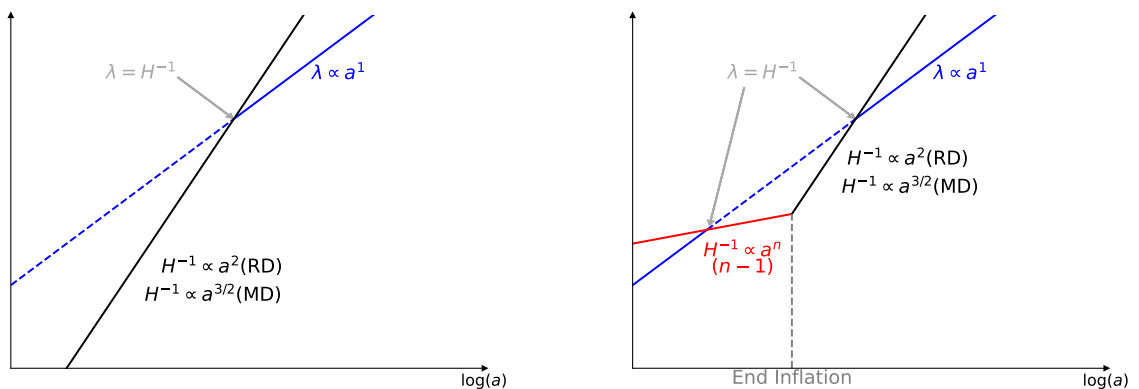


Fig. 6 – Schematic representation of the evolution of physical scales λ and of the Hubble radius H^{-1} in the standard hot Big-Bang model (left) and in an inflationary Universe (right).

The inflationary solution predicts an early period where the Hubble radius H^{-1} grew slower than a (see equation (7.5)). Then, λ starts smaller than H^{-1} , exits from the Hubble radius and then re-enters it later on.

Monopoles

Many high energy particle physics models predict the existence of magnetic monopoles and other stable relics coming from spontaneously broken gauge symmetries. In particular, the simplest predictions say that there should be 1 magnetic monopoles per nucleon in the Universe [47], which is in strong disagreement with the current observations which show a monopoles density of 10^{-30} per nucleon. The naive solution to this problem is that there may be no gauge group spontaneously broken to the standard model one so that stable relics were never produced. The other solution is given by inflation, which could have diluted sufficiently the monopoles in the Universe. A simple estimation says that the number of e -foldings necessary to have 10^{-30} monopoles per nucleon or less should be greater than 23.

Among the three problems aforementioned, the most serious is the horizon one since the others two can be solved without introducing the inflationary phase. However, it is interesting to notice that the number of e -foldings necessary to solve the horizon problem automatically solves also the flatness and the monopoles problems.

7.2 Single Field Inflation

The simplest model of inflation is the one where the energy density of a minimally coupled single scalar field $\phi(t, \mathbf{x})$, called inflaton, dominates the total energy density of the Universe. The action of this model is

$$S[\phi] \stackrel{\text{def}}{=} \int d^4x \sqrt{-g} \mathcal{L} = - \int d^4x \sqrt{-g} \left[\frac{1}{2} g^{\mu\nu} \partial_\mu \phi \partial_\nu \phi + V(\phi) \right], \quad (7.24)$$

where g is the determinant of $g_{\mu\nu}$. The energy-momentum tensor is

$$T_{\mu\nu} \stackrel{\text{def}}{=} - \frac{2}{\sqrt{-g}} \frac{\delta(\sqrt{-g} \mathcal{L})}{\delta g^{\mu\nu}} = \partial_\mu \phi \partial_\nu \phi + g_{\mu\nu} \mathcal{L}. \quad (7.25)$$

This has the same form as the energy-momentum tensor of a perfect fluid (1.17) with

$$\rho = - \frac{1}{2} g^{\mu\nu} \partial_\mu \phi \partial_\nu \phi + V(\phi) \quad (7.26a)$$

$$P = - \frac{1}{2} g^{\mu\nu} \partial_\mu \phi \partial_\nu \phi - V(\phi) \quad (7.26b)$$

$$u^\mu = - \left[-g^{\alpha\beta} \partial_\alpha \phi \partial_\beta \phi \right]^{-1/2} g^{\mu\rho} \partial_\rho \phi \quad (7.26c)$$

In a FLRW spacetime (2.1), the pressure and the energy density become

$$\rho = \frac{1}{2} \dot{\phi}^2 + \frac{1}{2} \frac{(\nabla\phi)^2}{a^2} + V(\phi), \quad P = \frac{1}{2} \dot{\phi}^2 - \frac{1}{2} \frac{(\nabla\phi)^2}{a^2} - V(\phi) \quad (7.27)$$

where $(\nabla\phi)^2 = \gamma_{ij} \partial^i \phi \partial^j \phi$. From now on we assume that ϕ is spatially homogeneous as the background FLRW metric so that ϕ depends only on the cosmic time. Thus, $(\nabla\phi)^2 = 0$. The

conservation of the energy momentum tensor $T^{\mu\nu}_{;\nu} = 0$ is equivalent to $\dot{\rho} = -3H(\rho + P)$, where $H = \dot{a}/a$. By inserting the equations for ρ and P into this relation, one gets the equation of motion for ϕ :

$$\ddot{\phi} + 3H\dot{\phi} + V'(\phi) = 0. \quad (7.28)$$

During inflation, the Hubble rate is given by

$$H = \sqrt{\frac{8\pi G\rho}{3}} \equiv \sqrt{\frac{8\pi G}{3} \left(\frac{1}{2}\dot{\phi}^2 + V(\phi) \right)}, \quad (7.29)$$

where the Universe was taken to be flat. By deriving the square of the previous equation and using equation (7.28), one gets

$$\dot{H} = -4\pi G\dot{\phi}^2. \quad (7.30)$$

Equations (7.29) and (7.30) allow to write the slowly-varying Hubble parameters (7.11) as

$$\epsilon_1 = -\frac{\dot{H}}{H^2} = \frac{\frac{3}{2}\dot{\phi}^2}{\frac{1}{2}\dot{\phi}^2 + V(\phi)} \equiv 4\pi G \frac{\dot{\phi}^2}{H^2} \equiv 4\pi G \left(\frac{d\phi}{d\mathcal{N}} \right)^2, \quad (7.31a)$$

$$\epsilon_2 = \frac{\dot{\epsilon}_1}{H\epsilon_1} = 2 \left(\frac{\ddot{\phi}}{H\dot{\phi}} - \frac{\dot{H}}{H^2} \right) = 2(\epsilon_1 - \delta), \quad (7.31b)$$

where $\delta \stackrel{\text{def}}{=} -\frac{\ddot{\phi}}{H\dot{\phi}}$ is the dimensionless acceleration per Hubble time. Clearly, the inflation conditions (7.13) are equivalent to $\{\epsilon_1, |\delta|\} \ll 1$.

Slow-roll approximation

Equation (7.31) translates the inflation condition $\epsilon_1 \ll 1$ into

$$\frac{3}{2}\dot{\phi}^2 \ll \frac{1}{2}\dot{\phi}^2 + V(\phi) \implies \dot{\phi}^2 \ll V(\phi) \quad \text{or} \quad \frac{1}{2M_{pl}^2} \left(\frac{d\phi}{d\mathcal{N}} \right)^2 \ll 1, \quad (7.32)$$

and the Hubble rate during inflation (7.29) is approximately

$$H \doteq \sqrt{\frac{8\pi G}{3} V(\phi)}. \quad (7.33)$$

The symbol \doteq means that the equality is true only in the slow-roll regime. This is the so-called slow-roll approximation or 'new-inflation', which is an inflationary model proposed by Linde[†] and Steinhardt, Albrecht[‡].

[†] A.D. Linde. "Scalar field fluctuations in the expanding universe and the new inflationary universe scenario". In: *Physics Letters B* 116.5 (1982), pp. 335–339. ISSN: 0370-2693. DOI: [https://doi.org/10.1016/0370-2693\(82\)90293-3](https://doi.org/10.1016/0370-2693(82)90293-3). URL: <https://www.sciencedirect.com/science/article/pii/0370269382902933>.

[‡] Andreas Albrecht and Paul J. Steinhardt. "Cosmology for Grand Unified Theories with Radiatively Induced Symmetry Breaking". In: *Phys. Rev. Lett.* 48 (17 Apr. 1982), pp. 1220–1223. DOI: [10.1103/PhysRevLett.48.1220](https://doi.org/10.1103/PhysRevLett.48.1220). URL: <https://link.aps.org/doi/10.1103/PhysRevLett.48.1220>.

If the slow-roll approximation holds, the equation of state of the scalar field is roughly $P = -\rho$, i.e. $w \approx -1 < -1/3$ as required. The condition $|\delta| \ll 1$, or equivalently $|\ddot{\phi}| \ll H\dot{\phi}$, allows to neglect the term $\ddot{\phi}$ in the equation of motion for ϕ (7.28), which then becomes

$$\dot{\phi} \doteq -\frac{V'(\phi)}{3H}. \quad (7.34)$$

The time derivative of the Hubble rate (7.30) is then approximated to

$$\dot{H} \doteq -\frac{4\pi G}{9H^2}V'^2 \approx -\frac{1}{6}\frac{V'^2}{V} \quad (7.35)$$

We can roughly write the slowly-varying Hubble parameters (7.31) as

$$\epsilon_1 \doteq \frac{1}{16\pi G} \left(\frac{V'}{V}\right)^2 \stackrel{\text{def}}{=} \epsilon_V \quad (7.36a)$$

$$\epsilon_2 \doteq -4\pi G \frac{V''V - V'^2}{V^2} = 4\epsilon_V - 2\eta_V \quad \text{where} \quad \eta_V \stackrel{\text{def}}{=} 8\pi G \frac{V''}{V} \quad (7.36b)$$

The parameters ϵ_V , η_V are called potential slow-roll parameters. Similarly, it is possible to define higher order potential slow-roll parameters. Inflation conditions (7.13) in the slow-roll approximation become constraints on the inflaton potential

$$\epsilon_V = \frac{1}{16\pi G} \left(\frac{V'}{V}\right)^2 \ll 1, \quad |\eta_V| = \frac{1}{8\pi G} \left|\frac{V''}{V}\right| \ll 1. \quad (7.37)$$

Inflation ends when the inflaton accelerates and the condition (7.32) is no longer true. Then, the inflaton starts oscillating around its minimum in the so-called reheating phase.. An example of inflaton potential that presents such dynamics is given in figure 7.

Under these 'slow-roll' conditions, the expansion is not strictly exponential, but it can be easily made exponentially large. Indeed, suppose that $\phi(t)$ grew from $\phi_i = \phi(t_i)$ to $\phi_f = \phi(t_f)$ with $0 < V(\phi_f) < V(\phi_i)$. Then, $\epsilon_V \ll 1$ implies that the expansion factor is exponentially large

$$\begin{aligned} \frac{a(t_f)}{a(t_i)} &= \exp \left[\int_{\phi_i}^{\phi_f} d\phi \frac{H}{\dot{\phi}} \right] \\ &\approx \exp \left[- \int_{\phi_i}^{\phi_f} d\phi \left(8\pi G \frac{V}{V'} \right) \right] \gg 1. \end{aligned} \quad (7.38)$$

The number of e -foldings in the slow-roll approximation is

$$\mathcal{N} \stackrel{\text{def}}{=} \int_{t_i}^{t_f} dt H \equiv \int_{\phi_i}^{\phi_f} d\phi \frac{H}{\dot{\phi}} \doteq \int_{\phi_i}^{\phi_f} d\phi \frac{V}{V'} \equiv M_{pl} \int_{\phi_i}^{\phi_f} \frac{d\phi}{\sqrt{2\epsilon_V}} \quad (7.39)$$

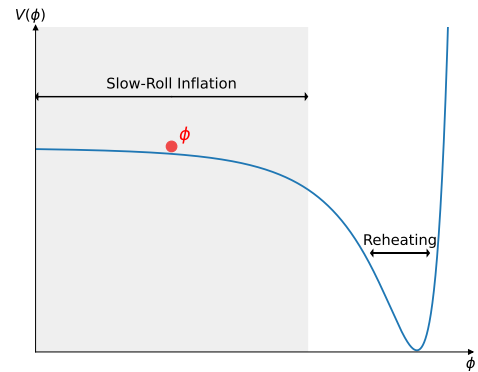


Fig. 7 – Schematic inflationary process.

8 Quantum Fluctuations during Inflation

Until now, the Universe was considered to be a perfectly homogeneous and isotropic manifold described by the FLRW metric. However, to explain the most interesting things in the present universe, like galaxy clusters, galaxies, stars and even us, deviations from the perfect homogeneity are needed. In the standard hot Big-Bang model, no mechanism explains the origin of these fluctuations, but quantum effects of the inflaton field are a valid explanation for their origin.

Quantum field theory predicts that a quantum field oscillates with all possible wavelengths maintaining zero average on a sufficient macroscopic time. During inflation the total energy density of the Universe is dominated by the inflaton potential energy and so quantum fluctuations in the inflaton field result in perturbations of the energy-momentum tensor. Due to the coupling between the energy-momentum tensor and the metric provided by Einstein equations, fluctuations of $T_{\mu\nu}$ induce metric perturbations. Thus, quantum oscillations in the inflaton field generate both energy density perturbations and metric inhomogeneities:

$$\delta\phi \Rightarrow \delta T_{\mu\nu} \Rightarrow \delta g_{\mu\nu}.$$

On the other hand, metric perturbations induce a back reaction on the evolution of the inflaton field:

$$\delta g_{\mu\nu} \Rightarrow \delta\phi.$$

Before analyzing cosmological perturbation, we introduce the following nomenclature. Let $k \propto \lambda^{-1}$ be the typical comoving wavenumber of cosmological fluctuations (λ is the typical wavelength). Then, one defines sub-Hubble-radius fluctuations as those perturbations whose wavenumber is much larger than the comoving Hubble radius: $k \gg aH$. Similarly, super-Hubble-radius perturbations are those such that $k < aH$.

Because of the rapid inflationary expansion, the wavelengths of energy density fluctuations can be stretched from short scales to cosmological ones, eventually making them exit from the Hubble radius. On super-Hubble-radius scales perturbations are frozen. Gravity drags these perturbations until they re-enter the Hubble-radius in the radiation- or matter-dominated era (see plot 6). Density perturbations that re-enter the Hubble radius seed the formation of the Large Scale Structures (LSS) and CMB anisotropies. In this sense, cosmological observables can be directly linked to quantum fluctuations of the inflaton field.

8.1 Cosmological Perturbations

To study how cosmological observables are affected by quantum fluctuations, it is necessary to know how the tensors involved are perturbed.

Metric perturbations

The perturbed FLRW metric can be decomposed as [48]:

$$g_{00} = -a^2(\eta) \left[1 + 2 \sum_{n=1}^{\infty} \frac{A^{(n)}}{n!} \right] \quad (8.1a)$$

$$g_{0i} = a(\eta) \sum_{n=1}^{\infty} \frac{B_i^{(n)}}{n!} \quad (8.1b)$$

$$g_{ij} = a^2(\eta) \left(\delta_{ij} + \sum_{n=1}^{\infty} \frac{h_{ij}^{(n)}}{n!} \right), \quad (8.1c)$$

where $A^{(n)}$, $B_i^{(n)}$, $h_{ij}^{(n)}$ are the n -th order perturbations of the metric. These quantities can be decomposed into scalar, vector and tensor perturbations according to their transformation properties under the group of 3-translations and 3-rotations. In particular, the Helmholtz theorem allows decomposing any vector object into a solenoidal (or transverse) and longitudinal part

$$B_i = \partial_i B^{\parallel} + B_i^{\perp} \equiv \partial_i B + \hat{B}_i, \quad (8.2)$$

where \hat{B}_i is solenoidal in the sense that $\partial^i \hat{B}_i = 0$. Similarly, h_{ij} can be expressed as

$$h_{ij} = -2C\delta_{ij} + 2E_{ij}. \quad (8.3)$$

E_{ij} can be further decomposed as

$$E_{ij} = E_{ij}^{\parallel} + E_{ij}^{\perp} + E_{ij}^T \stackrel{\text{def}}{=} \partial_{(i} \partial_{j)} E + \partial_{(i} \hat{E}_{j)} + \hat{E}_{ij}^T, \quad (8.4)$$

where the operators $\partial_{(i} \partial_{j)}$, $\partial_{(i} \hat{E}_{j)}$ are defined as

$$\partial_{(i} \partial_{j)} \stackrel{\text{def}}{=} \partial_i \partial_j - \frac{1}{3} \delta_{ij}, \quad \partial_{(i} \hat{E}_{j)} \stackrel{\text{def}}{=} \frac{1}{2} (\partial_i \hat{E}_j + \partial_j \hat{E}_i). \quad (8.5)$$

The component E_{ij}^{\parallel} is longitudinal, i.e. irrotational, $\epsilon_{ijk} \partial_j \partial_k E_{ij}^{\parallel}$. \hat{E}_i is transverse, i.e. divergenceless, $\partial^i \hat{E}_i = 0$. E_{ij}^T is both traceless and transverse: $\hat{E}_{ii}^T = 0$, $\partial^i \hat{E}_{ij}^T = 0$. An $\hat{}$ indicates a transverse quantity. A, B, C, E are the scalar perturbations of the metric, while \hat{B}_i and \hat{E}_i are the vector ones. Tensor perturbations are the traceless and transverse tensor \hat{E}_{ij}^T and they correspond to gravitational waves. The apex (n) was omitted for simplicity. From now on, when a perturbation is written without any apex, then it is of the first-order.

This decomposition is particularly useful since at linear order scalar, vector and tensor perturbations evolve independently. Vector perturbations cannot be created during inflation [49] and they decay with the expansion of the Universe. Thus, they will be ignored. Scalar perturbations will result in energy density fluctuations, while tensor ones will be observed as gravitational waves.

Gauge transformation

The spacetime interval is gauge-invariant, i.e. it is invariant under any coordinates transformation $x^\mu \rightarrow \tilde{x}^\mu$. Consider the generic gauge transformation

$$t \rightarrow \tilde{t} = t + \alpha, \quad x^i \rightarrow \tilde{x}^i = x^i + \partial^i \beta + \epsilon^i. \quad (8.6)$$

To have

$$d\tau^2 = -g_{\mu\nu} dx^\mu dx^\nu = -\tilde{g}_{\mu\nu} d\tilde{x}^\mu d\tilde{x}^\nu, \quad (8.7)$$

the perturbations should transform as

$$A \rightarrow \tilde{A} = A - \alpha' - \mathcal{H}\alpha, \quad (8.8a)$$

$$B \rightarrow \tilde{B} = B + \alpha - \beta', \quad (8.8b)$$

$$C \rightarrow \tilde{C} = C + (1/3)\nabla^2 \beta + \mathcal{H}\alpha, \quad (8.8c)$$

$$E \rightarrow \tilde{E} = E - \beta, \quad (8.8d)$$

$$\hat{B}_i \rightarrow \hat{\tilde{B}}_i = \hat{B}_i - \epsilon'_i \quad (8.8e)$$

$$\hat{E}_i \rightarrow \hat{\tilde{E}}_i = \hat{E}_i - \epsilon_i \quad (8.8f)$$

$$\hat{E}_{ij}^T \rightarrow \hat{\tilde{E}}_{ij}^T = \hat{E}_{ij}^{T\dagger}. \quad (8.8g)$$

By fixing α and β , one makes a gauge choice. There are many different possible gauge choices. Two of the most used are the synchronous and the conformal Newtonian gauge. In general, the Newtonian, or longitudinal, gauge, is obtained by setting that both g_{0i} and g_{ij} are transverse. This would correspond to $B = E = 0$ and $\hat{E}_i = 0$. A restricted version of this gauge, valid at linear order, is obtained by setting also $\hat{B}_i = 0$ and $\hat{E}_{ij}^T = 0$. Indeed, at higher order vector and tensor modes can be induced and could not be set to zero at the beginning. To be consistent with [48] it is necessary to redefine $A = \Psi$, $C = \Psi$ so that the Newtonian gauge at linear order implies that the metric has the form

$$ds^2 = a^2(\eta)[-(1 + 2\Psi)d\eta^2 + (1 - 2\Phi)\delta_{ij}dx^i dx^j] \quad (8.9)$$

The synchronous gauge is obtained with the conditions $A = B = 0$ and $\hat{B}_i = 0$, i.e. by imposing that all perturbations are confined in the spatial part of the metric. In this case, the metric becomes

$$ds^2 = a^2(\eta)[-d\eta^2 + (\delta_{ij} + h_{ij})dx^i dx^j]. \quad (8.10)$$

Notice that to compare the notation used in this work with the one in [48], one should redefine $2E = \mu$ and $-2C = h/3$. In Fourier space, the perturbations h_{ij} can be expanded

[†] This means that at linear order tensor perturbations are gauge-invariant.

in terms of two scalar functions h and χ (in [48] the function χ is labelled with η):

$$h_{ij}(\eta, \mathbf{x}) = \int d^3k e^{i\mathbf{k}\cdot\mathbf{x}} \left[\hat{\mathbf{k}}_i \hat{\mathbf{k}}_j h(\mathbf{k}, \eta) + \left(\hat{\mathbf{k}}_i \hat{\mathbf{k}}_j - \frac{1}{3} \delta_{ij} \right) 6\chi(\mathbf{k}, \eta) \right], \quad \mathbf{k} = k \hat{\mathbf{k}}. \quad (8.11)$$

Matter perturbations

In general, a perturbed energy-momentum tensor can be written at the first-order as

$$T^0_0 = -(\rho_0 + \delta\rho), \quad (8.12a)$$

$$T^0_i = (\rho_0 + P_0) v_i \stackrel{\text{def}}{=} (\delta q)_{,i} = -T^i_0, \quad (8.12b)$$

$$T^i_j = \delta^i_j (P_0 + \delta P) + \Sigma^i_j, \quad (8.12c)$$

where $v^i = dx^i/d\eta$, $\Sigma^i_j \stackrel{\text{def}}{=} T^i_j - \delta^i_j T^k_k/3$ is the traceless anisotropic shear perturbation to T^i_j and where $(\delta q)_{,i}$ is the momentum density. In Fourier space, it is useful to introduce the variables θ and σ defined by

$$\theta \stackrel{\text{def}}{=} i k^j v_j \quad (\rho_0 + P_0) \sigma \stackrel{\text{def}}{=} - \left(\hat{k}_i \hat{k}^j - \frac{1}{3} \delta_i^j \right) \Sigma^i_j \quad (8.13)$$

and the variable

$$\delta \stackrel{\text{def}}{=} \frac{\delta\rho}{\rho_0} \quad (8.14)$$

At linear, order these quantities in the synchronous and Newtonian gauges are related by

$$\delta(\text{Syn}) = \delta(\text{Newt}) - \alpha \frac{\rho'_0}{\rho_0}, \quad (8.15a)$$

$$\theta(\text{Syn}) = \theta(\text{Newt}) - \alpha k^2, \quad (8.15b)$$

$$\delta P(\text{Syn}) = \delta P(\text{Newt}) - \alpha P'_0 \quad (8.15c)$$

$$\sigma(\text{Syn}) = \sigma(\text{Newt}) \quad (8.15d)$$

Initial conditions

By perturbing Einstein equations and Boltzmann one, it is possible to derive the differential equations that describe the evolution of density and velocity perturbations of the matter or radiation components present in the primordial plasma. Inflation provides the initial conditions to solve such equations. By measuring the various perturbed quantities, it is possible to select between different inflationary scenarios. An example of this will be provided in section 9 where the temperature fluctuations of the CMB are studied.

In general, there are two different types of initial conditions: isocurvature and adiabatic initial conditions. To define these variables, consider the matter-radiation plasma in the early Universe. The entropy per matter particle is given by $\Gamma = T^3/n_m$, where n_m is the number density of matter particles. It is possible to define the entropy perturbation for a

system of two barotropic fluids, each with an equation of state $w_i = P_i/\rho_i$, as

$$\mathcal{S}_{ij} \stackrel{\text{def}}{=} \frac{\delta\Gamma_i}{\Gamma_i} - \frac{\delta\Gamma_j}{\Gamma_j} \equiv \frac{\delta_i}{1+w_i} - \frac{\delta_j}{1+w_j}. \quad (8.16)$$

In the case of a fluid with only matter and radiation, it becomes:

$$\mathcal{S} = \frac{3}{4}\delta_r - \delta_m. \quad (8.17)$$

By taking into account all the possible radiation/matter components, entropy perturbation vanishes if

$$\delta_\gamma \approx \delta_\nu \approx \frac{4}{3}\delta_{\text{CDM}} \approx \frac{4}{3}\delta_b. \quad (8.18)$$

Perturbations that satisfy the previous relationship are said to be adiabatic, or curvature, perturbations. The name curvature suggests that a local geometric perturbation is associated with the matter one. If the entropy term does not vanish, perturbations are called isocurvature perturbation. In case of isocurvature perturbations, the matter perturbations do not induce any metric perturbations. Isocurvature perturbations are very constrained by the current data. In general, isocurvature perturbations are not produced in single-field inflationary scenarios, but they can arise in multi-field models. Finally, it is possible to build a gauge-invariant entropy perturbation:

$$\mathcal{S} \stackrel{\text{def}}{=} H \left(\frac{\delta P}{\dot{p}} - \frac{\delta\rho}{\dot{\rho}} \right). \quad (8.19)$$

Curvature perturbation

Pressure fluctuations are related to the density ones as

$$\delta P = c_s^2 \delta\rho + \delta P_{\text{not-ad}} \quad (8.20)$$

where

$$c_s^2 = \left(\frac{\delta P}{\delta\rho} \right) \Big|_{\Gamma} \quad (8.21)$$

is the adiabatic speed of sound and

$$\delta P_{\text{not-ad}} = \left(\frac{\delta P}{\delta\Gamma} \right) \Big|_{\rho} \Gamma. \quad (8.22)$$

is the non-adiabatic contribution to the total pressure. The latter is related to the entropy perturbation by

$$\mathcal{S} = H \frac{\delta P_{\text{not-ad}}}{\dot{P}}. \quad (8.23)$$

Similarly, it is possible to introduce a gauge-invariant variable, called comoving curvature perturbation, defined as

$$\mathcal{R} \stackrel{\text{def}}{=} \Phi - \frac{H}{\rho_0 + P_0} \delta q \equiv \Phi + \mathcal{H} \frac{\theta}{k^2}. \quad (8.24)$$

The second equivalence holds in Newtonian gauge and in Fourier space. Geometrically, \mathcal{R} measures the spatial curvature of comoving hypersurfaces. During inflation \mathcal{R} and $-\zeta$ are equal because $\delta\rho/\dot{\rho}_0 = \delta\phi/\dot{\phi}_0$ and $T_i^0 = \partial_i\delta q = -\dot{\phi}_0\partial_i\delta\phi$. The evolution of \mathcal{R} is determined by the linearized Einstein equations in Fourier space:

$$\mathcal{R}' = \frac{\mathcal{H}}{\rho_0 + P_0} \delta P_{\text{not-ad}} + k^2 \frac{\mathcal{H}}{(4\pi G a^2 (\rho_0 + P_0))} \left[\left(c_s^2 - \frac{1}{3} \Psi + \frac{1}{3} \Phi \right) \right] \quad (8.25)$$

This equation suggests that for adiabatic perturbations, $\delta P_{\text{not-ad}} = 0$, the curvature perturbation is conserved on super-Hubble-radius scales. This is why, adiabatic perturbations are called also curvature perturbations. During inflation the energy density and pressure are dominated by the inflaton contribution. Then, quantum fluctuations in the inflaton field $\delta\phi$ leads to perturbations in ρ , P and hence they generate curvature perturbations. The latter is frozen on super-Hubble-radius scales. When \mathcal{R} re-enters the Hubble radius during the radiation-dominated era, it provides the initial conditions for the perturbed Universe observed today. Hence, to relate observables with inflation, it is necessary to compute the curvature perturbation produced during inflation at the Hubble-radius crossing.

Notice that in presence of isocurvature perturbations, the evolution of \mathcal{R} is more complicated since it is not frozen anymore on super-Hubble-radius scales

Statistics

Consider a generic random field $g(t, \mathbf{x})$, e.g. the comoving curvature perturbations \mathcal{R} . To characterize the properties of g it is useful to introduce the power spectrum. Consider the Fourier expansion of the field g

$$g(t, \mathbf{x}) = \int \frac{d^3k}{(2\pi)^{3/2}} e^{i\mathbf{k}\cdot\mathbf{x}} g_{\mathbf{k}}(t). \quad (8.26)$$

The dimensionless power spectrum $\mathcal{P}_g(k)$ is defined as

$$\langle g_{\mathbf{k}_1}, g_{\mathbf{k}_2}^* \rangle \stackrel{\text{def}}{=} \frac{2\pi^2}{k^3} \mathcal{P}_g(k) \delta^3(\mathbf{k}_1 - \mathbf{k}_2), \quad (8.27)$$

where $\langle \dots \rangle$ denotes the ensemble average. The power spectrum measures the amplitude of the fluctuation at a given mode k . From the definitions it is trivial to find that

$$\langle g^2(t, \mathbf{x}) \rangle = \int \frac{dk}{k} \mathcal{P}_g(k), \quad (8.28)$$

which tells that $\mathcal{P}_g(k)$ is the contribution to the variance of g per unit logarithmic interval in wave-number k . The scale dependence of the power spectrum is quantified by the scalar spectral index (or tilt)

$$n_g - 1 \stackrel{\text{def}}{=} \frac{d \ln \mathcal{P}_g(k)}{d \ln k}, \quad (8.29)$$

where scale-invariance corresponds to $n_g = 1$. Furthermore, one introduces also the running of the spectral index

$$\alpha_g \stackrel{\text{def}}{=} \frac{d \ln n_g}{d \ln k} \quad (8.30)$$

and the running of the running $d^2 n_g / d \ln k^2$, so that the power spectrum can be phenomenological parametrized as

$$\mathcal{P}_g(k) = A_g \left(\frac{k}{k_0} \right)^{n_g - 1 + \frac{1}{2} \frac{d \ln n_g}{d \ln k} \ln(k/k_0) + \frac{1}{6} \frac{d^2 n_g}{d \ln k^2} (\ln(k/k_0))^2 + \dots}, \quad (8.31)$$

where k_0 is some arbitrary pivot scale. If $g(t, \mathbf{x})$ is a Gaussian field, its power-spectrum contains all the statistical information. Non-Gaussianity is measured by higher-order correlation functions of g .

8.2 Scalar Fluctuations

Consider a real scalar field (e.g. the inflaton) minimally coupled to gravity. The action for this system is

$$S = - \int d^4 x \sqrt{-g} \left[\frac{1}{2} g^{\mu\nu} \partial_\mu \phi \partial_\nu \phi + V(\phi) - \frac{1}{16\pi G} R \right]. \quad (8.32)$$

To study quantum fluctuations it is convenient to split the metric and inflaton fields as

$$g_\mu \rightarrow g_{\mu\nu}^{FLRW} + \delta g_{\mu\nu}, \quad \phi \rightarrow \phi_0 + \delta\phi, \quad (8.33)$$

where $g_{\mu\nu}^{FLRW}$ is the FLRW (background) metric and ϕ_0 is the classical solution for the homogeneous and isotropic equation of motion for the inflaton field (7.28). To study only scalar perturbations, the most elegant gauge choice is

$$\delta\phi = 0, \quad g_{ij} = a^2 [(1 - 2\mathcal{R})\delta_{ij} + h_{ij}], \quad (8.34)$$

where all the scalar degrees are parametrized by \mathcal{R} and tensor ones by h_{ij} . Tensor modes will be neglected in this paragraph. The other scalar perturbations are related to \mathcal{R} by Einstein equations. This choice is particularly clever because \mathcal{R} does not evolve on super-Hubble-radius scales and so its statistical properties, such as the power spectrum, can be computed at the horizon crossing only. The action at second order in this gauge is

$$S_{(2)} = - \frac{1}{2} \int d^4 x a^3 \frac{\dot{\phi}_0^2}{H^2} [\dot{\mathcal{R}}^2 - a^{-2} (\partial_i \mathcal{R})^2]. \quad (8.35)$$

The complete proof requires the 3 + 1 (or ADM) decomposition formalism and can be found in appendix B of [49]. Notice that this action still depends on the inflaton potential. Indeed, ϕ_0 is the solution of the background equation (7.28) in which the potential appears. So, different choices for $V(\phi)$ will result in different background evolutions and hence different spectra for scalar perturbations.

By introducing the so-called Mukhanov-Sasaki variable:

$$\sigma = z\mathcal{R} \quad \text{where} \quad z \stackrel{\text{def}}{=} a \frac{\dot{\phi}_0}{H} \equiv a^2 \frac{\dot{\phi}_0}{\dot{a}} \equiv a^2 \frac{\phi_0'}{a'} \equiv a \frac{\phi_0'}{\mathcal{H}}, \quad (8.36)$$

and by using the conformal time η , the action $S_{(2)}$ becomes

$$S_{(2)} = -\frac{1}{2} \int d\eta d^3x \left[\sigma'^2 - (\partial_i \sigma)^2 + \frac{z''}{z} \sigma^2 \right], \quad (8.37)$$

where the apex ' indicates a partial derivative with respect to the conformal time. By varying $S_{(2)}$ one finds the equation of motion for the field σ :

$$\sigma'' - \nabla^2 \sigma - \frac{z''}{z} \sigma = 0, \quad (8.38)$$

which in terms of the Fourier transform of σ

$$\sigma(\eta, \mathbf{x}) = \int \frac{d^3k}{(2\pi)^{3/2}} \sigma_{\mathbf{k}}(\eta) e^{i\mathbf{k}\cdot\mathbf{x}}, \quad (8.39)$$

is simply

$$\sigma_{\mathbf{k}}'' + \left(\mathbf{k}^2 - \frac{z''}{z} \right) \sigma_{\mathbf{k}} = 0. \quad (8.40)$$

This is the Mukhanov-Sasaki equation. Formally, it is equivalent to an oscillator with a time-dependent effective mass $m_{\text{eff}}^2 = -z''/z$. Since $\sigma \in \mathbb{R}$, $\sigma_{\mathbf{k}}^* = \sigma_{-\mathbf{k}}$. Given that the equation of motion for $\sigma_{\mathbf{k}}''$ depends only on $|\mathbf{k}| \equiv k$, one can expand the Fourier modes $\sigma_{\mathbf{k}}$ as

$$\sigma_{\mathbf{k}}(\eta) = \frac{1}{\sqrt{2}} \left[a_{\mathbf{k}}^- v_{\mathbf{k}}^*(\eta) + a_{-\mathbf{k}}^+ v_{\mathbf{k}}(\eta) \right], \quad (8.41)$$

where $a_{\mp\mathbf{k}}^\pm$ are integration constants. $v_{\mathbf{k}}^*$, $v_{\mathbf{k}}$ are linearly independent solutions of equation

$$v_{\mathbf{k}}'' + \omega_{\mathbf{k}}^2 v_{\mathbf{k}} = 0 \quad \text{where} \quad \omega_{\mathbf{k}}^2 = \mathbf{k}^2 + m_{\text{eff}}^2, \quad m_{\text{eff}}^2 \stackrel{\text{def}}{=} -z''/z, \quad (8.42)$$

which is obtained by inserting the expansion (8.41) into equation (8.40). This solution is compact but exact at linear order. No slow-roll approximations were made so far. When $v_{\mathbf{k}}^*$, $v_{\mathbf{k}}$ are normalized such that

$$v_{\mathbf{k}}^* v_{\mathbf{k}}' - v_{\mathbf{k}} v_{\mathbf{k}}'^* = -i. \quad (8.43)$$

they are called mode functions. Note that $\sigma_{\mathbf{k}}^* = \sigma_{-\mathbf{k}}$ implies $(a_{\mathbf{k}}^-)^* = a_{\mathbf{k}}^+$. Therefore:

$$\sigma(\eta, \mathbf{x}) = \frac{1}{\sqrt{2}} \int \frac{d^3k}{(2\pi)^{3/2}} \left[a_{\mathbf{k}}^- v_{\mathbf{k}}^*(\eta) e^{i\mathbf{k}\cdot\mathbf{x}} + a_{-\mathbf{k}}^+ v_{\mathbf{k}}(\eta) e^{-i\mathbf{k}\cdot\mathbf{x}} \right]. \quad (8.44)$$

Finally, the canonical momentum is

$$\pi = \frac{\partial \mathcal{L}}{\partial \sigma'} = \sigma'. \quad (8.45)$$

Quantization of scalar perturbations

To quantize the perturbations in the canonical quantization scheme, one has to promote π and σ to operators on a Hilbert space obeying the equal time commutation relations

$$[\hat{\sigma}(\eta, \mathbf{x}), \hat{\sigma}(\eta, \mathbf{y})] = [\hat{\pi}(\eta, \mathbf{x}), \hat{\pi}(\eta, \mathbf{y})] = 0, \quad (8.46a)$$

$$[\hat{\sigma}(\eta, \mathbf{x}), \hat{\pi}(\eta, \mathbf{y})] = i\delta^3(\mathbf{x} - \mathbf{y}). \quad (8.46b)$$

In general, these commutation relations should be evaluated on a timelike surface. Fortunately, in the FLRW case the surface $\eta = \text{const}$ is timelike, exactly as it happens in the Minkowski case. Equivalently, to quantize the system $a_{\mp\mathbf{k}}^\pm$ should be promoted to operators. Starting from equations (8.46), one can prove that they obey the commutation relations

$$[\hat{a}_{\mathbf{k}}^-, \hat{a}_{\mathbf{k}'}^-] = [\hat{a}_{\mathbf{k}}^+, \hat{a}_{\mathbf{k}'}^+] = 0, \quad (8.47a)$$

$$[\hat{a}_{\mathbf{k}}^-, \hat{a}_{\mathbf{k}'}^+] = \delta^3(\mathbf{k} - \mathbf{k}'), \quad (8.47b)$$

and for this reason they are creation and annihilation operators. The states of the Hilbert space are constructed by defining a vacuum $|0\rangle$ such that

$$\hat{a}_{\mathbf{k}}^- |0\rangle = 0, \quad \forall \mathbf{k} \quad (8.48)$$

and by acting upon it with creation operators

$$|m_{\mathbf{k}_1} n_{\mathbf{k}_2} \dots\rangle = (m!n!)^{-1/2} \left((\hat{a}_{\mathbf{k}_1}^+)^m (\hat{a}_{\mathbf{k}_2}^+)^n \dots \right) |0\rangle \quad (8.49)$$

As it often happens in the quantization in curved spacetime, the vacuum is not uniquely defined. Indeed, one can perform the Bogolyubov transformation

$$u_{\mathbf{k}}(\eta) = \alpha_{\mathbf{k}} v_{\mathbf{k}}(\eta) + \beta_{\mathbf{k}} v_{\mathbf{k}}^*(\eta) \quad \text{whit} \quad |\alpha_{\mathbf{k}}|^2 - |\beta_{\mathbf{k}}|^2 = 1 \quad (8.50)$$

and expand the field operator σ as

$$\hat{\sigma}(\eta, \mathbf{x}) = \frac{1}{\sqrt{2}} \int \frac{d^3k}{(2\pi)^{3/2}} \left[\hat{b}_{\mathbf{k}}^- u_{\mathbf{k}}^*(\eta) e^{i\mathbf{k}\cdot\mathbf{x}} + \hat{b}_{-\mathbf{k}}^+ u_{\mathbf{k}}(\eta) e^{-i\mathbf{k}\cdot\mathbf{x}} \right], \quad (8.51)$$

where $\hat{b}_{\mathbf{k}}^{\pm}$ are creation/annihilation operators linked to $\hat{a}_{\mathbf{k}}^{\pm}$ by the transformations

$$\hat{a}_{\mathbf{k}}^{-} = \alpha_{\mathbf{k}}^* \hat{b}_{\mathbf{k}}^{-} + \beta_{\mathbf{k}} \hat{b}_{-\mathbf{k}}^{+}, \quad \hat{a}_{\mathbf{k}}^{+} = \alpha_{\mathbf{k}} \hat{b}_{\mathbf{k}}^{+} + \beta_{\mathbf{k}}^* \hat{b}_{-\mathbf{k}}^{-}; \quad (8.52)$$

or equivalently

$$\hat{b}_{\mathbf{k}}^{-} = \alpha_{\mathbf{k}} \hat{a}_{\mathbf{k}}^{-} - \beta_{\mathbf{k}} \hat{a}_{-\mathbf{k}}^{+}, \quad \hat{b}_{\mathbf{k}}^{+} = \alpha_{\mathbf{k}}^* \hat{a}_{\mathbf{k}}^{+} - \beta_{\mathbf{k}}^* \hat{a}_{-\mathbf{k}}^{-}. \quad (8.53)$$

Of course, mode functions $u_{\mathbf{k}}$, $u_{\mathbf{k}}^*$ are another set of linearly independent solutions of equation (8.42). Both $\hat{a}_{\mathbf{k}}^{\pm}$ and $\hat{b}_{\mathbf{k}}^{\pm}$ can be used to build an Hilbert space:

$$\hat{a}_{\mathbf{k}}^{-} |0\rangle_a = 0, \quad |m_{\mathbf{k}_1} n_{\mathbf{k}_2} \dots\rangle_a = \frac{1}{\sqrt{m!n!}} \left((\hat{a}_{\mathbf{k}_1}^{+})^m (\hat{a}_{\mathbf{k}_2}^{+})^n \dots \right) |0\rangle_a; \quad (8.54a)$$

$$\hat{b}_{\mathbf{k}}^{-} |0\rangle_b = 0, \quad |m_{\mathbf{k}_1} n_{\mathbf{k}_2} \dots\rangle_b = \frac{1}{\sqrt{m!n!}} \left((\hat{b}_{\mathbf{k}_1}^{+})^m (\hat{b}_{\mathbf{k}_2}^{+})^n \dots \right) |0\rangle_b. \quad (8.54b)$$

If the Bogolyubov transformation is not trivial, i.e. $\beta_{\mathbf{k}} \neq 0$, the b -vacuum contains 0 b -particles but it contains some a -particles (and viceversa). Indeed, it is possible to prove that

$${}_b\langle 0 | \hat{N}_{\mathbf{k}}^a | 0 \rangle_b \stackrel{\text{def}}{=} {}_b\langle 0 | \hat{a}_{\mathbf{k}}^{+} \hat{a}_{\mathbf{k}}^{-} | 0 \rangle_b = |\beta_{\mathbf{k}}|^2 {}_b\langle 0 | \hat{b}_{-\mathbf{k}}^{-} \hat{b}_{-\mathbf{k}}^{+} | 0 \rangle_b = |\beta_{\mathbf{k}}|^2 \delta^3(0), \quad (8.55)$$

where the divergent factor $\delta^3(0)$ is due the infinite spatial volume. However, the number density of a -particles in b -vacuum is $n_{\mathbf{k}}^a = |\beta_{\mathbf{k}}|^2$ so that the total density is

$$n^a = \int d^3k |\beta_{\mathbf{k}}|^2. \quad (8.56)$$

Vacuum and boundary conditions

The particle interpretation depends on the choice of the vacuum, or equivalently of the mode functions. One may ask which is the physical vacuum among all the possible ones. When quantizing in Minkowski spacetime, the vacuum is time independent and it is the eigenstate of the Hamiltonian with minimum energy. In analogy with this, in curved spacetime one can compute the Hamiltonian \hat{H} associated with the field σ and search for the lowest energy eigenstate. This will fix mode functions and the physical vacuum. In the case under study, the Hamiltonian is given by

$$\hat{H} = \frac{1}{2} \int d^3k \left[\hat{a}_{\mathbf{k}}^{-} \hat{a}_{-\mathbf{k}}^{-} F_{\mathbf{k}}^* + \hat{a}_{\mathbf{k}}^{+} \hat{a}_{-\mathbf{k}}^{+} F_{\mathbf{k}} + \left(2\hat{a}_{\mathbf{k}}^{+} \hat{a}_{\mathbf{k}}^{-} + \delta(0) \right) E_{\mathbf{k}} \right], \quad (8.57)$$

where

$$F_{\mathbf{k}}^* \stackrel{\text{def}}{=} v_{\mathbf{k}}'^2 + \omega_{\mathbf{k}}^2 v_{\mathbf{k}}^2, \quad E_{\mathbf{k}} \stackrel{\text{def}}{=} |v_{\mathbf{k}}'|^2 + \omega_{\mathbf{k}}^2 |v_{\mathbf{k}}|^2. \quad (8.58)$$

The physical vacuum $|0\rangle_v$ is the one for which the expected energy value, that is equal to

$${}_v\langle 0 | \hat{H} | 0 \rangle_v = \frac{\delta(0)}{2} \int d^3k E_{\mathbf{k}}, \quad (8.59)$$

is minimum. Clearly, ${}_v\langle 0 | \hat{H} | 0 \rangle_v$ is the lowest possible when $E_{\mathbf{k}}$ is minimum and this condition fixes the mode functions $v_{\mathbf{k}}$. By expanding

$$v_{\mathbf{k}}(\eta) = \pi_{\mathbf{k}}(\eta) e^{i\alpha_{\mathbf{k}}(\eta)}, \quad (8.60)$$

the equation (8.58) becomes

$$E_{\mathbf{k}} = (\pi'_{\mathbf{k}})^2 + \frac{1}{4\pi_{\mathbf{k}}^2} + \omega_{\mathbf{k}}^2 \pi_{\mathbf{k}}^2. \quad (8.61)$$

This energy has to be minimized

$$\frac{dE_{\mathbf{k}}}{dk} = 0 \implies \pi'_{\mathbf{k}} = 0, \quad (8.62a)$$

$$\frac{dE_{\mathbf{k}}}{d\eta} = 0 \implies \pi_{\mathbf{k}} = (2|\omega_{\mathbf{k}}|)^{-1/2}, \quad (8.62b)$$

where $k \stackrel{\text{def}}{=} |\mathbf{k}|$. Further, the normalization condition $\text{Im}\{v'v\} = 1/2$ implies that $\alpha'_{\mathbf{k}} \pi_{\mathbf{k}}^2 = 1/2$ and so

$$\alpha_{\mathbf{k}} = \int d\eta \frac{1}{2\pi_{\mathbf{k}}^2(\eta)} = |\omega_{\mathbf{k}}|\eta. \quad (8.63)$$

Finally, the mode functions that define the physical vacuum at some time η_0 are

$$v_{\mathbf{k}}(\eta_0) = \frac{1}{\sqrt{|\omega_{\mathbf{k}}(\eta_0)|}} e^{i|\omega_{\mathbf{k}}(\eta_0)|\eta_0}, \quad (8.64)$$

for which the Hamiltonian is diagonal since $E_{\mathbf{k}} = |\omega_{\mathbf{k}}|$ and $F_{\mathbf{k}} = 0$. There are still many vacua, one per each possible η_0 . One of the most common choices is $\eta_0 \rightarrow -\infty$. In this case, the mode functions become

$$v_{\mathbf{k}}^{(BD)} = \lim_{\eta_0 \rightarrow -\infty} v_{\mathbf{k}}(\eta_0) = \frac{e^{ik\eta}}{\sqrt{|2k|}}. \quad (8.65)$$

The vacuum defined by such mode functions is called Bunch-Davies vacuum. Equation (8.65) is nothing but the initial conditions for equation (8.42). Note that $|k\eta| = k/(aH)$ is directly proportional to the ratio between the background curvature L and the physical wavelength of the mode λ . Therefore, in the-so called ultraviolet limit $k \gg aH$ or $-k\eta \gg 1$, the background curvature is much larger than the typical size of the mode. Thus, in the early universe mode functions are not affected by the spacetime curvature and they behave as in flat spacetime, where mode functions are plane waves $e^{ik\eta}/\sqrt{2k}$. This is the physical meaning of the Bunch-Davies vacuum.

Slow-roll solution

Now, it is possible to solve equation (8.42) during slow-roll inflation, i.e. in a quasi-De Sitter spacetime, with boundary conditions (8.65). The z parameter (8.36) can be written in terms of the slow-roll Hubble parameters (7.11) as

$$z \equiv a^2 \frac{\dot{\phi}_0}{\dot{a}} = \frac{a\sqrt{2\epsilon_1}}{\sqrt{8\pi G}}. \quad (8.66)$$

In the second equality, equation (7.31) was used. After some computations, one finds:

$$z' = aHz \left(1 + \frac{\epsilon_2}{2}\right). \quad (8.67)$$

Then

$$z'' = z(aH)^2 \left[2 - \epsilon_1 + \frac{3}{2}\epsilon_2 + \epsilon_2^2 + \frac{\epsilon_1\epsilon_2}{2} + \frac{\epsilon_2\epsilon_3}{2}\right]. \quad (8.68)$$

In a quasi De Sitter space the scale factor is such that:

$$aH = -1/(\eta(1 - \epsilon)) \approx -(1 + \epsilon)/\eta. \quad (8.69)$$

Indeed

$$\frac{d}{d\eta} \left(\frac{1}{aH} \right) = -\frac{a'}{a^2H} - \frac{H'}{aH^2} \equiv -1 + \epsilon_1 \implies \frac{1}{aH} = (\epsilon_1 - 1)\eta. \quad (8.70)$$

Hence, by neglecting second-order slow-roll Hubble parameters, one gets

$$\frac{z''}{z} = \frac{1}{\eta^2} (1 + \epsilon)^2 \left(2 - \epsilon_1 + \frac{3}{2}\epsilon_2 + \epsilon_2^2 + \frac{\epsilon_1\epsilon_2}{2} + \frac{\epsilon_2\epsilon_3}{2}\right) \approx \frac{1}{\eta^2} \left(2 + 3\epsilon_1 + \frac{3}{2}\epsilon_2\right). \quad (8.71)$$

Equation (8.42) now reads

$$v_{\mathbf{k}}'' + \left[\mathbf{k}^2 - \frac{1}{\eta^2} \left(\nu^2 - \frac{1}{4} \right) \right] v_{\mathbf{k}} = 0, \quad \text{where} \quad \nu^2 \stackrel{\text{def}}{=} \frac{9}{4} + 3\epsilon_1 + \frac{3}{2}\epsilon_2. \quad (8.72)$$

Clearly, for small slow-roll parameters, ν is given by

$$\nu \approx \frac{3}{2} + \epsilon_1 + \frac{\epsilon_2}{2}. \quad (8.73)$$

The solution of equation (8.72), when ν is real, is a linear combination of Hankel functions of the first $H_\nu^{(1)}$ and second $H_\nu^{(2)}$ kind:

$$v_{\mathbf{k}}(\eta) = \sqrt{-\eta} \left[c_1(\eta) H_\nu^{(1)}(-k\eta) + c_2(\eta) H_\nu^{(2)}(-k\eta) \right]. \quad (8.74)$$

The integration constants $c_{1,2}$ are fixed by the Bunch-Davies boundary condition (8.65).

Given that

$$H_\nu^{(1)}(x \gg 1) \approx \sqrt{\frac{2}{\pi x}} e^{i(x - (\pi/2)\nu - \pi/4)}, \quad (8.75a)$$

$$H_\nu^{(2)}(x \gg 1) \approx \sqrt{\frac{2}{\pi x}} e^{-i(x - (\pi/2)\nu - \pi/4)}, \quad (8.75b)$$

the integration constants are forced to $c_1 = 0$ and $c_2 = \sqrt{\pi}/2$. Finally, the mode functions are

$$v_{\mathbf{k}}(\eta) = \frac{\sqrt{\pi}}{2} \sqrt{-\eta} H_\nu^{(2)}(-k\eta). \quad (8.76)$$

Note that this analytical solution was found in the slow-roll approximation. In the case of non-slow-roll inflation, the Mukhanov-Sasaki equation should be integrated numerically.

Power spectrum

As already mentioned, cosmological observables are affected by curvature perturbations \mathcal{R} once they re-enter the Hubble-radius. Since these perturbations are frozen on super-Hubble radius scales (8.25), their power spectrum is completely determined at the Hubble-radius-crossing, i.e. when $k = aH$.

At quantum level, \mathcal{R} is an operator that looks like $\hat{\mathcal{R}} = z^{-1}\hat{\sigma}$. The power spectrum of $\mathcal{R}_{\mathbf{k}}$ corresponds to the vacuum expectation value of the corresponding operator:

$$\begin{aligned} \langle 0 | \hat{\mathcal{R}}_{\mathbf{k}} \hat{\mathcal{R}}_{\mathbf{k}'} | 0 \rangle &= \frac{1}{z^2} \langle 0 | \hat{\sigma}_{\mathbf{k}} \hat{\sigma}_{\mathbf{k}'} | 0 \rangle = \\ &= \frac{1}{z^2} \langle 0 | [\hat{a}_{\mathbf{k}}^- v_{\mathbf{k}} + \hat{a}_{-\mathbf{k}}^+ v_{\mathbf{k}}^*] [\hat{a}_{\mathbf{k}'}^- v_{\mathbf{k}'} + \hat{a}_{-\mathbf{k}'}^+ v_{\mathbf{k}'}^*] | 0 \rangle = \\ &= \frac{1}{z^2} \langle 0 | \hat{a}_{\mathbf{k}}^- \hat{a}_{\mathbf{k}'}^+ v_{\mathbf{k}} v_{\mathbf{k}'}^* | 0 \rangle = \\ &= \frac{1}{z^2} \langle 0 | \hat{a}_{\mathbf{k}'}^+ \hat{a}_{\mathbf{k}}^- + \underbrace{[\hat{a}_{\mathbf{k}}^-, \hat{a}_{\mathbf{k}'}^+]}_{=\delta^3(\mathbf{k} + \mathbf{k}')} | 0 \rangle v_{\mathbf{k}} v_{\mathbf{k}'}^* = \\ &= \delta^3(\mathbf{k} + \mathbf{k}') \frac{|v_{\mathbf{k}}|^2}{z^2}. \end{aligned} \quad (8.77)$$

The comparison between this equation and equation (8.27) gives

$$\mathcal{P}_{\mathcal{R}} = \frac{k^3}{2\pi^2} \frac{|v_{\mathbf{k}}|^2}{z^2}. \quad (8.78)$$

The solution (8.76) on super-Hubble-radius scales is:

$$v_{\mathbf{k}} \stackrel{k \ll aH}{\approx} \sqrt{\frac{\pi}{k}} \frac{2^{\nu-1}}{\pi} \Gamma(\nu) \left(\frac{k}{aH} \right)^{\frac{1}{2}-\nu}. \quad (8.79)$$

Given the expression (8.66), one has that the power spectrum of curvature perturbations on

super-Hubble-radius scales is

$$\mathcal{P}_{\mathcal{R}} = 8\pi G \frac{H^2}{2\pi^3 \epsilon_1} 2^{2\nu-3} \Gamma^2(\nu) \left(\frac{k}{aH} \right)^{3-2\nu}. \quad (8.80)$$

For $\nu \approx 3/2 + \dots$, one has $\Gamma^2(\nu) \approx \pi/4$ and $2^{2\nu-3} \approx 1$ and so

$$\mathcal{P}_{\mathcal{R}}(k \ll aH) = 8\pi G \frac{H^2}{8\pi^2 \epsilon_1} \left(\frac{k}{aH} \right)^{3-2\nu}. \quad (8.81)$$

At the comoving Hubble radius crossing $k = aH$ is

$$\mathcal{P}_{\mathcal{R}} = \frac{8\pi G}{2\epsilon_1} \left(\frac{H^2}{2\pi} \right) \Big|_{k=aH}. \quad (8.82)$$

In slow-roll inflation H and ϵ_1 vary slowly and so one expects a scale invariant power spectrum, i.e. a power spectrum that does not depend on k . However, since H and ϵ_1 can be functions of time, there can be a little deviation from scale invariance. To measure this deviation one, the power spectrum is parameterized as in equation (8.31) and the index tilt is computed as

$$n_s - 1 = \frac{d \ln \mathcal{P}_{\mathcal{R}}}{d \ln k} = \frac{d \ln \mathcal{P}_{\mathcal{R}}}{d \mathcal{N}} \frac{d \mathcal{N}}{d \ln k}. \quad (8.83)$$

The derivative with respect to the e -folds number \mathcal{N} is

$$\frac{d \mathcal{P}_{\mathcal{R}}}{d \mathcal{N}} = \frac{d}{d \mathcal{N}} \frac{8\pi G}{2\epsilon_1} \left(\frac{H^2}{2\pi} \right) \Big|_{k=aH} = 2 \frac{d \ln H}{d \mathcal{N}} - \frac{d \ln \epsilon_1}{d \mathcal{N}}. \quad (8.84)$$

The first term is nothing but $-2\epsilon_1$ and the second one is $-\epsilon_2$. By using the fact that $\frac{d \ln \mathcal{P}_{\mathcal{R}}}{d \ln k}$ should be computed at $k = aH$, one can expand $\ln k = \mathcal{N} + \ln H$ so that

$$d \mathcal{N} / d \ln k = (d \ln k / d \mathcal{N})^{-1} = \left(1 + \frac{d \ln H}{d \mathcal{N}} \right)^{-1} \approx 1 + \epsilon_1. \quad (8.85)$$

The tilt is then equal to

$$n_s - 1 = -2\epsilon_1 - \epsilon_2 \equiv -6\epsilon_V + 2\eta_V. \quad (8.86)$$

Finally, by comparing equation (8.82) with the generic scale-invariant parametrization (8.31), one recognizes the amplitude $A_{\mathcal{R}}$ and the tilt n_s of the primordial power spectrum

$$A_{\mathcal{R}} = 8\pi G \frac{H^2}{8\pi^2 \epsilon_1} \equiv 8\pi G \frac{H^2}{8\pi^2 \epsilon_V} \quad (8.87a)$$

$$n_s - 1 = -2\epsilon_1 - \epsilon_2 \equiv -6\epsilon_V + 2\eta_V. \quad (8.87b)$$

At second order in the Hubble slow-roll parameters, the scalar tilt n_s and its running

$dn_s/d \ln k$ are given by:

$$n_s - 1 = -2\epsilon_1 - \epsilon_2 - 2\epsilon_1^2 - (2C + 3)\epsilon_1\epsilon_2 - C\epsilon_2\epsilon_3, \quad (8.88a)$$

$$dn_s/d \ln k = -2\epsilon_1\epsilon_2 - \epsilon_2\epsilon_3, \quad (8.88b)$$

where $C \stackrel{\text{def}}{=} \ln 2 + \gamma_E - 2 \approx -0.7296$ (γ_E is the Euler-Mascheroni constant). The potential slow-roll parameters ϵ_V and η_V can be written in terms of ϵ_i at second order as [50]:

$$\epsilon_V = \epsilon_1 \frac{(1 - \epsilon_1/3 + \epsilon_2/6)^2}{(1 - \epsilon_1/3)^2}, \quad (8.89a)$$

$$\eta_V = \frac{2\epsilon_1 - \epsilon_2/3 - 2\epsilon_1^2/3 + 5\epsilon_1\epsilon_2/6 - \epsilon_2^2/12 - \epsilon_2\epsilon_3/6}{1 - \epsilon_1/3}, \quad (8.89b)$$

$$\xi_V^2 \stackrel{\text{def}}{=} \frac{1}{(8\pi G)^2} \frac{V'V''''}{V^2} = \epsilon_1 \frac{1 - \epsilon_1/3 + \epsilon_2/6}{(1 - \epsilon_1/3)^2} \left[4\epsilon_1^2 - 3\epsilon_2\epsilon_3 + \frac{\epsilon_2\epsilon_3}{2} - \epsilon_1\epsilon_2^2 + 3\epsilon_1^2\epsilon_2 + \right. \\ \left. - \frac{4}{3}\epsilon_1^3 - \frac{7}{6}\epsilon_1\epsilon_2\epsilon_3 + \frac{\epsilon_2^2\epsilon_3 + \epsilon_2\epsilon_3^2 + \epsilon_2\epsilon_3\epsilon_4}{6} \right], \quad (8.89c)$$

where ξ_V is an higher order slow-roll potential parameter. The amplitude does not change at second order. The running appears only as a second-order effect. The running of the running is a third-order effect and it will be not mentioned anymore.

Measuring with high precision the primordial power spectrum of scalar perturbations means to know with precision $A_{\mathcal{R}}$ and the various slow-roll potential parameters and hence to select between different inflationary models.

8.3 Tensor Fluctuations

To study tensor perturbation consider the action (8.32) written in the convenient gauge (8.34). By considering only tensor perturbations h_{ij} , one can expand the action at second order as:

$$ds^2 = a^2(\eta) \left[d\eta^2 + (\delta_{ij} + h_{ij}) dx^i dx^j \right]. \quad (8.90)$$

The perturbed action (8.32) at first order in tensor modes is

$$S_{(2)} = \frac{1}{64\pi G} \int d\eta d^3x a^2 \left[(h'_{ij})^2 - (\nabla h_{ij})^2 \right]. \quad (8.91)$$

Since h_{ij} is traceless and transverse, it has only two physical polarizations, corresponding to gravitational waves. If it propagates along x^3 , it can be expanded as

$$h_{ij} = \begin{pmatrix} h_+ & h_x & 0 \\ h_x & -h_+ & 0 \\ 0 & 0 & 0 \end{pmatrix} \equiv \sum_{\lambda} e_{ij}^{(\lambda)} h^{(\lambda)}, \quad \text{where } \lambda = +, \times \quad (8.92)$$

and where $e_{ij}^{(\lambda)} e_{ij}^{(\lambda')} = \delta_{\lambda\lambda'}$. The action $S_{(2)}$ can now be written as

$$S_{(2)} = \frac{1}{64\pi G} \sum_{\lambda} \int d\eta d^3x a^2 \left[(h^{(\lambda)'})^2 - (\nabla h^{(\lambda)})^2 \right]. \quad (8.93)$$

By defining the canonical variable

$$\sigma^{(\lambda)} = \frac{a}{2\sqrt{8\pi G}} h^{(\lambda)}, \quad (8.94)$$

the perturbed action takes a simple form

$$S_{(2)} = \frac{1}{2} \sum_{\lambda} \int d\eta d^3x \left[(\sigma^{(\lambda)'})^2 + \frac{a''}{a} (\sigma^{(\lambda)})^2 - (\nabla \sigma^{(\lambda)})^2 \right]. \quad (8.95)$$

This action is identical to the one for scalar perturbation (8.37) except by the fact that the effective mass z''/z is replaced by a''/a . Thus, the results for tensor perturbations are the same for scalar ones, except for the effective mass, which can be generally expanded as

$$\frac{a''}{a} \stackrel{\text{def}}{=} \frac{1}{\eta^2} \left[\nu_T^2 - \frac{1}{4} \right]. \quad (8.96)$$

Thus, all the results for tensor perturbations are the same for the scalar ones, except for the index ν . The expression for such index in a slowly-rolling background follows from equation (8.69). Indeed, the integration of that equation gives $a = \eta^{-(1+\epsilon_1)}$ and so

$$\frac{a''}{a} = \frac{2 + 3\epsilon_1 + O(\epsilon_1^2)}{\eta^2}. \quad (8.97)$$

Thus, in the tensorial case, the index ν_T is

$$\nu_T^2 = \frac{9}{4} + 3\epsilon_1 \quad (8.98)$$

and in the slow-roll approximation is

$$\nu_T \approx \frac{3}{2} + \epsilon_1. \quad (8.99)$$

Then, one has to expand $\sigma^{(\lambda)}$ (or similarly $h^{(\lambda)}$) in Fourier space. The expansion will look similar to (8.44) and the equation for corresponding tensorial mode functions $v_{\mathbf{k}}^{(\lambda)}$ are immediately obtained by replacing the new effective mass into the equation of the scalar case (8.42):

$$v_{\mathbf{k}}^{(\lambda)''} + \left(k^2 - \frac{a''}{a} \right) v_{\mathbf{k}}^{(\lambda)} \equiv v_{\mathbf{k}}^{(\lambda)''} + \left(k^2 - \frac{1}{\eta^2} \left[\nu_T^2 - \frac{1}{4} \right] \right) v_{\mathbf{k}}^{(\lambda)} = 0, \quad \nu_T \approx \frac{3}{2} + \epsilon_1. \quad (8.100)$$

The solution on super-Hubble-radius scales is

$$v_k^{(\lambda)}(\eta) \equiv \frac{a}{2\sqrt{8\pi G}} h_k^{(\lambda)} \stackrel{k \ll aH}{\approx} \sqrt{\frac{\pi}{k}} \frac{2^{\nu_T-1}}{\pi} \Gamma(\nu_T) \left(\frac{k}{aH}\right)^{\frac{1}{2}-\nu_T}. \quad (8.101)$$

Finally, the power spectrum for tensorial perturbations on super-Hubble-radius scales is

$$\mathcal{P}_T(k \ll aH) = \frac{k^3}{2\pi^2} \sum_{\lambda} |h_k^{(\lambda)}|^2 = \frac{k^3}{\pi^2} \frac{16\pi G}{a^2} \sum_{\lambda} |v_k^{(\lambda)}|^2 = 8\pi G \frac{2H^2}{\pi^2} \left(\frac{k}{aH}\right)^{3-2\nu_T}. \quad (8.102)$$

At the Hubble-radius crossing, the power spectrum is equal to

$$\mathcal{P}_T = 8\pi G \frac{2H^2}{\pi^2} \Big|_{k=aH}. \quad (8.103)$$

Usually the tensor power spectrum is parametrized as

$$\mathcal{P}_T \equiv A_T \left(\frac{k}{k_*}\right)^{n_t + \frac{1}{2} \frac{dn_t}{d \ln k} \ln(k/k_*) + \dots} \quad (8.104)$$

where the scale invariance case now corresponds to $n_t = 0$. At first order in the slow-roll approximation, the tensor amplitude and tilt are

$$A_T = 8\pi G \frac{2H^2}{\pi^2} \quad (8.105a)$$

$$\begin{aligned} n_t &\stackrel{\text{def}}{=} \frac{d \ln \mathcal{P}_T}{d \ln k} = 2 \frac{d \ln H}{d \mathcal{N}} \frac{d \mathcal{N}}{d \ln k} = \\ &= -2\epsilon_1 \left(\frac{d \ln k}{d \mathcal{N}}\right)^{-1} = -2 \frac{\epsilon_1}{1 - \epsilon_1} = \\ &\approx -2\epsilon_1 + \mathcal{O}(\epsilon_1^2) \equiv -2\epsilon_V. \end{aligned} \quad (8.105b)$$

Notice that there is an additional factor 2 coming from the summation over λ . The main difference between $A_{\mathcal{R}}$ and A_T is that the latter does not depend on ϵ_1 . This is because in the tensorial case the canonical variable $\sigma^{(\lambda)}$ is proportional to a^{-1} and not to z^{-1} , that depends on ϵ_1 , as in the scalar case. This explains also the difference between n_s and n_t .

The running of the tensor tilt is a second-order parameter. At second order, the tensor tilt and its running are given by

$$n_t = -2\epsilon_1 - 2\epsilon_1^2 - 2(C+1)\epsilon_1\epsilon_2, \quad (8.106a)$$

$$dn_t/d \ln k = -2\epsilon_1\epsilon_2. \quad (8.106b)$$

Again ϵ_i are linked to $\epsilon_V, \eta_V, \xi_V^2$ by equations (8.89).

Consistency relation

The obtained amplitudes for the scalar and tensor perturbations allow us predicting a consistency relation which holds for the single-field models of inflation studied so far. It is possible to define a tensor-to-scalar ratio

$$r(k) \stackrel{\text{def}}{=} \frac{\mathcal{P}_T(k)}{\mathcal{P}_\mathcal{R}(k)}. \quad (8.107)$$

For single-field models of inflation this ratio is simply

$$r(k_*) \equiv r_* = 16\epsilon_V = -8n_t. \quad (8.108)$$

If r_* deviates from $-8n_t$, then the inflationary phase was not driven by a single scalar field. The consistency relation helps in understanding how r is connected to the evolution of the inflaton [51]:

$$\frac{\Delta\phi}{M_{pl}} \approx \frac{1}{\sqrt{8}} \int_0^{\mathcal{N}} d\mathcal{N} \sqrt{\dot{\phi}}. \quad (8.109)$$

This relation is called Lyth bound and it implies that inflaton variations of the order of the Planck mass cause $r \gtrsim 0.01$. This threshold is used to broadly and approximately classify large (small) field models of inflation, where $\phi > M_{pl}$ ($\phi < M_{pl}$). Notice however that large field models predicting $r \sim 10^{-4}$ exist.

8.4 Short catalog of inflationary models

In this section, all the inflationary models that can be described by the primordial power spectrum parameters $A_\mathcal{R}$, n_s , r (all defined at the pivot scale k_*), are examined. It is assumed a negligible running of the spectral index and its independence on the wave number k .

Measurement of $A_\mathcal{R}$, n_s , r are the only way for constraining slow-roll inflation. The current constraints on $A_\mathcal{R}$ and n_s are taken from [18] and they are

$$\ln(10^{10} A_\mathcal{R}) = 3.044 \pm 0.014, \quad n_s = 0.9649 \pm 0.0042. \quad (8.110)$$

The constraint on the tensor-to-scalar ratio comes from the *Planck* 2018 data combined with those of the BICEP-Keck Array (BK18) [52]:

$$r_{0.002\text{Mpc}^{-1}} < 0.035. \quad (8.111)$$

Such data allows constraining many different inflationary models, which are briefly reviewed in this section.

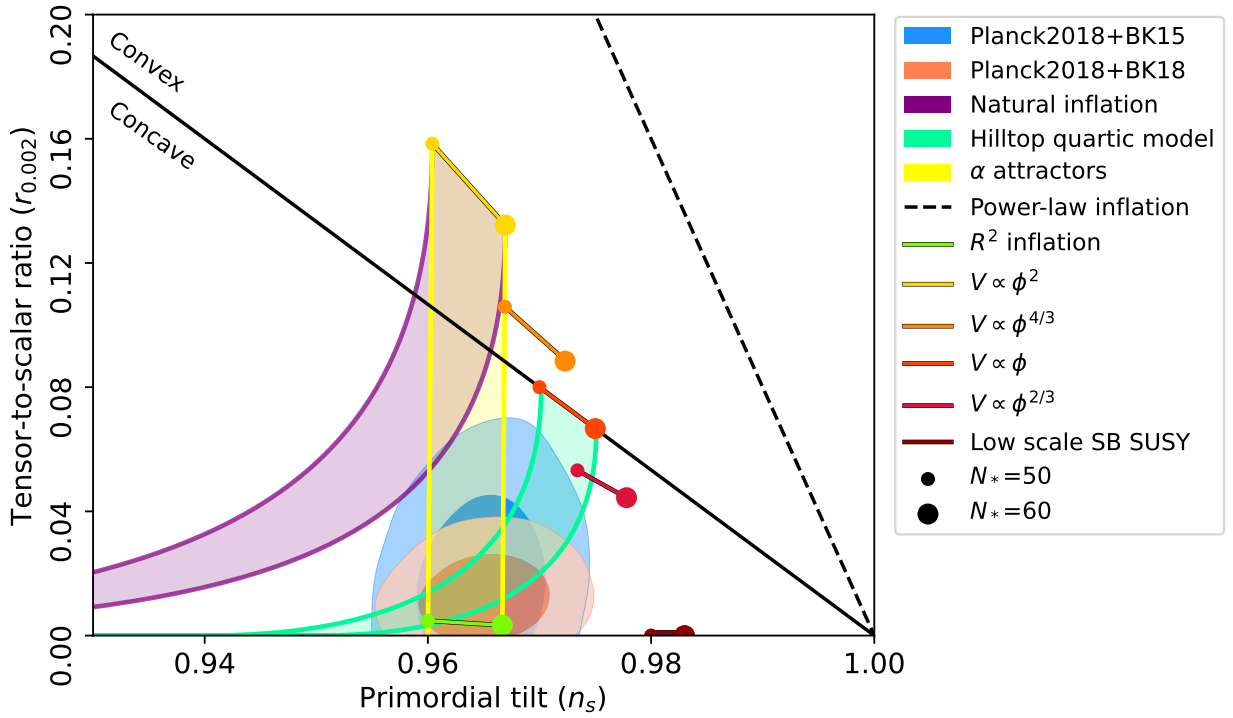


Fig. 8 – Marginalized joint 68% and 95% CL regions for n_s and $r_{0.002}$ from *Planck* in combination with *BICEP/Keck Array 2018* and *2015* data compared to the theoretical predictions of selected inflationary models with the uncertainty in the number of e -foldings $\mathcal{N} \equiv \mathcal{N}_*$ in the range (50, 60). Image taken from [52].

Power law potential and chaotic inflation

The simplest inflationary models are those characterized by a monomial potential of the form

$$V(\phi) = \lambda M_{pl}^4 \left(\frac{\phi}{M_{pl}} \right)^n. \quad (8.112)$$

This class of potentials contains large field models, also called chaotic models of inflation. This class of potential predicts

$$n_s = 1 - 2 \frac{n+2}{4\mathcal{N}_* + n} \quad r = \frac{16n}{4\mathcal{N}_* + n}, \quad (8.113)$$

where \mathcal{N}_* is the number of e -foldings.

In figure 8, taken from [52], the marginalized joint 68% and 95% confidence level regions for n_s and $r_{0.002}$ from *Planck* in combination with *BICEP/Keck Array* (BK) 2015 and 2018 data are presented and compared with the theoretical predictions of selected inflationary models. This class of potentials is now disfavored by the *Planck* and BK18 data.

Exponential potential and power law potential

When the inflaton potential is the exponential one

$$V(\phi) = \Lambda^4 \exp\left(-\lambda \frac{\phi}{M_{pl}}\right) \quad (8.114)$$

the scale factor can be found analytically and the result is $a(t) = t^{2/\lambda^2}$. This model is incomplete since it does not predict inflation to end. However, even if it exists a mechanism for stopping inflation, the prediction $r = -8(n_s - 1)$ lies outside the allowed regions (see figure 8).

Hilltop models

This class of potentials predicts that the inflaton rolls away from an unstable false vacuum as in the old inflation model:

$$V(\phi) \approx \Lambda^4 \left(1 - \frac{\phi^p}{\mu^p} + \dots\right). \quad (8.115)$$

The dots indicate higher-order terms that are negligible during inflation but ensure the potential to be positive. This class of models predicts at first order in the slow-roll approximation the following quantities: $r = 8p^2(M_{pl}/\mu)^2 x^{2p-2}/(1-x^p)^2$, $n_s = 1 - 2p(p-1)(M_{pl}/\mu)^2 x^{p-2}/(1-x^p) - 3r/8$, where $x = \phi_*/\mu$.

In figure 8, a Hilltop model with $p = 4$ is shown for different values of μ . This model is not ruled out by the data for super-Planckian values of μ : $\mu > 10^{1.05} M_{pl}$.

Natural inflation

The origin of natural inflation models lies in some symmetry-breaking theories, which attempted to naturally give rise to the extremely flat potentials required for inflationary cosmology. The effective one-dimensional potential in natural inflation has the form

$$V(\phi) = \Lambda^4 [1 + \cos(\phi/f)], \quad (8.116)$$

where f is the scale representing the slope of the potential. Depending on such scale f , the natural inflation models can be either large field models or small field ones. In particular, for $f > 1.5M_{pl}$ the model is a large field one while for $f < 1.5M_{pl}$ it is a small field one. Planck and BK18 data now disfavor this model [52].

Hybrid inflation and spontaneously broken SUSY

Hybrid inflation models are multi-field inflationary models where a second field χ , coupled to the inflaton ϕ , undergoes a symmetry breaking. The simplest example of this class of

models is

$$V(\phi, \chi) = \Lambda^4 \left(-\frac{\chi^2}{\mu^2} \right) + U(\phi) + \frac{g^2}{2} \phi^2 \chi^2. \quad (8.117)$$

Over most of their parameter space, these models behave as a single-field model. The field χ is close to the origin during the slow-roll regime for ϕ . Inflation ends either when the slow-roll parameters of the inflaton become

$$\epsilon_\phi = M_{pl}^2 \left(\frac{dU/d\phi}{\Lambda^4 + U(\phi)} \right)^2 \approx 1 \quad (8.118)$$

or when the waterfall transition of χ occurs. The simplest model with $U(\phi) = m^2 \phi^2/2$ is ruled out by the data. Models with $U(\phi) \approx \Lambda^4$ are disfavoured due to the high tensor-to-scalar ratio, while models with $U(\phi) \ll \Lambda^4$ predict $n_s > 1$ which is not observed.

An example of a hybrid inflation model in which $n_s < 1$ is the spontaneously broken SUSY model

$$U(\phi) = \alpha_h \Lambda^4 \ln \left(\frac{\phi}{\mu} \right), \quad (8.119)$$

that predicts $n_s = 1 - (1 + 3\alpha_h/2)\mathcal{N}_*^{-1}$ and $r \approx 8\alpha_h \mathcal{N}_*^{-1}$. If $\alpha_h \ll 1$ and $\mathcal{N}_* \approx 50$, $n_s \approx 0.98$ is excluded by the data.

R² inflation

Inflationary models can derive also from extended theories of gravity. One of the first inflation models proposed was based on higher-order terms in gravitational action, e.g.

$$S = \int d^4x \sqrt{-g} \frac{M_{pl}^2}{2} \left(R + \frac{R^2}{2M^2} \right), \quad (8.120)$$

originally included in the action to take into account semi-classical quantum effects. This model corresponds to the potential

$$V(\phi) = \Lambda^4 \left(1 - e^{-\sqrt{2/3}\phi/M_{pl}} \right)^2 \quad (8.121)$$

This is the so called Starobinsky potential and it predicts $n_s \approx 1 - 2\mathcal{N}_*^{-1}$ and $r \approx 12/\mathcal{N}_*^2$. Since r scales with \mathcal{N}_*^2 , it predicts a tiny amount of tensor modes, i.e. gravitational waves. For $\mathcal{N}_* = 55$, the tilt predicted by this model is 0.963 which is perfectly consistent with the *Planck* data.

α -attractors

There are two categories of α -attractors models of inflation. The first one comes from supergravity theories in which the inflaton it is associated with vector field super-partner

(instead of a chiral multiplet). The resulting potential is

$$V(\phi) = \Lambda^4 \left(1 - e^{-\sqrt{2}\phi/(M_{pl}\sqrt{3\alpha})}\right)^2. \quad (8.122)$$

The predictions for the tilt and the tensor-to-scalar ratio are $n_s = 1 - 8(1 + e^{\sqrt{2}\phi/(M_{pl}\sqrt{3\alpha})})/[3\alpha(1 - e^{\sqrt{2}\phi/(M_{pl}\sqrt{3\alpha})})^2]$ and $r = 64/[3\alpha(1 - e^{\sqrt{2}\phi/(M_{pl}\sqrt{3\alpha})})^2]$.

The second class is called super-conformal α attractors. It can be understood as originating from a different generating function with respect to the first class. To this class it corresponds the potential

$$V(\phi) = \Lambda^4 \tanh^{2m} \left(\frac{\phi}{M_{pl}\sqrt{6\alpha}} \right) \quad (8.123)$$

and for $\alpha = m = 1$ it reduces to a model with spontaneous symmetry breaking of conformal symmetry. The slow-roll prediction of this class of models are

$$n_s = 1 - \frac{8m\mathcal{N} + 6\alpha m + 2g(\alpha, m)}{4m\mathcal{N}^2 + 2\mathcal{N}g(\alpha, m) + 3\alpha m}, \quad \text{where } g(\alpha, m) \stackrel{\text{def}}{=} \sqrt{3\alpha(4m^2 + 3\alpha)} \quad (8.124a)$$

$$r = \frac{48\alpha m}{4m\mathcal{N}^2 + 2\mathcal{N}g(\alpha, m) + 3\alpha m} \quad (8.124b)$$

Non-minimally coupled inflation

Other models of inflation arise when one considers the inflaton field non-minimally coupled to gravity. The action for this system is

$$S = \int d^4x \sqrt{-g} \left[\frac{M_{pl}^2 + \xi\phi^2}{2} - \frac{1}{2}g^{\mu\nu}\partial_\mu\phi\partial_\nu\phi - \frac{\lambda}{4}(\phi^2 - \phi_0^2)^2 \right]. \quad (8.125)$$

In the case of a massless inflaton, $\phi_0 = 0$, the model agrees with data for $\xi > 0$. The amplitude of scalar perturbations is proportional to λ/ξ^2 for $\xi \gg 1$. Therefore, the UV sensitivity problem can be alleviated in this class of models. The small field case $\phi \ll M_{pl}$ is allowed and, in particular, ϕ can be the Standard Model Higgs boson. The Higgs case with $\xi \gg 1$ has the same predictions of the R^2 -inflation in terms of \mathcal{N}_* and thus it is consistent with the current data. When $\xi < 0$, only the large field case is not excluded by the observations.

IV

CMB ANISOTROPIES, SILK DAMPING SPECTRAL DISTORTIONS AND SCALAR-INDUCED GRAVITATIONAL WAVES

The main purpose of this thesis is to study the consequences of small-scale large peaks in the primordial power spectrum of curvature perturbations (PPS). We use different cosmological observables to constrain such peaks. In particular, we consider anisotropies and spectral distortions of the cosmic microwave background and scalar-induced primordial gravitational waves. In this chapter, a short review of these observables is given and the equations that determine their dependence on the form of the PPS are derived.

9 Anisotropies of the cosmic microwave background

Perturbations of the metric field generate fluctuations in CMB temperature, which reflect how photons propagate in a perturbed Universe. Metric perturbations are generated during inflation and so CMB anisotropies can be used to test different inflationary scenarios. In this section, we describe the dependence of CMB anisotropies on the PPS.

9.1 Photons Boltzmann equation in a perturbed Universe

We study CMB anisotropies by following the evolution of the photon phase space distribution in a perturbed Universe.

For simplicity, we consider the conformal Newtonian gauge (8.9). The derivation of the perturbed Boltzmann equation in the synchronous gauge can be found in [48]. In the Newtonian gauge, the Liouville operator is [27]:

$$\hat{\mathbf{L}}f = \frac{\partial f}{\partial t} + \frac{\partial f}{\partial x^i} \frac{\hat{p}^i}{a} - p \left(H - \frac{\partial \Phi}{\partial t} + \frac{\partial \Psi}{\partial x^i} \frac{\hat{p}^i}{a} \right) \frac{\partial f}{\partial p}, \quad (9.1)$$

where \hat{p}^i and p are the direction and the amplitude of p^i respectively. We split the phase space distribution function as

$$f(t, p, \mathbf{x}, \hat{\mathbf{p}}) = \bar{f}(t, p) + \Upsilon(t, p, \mathbf{x}, \hat{\mathbf{p}}). \quad (9.2)$$

For photons, the expansion looks like

$$f(t, x^i, p, \hat{p}^i) = \left[\exp\left(\frac{p}{\bar{T}(1 + \Theta(t, x^i, p, \hat{p}^i))} - 1\right) \right]^{-1}, \quad (9.3)$$

where $\Theta = (T - \bar{T})/\bar{T}$ is the local temperature perturbation. Here \bar{T} indicates the temperature in absence of perturbations. By expanding f for small Θ we can recognize

$$\Upsilon(t, p, \mathbf{x}, \hat{\mathbf{p}}) = -\Theta p \frac{\partial \bar{f}}{\partial p}. \quad (9.4)$$

The 0-th order Liouville operator is

$$\hat{\mathbf{L}}\bar{f} = \frac{\partial \bar{f}}{\partial t} - Hp \frac{\partial \bar{f}}{\partial p}, \quad (9.5)$$

while the 1-st order one is

$$\hat{\mathbf{L}}\Upsilon = -p \frac{\partial \bar{f}}{\partial p} \left[\frac{\partial \Theta}{\partial t} + \frac{\hat{p}^i}{a} \frac{\partial \Theta}{\partial x^i} - \frac{\partial \Psi}{\partial t} + \frac{\hat{p}^i}{a} \frac{\partial \Phi}{\partial x^i} \right]. \quad (9.6)$$

The first two terms are those responsible for the free streaming, while the last two account for the effects of gravity.

The interaction that is mainly able to modify CMB anisotropies is Compton scattering, which is a first-order effect. Indeed, at the 0-th order photons are in thermal equilibrium and their collision operator vanishes. At first order, one has instead [27]:

$$\mathcal{C}[\Upsilon]|_{\text{CS}} = -p^2 \frac{\partial \bar{f}}{\partial p} n_e \sigma_T [\Theta_0 - \Theta(\hat{\mathbf{p}}) + \hat{\mathbf{p}} \cdot \mathbf{v}_b], \quad (9.7)$$

where \mathbf{v}_b is the electron bulk velocity and Θ_0 is the anisotropy monopole, defined as

$$\Theta_0(t, \mathbf{x}) = \frac{1}{4\pi} \int d\Omega \Theta(\hat{\mathbf{p}}, t, \mathbf{x}). \quad (9.8)$$

If $\mathbf{v}_b = 0$ and if the Compton scattering is efficient, it drives Θ to the monopole solution, which means that the temperature in the sky is uniform.

By equating (9.6) and (9.8), we find the equation that determines CMB anisotropies:

$$\frac{\partial \Theta}{\partial t} + \frac{\hat{p}^i}{a} \frac{\partial \Theta}{\partial x^i} - \frac{\partial \Phi}{\partial t} + \frac{\hat{p}^i}{a} \frac{\partial \Psi}{\partial x^i} = n_e \sigma_T [\Theta_0 - \Theta(\hat{\mathbf{p}}) + \hat{\mathbf{p}} \cdot \mathbf{v}_b]. \quad (9.9)$$

This equation simplifies in Fourier space:

$$\Theta(\mathbf{x}) = \int \frac{d^3 k}{(2\pi)^3} e^{i\mathbf{k} \cdot \mathbf{x}} \Theta(\mathbf{k}). \quad (9.10)$$

A useful quantity is the cosine of the angle between the Fourier wavevector \mathbf{k} and the

momentum direction $\hat{\mathbf{p}}$:

$$\mu = \frac{\hat{\mathbf{p}} \cdot \mathbf{k}}{k}. \quad (9.11)$$

In Fourier space, the baryon bulk velocity \mathbf{v}_b is simply $\mathbf{v}_b = iv_b \mathbf{k}/k$ if it is curl-less. The first-order Boltzmann equation in Fourier space is then

$$\frac{\partial \Theta}{\partial t} + \frac{ik\mu}{a} \Theta - \frac{\partial \Phi}{\partial t} + \frac{ik\mu}{a} \Psi = n_e \sigma_T \left[\Theta_0 - \Theta + i\mu v_b - \frac{3\mu^2 - 1}{4} \Pi \right], \quad (9.12)$$

where Π is the quadrupole of Θ

$$\Pi = -\frac{1}{2} \int_{-1}^1 d\mu \frac{3\mu^2 - 1}{2} \Theta \equiv \Theta_2. \quad (9.13)$$

Multipoles expansion

To get a simpler set of equations, we expand the μ -dependence of Θ in Legendre polynomials $P_\ell(\mu)$

$$\Theta(t, k, \mu) = \sum_{\ell=0}^{\infty} \frac{2\ell + 1}{i^\ell} \Theta_\ell(t, k) P_\ell(\mu), \quad (9.14)$$

where Θ_ℓ are the multipoles, or photon transfer functions, defined as

$$\Theta_\ell(t, k) = \frac{i^\ell}{2} \int_{-1}^1 d\mu \Theta(t, k, \mu) P_\ell(\mu). \quad (9.15)$$

Until now, we encountered only the monopole Θ_0 and the quadrupole $\Theta_2 \equiv \Pi$. The monopole is linked to the density perturbation of the photon field $\delta_\gamma = \delta\rho_\gamma/\bar{\rho}_\gamma$ by the relation: $\delta_\gamma = 4\Theta_0$. Θ_1 is the dipole momentum and it is linked to photon velocity by $v_\gamma = -3\Theta_1$. Higher-order momenta describe other kinds of anisotropies.

The Legendre polynomials can be computed with $P_0 = 1$, $P_1 = \mu$, $P_2 = (3\mu^2 - 1)/2$ and the use of the Bonnet's recursive formula

$$\mu P_\ell = \frac{\ell + 1}{2\ell + 1} P_{\ell+1} + \frac{\ell}{2\ell + 1} P_{\ell-1}, \quad \ell > 0. \quad (9.16)$$

With this formula, equation (9.12) splits into

$$\Theta'_0 = -\frac{k}{\mathcal{H}} \Theta_1 + \Phi' \quad (9.17a)$$

$$\Theta'_1 = \frac{k}{3\mathcal{H}} \Theta_0 - \frac{2k}{3\mathcal{H}} \Theta_2 + \frac{k}{3\mathcal{H}} \Psi + \tau' [\Theta_1 + v_b/3] \quad (9.17b)$$

$$\Theta'_\ell = \frac{\ell k}{(2\ell + 1)\mathcal{H}} \Theta_{\ell-1} - \frac{\ell + 1}{2\ell + 1} \frac{k}{\mathcal{H}} \Theta_{\ell+1} + \tau' \left[\Theta_\ell - \frac{1}{10} \Pi \delta_{\ell,2} \right], \quad \ell \geq 2 \quad (9.17c)$$

where \mathcal{H} is given in equation (2.40) and where the prime now indicates a derivative with respect to the variable $x = \log a$. Notice that the $\delta_{\ell,2}$ is a Kronecker delta. The first (second) equation is the perturbed version of the continuity (Euler) equation.

If polarization is included, one has to add two more equations to the previous set of equations:

$$\Theta'_{P0} = -\frac{ck}{\mathcal{H}}\Theta_{P1} + \tau' \left[\Theta_{P0} - \frac{1}{2}\Pi \right], \quad (9.18a)$$

$$\Theta'_{P\ell} = \frac{\ell ck}{(2\ell+1)\mathcal{H}}\Theta_{P\ell-1} - \frac{(\ell+1)ck}{(2\ell+1)\mathcal{H}}\Theta_{P\ell+1} + \tau' \left[\Theta_{\ell}^P - \frac{1}{10}\Pi\delta_{\ell,2} \right], \quad 1 \leq \ell, \quad (9.18b)$$

and Π has to be modified in $\Pi = \Theta_2 + \Theta_{P0} + \Theta_{P2}$.

These equations are coupled to those for the evolution of baryons, neutrinos and cold dark matter. To close the system it is necessary to keep track of the evolution of Φ and Ψ by solving the perturbed Einstein equations $\delta G_{\mu\nu} = 8\pi G T_{\mu\nu}$. The system can be numerically integrated once initial conditions for perturbations are given. In case of adiabatic initial conditions, they are completely determined by the values of Φ and Ψ , or analogously \mathcal{R} , at Hubble-radius re-entering. Since \mathcal{R} is constant outside the horizon, its PPS at Hubble-radius re-entering coincides to those at Hubble-radius crossing set up in the very early Universe by inflation. Therefore, CMB anisotropies can be used to test different inflationary models. We summarize the equations and the adiabatic initial conditions for all species in appendix A.

9.2 CMB angular power spectra

Experiments measure CMB temperature as a function of the direction $T(\hat{n})$, i.e. $\delta T/T = \Theta(\mathbf{x}, \hat{\mathbf{p}}, t)$, where \mathbf{x} is the observer position, $\hat{\mathbf{p}}$ the direction of observation and $t = t_0$ the time of the observation. Θ can be expanded in spherical harmonics

$$\Theta(\mathbf{x}, \hat{\mathbf{p}}, t) = \sum_{\ell=1}^{\infty} \sum_{m=-\ell}^{\ell} a_{\ell m}(t, \mathbf{x}) Y_{\ell m}(\hat{\mathbf{p}}), \quad (9.19)$$

where the coefficients $a_{\ell m}$ are given by

$$a_{\ell m}(t, \mathbf{x}) = \int d\Omega_{\hat{\mathbf{p}}} Y_{\ell m}^*(\hat{\mathbf{p}}) \Theta(\mathbf{x}, \hat{\mathbf{p}}, t) \equiv \int \frac{d^3k}{(2\pi)^3} e^{i\vec{k}\cdot\vec{x}} \int d\Omega_{\hat{\mathbf{p}}} Y_{\ell m}^*(\hat{\mathbf{p}}) \Theta(\mathbf{k}, \hat{\mathbf{p}}, t), \quad (9.20)$$

and normalized as

$$\langle a_{\ell m} a_{\ell' m'}^* \rangle = \delta_{\ell\ell'} \delta_{mm'} C_{\ell}. \quad (9.21)$$

$C_{\ell} \stackrel{\text{def}}{=} \langle |a_{\ell m}|^2 \rangle$ is the angular power spectrum of CMB anisotropies. The angular brackets denote an ensemble average, where the ensemble is made by different realizations of our Universe. Since we measure a particular realization of the Universe and since for each ℓ there are $2\ell + 1$ possible values of m , we can estimate the angular power spectrum as

$$\hat{C}_{\ell} = \frac{1}{2\ell+1} \sum_{m=-\ell}^{\ell} |a_{\ell m}|^2. \quad (9.22)$$

The error done by approximating C_ℓ with \hat{C}_ℓ is the so-called cosmic variance

$$\Delta C_\ell = \sqrt{\frac{2}{2\ell + 1}} C_\ell. \quad (9.23)$$

Obviously, $\Delta C_\ell/C_\ell$ is large at small ℓ . By using the multipoles expansion of Θ , we write the expression for $a_{\ell m}$ as

$$a_{\ell m}(\mathbf{x}, t) = \sum_{\ell} (2\ell + 1) (-i)^\ell \int \frac{d^3k}{(2\pi)^3} e^{i\vec{k}\cdot\vec{x}} \int d\Omega_{\hat{\mathbf{p}}} Y_{\ell m}^*(\hat{\mathbf{p}}) P_\ell(\mu) \Theta_\ell(\mathbf{k}, t). \quad (9.24)$$

Photon perturbations $\Theta_\ell(\mathbf{k}, t)$ depend on the initial conditions set during inflation by the quantum fluctuations of the inflaton field. Such dependence is usually decomposed as

$$\Theta_\ell(\mathbf{k}, t) = \mathcal{R}(\mathbf{k}) \Theta_\ell(k, t_0), \quad (9.25)$$

where $\Theta_\ell(k, t_0)$ are solutions of equation (9.17) with $\mathcal{R} = 1$ evaluated today $t = t_0$. They are called photon transfer functions and they determine the evolution of photon multipoles from the Hubble-radius re-entering of inflationary quantum fluctuations until today. Therefore, the angular power spectrum of CMB anisotropies is linked to the PPS by the equation

$$C_\ell = 4\pi \int \frac{dk}{k} |\Theta_\ell(k, t)|^2 \mathcal{P}_{\mathcal{R}}(k). \quad (9.26)$$

Line of sight integration

To compute the CMB angular power spectrum it is necessary to know the transfer functions Θ_ℓ . Their expressions are found by solving the full set of equations present in appendix A given the initial conditions $\mathcal{R} = 1$. Today, the angular power spectrum is measured until $\ell \sim 2500$. Numerically, it is demanding to solve a system with ~ 2500 coupled partial differential equations. The line-of-sight integration, introduced in [53], allows to compute photon transfer functions as

$$\Theta_\ell(k, x = 0) = \int_{-\infty}^0 dx \tilde{S}(k, x) j_\ell[k(\eta_0 - \eta)], \quad (9.27)$$

where $\tilde{S}(k, x)$ is a source function defined as

$$\tilde{S}(k, x) = \tilde{g} \left[\Theta_0 + \Psi + \frac{1}{4}\Pi \right] + e^{-\tau} [\Psi' + \Phi'] - \frac{1}{ck} \frac{d}{dx} (\mathcal{H} \tilde{g} v_b) + \frac{3}{4c^2 k^2} \frac{d}{dx} \left[\mathcal{H} \frac{d}{dx} (\mathcal{H} \tilde{g} \Pi) \right]. \quad (9.28)$$

and where $x = \log a$. The function \tilde{g} is nothing but the visibility function defined in equation (3.40) times \mathcal{H} : $\tilde{g} = -(\mathrm{d}\tau/\mathrm{d}x)e^{-\tau} = \mathcal{H}g$. j_ℓ are spherical Bessel functions and project temperature anisotropies from recombination to the present day. Line-of-sight integration requires to know only Π , Φ , Ψ , Θ_0 and v_b and the respective derivatives. To accurately compute the highest necessary multipole (Θ_2) it is sufficient to truncate Boltzmann equations.

This reduces significantly the dimension of the set of equations and all Einstein-Boltzmann solvers, like CLASS, use such integration technique.

Polarization

The number of photon polarizations is $g_\gamma = 2$ and so we can split the phase space distribution as $f_\gamma = f_\gamma^{(1)} + f_\gamma^{(2)}$. Each contribution gets a perturbation $\Theta^{(i)}$. The equation for polarization presented in (9.18) is roughly valid for $\Theta_P = 0.5(\Theta^{(1)} - \Theta^{(2)})$.

To discuss in general CMB polarization, consider a monochromatic electromagnetic plane wave propagating in the z -direction. The electric field is

$$\mathbf{E}(z, t) = \text{Re}\left\{(E_x \hat{\mathbf{x}} + E_y \hat{\mathbf{y}})e^{ik(z-t)}\right\}. \quad (9.29)$$

The complex amplitudes of the electric field are $E_x = |E_x|e^{i\phi_x}$ and $E_y = |E_y|e^{i\phi_y}$. The electric field at $z = 0$ is an ellipse in the xy plane described by the equation

$$\mathbf{E}(t) = |E_x| \cos(\omega t) \hat{\mathbf{x}} + |E_y| \cos(\omega t - \phi) \hat{\mathbf{y}}, \quad \text{with } \phi = \phi_y - \phi_x. \quad (9.30)$$

For $\phi = 0, \pi$ the radiation is said to be linearly polarized because the x and y field components oscillate in phase (or anti-phase) and the ellipse collapses into a line. Similarly, for $\phi = \pm\pi/2$ the wave is circularly polarized since the ellipse reduces to a circle. The electromagnetic radiation polarization can be described with the Stokes parameters

$$\begin{aligned} I &\stackrel{\text{def}}{=} |E_x|^2 + |E_y|^2 & Q &\stackrel{\text{def}}{=} |E_x|^2 - |E_y|^2 \\ U &\stackrel{\text{def}}{=} 2|E_x||E_y| \cos \phi & V &\stackrel{\text{def}}{=} 2|E_x||E_y| \sin \phi. \end{aligned} \quad (9.31)$$

I measures the intensity of the radiation, while Q, U, V describe its polarization state. In particular, for a linear polarized wave $V = 0$. In the Early Universe and in the standard cosmological model, only linear polarization is expected to be generated and so we set $V = 0$ from now on. Under a rotation by an angle φ in the xy plane, Stokes parameters transform as

$$I' = |E'_x|^2 + |E'_y|^2 \equiv I, \quad Q' \pm iU' = e^{\mp 2i\varphi}(Q \pm iU). \quad (9.32)$$

We recognize that I is a scalar, while $Q \pm iU$ are spin-2 fields. We can replace Q and U with two scalar fields describing the so-called E and B polarization modes. These modes have coefficients

$$a_{\ell m}^E = -\frac{1}{2} \left(a_{\ell m}^{(2)} + a_{\ell m}^{(-2)} \right), \quad a_{\ell m}^B = -\frac{1}{2i} \left(a_{\ell m}^{(2)} - a_{\ell m}^{(-2)} \right), \quad (9.33)$$

where $a_{\ell m}^{(\pm 2)}$ are defined in the $Q \pm iU$ spherical harmonics expansion

$$(Q \pm iU)(\hat{\mathbf{n}}) = \sum_{\ell=0}^{\infty} \sum_{m=-\ell}^{\ell} a_{\ell m}^{(\pm 2)} Y_{\ell m}^{(\pm 2)}(\hat{\mathbf{n}}). \quad (9.34)$$

The final expressions for E and B modes are

$$E(\hat{\mathbf{n}}) = \sum_{\ell=0}^{\infty} \sum_{m=-\ell}^{\ell} a_{\ell m}^E Y_{\ell m}^{(\pm 2)}(\hat{\mathbf{n}}) \quad (9.35a)$$

$$B(\hat{\mathbf{n}}) = \sum_{\ell=0}^{\infty} \sum_{m=-\ell}^{\ell} a_{\ell m}^B Y_{\ell m}^{(\pm 2)}(\hat{\mathbf{n}}) \quad (9.35b)$$

and their power spectra are defined as usual

$$\langle a_{\ell m}^T a_{\ell' m'}^{E*} \rangle = C_{\ell}^{TE} \delta_{\ell\ell'} \delta_{mm'} \quad (9.36a)$$

$$\langle a_{\ell m}^E a_{\ell' m'}^{E*} \rangle = C_{\ell}^{EE} \delta_{\ell\ell'} \delta_{mm'} \quad (9.36b)$$

$$\langle a_{\ell m}^B a_{\ell' m'}^{EB*} \rangle = C_{\ell}^{BB} \delta_{\ell\ell'} \delta_{mm'} \quad (9.36c)$$

where we introduced the superscript T to distinguish the temperature angular power spectra discussed previously from the polarization ones.

CMB is expected to become polarized via Thomson scattering, whose angular dependence is

$$\frac{d\sigma}{d\Omega} = \frac{3}{8\pi} \sigma_T |\hat{\mathbf{e}}' \cdot \hat{\mathbf{e}}|^2, \quad (9.37)$$

where $\hat{\mathbf{e}}'$ and $\hat{\mathbf{e}}$ are the incident and scattered directions. The Stokes parameters Q , U in this case are

$$Q(\hat{\mathbf{z}}) \propto \int d\Omega' f(\hat{\mathbf{n}}') \sum_{j=1}^2 \left(|\hat{\mathbf{x}} \cdot \hat{\mathbf{e}}'_j|^2 - |\hat{\mathbf{y}} \cdot \hat{\mathbf{e}}'_j|^2 \right), \quad (9.38a)$$

$$U(\hat{\mathbf{z}}) \propto - \int d\Omega' f(\hat{\mathbf{n}}') \sin^2 \theta' \sin 2\phi'. \quad (9.38b)$$

where f is the photons phase space distribution and it includes temperature fluctuations Θ . We write the previous equations in Fourier space by using E and B according to [24]:

$$E(\hat{\mathbf{z}}, \mathbf{k}) \propto \frac{4\pi}{5} \sin^2 \Theta_k \Theta_2(k), \quad (9.39a)$$

$$B(\hat{\mathbf{z}}, \mathbf{k}) \propto 0. \quad (9.39b)$$

We deduce that scalar perturbations induce only E -modes. On the other hand, B -modes are sourced by primordial tensorial fluctuations. Future measurements of B -modes will prove the existence of primordial gravitational waves generated during inflation. The EE -power spectrum generated by scalar perturbations during inflation is

$$C_{\ell}^{EE} = 4\pi \int \frac{dk}{k} |\Theta_{\ell}^E(k, t)|^2 \mathcal{P}_{\mathcal{R}}(k), \quad (9.40)$$

where the transfer function Θ_ℓ^E are given by [24]:

$$\Theta_\ell^E(k) \propto \frac{k}{\Gamma} G_*(k) \frac{\ell^2}{(k\tau_0)^2} j_\ell(k\tau_0), \quad (9.41)$$

where τ_0 is the conformal time today, Γ is the mean free path of photons and $G_* = v_b/\mathcal{R}(\mathbf{k})$ the baryon transfer function. Similarly, it is possible to compute the C_ℓ^{TE} spectrum. We show in figure 9 the CMB angular power spectra measured by the Planck collaboration.

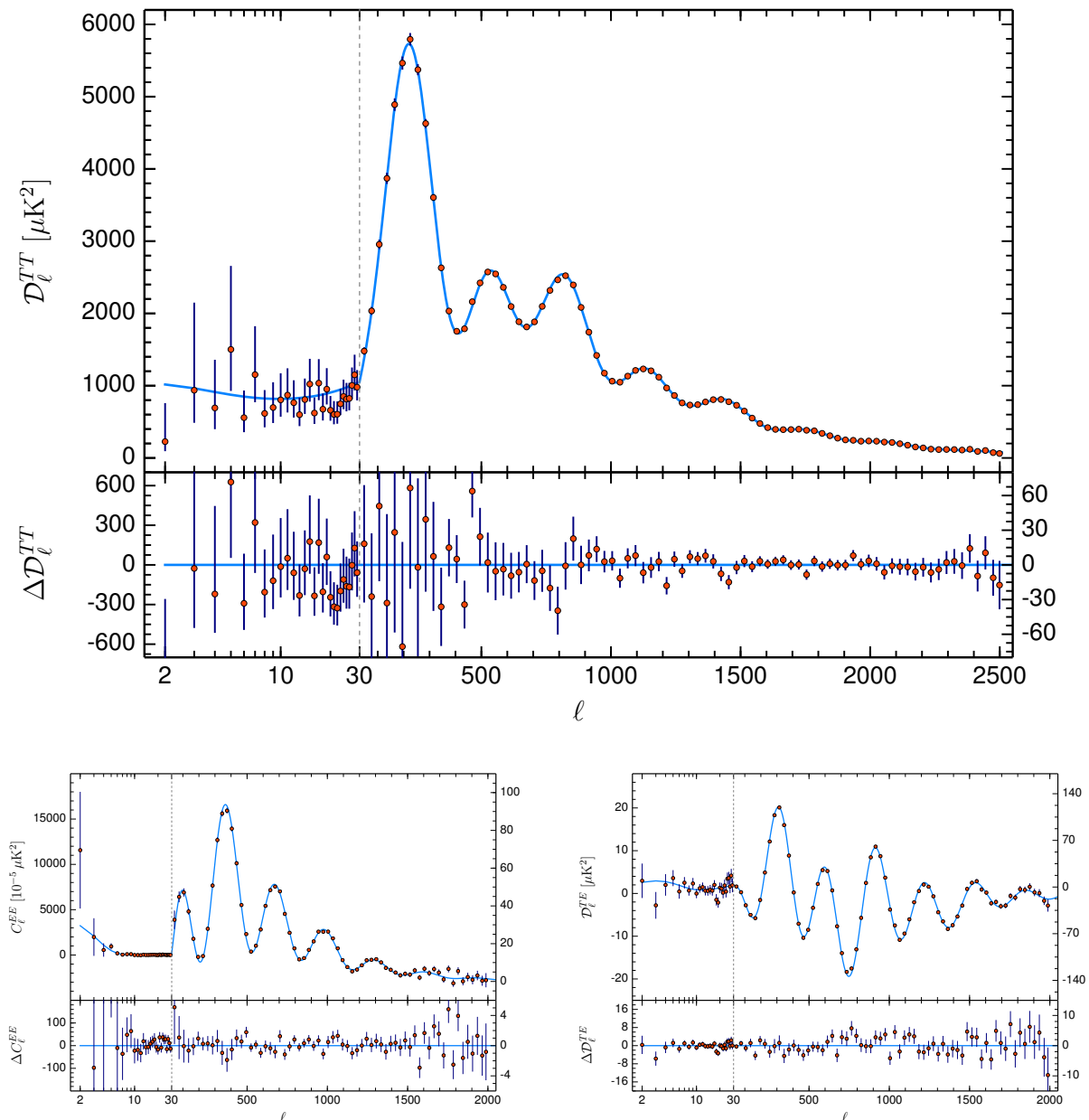


Fig. 9 – TT (top), EE (bottom left) and TE (bottom right) angular power spectra measured by Planck. The plotted quantities are $\mathcal{D}_\ell^{(XY)} = \ell(\ell + 1)T_0^2 C_\ell^{(XY)}/2\pi$. The blue solid lines are the Λ CDM best fit theoretical spectra and in the bottom panels the residuals with respect to this model are shown. Figures are taken from [18].

Dependence on cosmological parameters

The power of the Λ CDM cosmological model is that it can fit cosmological data with only 6 free parameters, whose measured values by the *Planck* mission are [18]:

1. Present-day baryons energy density: $h^2\Omega_{b,0} = 0.02237 \pm 0.00015$.
2. Present-day cold dark matter density: $h^2\Omega_{\text{CDM},0} = 0.1200 \pm 0.0012$.
3. Angular scale of the comoving sound horizon θ_s , defined as

$$\theta_s = \frac{r_s}{D_A(a_{\text{rec}})/a_{\text{rec}}}, \quad (9.42)$$

where $r_s = s(\eta_{\text{rec}})$ and D_A is the angular diameter distance. This parameter depends on $\Omega_{b,0}$, $\Omega_{\text{CDM},0}$, $\Omega_{K,0}$, $\Omega_{\Lambda,0}$ and on the effective number of relativistic species N_{eff} in the primordial plasma. Only neutrinos were present but since they decoupled in a slightly different moment, the value of N_{eff} is 3.046. θ_s is a way to measure the Hubble parameter H_0 . Planck measured $100\theta_s = 1.04092 \pm 0.00031$.

4. Optical depth at reionization $\tau = 0.0544 \pm 0.0073$.
5. Amplitude of the PPS A_s , which determines the amplitude of primordial scalar fluctuations from inflation: $\ln(10^{10}A_s) = 3.044 \pm 0.014$.
6. Tilt of the PPS $n_s = 0.9649 \pm 0.0042$. The PPS is slightly red with respect to scale invariance and so perturbations at large scales are larger than those at small scales.

The quantity A_s and n_s are computed at the reference scale $k_* = 0.05 \text{ Mpc}^{-1}$ or $k_* = 0.002 \text{ Mpc}^{-1}$. Another important parameter of the Λ CDM model is the tensor-to-scalar ratio r , which has not been detected yet. Therefore, the existence of tensor modes is not proved yet.

The shape of CMB angular power spectra strongly depends on cosmological parameters. At large angular scales, precisely for $\ell \lesssim 20$, the CMB angular power spectra has an almost constant value:

$$\ell(\ell + 1)C_\ell^{TT}/2\pi = A_s|(\Theta_0 + \Psi)_{\text{ini}}|^2 = \text{constant}. \quad (9.43)$$

This effect is known as Sachs-Wolf plateau and the constant is a measure of A_s . The location of the first three peaks in C_ℓ^{TT} depends on present-day densities and on Θ_s . In particular, θ_s is completely determined by the location of the first peak $\ell \sim 200$. At small scales, Silk damping takes place. This effect arises from the fact that at small scales photons diffuse from hot regions of the plasma to colder ones. The superposition of black bodies smooths temperature fluctuations. So, CMB anisotropies show a decreasing behavior at small scales. The Silk scale, which represents the scale under which Silk damping occurs, is computed as $ak_S^{-1} \approx \sqrt{t/(n_e\sigma_T)}$ and at recombination is roughly 8 Mpc^{-1} . For $k > k_S$, i.e for $\ell \gtrsim 800$, C_ℓ^{TT} is proportional to ℓ^{n_s-1} and this allows to measure n_s . C_ℓ^{EE} allows to measure τ

because for $\ell \leq 10$ C_ℓ^{EE} shows a bump whose amplitude is roughly proportional to τ^2 . The tensor-to-scalar ratio can be measured from the B -mode power spectra.

The Sachs-Wolf plateau, acoustics peaks and Silk damping are said to be primary sources of anisotropies. All of them occur for $\ell \geq 2$. $\ell = 0$ is the monopole term and it is related to the average temperature of CMB. The dipole ($\ell = 1$) is dominated by the kinematic effect caused by the relative motion of Earth with respect to CMB. It is the largest contribution to temperature fluctuations.

As the name suggests, primary anisotropies are not the only sources for CMB anisotropies. Indeed, there are also the so-called secondary sources of fluctuations:

- Integrated Sachs-Wolf effect. This effect is due to the time-varying gravitational potentials that CMB encounters along the line of sight.
- Reionization. Around $z \sim 7$, the formation of the first stars caused the reionization of the plasma and hence an increment of the optical depth τ . Reionization affects the amplitude of the CMB power spectra which is proportional to $A_s e^{-\tau}$. If one does not include CMB polarization power spectra, τ and A_s are degenerate parameters: they cannot be measured independently. Fortunately, CMB polarization power spectra break this degeneracy since the first peaks of the EE power spectrum depend only on τ .
- SZ effect. Free electrons present inside galaxy clusters cause distortions of the CMB black body due to the inverse Compton scattering with CMB photons. This affects also CMB temperature fluctuations.
- Gravitational lensing. The presence of structures along the line of sight to the last scattering surface deflects photons. This effect is known as gravitational lensing and it is one of the most important predictions of General Relativity. At the CMB level, the gravitational lensing generates a smoothing of the acoustic peaks in the TT -power spectra and it creates B -mode polarization. Thus, we observe B modes but not those to tensor fluctuations.

10 Silk damping spectral distortions

The presence of primordial fluctuation generated during inflation causes some regions of the primordial plasma to be hotter and denser than others. The various regions of the plasma at different temperatures are all represented by a black body spectrum. Photons diffuse from overdense regions to underdense ones and vice versa. This superposition of black bodies at different temperatures, known as Silk damping, generates an isotropization of the photon phase space distribution at small scales but also CMB SDs because, in general, the superposition of two or more black body spectra does not simply result in another black body at different temperature. We will prove that SDs generated by Silk damping depend

on the PPS and so they can be used to constrain its shape. This is one of the standard mechanisms in the Λ CDM model that predicts SDs and it provides a scientific goal for future experiments. Indeed, a measure of SDs due to Silk damping would provide an independent test of the Λ CDM model at scales never tested before.

10.1 Superposition of black bodies

Consider a black body radiation. Its spectral intensity is described by the Planck law (3.47). Similarly, its energy per unit of frequency and the total energy integrated over frequencies are given by

$$E_\nu = 8\pi \frac{\nu^3}{e^{\nu/(k_B T)} - 1}, \quad E = a_R T^4, \quad (10.1)$$

where the radiation constant is defined as $a_R \stackrel{\text{def}}{=} (8\pi^5/15)k_B^4$. The number of photons for such black body is

$$N = b_R T^3, \quad \text{where} \quad b_R = 16\pi k_B^3 \zeta(3). \quad (10.2)$$

Finally, the entropy is

$$S = \frac{4}{3} \frac{E}{T} = \frac{4}{3} a_R T^3. \quad (10.3)$$

Consider now the CMB with its temperature fluctuations $\Theta = \Delta T/T$. The photon phase space distribution of a black body at temperature $T + \Delta T$ at second order in Θ is (see (5.21))

$$B\left(\frac{\nu}{k_B \bar{T}(1 + \Theta)}\right) \approx B(\bar{x}) + G(\bar{x}) [\Theta + \Theta^2] + \frac{1}{2} Y(\bar{x}) \Theta^2 + \mathcal{O}(\Theta^3), \quad (10.4)$$

where $\bar{T} \stackrel{\text{def}}{=} \langle T \rangle$ is the spatially averaged temperature. We now take the ensemble average and by using the fact that $\langle \Theta \rangle = 0$, we get

$$\left\langle B\left(\frac{\nu}{k_B \bar{T}(1 + \Theta)}\right) \right\rangle \approx B(\bar{x}) + G(\bar{x}) \langle \Theta^2 \rangle + \frac{1}{2} Y(\bar{x}) \langle \Theta^2 \rangle + \mathcal{O}(\Theta^3) \quad (10.5)$$

The term representing the temperature shift can be absorbed in the first one by introducing a new reference temperature:

$$T_{\text{new}} = \bar{T} [1 + \Theta^2]. \quad (10.6)$$

Indeed, the ensemble average of $B(x_{\text{new}})$ at second order in Θ is exactly equal to the first two terms of equation (10.5). Therefore, we get

$$\left\langle B\left(\frac{\nu}{k_B \bar{T}(1 + \Theta)}\right) \right\rangle \approx B(x_{\text{new}}) + \frac{1}{2} Y(\bar{x}) \langle \Theta^2 \rangle + \mathcal{O}(\Theta^3). \quad (10.7)$$

The y -type distortion term cannot be absorbed by any re-definition of the reference temperature and so Silk damping produces a black body at higher temperature $T_{\text{new}} > \bar{T}$ plus a y -type CMB spectral distortion with amplitude $y = 0.5 \langle \Theta^2 \rangle$.

To understand why Silk damping produces SDs, consider two black body spectra with

temperatures $T_1 = T + \Delta T$ and $T_2 = T - \Delta T$. Their average temperature is T . The total energy, number of photons and entropy of a black body at temperature T are given in equations (10.1), (10.2), (10.3). The average initial total energy, number of photons and entropy of the two not super-imposed black bodies are instead given by

$$E_{\text{initial}} = a_R \frac{T_1^4 + T_2^4}{2} \approx a_R T^4 \left[1 + 6 \left(\frac{\Delta T}{T} \right)^2 \right] > a_R T^4 \quad (10.8a)$$

$$N_{\text{initial}} = b_R \frac{T_1^3 + T_2^3}{2} \approx b_R T^3 \left[1 + 3 \left(\frac{\Delta T}{T} \right)^2 \right] > b_R T^3 \quad (10.8b)$$

$$S_{\text{initial}} = \frac{4a_R}{3} \frac{T_1^3 + T_2^3}{2} \approx \frac{4a_R}{3} T^3 \left[1 + 3 \left(\frac{\Delta T}{T} \right)^2 \right] > \frac{4a_R}{3} T^3 \quad (10.8c)$$

The spatially-averaged superposition of these two black bodies gives a black body whose final temperature is given in equation (10.6) plus a y -type distortion term. The final temperature is the one of a black body that has the same number of photons as the initial average one N_{initial} :

$$T_{\text{final}} = \left(\frac{N_{\text{initial}}}{b_R} \right)^{1/3} \approx T \left[1 + \left(\frac{\Delta T}{T} \right)^2 \right] \equiv T_{\text{new}}. \quad (10.9)$$

Thus, the number of photons of the final black body coincides with the initial average. Since the entropy scales with T^3 as the number of photons, also the final entropy is equal to the initial average one. However, the energy changes:

$$E_{\text{final}} = a_R T_{\text{final}}^4 \approx a_R T^4 \left[1 + 4 \left(\frac{\Delta T}{T} \right)^2 \right] < E_{\text{initial}}. \quad (10.10)$$

The final black body has a lower energy than the average initial one. The missing energy goes into SDs. To quantify how much is the missing energy that contributes to SDs, we multiply equation (10.7) by ν^3 and we integrate over frequencies. The result is [54]:

$$E_{\text{final}} - a_R T^4 = 2/3 (E_{\text{initial}} - a_R T^4) \quad (10.11a)$$

$$1/3 (E_{\text{initial}} - a_R T^4) = 2\Theta^2 a_R T^4 \propto \frac{1}{2} \Theta^2 \int dx x^3 Y(x). \quad (10.11b)$$

2/3 of the initial average energy goes in the final black body spectrum, while 1/3 goes into the distortion term.

Comptonization

If the Compton scattering is efficient during the superposition of black bodies, it can comptonize the final spectrum, i.e. the new black body plus a y -type distortion, and create a Bose-Einstein spectrum with some temperature T_{BE} and chemical potential μ . These two parameters can be computed by equating the average initial number of photons N_{initial}

and energy E_{initial} with the number of photons and energy of a Bose-Einstein spectrum $f_{\text{BE}}(x) = \left[\exp\left(\frac{\nu}{k_B T_{\text{BE}}} + \mu\right) - 1 \right]^{-1}$. The result is

$$\mu = 1.401 \left[1/3(E_{\text{initial}} - a_R T^4) \right] = 2.8\Theta^2 \quad (10.12a)$$

$$\delta T_{\text{BE}} \stackrel{\text{def}}{=} \frac{T_{\text{BE}} - T_{\text{new}}}{T_{\text{new}}} = \frac{\mu}{2.19} = 1.278\Theta^2. \quad (10.12b)$$

We would get the same result if we add an energy $\Delta E = 1/3(E_{\text{initial}} - a_R T^4)$ to a black body at temperature T_{new} .

10.2 Dissipation of primordial acoustic waves

The angular average energy in CMB anisotropies is equal to [55]:

$$\frac{\Delta E}{E_\gamma} = 4\langle\Theta^2\rangle \approx 9.6 \times 10^{-9}, \quad (10.13)$$

where E_γ is the energy density of CMB photons. 1/3 of this energy creates a y -type distortion with magnitude $y = 0.5\langle\Theta^2\rangle = 8 \times 10^{-10}$, which eventually comptonize in a μ -type distortion. The dissipated energy by the Silk damping in Fourier space is given by

$$\begin{aligned} \left. \frac{\Delta E}{E_\gamma} \right|_{\text{Silk}} &= 4\langle\Theta^2\rangle = 6 \int \frac{d^3k}{(2\pi)^3} e^{ik \cdot x} \int \frac{d^3k'}{(2\pi)^3} \langle \Theta(\mathbf{k}', \mathbf{n}') \Theta(\mathbf{k} - \mathbf{k}', \mathbf{n}) \rangle = \\ &= 6 \int \frac{dk}{d} \mathcal{P}_{\mathcal{R}}(k) \left[\sum_{\ell=0}^{\infty} (2\ell + 1) \Theta_\ell^2(k) \right] \end{aligned} \quad (10.14)$$

where the multipoles expansion of Θ was used. As mentioned above, only 1/3 of this energy creates distortions.

For $z \sim 6000$, electrons and baryons are tightly coupled and $\ell > 2$ modes can be neglected. Furthermore, the relation between the monopole and the dipole in the tightly coupled regime $\Theta_1 = \Theta_0/\sqrt{3}$ can be used. Hence, in this regime the dissipated energy that contributes to a y -type SD, which immediately is comptonized into a μ -one, is:

$$\left. \frac{\Delta E}{E_\gamma} \right|_{\text{distortion}} = 2 \int \frac{dk}{d} \mathcal{P}_{\mathcal{R}}(k) \left[\Theta_0^2 + 3\Theta_1^2 \right] = 2 \int \frac{dk}{d} \mathcal{P}_{\mathcal{R}}(k) \left[12\Theta_0^2 \right] \quad (10.15)$$

To compute the amplitudes of the various CMB SDs created by the Silk damping, one has to take the time derivative of equation (10.14):

$$\begin{aligned} \frac{d}{dt} \left. \frac{\Delta E}{E_\gamma} \right|_{\text{distortion}} &= \frac{d}{dt} \frac{1}{3} \left. \frac{\Delta E}{E_\gamma} \right|_{\text{Silk}} = \\ &= 4\dot{\tau}\sigma_T \int \frac{dk}{d} \mathcal{P}_{\mathcal{R}}(k) \left[\frac{(3\Theta_1^2 - v_b)^2}{3} + \right. \\ &\quad \left. + \frac{9}{2}\Theta_2^2 - \frac{1}{2}\Theta_2 \left(\Theta_2^P + \Theta_0^P \right) \sum_{\ell=3}^{\infty} (2\ell + 1) \Theta_\ell^2 \right]. \end{aligned} \quad (10.16)$$

The derivation is easily performed by using the first-order Boltzmann equation for Θ , provided that we ignore metric perturbations and imposes gauge invariance. Another derivation that is manifestly gauge invariant, but that uses second order Boltzmann equation, can be found in [56]. The previous quantity is the rate of the injected energy in the plasma due to the Silk damping. In chapter II we label such quantity with $\dot{Q}_{\text{non-inj}}$. To simplify the previous equation, we apply the tight-coupling approximation. In this limit, baryons and photons velocities are almost equal and $\Theta_{\ell \geq 2} = \Theta_{\ell \geq 0}^P \approx 0$. Furthermore, the dipole on sub-horizon scales is roughly equal to

$$\Theta_1 = v_\gamma/3 \approx A \frac{c_s^2}{(1+R)^{1/4}} \sin(kr_s) e^{-(k/k_D)^2}, \quad R \stackrel{\text{def}}{=} \frac{4\rho_\gamma}{3\rho_b} \quad (10.17)$$

where the normalization constant A is given by

$$A \approx \left(1 + \frac{4}{15} f_\nu\right)^{-1} \stackrel{\text{def}}{=} \left(1 + \frac{4}{15} \frac{\rho_\nu}{\rho_\gamma}\right)^{-1} \quad (10.18)$$

and the damping scale k_D is defined as

$$k_D \stackrel{\text{def}}{=} \frac{2\pi}{r_D} = 2\pi \left[\int dz \frac{c_s^2}{2\dot{\tau}H} \left(\frac{R^2}{1+R} + \frac{16}{15} \right) \right]^{-1/2}. \quad (10.19)$$

f_ν can be expressed also in terms of the effective number of ultra-relativistic species N_{eff} in the primordial plasma as

$$f_\nu \stackrel{\text{def}}{=} \frac{f_\nu}{f_\gamma} = \left(1 + \frac{8}{7} \left(\frac{4}{11}\right)^{-1/3} \frac{1}{N_{\text{eff}}}\right)^{-1}. \quad (10.20)$$

Finally, c_s is the speed of sound of the primordial plasma and $r_s(z)$ is the comoving sound horizon. Putting all this together, we get the final expression for the rate of injected energy due to Silk damping

$$\dot{Q}_{\text{non-inj}} = 4A^2 \rho_\gamma \int \frac{dk}{k} \mathcal{P}_{\mathcal{R}}(k) k^2 (\partial_t k_D^{-2}) e^{-2(k/k_D)^2}. \quad (10.21)$$

Once we know $\dot{Q}_{\text{non-inj}}$ through equation (10.21), we can compute spectral distortion amplitudes with equation (5.31). The result depends on which approximation we use for the branching ratios. The most precise possibility is to use the Green's functions method and PCA decomposition, even if the resulting amplitudes are detector-dependent. However, to roughly estimate the SDs due to the Silk damping, one can use the approximation (5.39) for branching ratios. This approximation is accurate at the level of $\sim 20\%$ with respect to the Green's function calculation [41]. In this approximation, the μ and y amplitudes are given by [57]:

$$\mu = \int_{k_{\text{min}}}^{\infty} \frac{dk}{k} \mathcal{P}_{\mathcal{R}} W_\mu(k), \quad y = \int_{k_{\text{min}}}^{\infty} \frac{dk}{k} \mathcal{P}_{\mathcal{R}} W_y(k) \quad (10.22)$$

where W_μ and W_y are the μ - and y - window functions:

$$W_\mu(k) \approx 2.27 \left[\exp\left(-\frac{(\hat{k}/1360)^2}{1 + (\hat{k}/260)^{0.3} + \hat{k}/340}\right) - \exp(-(\hat{k}/32)^2) \right] \quad (10.23a)$$

$$W_y(k) \approx 0.45 \exp[-(\hat{k}/32)^2]. \quad (10.23b)$$

In the previous expressions, we used \hat{k} to denote $k/[\text{Mpc}^{-1}]$. The cut-off scale k_{\min} is usually set equal to 1 Mpc^{-1} . This scale is introduced because for $k < k_{\min}$ the approximation used for the photons transfer functions is not valid anymore. The window functions (10.23) are plotted in figure 10. As the plot suggests, the two window functions have support in the range $[1, 10^4 - 10^5] \text{ Mpc}^{-1}$. This is roughly the range of comoving wavenumbers on which CMB SDs can test the PPS and it is complementary to those tested by CMB anisotropies, which is roughly $k \sim [1 \times 10^{-4}, 5 \times 10^{-1}] \text{ Mpc}^{-1}$.

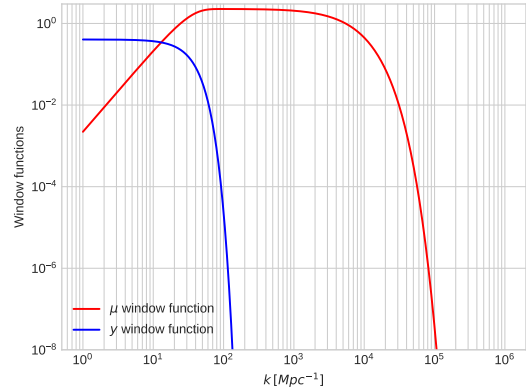


Fig. 10 – Window functions for CMB SDs due to Silk damping.

11 Primordial gravitational waves

Transverse and traceless tensor modes of metric perturbations that propagate in the FLRW spacetime are gravitational waves (GWs). Gravitational waves that have an inflationary origin are called primordial gravitational waves and they contribute to the so-called stochastic gravitational waves background. Other contributions to this irreducible background of gravitational waves come from standard processes like black holes mergers. Future space- and ground-based interferometers, such as LISA [21] or Einstein Telescope [58], will be in principle able to measure the stochastic gravitational waves background.

In this chapter, primordial gravitational waves are briefly reviewed. In the first section, gravitational waves coming from primordial tensor modes are discussed. In the second section, second-order perturbation theory is studied. At second order in cosmological fluctuations, tensor and scalar modes are not decoupled. Hence, scalar modes can induce primordial gravitational waves. We will prove that the power of the scalar-induced GWs depends on the PPS and so they can be used to constrain its shape.

11.1 Gravitational waves from inflation

The primordial power spectrum of tensor modes at the Hubble radius crossing is given in equation (8.103). As it happens for scalar perturbations, inflation stretches tensor wavelengths to super-Hubble-radius scales, making their amplitude frozen. Then, these perturbations re-enter the Hubble radius in the radiation- or matter-dominated era. Modes that re-enter the Hubble radius start to oscillate and the amplitude is damped by a factor $1/a$. So, once tensor modes re-enter the Hubble radius, the equation they satisfy (8.101) turns into a Bessel equation, whose solution in terms of $h_{\mathbf{k}}(\eta)$ is:

$$h_{\mathbf{k}}(\eta) = h_{\mathbf{k},*} j_0(k\tau), \quad h_{\mathbf{k}}(\eta) = h_{\mathbf{k},*} \left(\frac{3j_1(k\eta)}{k\eta} \right) \quad (11.1)$$

where $h_{\mathbf{k},*}$ is the amplitude at Hubble radius crossing. Bessel functions represent the transfer functions for the tensor modes from the Hubble radius re-enter until η (usually today). This solution tells that the damping factor is greater for high-frequency gravitational waves.

A GWs detector measures the gravitational wave strain at a given time and frequency. In the case of the stochastic gravitational waves background, one measures the time and ensemble average of the superposition of all the incoming signals. Usually, cosmologists use the energy density fraction of GWs as observable. In general, it is not easy to associate an energy density to GWs because in general relativity it is always possible to go to a local inertial frame of reference where there is no sign of gravity and hence it is not possible to associate an energy density to the gravitational field. However, GWs carry energy and momentum, or they would not have been detected by the Ligo-Virgo collaboration [16]. Indeed, the energy of GWs can be defined in some limits of interest. Consider GWs propagating in vacuum. It satisfies Einstein equations in vacuum $G_{\mu\nu} = 0$. In the weak field limit the metric can be split as $g_{\mu\nu} = \bar{g}_{\mu\nu} + h_{\mu\nu}$, with $h_{\mu\nu} \ll 1$. In this limit, GWs $h_{\mu\nu}$ are treated as high-frequency perturbations up to the background metric $\bar{g}_{\mu\nu}$. Since gravity is highly non-linear, GWs backreact on the background metric. Indeed, by expanding the Einstein tensor $G_{\mu\nu}$ at second order one finds that quadratic terms in $h_{\mu\nu}$ can be treated as a source of the gravitational field and Einstein equations become:

$$\bar{G}_{\mu\nu}[\bar{g}_{\mu\nu}] = M_{pl}^{-2} G_{\mu\nu}^{t\text{GW}}[h_{\mu\nu}]. \quad (11.2)$$

$t_{\mu\nu}^{\text{GW}}$ is the pseudo-energy-momentum tensor of GWs and it is given by

$$t_{\mu\nu}^{\text{GW}} = \frac{M_{pl}^4}{4} \left\langle \partial_\mu h^{\alpha\beta} \partial_\nu h_{\alpha\beta} - \frac{1}{2} \bar{g}_{\mu\nu} \partial_\rho h^{\alpha\beta} \partial^\rho h_{\mu\nu} \right\rangle, \quad (11.3)$$

where all the contractions are performed with the background metric. The angular brackets indicate a volume and/or time averaging of all the GWs going through a small box.

[60]. It is convenient to work in a Newtonian gauge with an exponential notation

$$ds^2 = g_{\mu\nu}dx^\mu dx^\nu = -e^{2\Psi}dt^2 + a^2(t)e^{-2\Phi}Y_{ij}dx^i dx^j. \quad (11.11)$$

In the flat FLRW background case $Y_{ij} = \delta_{ij}$. Y_{ij} contains only the transverse and traceless degrees of freedom and it satisfies the condition

$$\frac{\partial}{\partial t} \det Y = Y^{ij} \frac{\partial}{\partial t} Y_{ij} = 0. \quad (11.12)$$

The action of the inflaton field coupled to the gravitational one is given in equation (8.32). In the (3 + 1) conformal decomposition, after some integration by parts and some algebra, the action becomes

$$S = \int d^3x dt \left[a e^{\Psi-\Phi} \left(\frac{R^{(3)}[Y_{ij}]}{16\pi G} + 2Y^{ij} D_i D_j \Phi - Y^{ij} D_i \Phi D_j \Phi - \frac{Y^{ij}}{2} D_i \phi D_j \phi \right) + a^3 e^{-(3\Phi+\Psi)} \left(\frac{1}{8} Y^{ij} Y^{kl} \dot{Y}_{ik} \dot{Y}_{jl} - 3(H - \dot{\Phi})^2 + \frac{\dot{\phi}^2}{2} \right) - a^3 e^{\Psi-3\Phi} V(\phi) \right], \quad (11.13)$$

where $R^{(3)}[Y_{ij}]$ and D_i are respectively the 3-dimensional Ricci scalar and the covariant derivative associated with Y_{ij} .

At second order, Y_{ij} is decomposed as

$$Y_{ij} \stackrel{\text{def}}{=} (e^h)_{ij} = \delta_{ij} + h_{ij} + \frac{1}{2} \delta^{kl} h_{ik} h_{jl} + \mathcal{O}(h^3). \quad (11.14)$$

h_{ij} are the usual transverse and traceless tensor modes representing GWs. The inverse is simply $Y^{ij} = \delta^{ik} \delta^{jl} (e^{-h})_{kl}$. The 3-dimensional scalar is given by

$$R^{(3)}[e^h] = -\frac{1}{4} \partial_i h_{kl} \partial^i h^{kl} + \mathcal{O}(h^3). \quad (11.15)$$

Metric perturbations Φ and Ψ are not expanded, while the inflation field split as usual: $\phi = \bar{\phi} + \delta\phi$. The expanded action contains a lot of terms. Scalar-induced GWs correspond to those with two scalar and one traceless and transverse tensor modes:

$$S \subset \int d^3x dt \left[\frac{a^3}{8} \dot{h}^{ij} \dot{h}_{ij} - \frac{a}{8} \partial_i h_{kl} \partial^i h^{kl} + 2ah^{ij} \partial_i (\Psi - \Phi) \partial_j \Phi + ah^{ij} \partial_i \Phi \partial_j \Phi + \frac{a}{2} h^{ij} \partial_i \delta\phi \partial_j \delta\phi \right].$$

By varying the previous action with respect to h_{ij} , we get the equations of motion for scalar-induced GWs:

$$\ddot{h}_{ij} + 3H\dot{h}_{ij} - a^{-2} \nabla^2 h_{ij} = a^{-2} P^{ab}_{ij} \{ 8\partial_a (\Psi - \Phi) \partial_b \Phi + 4\partial_a \Phi \partial_b \Phi + 2\partial_a \delta\phi \partial_b \delta\phi \}, \quad (11.16)$$

with the transverse and traceless projection operator P_{ij}^{ab} given by

$$P_{ij}^{ab} \stackrel{\text{def}}{=} \left(\delta_i^{(a} - \partial_i \partial^{(a} \Delta^{-1} \right) \left(\delta_j^{b)} - \partial_j \partial^{b)} \Delta^{-1} \right) - \frac{1}{2} \left(\delta_{ij} - \partial_i \partial_j \Delta^{-1} \right) \left(\delta^{ab} - \partial^a \partial^b \Delta^{-1} \right), \quad (11.17)$$

where the parenthesis in the indexes denotes normalized symmetrization. Equations of motion simplify if we use the condition $\Phi - \Psi = 0$, obtained from linearized Einstein equations. Furthermore, we can write the term containing $\delta\phi$ in terms of the energy-momentum tensor associated to the inflaton field (7.25):

$$\ddot{h}_{ij} + 3H\dot{h}_{ij} - a^{-2}\nabla^2 h_{ij} = a^{-2}P_{ij}^{ab} \{4\partial_a \Phi \partial_b \Phi + 2(\rho + P)\partial_a v \partial_b v\}, \quad (11.18)$$

where v is such that $u_i = \partial_i v$ and u_i is defined in (7.26). Perturbations in the inflaton field $\delta\phi$ are related to Φ by the relation

$$\delta\phi = \sqrt{\frac{2}{\epsilon_1}} \left(\Phi + \frac{\Phi'}{\mathcal{H}} \right) \quad (11.19)$$

and so we can solve for scalar degrees of freedom Φ only. Here the $'$ indicates a derivative with respect to the conformal time. To solve the equation for Φ we work in Fourier space and we split it in some initial value Φ_k times a transfer function $T_\Phi(k, \eta)$ that relates the initial value to those measured at η

$$\Phi(\mathbf{k}, \eta) = T_\Phi(k, \eta)\Phi_k. \quad (11.20)$$

The initial value Φ_k is set on super-Hubble-radius scales ($k\eta \ll 1$) by quantum fluctuations during inflation. We can now write the equations of motion for scalar-induced GWs as

$$h_{\mathbf{k}}^{(\lambda)''} + 2\mathcal{H}h_{\mathbf{k}}^{(\lambda)'} + k^2 h_{\mathbf{k}}^{(\lambda)} = S_{\mathbf{k}}^{(\lambda)}, \quad (11.21)$$

where the source term S is given by

$$S_{\mathbf{k}}^{(\lambda)} = 4 \int \frac{d^3q}{(2\pi)^2} e_{ij}^{(\lambda)} q^i q^j \Phi_q \Phi_{|\mathbf{k}-\mathbf{q}|} f(\eta, q, |\mathbf{k} - \mathbf{q}|) \quad (11.22)$$

and

$$f(\eta, q, |\mathbf{k} - \mathbf{q}|) = T_\Phi(q\eta)T_\Phi(|\mathbf{k} - \mathbf{q}|\eta) + \frac{1+b}{2+b} \left(T_\Phi(q\eta) + \frac{T'_\Phi(q\eta)}{\mathcal{H}} \right) \left(T_\Phi(|\mathbf{k} - \mathbf{q}|\eta) + \frac{T'_\Phi(|\mathbf{k} - \mathbf{q}|\eta)}{\mathcal{H}} \right), \quad (11.23)$$

where ϵ_1 was written in terms of the parameter b defined in equation (7.10) by using the equation (7.12). The tensor $e_{ij}^{(\lambda)}$ is defined in equation (8.92). We also used the fact that $e^{ij}P_{ij}^{ab} = e^{ab}$.

The Green's function solution to such equations with initial conditions $h_{\mathbf{k}}^{(\lambda)} = h_{\mathbf{k}}^{(\lambda)'} = 0$ is

$$h_{\mathbf{k}}^{(\lambda)}(\eta) = \int_{\eta_i}^{\eta} d\tilde{\eta} G_h(\eta, \tilde{\eta}) S_{\mathbf{k}}^{(\lambda)}(\tilde{\eta}). \quad (11.24)$$

In Fourier space, the Green's function solves

$$G_{\mathbf{k}}^{(\lambda)''}(\eta, \tilde{\eta}) + 2\mathcal{H}G_{\mathbf{k}}^{(\lambda)' }(\eta, \tilde{\eta}) + k^2 G_{\mathbf{k}}^{(\lambda)}(\eta, \tilde{\eta}) = \delta(\eta - \tilde{\eta}). \quad (11.25)$$

We can write G_h in terms of two homogeneous solutions $h_{1,2}$, G_h :

$$G(\eta, \tilde{\eta}) = \frac{h_1(\eta)h_2(\tilde{\eta}) - h_1(\tilde{\eta})h_2(\eta)}{W(h_1, h_2, \tilde{\eta})}, \quad (11.26)$$

where the Wronskian is defined as

$$W(h_1, h_2, \tilde{\eta}) \stackrel{\text{def}}{=} h_1'(\tilde{\eta})h_2(\tilde{\eta}) - h_1(\tilde{\eta})h_2'(\tilde{\eta}). \quad (11.27)$$

We want to compute the scalar-induced GW power $\Omega_{\text{GW}}^{\text{ind}}$. Equation (11.9) suggests that we have to know the scalar-induced primordial power spectrum of tensor perturbations. We first compute the 2-point correlation function of the scalar-induced tensor modes $h_{\mathbf{k}}^{\lambda}$ by using the Green's function solution (11.24):

$$\langle h_{\mathbf{k}}^{\lambda}(\eta) h_{\mathbf{k}'}^{\lambda}(\eta) \rangle = \int_0^{\eta} d\eta_1 \int_0^{\eta} d\eta_2 G(\eta, \eta_1) G(\eta, \eta_2) \langle S_{\mathbf{k}}^{(\lambda)}(\eta_1) S_{\mathbf{k}'}^{(\lambda)}(\eta_2) \rangle. \quad (11.28)$$

We neglected non-trivial tensor-scalar-scalar interactions in the inflaton potential for simplicity so that the 2-point correlation function is due only to the coupling at second order in cosmological perturbation theory. We calculate the 2-point function for the source term S with equation (11.22):

$$\begin{aligned} \langle S_{\mathbf{k}}^{(\lambda)}(\eta_1) S_{\mathbf{k}'}^{(\lambda)}(\eta_2) \rangle &= 16 \int \frac{d^3 q}{(2\pi)^3} \int \frac{d^3 q'}{(2\pi)^3} e_{ij}^{(\lambda)}(k) q^i q^j e_{mn}^{(\lambda)}(k') q'^m q'^n \times \\ &\times f(\eta_1, q, |\mathbf{k} - \mathbf{q}|) f(\eta_2, q', |\mathbf{k}' - \mathbf{q}'|) \langle \Phi_q \Phi_{|\mathbf{k}-\mathbf{q}|} \Phi_{q'} \Phi_{|\mathbf{k}'-\mathbf{q}'|} \rangle. \end{aligned} \quad (11.29)$$

In the hypothesis that all scalar fluctuations are Gaussian, the Wick theorem allows us to easily compute the 4-points correlation function appearing in the last equation:

$$\begin{aligned} \langle \Phi_q \Phi_{|\mathbf{k}-\mathbf{q}|} \Phi_{q'} \Phi_{|\mathbf{k}'-\mathbf{q}'|} \rangle &= \frac{2\pi^2}{q^3} \mathcal{P}_{\Phi}(q) \frac{2\pi^2}{|\mathbf{k} - \mathbf{q}|^3} \mathcal{P}_{\Phi}(|\mathbf{k} - \mathbf{q}|) \\ &\times (2\pi)^6 \delta^3(\mathbf{q} + \mathbf{q}') \delta^3(\mathbf{k} + \mathbf{k}' - \mathbf{q} - \mathbf{q}') + (\mathbf{q} \leftrightarrow \mathbf{k} - \mathbf{q}). \end{aligned} \quad (11.30)$$

Then, we time average the induced primordial power spectrum of tensor modes

$$\mathcal{P}_T^{\text{ind}} = 8 \int_0^{\infty} dv \int_{|1-v|}^{1+v} du \left(\frac{4v^2 - (1 - u^2 + v^2)^2}{4uv} \right)^2 \overline{I^2(\eta, k, v, u)} \mathcal{P}_{\Phi}(ku) \mathcal{P}_{\Phi}(kv), \quad (11.31)$$

where the variables v, u are defined as

$$v \stackrel{\text{def}}{=} \frac{q}{k}, \quad u \stackrel{\text{def}}{=} \frac{|\mathbf{k} - \mathbf{q}|}{k}. \quad (11.32)$$

All the time dependence is contained in a kernel, or transfer function, defined as

$$I(\eta, k, u, v) \stackrel{\text{def}}{=} \int_{\eta_i}^{\eta} d\tilde{\eta} G(\eta, \tilde{\eta}) f(\tilde{\eta}, k, u, v). \quad (11.33)$$

Once we know $\mathcal{P}_T^{\text{ind}}$, we can compute $\Omega_{\text{GW}}^{\text{ind}}$ with equation (11.9). Finally, we want to constrain the shape of the primordial power spectrum of curvature perturbations and so we have to relate Φ with \mathcal{R} . At linear order in Newtonian gauge we have

$$\mathcal{R} = -\frac{5 + 3w}{3(1 + w)}\Phi = -\frac{2b + 3}{b + 2}\Phi. \quad (11.34)$$

and therefore the two primordial power spectra are related by a simple numerical factor

$$\mathcal{P}_{\Phi} = \left(\frac{b + 2}{2b + 3}\right)^2 \mathcal{P}_{\mathcal{R}}. \quad (11.35)$$

Analytical solutions.

For a constant equation of state w , we can analytically compute the kernel I . The equation for the Newtonian potential reads

$$\Phi'' + 3\mathcal{H}(1 + c_w^2)\Phi' + (2\mathcal{H}' + (1 + 3c_w^2)\mathcal{H}^2)\Phi + c_s^2 k^2 \Phi = 0, \quad (11.36)$$

where $c_w^2 = \dot{P}/\dot{\rho}$ and $c_s^2 = \delta P/\delta\rho$. A perfect fluid has $c_w^2 = c_s^2 = w$, while in the single field inflationary model we have $c_w^2 = w$ and $c_s^2 = 1$. c_s represents the speed of propagation of perturbations. In the single-field case, it is equal to the speed of light. There are some inflationary models where $c_s < 1$. For a review of these models, see [61]. The solution of equation (11.36) with initial condition $\Phi \rightarrow \Phi_{\mathbf{k}}$ for $c_s k \eta \ll 1$ is

$$\Phi(k\eta) = \Phi_{\mathbf{k}} 2^{b+3/2} \Gamma(b + 5/2) (c_s k \eta)^{-b-3/2} J_{b+3/2}(c_s k \eta), \quad (11.37)$$

where J is a Bessel function of the first kind. We can now recognize the transfer function T_{Φ} and so, by using some properties of Bessel functions, compute the function f defined in equation (11.23):

$$f(x, u, v) = \frac{2^{2b+3} \Gamma^2[b + 5/2]}{(2b + 3)(b + 2)} (x)^{-2b-1} (uv)^{-b-1/2} \times \left(J_{b+1/2}(c_s v x) J_{b+1/2}(c_s u x) + \frac{b + 2}{b + 1} J_{b+5/2}(v x) J_{b+5/2}(c_s u x) \right), \quad (11.38)$$

where $x = k\eta$. The two homogeneous solutions $h_{1,2}$ are instead given by

$$h_1(x) = (x)^{-b-1/2} J_{b+1/2}(x) \quad \text{and} \quad h_2(x) = (x)^{-b-1/2} Y_{b+1/2}(x), \quad (11.39)$$

where Y is the Bessel function of the second kind. Given these solutions, the Green's function is equal to

$$G(\eta, \tilde{\eta}) = \frac{\pi}{2k} \frac{(\tilde{x})^{b+3/2}}{(x)^{b+1/2}} \left(J_{b+1/2}(\tilde{x}) Y_{b+1/2}(\tilde{x}) - J_{b+1/2}(x) Y_{b+1/2}(x) \right). \quad (11.40)$$

The kernel I (11.33) is finally equal to

$$I(x, u, v) = \pi 4^b \Gamma^2[b + 3/2] \frac{2b + 3}{b + 2} \left(c_s^2 u v x \right)^{-b-1/2} \left(J_{b+1/2}(x) \mathcal{I}_Y - Y_{b+1/2}(x) \mathcal{I}_J \right), \quad (11.41)$$

where the function $\mathcal{I}_{J/Y}$ are defined as

$$\begin{aligned} \mathcal{I}_{J,Y}(u, v) &\stackrel{\text{def}}{=} \int_0^x d\tilde{x} \tilde{x}^{1/2-b} \begin{Bmatrix} J_{b+1/2}(\tilde{x}) \\ Y_{b+1/2}(\tilde{x}) \end{Bmatrix} \\ &\times \left(J_{b+1/2}(c_s v \tilde{x}) J_{b+1/2}(c_s u \tilde{x}) + \frac{b+2}{b+1} J_{b+5/2}(c_s v \tilde{x}) J_{b+5/2}(c_s u \tilde{x}) \right). \end{aligned} \quad (11.42)$$

Inflation is expected to be followed by the radiation-dominated era. Thus, in the previous equations we can set $b = 0$, which corresponds to $w = 1/3$.

In this case, the present-day scalar-induced GW power (11.9) is

$$\begin{aligned} \Omega_{\text{GW}}^{\text{ind}}(\eta_0, k) &= \frac{\Omega_{r,0}}{36} \int_0^{\frac{1}{\sqrt{3}}} dd \int_{\frac{1}{\sqrt{3}}}^{\infty} ds \left[\frac{(d^2 - 1/3)(s^2 - 1/3)}{s^2 - d^2} \right]^2 \times \\ &\times \mathcal{P}_{\mathcal{R}} \left(\frac{k\sqrt{3}}{2}(s+d) \right) \mathcal{P}_{\mathcal{R}} \left(\frac{k\sqrt{3}}{2}(s-d) \right) \left[\mathcal{I}_J(d, s)^2 + \mathcal{I}_Y(d, s)^2 \right], \end{aligned} \quad (11.43)$$

where we introduced the new variables

$$d = \frac{1}{\sqrt{3}}|u - v|, \quad s = \frac{1}{\sqrt{3}}(u + v), \quad (d, s) \in [0, 1/\sqrt{3}] \times [1/\sqrt{3}, \infty]. \quad (11.44)$$

and where the analytical expressions for $\mathcal{I}_{J,Y}$ are [62]:

$$\mathcal{I}_J(d, s) = -36\pi \frac{(s^2 + d^2 - 2)^2}{(s^2 - d^2)^3} \Theta_H(s - 1), \quad (11.45a)$$

$$\mathcal{I}_Y(d, s) = -36 \frac{(s^2 + d^2 - 2)}{(s^2 - d^2)^2} \left[\frac{(s^2 + d^2 - 2)}{(s^2 - d^2)} \log \frac{(1 - d^2)}{|s^2 - 1|} + 2 \right]. \quad (11.45b)$$

$\Omega_{r,0} \approx 8.6 \times 10^{-5}$ is the density of radiation today.

Equation (11.43) suggests that $\Omega_{\text{GW}}^{\text{ind}}(k) \propto \mathcal{P}_{\mathcal{R}}(k)$ and therefore $\Omega_{\text{GW}}^{\text{ind}}$ has the same spectral dependence on model parameters of the PPS.

SMALL-SCALE PRIMORDIAL FEATURES

The simplest single-field slow-roll inflationary scenarios predict a near scale invariant primordial power spectrum consistent with CMB data. However, there exist many models of inflation that predict features at small scales, where the primordial power spectrum is not constrained.

The purpose of this thesis is to investigate the imprints of small-scale bumps in the primordial power spectrum on several cosmological observables. In the first part of this chapter we introduce two inflationary models that predict a peak in the primordial power spectrum. Then, we derive phenomenological templates that capture their shape. We end this chapter by investigating the imprints by varying the template parameters on cosmological observables.

12 Primordial black holes formation from large overdensities

In the '60s-'70s, it was realized that the gravitational collapse of very large primordial overdensities could form the so-called Primordial Black Holes [63, 64]. It was later proposed that primordial black holes may constitute a large fraction of the total dark matter of the Universe and seed the formation of the supermassive black holes at the center of galaxies [65, 66]. Recently, interest in primordial black holes has been revived after the LIGO detection [16] of a binary black hole merger. Several groups proposed primordial black holes as an explanation of that event [13, 14, 15]. The latest O3 catalog of the LIGO/VIRGO/KAGRA collaboration consists of nearly 100 detection and it is widely accepted that a population of primordial black holes, if existing, must be subdominant and cannot constitute the whole abundance of cold dark matter. Nevertheless, even a small abundance of primordial black holes can have interesting astrophysical and cosmological implications.

As we will see, the amplitude of the primordial power spectrum needed for primordial overdensities to collapse into primordial black holes is of order 1×10^{-2} . Given that temperature fluctuations of the CMB constrain its amplitude to $A_s \sim 1 \times 10^{-9}$, this requires an amplification of about 7 orders of magnitude from CMB scales. Several single- [67, 68] and multi-field [69, 70, 71, 72] models of inflation have been proved to generate such amplification in the primordial power spectrum. Investigating imprints of such bumps on cosmological observables has therefore become an important topic in the literature independently from its original motivation to form primordial black holes.

As mentioned before, a primordial black hole forms when an overdensity δ that re-enters the Hubble radius during radiation domination exceeds some critical value δ_c and collapses. The mass of the produced primordial black hole M is proportional to the mass inside the Hubble volume at the time of formation $M_H = (4/3)\pi\rho H^{-3}$. The proportionality constant is labeled with γ and it depends on the specific model of gravitational collapse. A common value that can be found in literature is $\gamma = 0.2$, but γ can be seen as a varying phenomenological parameter. It is possible to find a relation between the comoving wavenumber k at which an overdensity creates a PBH and its mass by using the conservation of entropy. The result is [67]:

$$M(k) = \gamma M_{H(eq)} \left(\frac{g_*(T_f)}{g(T_{eq})} \right)^{1/2} \left(\frac{g_{*S}(T_f)}{g_s(T_{eq})} \right)^{-2/3} \left(\frac{k}{k_{eq}} \right)^{-2}, \quad (12.1)$$

where the subscript $_{eq}$ and $_f$ refer to the times of matter-radiation equality and primordial black hole formation. $M_{H(eq)}$ is the mass inside the Hubble volume at matter-radiation equality. The previous result can be written as

$$\frac{M(k)}{M_\odot} = 30 \left(\frac{\gamma}{0.2} \right) \left(\frac{g_*(T_f)}{10.75} \right)^{-1/6} \left(\frac{k}{2.9 \times 10^5 \text{ Mpc}^{-1}} \right)^{-2}. \quad (12.2)$$

We stress that this is the primordial black hole mass at the formation, while the observed one depends on accretion of matter into the black hole or the merging with other compact objects. Furthermore, the dependence on γ and $g_*(T_f)$ is small compared to the one on k . Thus, a good approximation is to set $\gamma = 0.2$ and $g_*(T_f) = 10.75$ so that $M(k)$ depends exclusively on k .

We now claim to provide a rough estimate for the magnitude of overdensities that can lead to primordial black holes formation. The formation of primordial black holes is a causal process. In the Press-Schechter model of gravitational collapse, the fraction $\beta(M)$ of the universe collapsing into primordial black holes of mass M is

$$\beta(M) = \int_{\delta_c}^{\infty} d\delta P(\delta, M). \quad (12.3)$$

where P is the probability that an overdensity larger than some critical value δ_c collapses. From $\beta(M)$, we compute the abundance of primordial black holes of mass M , denoted with $\Omega_{\text{PBH}}(M)$. Dividing this value by Ω_{DM} , one has

$$f_{\text{PBH}}(M) \stackrel{\text{def}}{=} \frac{\Omega_{\text{PBH}}}{\Omega_{\text{DM}}} = 2.7 \times 10^8 \left(\frac{0.2}{\gamma} \frac{M}{M_\odot} \sqrt{\frac{g_*(T_f)}{10.75}} \right)^{-1/2} \beta(M). \quad (12.4)$$

Finally, the total fraction of primordial black holes against dark matter is obtained by integrating the previous functions over all the possible mass values

$$f_{\text{PBH}}^{\text{tot}} \stackrel{\text{def}}{=} \frac{\Omega_{\text{PBH}}}{\Omega_{\text{DM}}} = \int \frac{dM}{M} f_{\text{PBH}}(M). \quad (12.5)$$

The computation of $f_{\text{PBH}}^{\text{tot}}$ is strongly model dependent. Indeed, it depends on the arbitrary threshold value δ_c , on the details of the collapsing model through γ and on the probability distribution for δ . All these phenomenological parameters reflect the fact that the details of primordial black hole formation are not known. By assuming a Gaussian probability distribution, one has that

$$\beta(M) = \frac{1}{2} \text{Erfc} \left(\frac{\delta_c}{\sqrt{2}\sigma} \right), \quad (12.6)$$

where

$$\sigma^2(M) = \int_0^\infty d \ln k W^2(kR) \frac{16}{81} (kR)^4 \mathcal{P}_{\mathcal{R}}(k) \quad (12.7)$$

is the variance of δ . W is a smoothing window function and $R = 1/k_f$ is the scale at which the primordial black hole is produced. The previous equations suggest that $\beta(M)$ is exponentially sensitive to δ_c and $\mathcal{P}_{\mathcal{R}}$. Therefore, small variations of these parameters can result to very different values of f_{PBH} . For $\delta_c = 0.45$, one has that $f_{\text{PBH}} = 1$ is achieved when the amplitude of the primordial power spectrum is around 0.01. If the distribution is non-Gaussian, the amplitude can vary significantly.

For this reason, we decide to focus only on the primordial power spectrum imprints on cosmological observables. Nevertheless, in some figures we will show the mass of the possibly produced primordial black holes, since it depends almost exclusively on the comoving wavenumber at which the primordial power spectrum exceeds the model-dependent threshold value.

13 Small-scale features in two-field models of inflation

In this section we introduce two examples of multi-field models of inflation that predict a small-scale bump in the primordial power spectrum. An in-depth discussion of these models is given in [71, 73, 72].

We choose to focus on bumps predicted by multi-field inflationary scenarios because they can be easily described in a model-independent way with semi-analytical templates. Bumps generated in single-field scenarios including an ultra-slow-roll phase are often preceded by a dip [67, 68], that is not easily captured by a semi-analytical template and that generates important effects on observables. Indeed, the comoving wavenumbers of the dip and of the peak are related by $k_{\text{dip}}/k_{\text{peak}} \approx 10^{-2}$ [74]. Hence, a peak at SDs scales would be preceded by a dip at anisotropies scales and this scenario is excluded by the recent *Planck* data. If the peak is at smaller scales, the dip affects spectral distortions, leading to a rich phenomenology discussed for example in [74, 75, 76].

13.1 Two-stage inflation

The first multi-field model is described by the following action (see e.g. [71], [77])

$$S[\phi, \chi] = \int d^4x \sqrt{-g} \left[\frac{M_{pl}^2}{2} R - \frac{1}{2} \partial_\mu \phi \partial^\mu \phi - \frac{f(\phi)}{2} \partial_\mu \chi \partial^\mu \chi - V(\phi, \chi) \right]. \quad (13.1)$$

where two fields interact through the non-canonical kinetic term $0.5f(\phi)(\partial\chi)^2$. We choose the model parameters to obtain two stages of inflation as in the double inflation scenario described in [78].

The first (second) stage is driven by the effectively heavier (lighter) field ϕ (χ). The coupling $f(\phi)$ is crucial to generate a bump in the curvature spectrum.

As in Refs. [79, 80] we define $f(\phi) = e^{2b(\phi)}$. In a smooth FLRW background, the equations of motion are

$$\ddot{\phi} + 3H\dot{\phi} + V_{,\phi} = b_{,\phi} e^{2b} \dot{\chi}^2, \quad (13.2a)$$

$$\ddot{\chi} + (3H + 2b_{,\phi} \dot{\phi}) \dot{\chi} + e^{-2b} V_{,\chi} = 0, \quad (13.2b)$$

where $_{,\phi/\chi}$ denotes a derivation with respect to ϕ/χ as usual. The Friedmann equations are

$$H^2 = \frac{1}{3M_{pl}^2} \left[\frac{\dot{\phi}^2}{2} + e^{2b} \frac{\dot{\chi}^2}{2} + V \right] \quad (13.3a)$$

$$\dot{H} = -\frac{1}{2M_{pl}^2} \left[\dot{\phi}^2 + e^{2b} \dot{\chi}^2 \right] \quad (13.3b)$$

To study the dynamics of the inflaton field, it is useful to keep track of the Hubble slow roll parameters (7.11) because they define the slow-roll regime ($\epsilon_1 \ll 1$, $\epsilon_2 \ll 1$) and the end of inflation ($\epsilon_1 = 1$) as in the single-field case. In particular, the first Hubble parameter is equal to

$$\epsilon_1 = -\frac{\dot{H}}{H^2} = \frac{1}{2M_{pl}^2} \left[\left(\frac{d\phi}{d\mathcal{N}} \right)^2 + \left(e^b \frac{d\chi}{d\mathcal{N}} \right)^2 \right] \quad (13.4)$$

Linear perturbations

Now, we briefly examine the dynamics of perturbations around the background solutions. The gauge used is the Newtonian one (8.9), with $\Phi = \Psi$ because of the absence of anisotropic stresses. A common practice is to decompose the scalar fields' perturbations, $\delta\phi$ and $\delta\chi$, along parallel and orthogonal directions to the trajectory in the field space:

$$\delta\sigma = \cos\theta \delta\phi + \sin\theta e^b \delta\chi, \quad \delta s = -\sin\theta \delta\phi + \cos\theta e^b \delta\chi, \quad (13.5)$$

with

$$\cos\theta = \frac{\dot{\phi}}{\dot{\sigma}}, \quad \sin\theta = e^b \frac{\dot{\chi}}{\dot{\sigma}}, \quad \dot{\sigma}^2 = \dot{\phi}^2 + e^{2b} \dot{\chi}^2. \quad (13.6)$$

$\delta\sigma$ and δs correspond to the instantaneous adiabatic and isocurvature perturbations. The equations describing the evolution of θ and σ are derived from the background equations

$$\ddot{\sigma} + 3H\dot{\sigma} + V_\sigma = 0, \quad \dot{\theta} = -\frac{V_s}{\dot{\sigma}} - b_{,\phi}\dot{\sigma} \sin\theta, \quad (13.7)$$

where the quantities

$$V_\sigma = -V_{,\phi} \sin\theta + e^{-b}V_{,\chi} \sin\theta, \quad V_s = -V_{,\phi} \sin\theta + e^{-b} \cos\theta \quad (13.8)$$

were defined. Other quantities that will be useful are

$$V_{\sigma\sigma} = V_{,\phi\phi} \cos^2\theta + e^{-b}V_{,\phi\chi} \sin 2\theta + e^{-2b}V_{,\chi\chi} \sin^2\theta, \quad (13.9a)$$

$$V_{ss} = V_{,\phi\phi} \sin^2\theta - e^{-b}V_{,\phi\chi} \sin 2\theta + e^{-2b}V_{,\chi\chi} \cos^2\theta, \quad (13.9b)$$

$$V_{\sigma s} = -V_{,\phi\phi} \cos\theta \sin\theta + e^{-b}V_{,\phi\chi} (\cos^2\theta - \sin^2\theta) + e^{-2b}V_{,\chi\chi} \cos\theta \sin\theta. \quad (13.9c)$$

To treat perturbations in a gauge-invariant way, we introduce the Mukhanov-Sasaki variable associated with $\delta\sigma$, $Q_\sigma = \delta\sigma + (\dot{\sigma}/H)\Phi$. δs is already gauge invariant. We set Bunch-Davies initial conditions when the modes are deep inside the Hubble-radius

$$Q_\sigma(\eta) \approx \delta s(\eta) \approx \frac{1}{a(\eta)} \frac{e^{ik\eta}}{\sqrt{2k}}. \quad (13.10)$$

It is also useful to introduce the curvature and isocurvature variables

$$\mathcal{R} = \frac{H}{\dot{\sigma}} Q_\sigma, \quad \mathcal{S} = \frac{H}{\dot{\sigma}} \delta s, \quad (13.11)$$

whose equations of motion are

$$\begin{aligned} \ddot{\mathcal{R}} + \left(H + 2\frac{\dot{z}}{z}\right) \dot{\mathcal{R}} + \frac{k^2}{a^2} \mathcal{R} = & -\frac{2V_s}{\dot{\sigma}} \dot{\mathcal{S}} - 2 \left(-e^{-b} b_{,\phi} \cos^2\theta V_{,\chi} + \sin\theta b_{,\phi} V_\sigma \right. \\ & \left. + V_{\sigma s} + \frac{\dot{\sigma}}{HM_{\text{pl}}^2} V_s \right) \mathcal{S}, \end{aligned} \quad (13.12a)$$

$$\begin{aligned} \ddot{\mathcal{S}} + \left(H + 2\frac{\dot{z}}{z}\right) \dot{\mathcal{S}} + \left\{ \frac{k^2}{a^2} - 2H^2 - \dot{H} + \frac{H\dot{z}}{z} + \frac{\ddot{z}}{z} - \dot{\theta}^2 - \dot{\sigma}^2 b_\phi^2 \cos^2\theta - \dot{\sigma}^2 b_{,\phi\phi} + V_{ss} \right. \\ \left. + b_{,\phi} [4\sin\theta V_s + (1 + \sin^2\theta)V_{,\phi}] \right\} \mathcal{S} = \frac{2V_s}{\dot{\sigma}} \dot{\mathcal{R}}, \end{aligned} \quad (13.12b)$$

where $z \stackrel{\text{def}}{=} a\dot{\sigma}/H$.

Generating a bump

Once the potential $V(\phi, \chi)$ and the kinetic term $b(\phi)$ are chosen, the background equations can be integrated numerically. As usual, it is convenient to use the number of e -foldings as a time variable. We assume that the pivot scale $k = 0.05 \text{ Mpc}^{-1}$ exits the Hubble radius

at $\mathcal{N} = 50$ before the end of inflation. Once the background quantities are known, it is possible to solve the equations for curvature and isocurvature perturbations. To compute the primordial power spectra of \mathcal{R} and \mathcal{S} , the integration for the perturbations are integrated twice [81, 79, 80]. The first set of solutions corresponds to imposing Bunch-Davies initial conditions on \mathcal{Q}_σ while the initial value of \mathcal{S} is set to zero. When the equations are integrated the second time, the initial conditions on \mathcal{R} and \mathcal{S} are switched. By denoting the two sets of solutions as $(\mathcal{R}_1, \mathcal{S}_1)$ and $(\mathcal{R}_2, \mathcal{S}_2)$, the primordial power spectrum of curvature perturbations is

$$\mathcal{P}_{\mathcal{R}}(k) = \frac{k^3}{2\pi^2} (|\mathcal{R}_1|^2 + |\mathcal{R}_2|^2) = \mathcal{P}_{\mathcal{R}_1}(k) + \mathcal{P}_{\mathcal{R}_2}(k) \quad (13.13)$$

and it is calculated at the end of inflation.

To generate a bump in the primordial power spectrum of curvature perturbations, consider the potential

$$V(\phi, \chi) = V_0 \frac{\phi^2}{\phi_0^2 + \phi^2} + \frac{m_\chi^2}{2} \chi^2 \stackrel{\text{def}}{=} U(\phi) + W(\chi). \quad (13.14)$$

and the cases

$$f_A(\phi) \equiv e^{2b_A(\phi)} \stackrel{\text{def}}{=} e^{2b_1\phi}, \quad f_B(\phi) \equiv e^{2b_B(\phi)} \stackrel{\text{def}}{=} e^{2b_2\phi^2} \quad (13.15)$$

as in [71]. The potential parameters are chosen so that the field ϕ is effectively heavier than χ . The effective mass of ϕ is defined as $m_\phi^2 = V_{,\phi\phi}|_{\phi=0} = V_0/(3M_{pl}^2)$. In particular, we choose $\phi_0 = \sqrt{6}M_{pl}$, $V_0/(m_\chi M_{pl})^2 = 500$. The numerical integration of the background equations in the case for the model f_A is presented in figure 1 of [71].

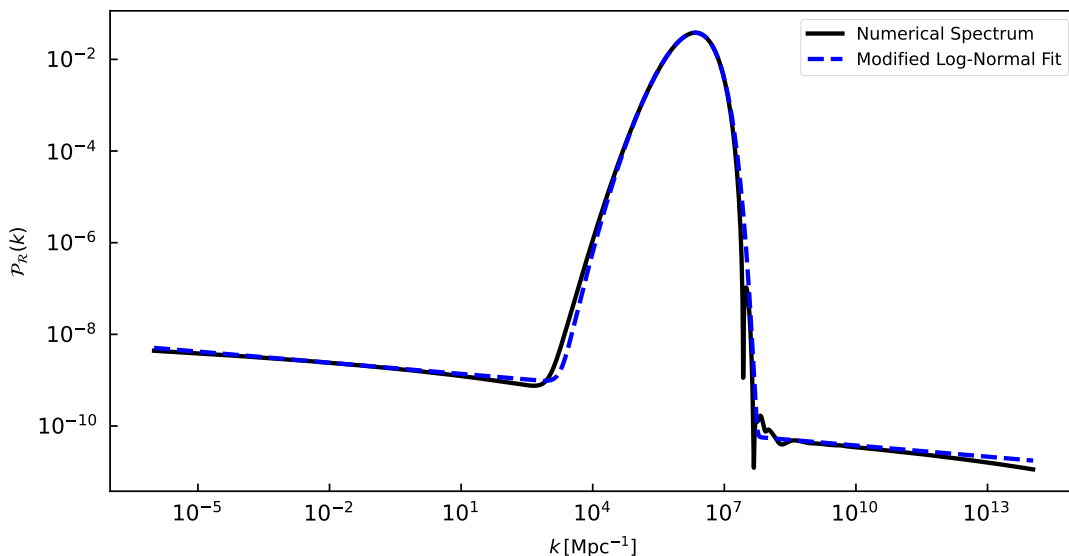


Fig. 11 – Numerical spectrum produced by the two-stage model of inflation described in 13.1. This curve corresponds to the red one of figure 2 in [71]. The blue curve is the numerical fit of the bump with the modified log-normal template given in equations (14.3)-(14.4).

The result clearly shows two stages of inflation. The first stage, lasting about 65 e -folds,

is driven by the effectively heavier field ϕ that rolls down its potential while the lighter field χ remains frozen. At the end of the first stage, ϕ undergoes a few damped oscillations around its effective minimum before settling there. In the second stage lasting $\sim 20e$ -folds, the energy density is dominated by the second field χ which slowly rolls down its potential. Between the two phases, the slow-roll parameters ϵ_1, ϵ_2 are larger than 1 indicating that slow-roll conditions are temporarily violated. The numerical result for the curvature primordial power spectrum is plotted with a black solid line in figure 11, where we can see a bump in the primordial power spectrum. This specific case is obtained by assuming $b_1 = 8.4$ and initial conditions $\phi_i = 7.0M_{pl}, \chi_i = 9.3M_{pl}$ so that the bump falls into the sensitivity range of the Square Kilometer Array (SKA) experiment. With different choices of initial conditions, the bump occurs at smaller or larger scales. In particular, the power spectrum can peak at spectral distortions scales, or at scales accessible to present and future gravitational waves interferometers such as LISA or ET, see [71].

The physical mechanism that leads to this bump is the following. Given a large enough coupling $f_1(\phi)$, the isocurvature effective mass, defined as

$$m_{\text{eff}}^2 = V_{ss} + 3\dot{\theta}^2 + b_{,\phi}^2 g(t) + b_{,\phi} f(t) - b_{,\phi\phi} \dot{\sigma}^2 - 4 \frac{V_s^2}{\dot{\sigma}^2}, \quad (13.16)$$

where the functions g and f are

$$g(t) \stackrel{\text{def}}{=} \dot{\sigma}^2 (1 + 2 \sin^2 \theta) \quad f(t) \stackrel{\text{def}}{=} V_{,\phi} (1 + \sin^2 \theta) - 4V_s \sin \theta, \quad (13.17)$$

becomes temporarily negative during the transition between the two stages of inflation. This causes a tachyonic amplification of isocurvature perturbations together with an enhancement of the coupling between curvature and isocurvature perturbations[†]. The amplification of isocurvature perturbations is transferred to the curvature ones leading to a large peak in $\mathcal{P}_{\mathcal{R}}$.

13.2 Hybrid inflation α -attractors

Hybrid inflation is a two-field inflationary scenario where the kinetic terms of the two fields are canonically normalized and the effective potential has the form [82]

$$V(\chi, \phi) = \frac{1}{4\lambda} (M^2 - \lambda\chi^2)^2 + \frac{m^2}{2} \phi^2 + \frac{g^2}{2} \phi^2 \chi^2. \quad (13.18)$$

The effective mass of χ is $V_{,\chi\chi} = -M^2 + g^2\phi^2$. Hence, when the field ϕ is larger than the critical value $\phi_c \stackrel{\text{def}}{=} M/g$, the only minimum of the effective potential with respect to the so-called hybrid field χ is at $\chi = 0$. Furthermore, at large ϕ , the curvature of the effective potential is much larger in the χ -direction with respect to the ϕ -direction. Hence, in the first stage of inflation, χ is expected to roll down towards $\chi = 0$, while the inflaton field goes

[†] Also in single-field inflation, curvature and isocurvature perturbations are coupled. See equation (8.25).

along the ϕ -direction. In this regime, the potential of the inflaton field is $V(\phi) \equiv V(\chi = 0, \phi) = \frac{m^2}{2}\phi^2 + \frac{M^2}{4\lambda} \stackrel{\text{def}}{=} \frac{m^2}{2}\phi^2 + V_{\text{uplift}}$.

When $\phi \lesssim \phi_c$, the effective squared mass at $\chi = 0$ of χ becomes negative (tachyonic), quantum fluctuations of χ begin to grow, and a transition with symmetry breaking occurs (waterfall phase). For a proper choice of parameters, this phase transition occurs rapidly and inflation ends. However, there are cases where inflation continues driven by the hybrid field. In this second inflationary stage the amplitude of perturbations can be extremely large and a peak in the primordial power spectrum can be produced.

The perturbations can be so large to induce a process of eternal inflation inside some regions of the observable Universe. To regularize such fluctuations, a linear term in χ ($\mu^3\chi$) can be added to the original potential, which is written in a slightly different, but more convenient, form:

$$V(\chi, \phi) = M^2 \left[\frac{(\chi^2 - \chi_0^2)^2}{4\chi_0^2} + \frac{\tilde{m}^2}{2}\phi^2 + \frac{\tilde{g}^2}{2}\phi^2\chi^2 + d\chi \right], \quad (13.19)$$

where $\tilde{g} = g/M$, $\tilde{m} = m/M$ and $d = \mu^3/M^2$. This linear term can control the amplitude generated during the second stage of inflation. Here we use units so that $M_{pl} = 1$.

Hybrid inflation suffers from another problem. In particular, the simplest hybrid inflation models predicting large bumps in the primordial spectrum also imply a spectral index $n_s = 1 + 2m^2/V_{\text{uplift}} > 1$, which do not match Planck data. This problem can be solved in the α -attractors version of hybrid inflation.

In the α -attractors version of hybrid inflation, the kinetic term of the field ϕ is not canonically normalized:

$$\frac{\mathcal{L}}{\sqrt{-g}} = \frac{R}{2} - \frac{1}{2} \frac{\partial_\mu \phi \partial^\mu \phi}{\left(1 - \frac{\phi^2}{6\alpha}\right)^2} - \frac{1}{2} \partial_\mu \chi \partial^\mu \chi - V(\chi, \phi). \quad (13.20)$$

By properly setting α , it is possible to have a red tilt index $n_s < 1$.

To produce a bump feature in the primordial power spectrum, we choose $M \sim m \sim \mu \sim g \sim d \sim 10^{-5}$. It is possible to perform a transformation $\phi \rightarrow \varphi$, where φ is a canonically normalized field. Upon this transformation, the potential becomes

$$V(\chi, \varphi) = M^2 \left[\frac{(\chi^2 - \chi_0^2)^2}{4\chi_0^2} + 3\alpha(\tilde{m}^2 + \tilde{g}^2\chi^2) \tanh^2 \frac{\varphi}{\sqrt{6\alpha}} + d\chi \right]. \quad (13.21)$$

This potential evaluated at $\chi = 0$ provides the simplest example of α -attractor model described briefly also in 8.4, plus an uplift term $M^2\chi_0^2/4$.

Given a Lagrangian with two canonically normalized fields φ and χ and the potential (13.21), the procedure to compute the power spectrum of curvature and isocurvature perturbations is the same described in the previous subsection.

The mechanism to produce the large peak in the primordial power spectrum is the fol-

lowing. The effective square mass of χ at $\chi = 0$ is

$$M_\chi^2 = V_{,\chi\chi}(\chi = 0) = M^2 \left(-1 + 6\alpha\tilde{g}^2 \tanh^2 \frac{\varphi}{\sqrt{6\alpha}} \right). \quad (13.22)$$

We consider the case where $6\alpha\tilde{g}^2 > 1$, so that $M_\chi^2 > 0$ for $\varphi > \varphi_c$, where the critical value of the canonical field φ is defined by

$$\tanh^2 \frac{\varphi_c}{\sqrt{6\alpha}} = \frac{1}{6\alpha\tilde{g}^2}. \quad (13.23)$$

For $\varphi < \varphi_c$ the effective mass of the hybrid field becomes negative, causing a tachyonic instability. For $\chi_0 \gg 1$ the tachyonic instability is very fast to develop and this leads to the end of inflation when $\varphi \approx \varphi_c$. To produce a bump in the primordial power spectrum, the opposite regime $\chi_0 \gtrsim 2\sqrt{3}$ should be considered. In this situation, the tachyonic instability is very slow to develop and the isocurvature perturbations start to grow exponentially. Furthermore, the coupling between isocurvature and curvature perturbations increases so that the exponentially growing of isocurvature perturbations is transmitted to the curvature ones. The result is a large peak in the primordial power spectrum of curvature perturbations. Given the parameters

$$M = 9.48 \times 10^{-6}, \quad \alpha = 1, \quad \tilde{g} = 1, \quad \tilde{m} = 1, \quad \chi_0 = 2.58, \quad d = -1 \times 10^{-5} \quad (13.24)$$

as in Ref. [72], the numerical result for $\mathcal{P}_\mathcal{R}$ is presented in figure 12.

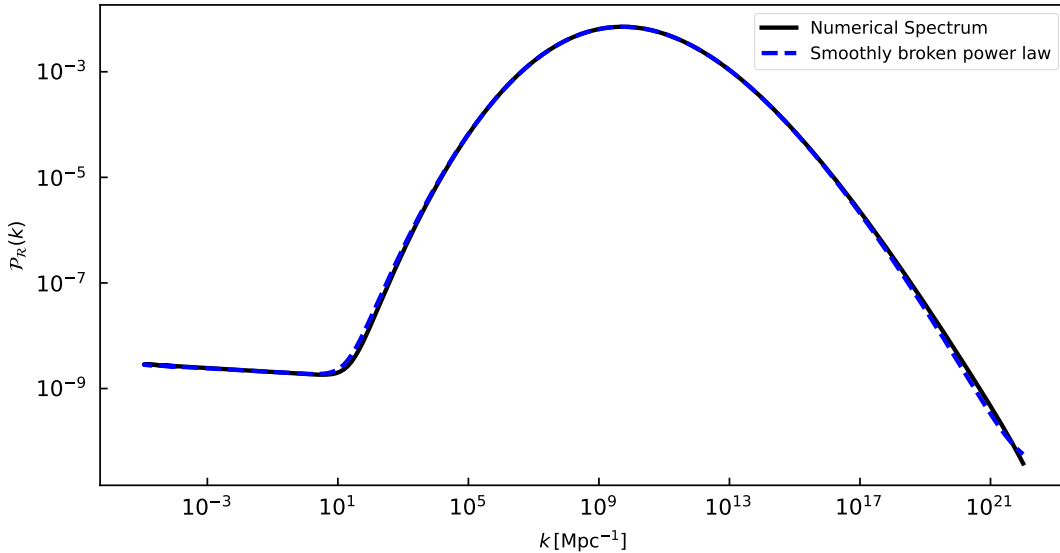


Fig. 12 – Numerical spectrum produced by the hybrid α -attractor model of inflation described in [72]. The black curve corresponds to the spectrum given in figure 5 in [72]. The blue curve is the numerical fit of the bump with the smoothly broken power law template given in equation (14.10).

14 Phenomenological templates

In this section we present two semi-analytical templates able to mimic the shape of the primordial power spectra introduced in the previous section. Then, we present also an analytical formula for a primordial spectrum with oscillatory features. The use of phenomenological templates allows investigating the effects of small-scale bumps in a model-independent way without focusing on a specific inflationary scenario.

The templates are formally decomposed as

$$\mathcal{P}_{\mathcal{R}}(k) = \mathcal{P}_{\mathcal{R}}^0(k) + \mathcal{P}_{\mathcal{R}}^{\text{bump}}(k) \quad (14.1)$$

where $\mathcal{P}_{\mathcal{R}}^0(k)$ represents the near scale invariant background contribution measured by Planck $\mathcal{P}_{\mathcal{R}}(k) = A_s (k/k_*)^{n_s-1}$, while $\mathcal{P}_{\mathcal{R}}^{\text{bump}}(k)$ describes the bump. However, this simple choice is not able to correctly reproduce the behavior of the full power spectrum at very small scales. Indeed, inflationary models could predict a different amplitude and tilt after the bump. An example is given in figure 11. To capture this behavior, it is necessary to modify the background assumption into

$$\mathcal{P}_{\mathcal{R}}^0(k) = A_{\mathcal{R}} \left(\frac{k}{k_*} \right)^{n_s-1} \left[1 - \epsilon \arctan \left(\frac{k}{k_{\text{loc}}} \right) \right] \quad (14.2)$$

where ϵ is the parameter that measures the change of slope before and after the peak and k_{loc} is the comoving wavenumber at which the feature is centered. Therefore, all the phenomenological templates can be written as

$$\mathcal{P}_{\mathcal{R}}(k) = A_{\mathcal{R}} \left(\frac{k}{k_*} \right)^{n_s-1} \left[1 - \epsilon \arctan \left(\frac{k}{k_{\text{loc}}} \right) \right] + \mathcal{P}_{\mathcal{R}}^{\text{bump}}(k) \quad (14.3)$$

14.1 Modified log-normal bump

The power spectrum presented in figure 11 can be captured by a lognormal distribution with an ultraviolet cutoff α :

$$\mathcal{P}_{\mathcal{R}}^{\text{bump}}(k) = A \cdot \exp \left\{ \beta \left[1 - \frac{k}{k_{\text{loc}}} + \ln^2 \left(\frac{k}{k_{\text{loc}}} \right) \right] - \alpha \ln^2 \left(\frac{k}{k_{\text{loc}}} \right) \right\}. \quad (14.4)$$

A is the amplitude of the bump, while α and β describe its width. The blue curve in figure 11 represents the fit of the numerical spectrum with the template (14.3)-(14.4). This template depends on a few parameters ($A_s, n_s, A, k_{\text{loc}}, \alpha, \beta$).

The fit parameters are

$$\ln \left(10^{10} A_s \right) = 3.044, \quad n_s = 0.918, \quad \epsilon = 0.85 \quad (14.5a)$$

$$\log_{10} A = -1.418, \quad \log_{10} k_{\text{loc}} = 6.341 \quad (14.5b)$$

$$\log_{10} \alpha = -0.601, \quad \log_{10} \beta = -0.070 \quad (14.5c)$$

The value of the scalar tilt n_s does not match Planck measure, but it is chosen only to fit the numerical spectrum also at large scales. Indeed, multi-field inflationary scenarios often predict a slightly redder spectral index than those measured by Planck [72] unless the bump is at sufficiently small scales. However, with fine tuning of the model parameters, it is possible to predict a power spectrum with both the correct value of n_s and a large peak at smaller scales. Therefore, in studying the effects of these templates on cosmological observables we set the latest value of n_s provided by Planck data (8.110) since we are only interested in the phenomenological effects of the bump.

Notice that the small oscillation at the end of the bump is not captured by these simple templates. However, the considered observable are mainly affected by the amplitude and the width of the peak.

14.2 Smoothly broken power law bump

The second analytical template considered is a smoothly broken power law:

$$\mathcal{P}_{\mathcal{R}}^{\text{bump}}(k) = a \left(\frac{k}{k_b} \right)^{-\alpha_1} \left\{ \frac{1}{2} \left[1 + \left(\frac{k}{k_b} \right)^{1/\Delta} \right] \right\}^{(\alpha_1 - \alpha_2)\Delta}. \quad (14.6)$$

k_b represents the comoving wavenumber at which we have a transition from the first to the second power law. a is the model amplitude at the breaking point. α_1 represents the spectral index for $k \ll k_b$, while α_2 is the spectral index for $k \gg k_b$. Δ is the parameter that smooths the transition at k_b . Indeed, the change of slopes occurs between two comoving wavenumbers k_1 and k_2 so that

$$\log_{10} \frac{k_2}{k_b} = \log_{10} \frac{k_b}{k_1} \approx \Delta. \quad (14.7)$$

For $k \lesssim k_1$ ($k \gtrsim k_2$) the template has spectral index α_1 (α_2). To describe a bump, it is necessary to have $\alpha < 0$. Then, we redefine the power law tilts as

$$n_1 \stackrel{\text{def}}{=} -\alpha_1, \quad n_2 = \alpha_2. \quad (14.8)$$

The log-normal template is particularly convenient since in that case A represents the value of the maximum and k_{loc} its location. In the case of the smoothly broken power law, the transition point k_b is not the wavenumber at which the maximum is located and a is not the maximum value of the function. To avoid these issues, we introduced two parameters k_{loc} , A in the following way:

$$k_b = k_{\text{loc}} \left(\frac{n_1}{n_2} \right)^{-\Delta}, \quad a = \frac{A}{\left(\frac{n_1}{n_2} \right)^{n_1 \Delta} \left[\frac{1}{2} \left(1 + \frac{n_1}{n_2} \right) \right]^{-(n_1 + n_2)\Delta}}. \quad (14.9)$$

In the new parametrization, the smoothly broken power law looks like

$$\mathcal{P}_{\mathcal{R}}^{\text{bump}}(k) = \frac{A}{\left[\frac{1}{2} \left(1 + \frac{n_1}{n_2}\right)\right]^{-(n_1+n_2)\Delta}} \left(\frac{k}{k_{\text{loc}}}\right)^{n_1} \left\{ \frac{1}{2} \left[1 + \frac{n_1}{n_2} \left(\frac{k}{k_{\text{loc}}}\right)^{1/\Delta} \right] \right\}^{-(n_1+n_2)\Delta}. \quad (14.10)$$

The new parametrization is motivated by the fact that in the original form the maximum is located at $k_b(n_1/n_2)^\Delta$ and has value $a \left(\frac{n_1}{n_2}\right)^{n_1\Delta} \left[\frac{1}{2} \left(1 + \frac{n_1}{n_2}\right)\right]^{-(n_1+n_2)\Delta}$. The new parametrization shifts the maximum at k_{loc} with value A . At the end, this template depends only the parameters $(A_s, n_s, A, k_{\text{loc}}, n_1, n_2, \Delta)$.

The parameters that fit the numerical spectrum given in figure 12 are:

$$\ln(10^{10} A_s) = 3.044, \quad n_s = 0.965, \quad \epsilon = 0.90 \quad (14.11a)$$

$$\log_{10} A = -2.145, \quad \log_{10} k_{\text{loc}} = 9.719 \quad (14.11b)$$

$$\log_{10} n_1 = 0.460, \quad \log_{10} n_2 = 0.098, \quad \log_{10} \Delta = 1.081 \quad (14.11c)$$

14.3 Oscillating bump

Another interesting case where the primordial power spectrum is described by a rather simple analytic expression that depends only on few parameters can be found in [83, 73], where a power spectrum with an oscillatory bump is studied. The oscillatory bump is presented in figure 13. In this case, the template is parametrized as

$$\mathcal{P}_{\mathcal{R}}(k) = \mathcal{P}_{\mathcal{R}}^0(k) \cdot \mathcal{P}_{\mathcal{R}}^{\text{bump}}(k), \quad (14.12)$$

where $\mathcal{P}_{\mathcal{R}}^{\text{bump}}$ must tend to 1 at large scales to be consistent with Planck data.

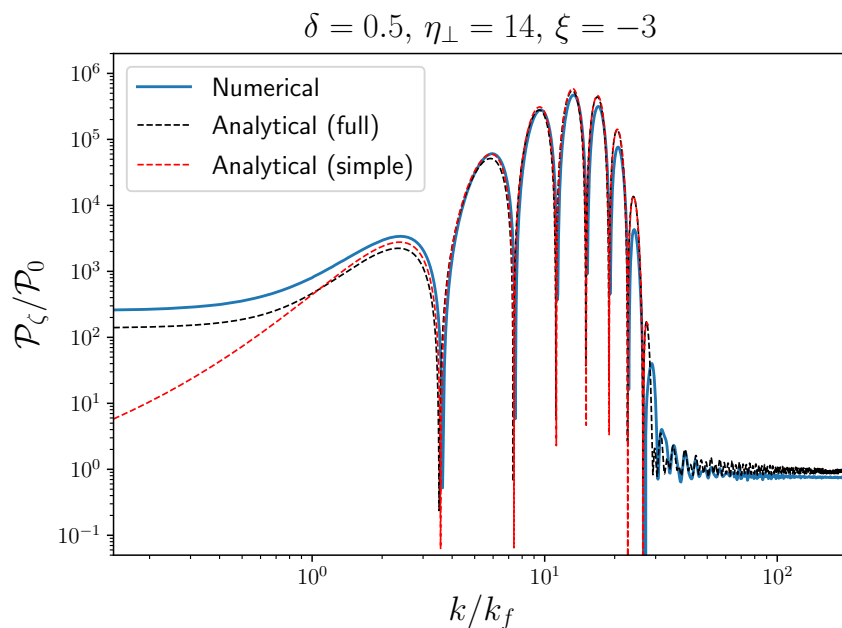


Fig. 13 – Example of power spectrum with an oscillatory bump. Figure taken from [83].

The bump factor depends on three parameters: the location at which oscillations start k_{loc} and two parameters governing the number and the amplitude of the oscillations δN , λ_0 . Generically, this factor can be written as

$$\mathcal{P}_{\mathcal{R}}^{\text{bump}}(k) = \frac{\Delta(k, k_{\text{loc}}, \delta N, \lambda_0)}{\Delta(k_{\text{loc}} \cdot 10^{-9}, k_{\text{loc}}, \delta N, \lambda_0)} \quad (14.13)$$

where the denominator is a normalization constant chosen so that $\mathcal{P}_{\mathcal{R}}^{\text{bump}}(k \ll 1 \text{ Mpc}^{-1}) \approx 1$. The function Δ is defined as

$$\Delta(k, k_{\text{loc}}, \delta N, \lambda_0) = \frac{k^3}{2\pi^3} (|a_\zeta|^2 + |a_\psi|^2) \quad (14.14)$$

The dependence of k_{loc} , δN and λ_0 is hidden inside the coefficients a_ζ and a_ψ , that are equal to

$$a_\zeta = \frac{ie^{2i\frac{k}{k_{\text{loc}}}\sinh\frac{\delta N}{2}}}{2\sqrt{2k^3}} \left[\cos\left(\frac{\omega_+\delta N}{k_{\text{loc}}}\right) - i\frac{k_{\text{loc}}^2 + k^2 + \omega_+^2}{2k\omega_+} \sin\left(\frac{\omega_+\delta N}{k_{\text{loc}}}\right) + \right. \\ \left. - i\frac{e^{2i\frac{k}{k_{\text{loc}}}e^{-\frac{\delta N}{2}}}(k + ik_{\text{loc}})^2 - \omega_+^2}{k\omega_+} \sin\left(\frac{\omega_+\delta N}{k_{\text{loc}}}\right) \right] + \text{same but with } \omega_+ \leftrightarrow \omega_- \quad (14.15)$$

$$a_\psi = \frac{e^{2i\frac{k}{k_{\text{loc}}}\sinh\frac{\delta N}{2}}}{4\sqrt{2k^3}} \left\{ \left(2 + \frac{k_{\text{loc}}^2}{k^2} \right) \cos\left(\frac{\omega_+\delta N}{k_{\text{loc}}}\right) - \frac{k^2(ik + k_{\text{loc}}) - \omega_+^2(-ik + k_{\text{loc}})}{\omega_+k^2} \sin\left(\frac{\omega_+\delta N}{k_{\text{loc}}}\right) + \right. \\ \left. - e^{2ie^{-\frac{\delta N}{2}}\frac{k}{k_{\text{loc}}}} \cdot \left[k_{\text{loc}} \frac{-2ik + k_{\text{loc}}}{k^2} \cos\left(\frac{\omega_+\delta N}{k_{\text{loc}}}\right) + \frac{(-ik + k_{\text{loc}})(\omega_+^2 - k^2)}{\omega_+k^2} \right] \sin\left(\frac{\omega_+\delta N}{k_{\text{loc}}}\right) \right\} + \\ - \text{same but with } \omega_+ \leftrightarrow \omega_- \quad (14.16)$$

where

$$\omega_\pm \stackrel{\text{def}}{=} \sqrt{k^2 \pm kk_{\text{loc}}\lambda_0} \quad (14.17)$$

For a complete derivation of such power spectrum refer to [83, 84]. Even if the spectrum is described by a rather complicated expression, it depends only on a few parameters: $(A_s, n_s, k_{\text{loc}}, \delta N, \lambda_0)$. This template is particularly interesting since it allows to look at imprints of large oscillations in the power spectrum on cosmological observables.

15 Impact on observables

In this section we show the effects of a large bump at small scales in the primordial power spectrum on CMB anisotropies, spectral distortions and scalar-induced gravitational waves. Effects on the first two observables are computed with a modified version of CLASS, where we implemented the three analytical templates described in the previous section. CLASS computes CMB anisotropies with the line-of-sight integration, while CMB SDs are computed with the Green's functions technique, described in section 5. We show only the contribution

to SDs due to Silk damping, which can be computed by inserting the corresponding effective heating rate (10.21) into the generic expression for the amplitudes (5.31), where the branching ratios are computed assuming a specific detector [†]. As a reference detector, we choose FIRAS. This methodology to compute spectral distortions is slightly more accurate than the approximated formula that uses the window function (10.23). To compute scalar-induced gravitational wave power we solved numerically the double integral (11.43).

A similar work where multi-messenger effects of large bumps in the primordial power spectrum are studied can be found in [85]. However, in [85], the authors use the approximated formula with the Window function for μ -distortions and they do not take into account y -type distortions. We choose to take into account y -distortions, even if the late time contribution $y_{SZ} \sim 2 \times 10^{-6}$ is larger than the typical early time contribution because future spectrometers like PIXIE will in principle be able to distinguish between the two different contributions. The most important difference between this work and [85] is that we do not discuss primordial black holes formation, which is very model-dependent. For this reason we do not take into account other effects related to primordial black holes, such as SDs due to evaporation and accretion of matter into primordial black holes. In order to do that we choose to fix the maximum amplitude allowed for our peak to 1×10^{-3} , which is a conservative threshold value for the formation of primordial black holes [72]. Furthermore, in the next section we present for the first time an MCMC forecast analysis to show the prospects of constraining the primordial power spectrum with SDs.

This section is divided into three subsections, one for each template. In each subsection, we present the chosen baseline parameters for the primordial power spectrum. We then vary one parameter, while keeping fixed the others, and we plot the corresponding effects on observables. Each figure contains 5 plots. In all plots there are at least three curves. One corresponds to the baseline parameters, while each of the other two refers to a different value of the considered parameter. In the first plot on the top left we show the primordial power spectrum as a function of the comoving wavenumber. The TT and TE CMB angular spectra are shown in the top center and top right plots, respectively. In particular, we choose to plot the difference between the computed angular spectra with those computed by using the Planck baseline parameters [18]. The grey scatter points present in this plot represent the difference between the angular power spectra computed with Planck baseline parameters and the real data of Planck. The corresponding error bars are the uncertainties of the real data. We do not plot the coefficients C_ℓ , but a related quantity:

$$D_\ell^{XX} = T_{\text{CMB}}^2 C_\ell^{XX} \ell(\ell + 1)/2\pi, \quad X = T, E \quad (15.1)$$

In the bottom left panel, SDs are plotted. The solid lines refer to the μ -distortion contribution, while the dashed ones represent the y -type distortions. We also plot the sensitivity of FIRAS and of future spectrometers such as PIXIE [8] and PRISTINE. To get an insight

[†] In CLASS it is also possible to use the approximated analytical expressions (5.39) for the branching ratios.

on how much the primordial power spectrum affects μ - or y -type distortions, we plot the supports of the μ and y window functions (10.23). We also plot the total astrophysical foregrounds for CMB radiance intensity. Finally, the power of scalar-induced gravitational waves is shown in the bottom center panel. In that plot, we also show the sensitivities area of future experiments able to probe the stochastic gravitational waves background, e.g SKA [20], LISA [21] and Big Bang Observer (BBO) [86]. We also plot a small black star representing the recent claim of a detection from the NANOgrav collaboration [87]. However, since there is no evidence yet that the signal is a sign of the stochastic gravitational waves background, we interpret this point as an upper bound. In the plot, the galactic and extra-galactic foregrounds of gravitational waves are plotted. These foregrounds are computed according to [88]. We summarize the information in a legend and write the parameters generating the curves in the figure caption.

15.1 Modified log-normal template

The baseline parameters for the modified log-normal template are

$$\ln(10^{10} A_s) = 3.0448, \quad n_s = 0.96605, \quad \epsilon = 0, \quad (15.2a)$$

$$\log_{10} A = -3, \quad \log_{10} k_{\text{loc}} = 6.5, \quad (15.2b)$$

$$\log_{10} \alpha = -0.9, \quad \log_{10} \beta = -0.07. \quad (15.2c)$$

Since we are interested in the effects of the bump, we set $\epsilon = 0$ for simplicity. Indeed, the different slope of the primordial power spectrum after the bump does not affect the observables we studied. Furthermore, we choose the values of A_s , n_s according to Planck best fit ones, even if the fit parameters of theoretical models presented before are different (14.5). This choice is motivated by the fact that at large scales the primordial power spectrum has to be consistent with Planck data and because the parameters of the theoretical model can be fine-tuned in order to reproduce the correct behavior. Hence, CMB anisotropies are used to constrain only the location and the width of the bump and not the parameters of the background scale invariant spectrum.

Varying A

To show the effect of the amplitude A we generated three different spectra where the amplitude takes the values

$$\log_{10} A_1 = -3, \quad \log_{10} A_2 = -4, \quad \log_{10} A_3 = -5, \quad (15.3)$$

while the other parameters are set equal to the baseline ones (15.2b) in all three cases.

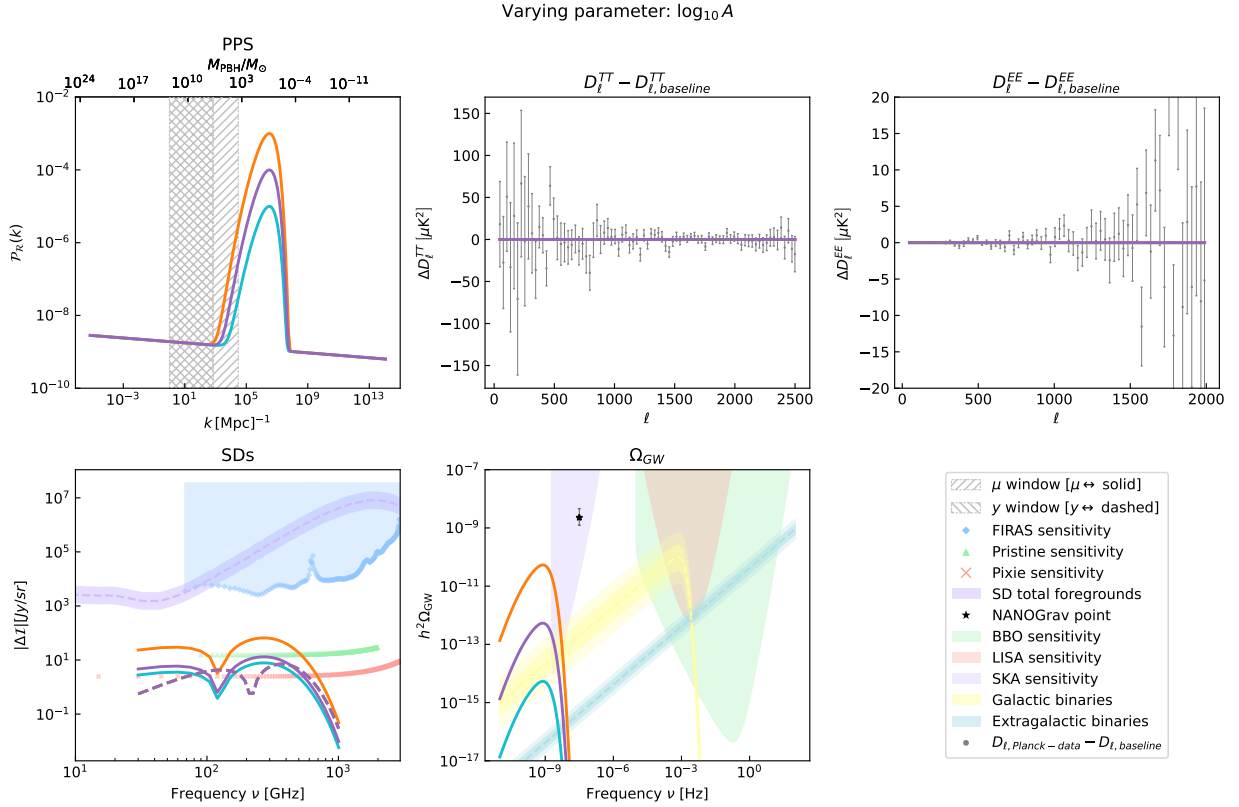


Fig. 14 – Impact of the amplitude A of the modified log-normal template on observables. The orange, purple and cyan curves correspond to the cases $A = A_1, A_2, A_3$, respectively.

The effects on the different observables are shown in figure 14. In all cases, there are no effects on CMB anisotropies. The kink at the beginning of the bump is placed in the middle of the μ -window function. Spectral distortions are tiny because the power spectrum is not large within the windows functions. Nevertheless, a PIXIE-like experiment could be able to detect such signal. For the case $A = A_1$ a future detection of gravitational waves by SKA is possible.

Varying k_{loc}

The location of the bump k_{loc} varies as

$$\log_{10} k_{\text{loc},1} = 4.5, \quad \log_{10} k_{\text{loc},2} = 6.5, \quad \log_{10} k_{\text{loc},3} = 8.5, \quad (15.4)$$

while the other parameters are again set equal to the baseline ones (15.2b). The case with $k_{\text{loc}} = k_{\text{loc},2}$ corresponds to the baseline spectrum. The effects on the different observables are shown in figure 15

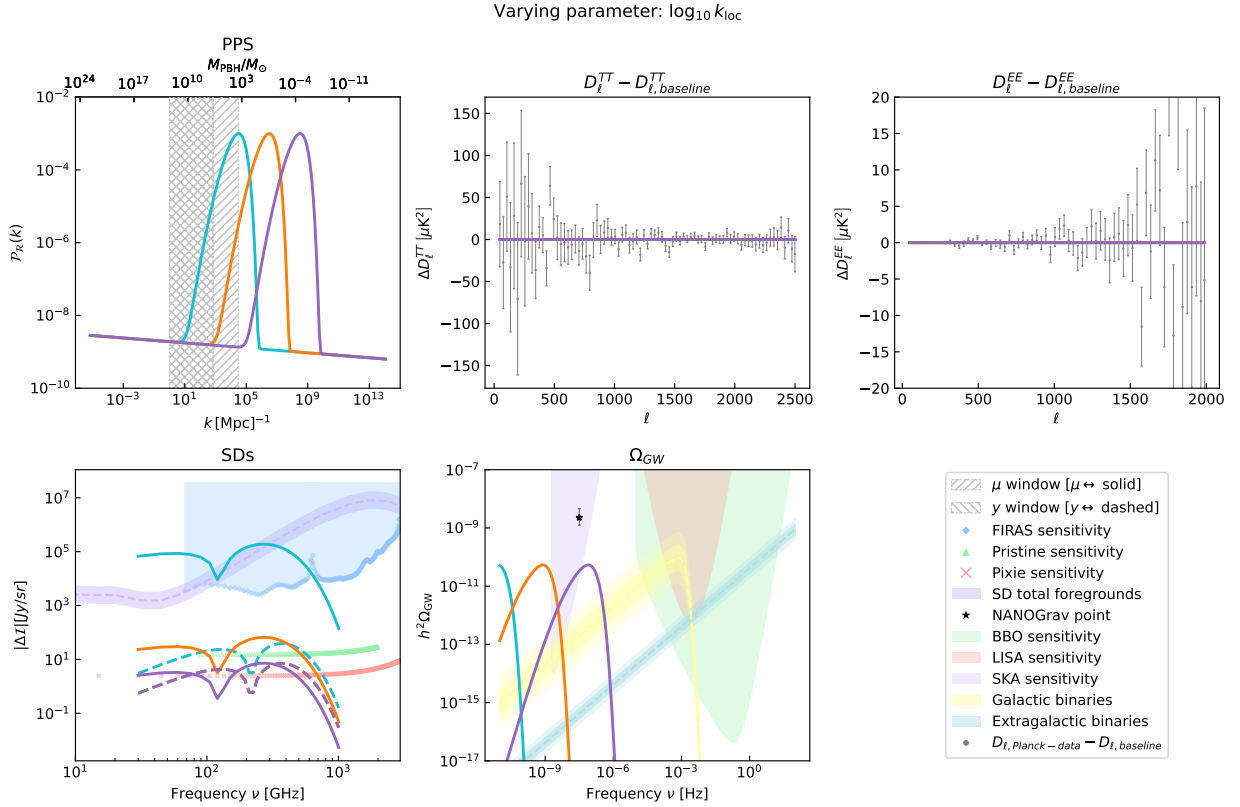


Fig. 15 – Impact of the peak location k_{loc} of the modified log-normal template on observables. The cyan, orange and purple curves correspond to the cases $\log_{10} k_{\text{loc}} = 4.5, 6.5, 8.5$, respectively.

Clearly, as the peak moves at smaller scales the effects on gravitational waves move at higher frequencies. In particular, a spectrum like the purple curve in figure 15 is expected to give a contribution to the stochastic gravitational waves background that could be detected by SKA. Notice also that the cyan spectrum has large enough values in the μ -window function to be already excluded by FIRAS data.

Varying α

In the modified log-normal templates, the width of the bump is controlled by α and β . To show their effects on the width, it is necessary to keep fixed one of them and to vary the other one. In figure 16, we show effects on observables when α takes the values

$$\log_{10} \alpha_1 = -2.9, \quad \log_{10} \alpha_2 = -0.9, \quad \log_{10} \alpha_3 = 1.1, \quad (15.5)$$

while β and the other parameters are fixed.

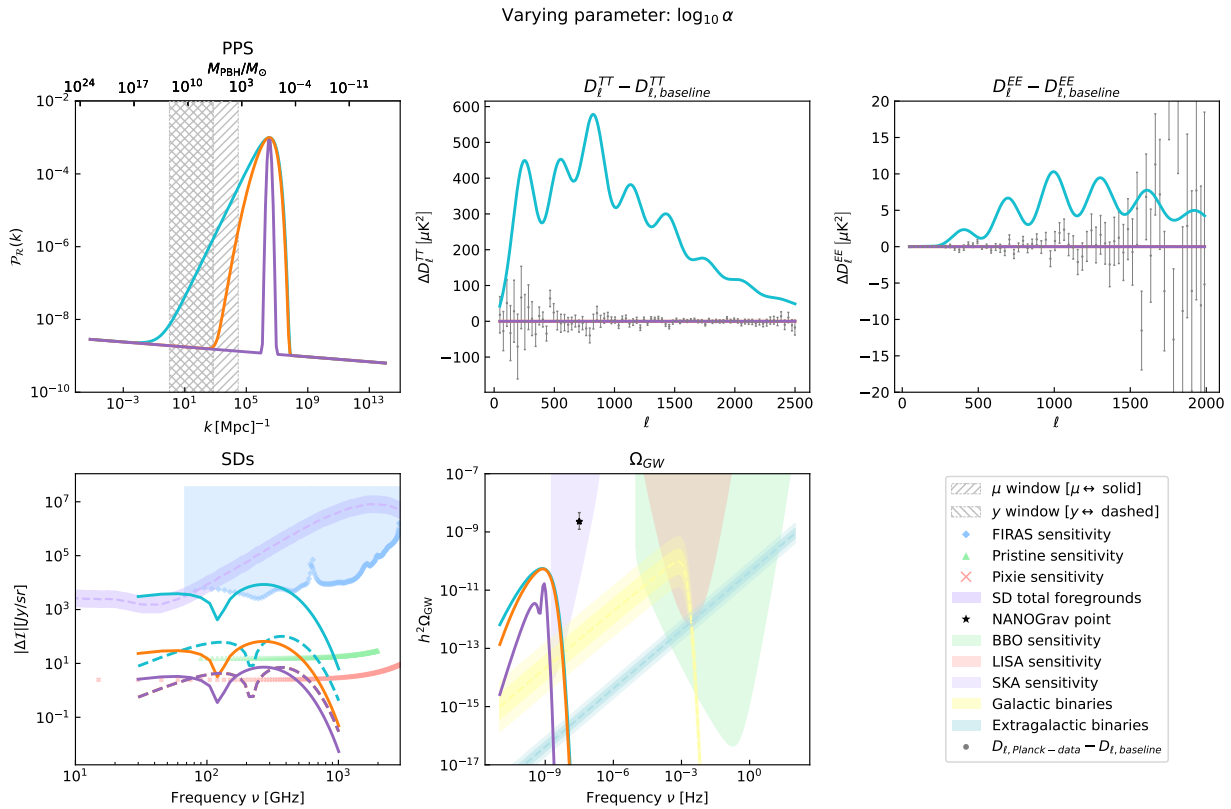


Fig. 16 – Impact of α (modified log-normal template) on observables. The cyan, orange and purple curves correspond to the cases $\log_{10} \alpha = -2.9, -0.9, 1.1$, respectively.

Again, the orange curve corresponds to the baseline spectrum. α mainly affects the slope of the rising part of the peak. In particular, for small α the peak is wide and the kink is shifted at large scales. In the figure, the cyan curve corresponds to the case $\log_{10} \alpha = -2.9$ and it is a case excluded by Planck (of course, given the particular combination with the other baseline parameters). A wider peak could enter more consistently in the μ window function and hence could leave an imprint on CMB SDs. For example, the cyan curve is a case excluded also by FIRAS data. Given the baseline location of the bump, no evident effects on gravitational waves are seen in this case. This is because the shape of the bump at small scales is almost the same in the three cases. However, the purple curve, which corresponds to a narrow peak, leads to a particular shape of Ω_{GW} . If the peak would have been located at a wavenumber larger by one order of magnitude than the baseline case, there could have been a unique imprint on gravitational wave power.

Varying β

When α is fixed and β varies, the effect on the bump width is completely different. Indeed, one could expect only the slope of the right part of the peak to change. However, figure 17 shows that β affects the overall width of the bump. The three curves in the figures

correspond to the values:

$$\log_{10} \beta_1 = -2.07, \quad \log_{10} \beta_2 = -0.07, \quad \log_{10} \beta_3 = 1.93. \quad (15.6)$$

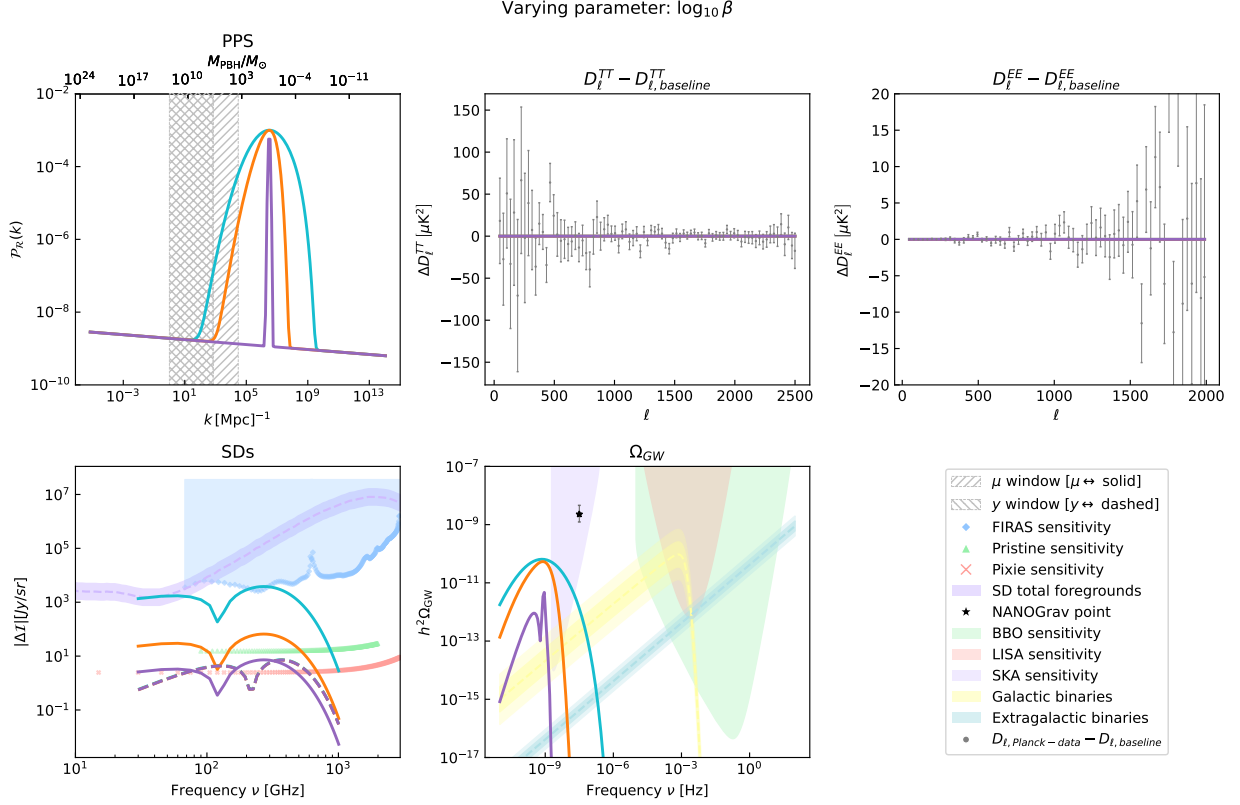


Fig. 17 – Impact of β (modified log-normal template) on observables. The cyan, orange and purple curves correspond to the cases $\log_{10} \beta = -2.07, -0.07, 1.93$, respectively.

The smaller β is, the wider the bump. The discussion on the effects is analogous to the previous case.

15.2 Smoothly broken power law template

The baseline parameters for the bumps described by the smoothly broken power law are

$$\ln(10^{10} A_s) = 3.0448, \quad n_s = 0.96605, \quad \epsilon = 0, \quad (15.7a)$$

$$\log_{10} A = -3, \quad \log_{10} k_{\text{loc}} = 9, \quad (15.7b)$$

$$\log_{10} n_1 = 0.75, \quad \log_{10} n_2 = 0.10, \quad \log_{10} \Delta = 0.85. \quad (15.7c)$$

The motivation for the background parameters is the same given for the previous template.

Varying A

The amplitude is varied as in the previous case (15.3) and the result is given in figure 18

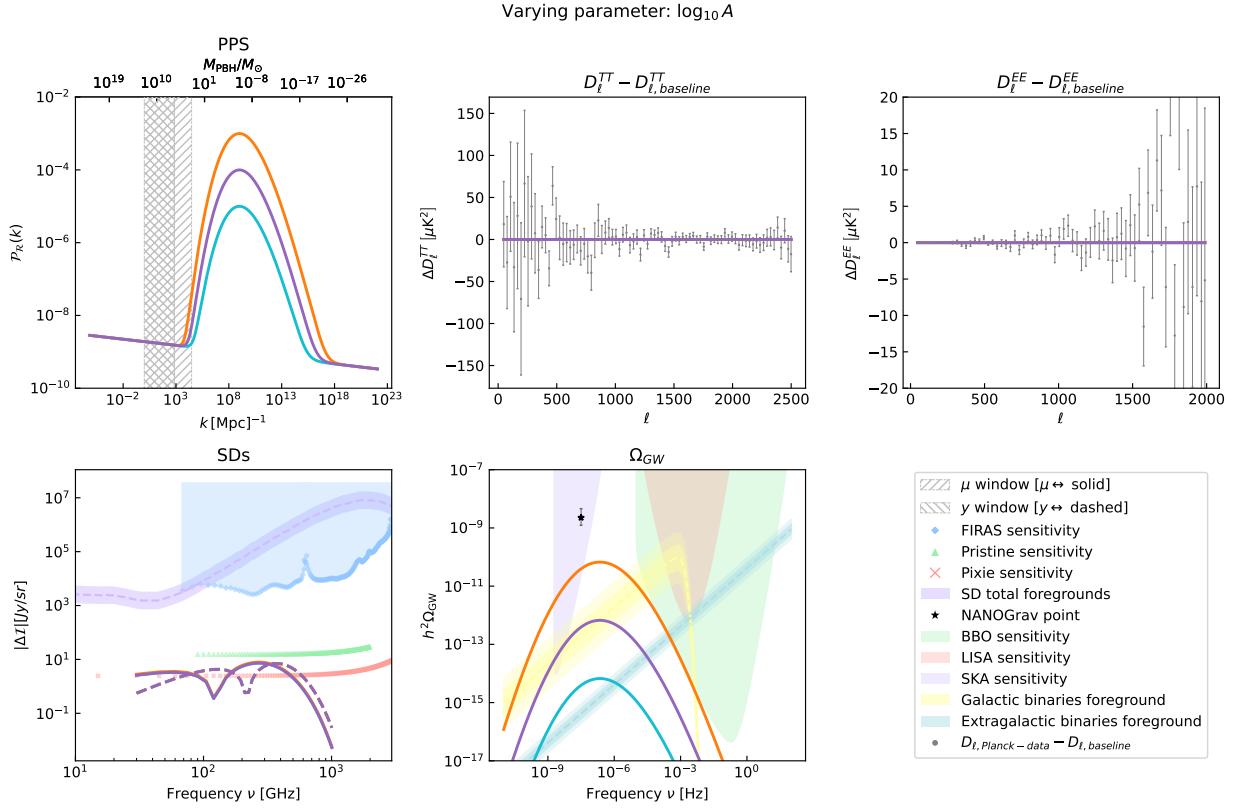


Fig. 18 – Impact of the amplitude A of the smoothly broken power law template on observables. The orange, purple and cyan curves correspond to the cases $\log_{10} A = -3, -4, -5$, respectively.

Since the baseline location of the peak is at smaller scales than in the previous case, a larger effect on gravitational waves is produced. In particular, for $\log_{10} A = -3$ a signal in the range of sensitivity of BBO is generated.

Varying k_{loc}

As in the modified log-normal case, we vary the location of the peak of two orders of magnitudes with respect to the baseline value:

$$\log_{10} k_{\text{loc},1} = 7, \quad \log_{10} k_{\text{loc},2} = 9, \quad \log_{10} k_{\text{loc},3} = 11. \quad (15.8a)$$

One expects that in the case of $\log_{10} k_{\text{loc}} = 7$ the effect on Ω_{GW} could be detected only by SKA, while for $\log_{10} k_{\text{loc}} = 11$ the signal lies in the LISA window. The results are given in figure 19

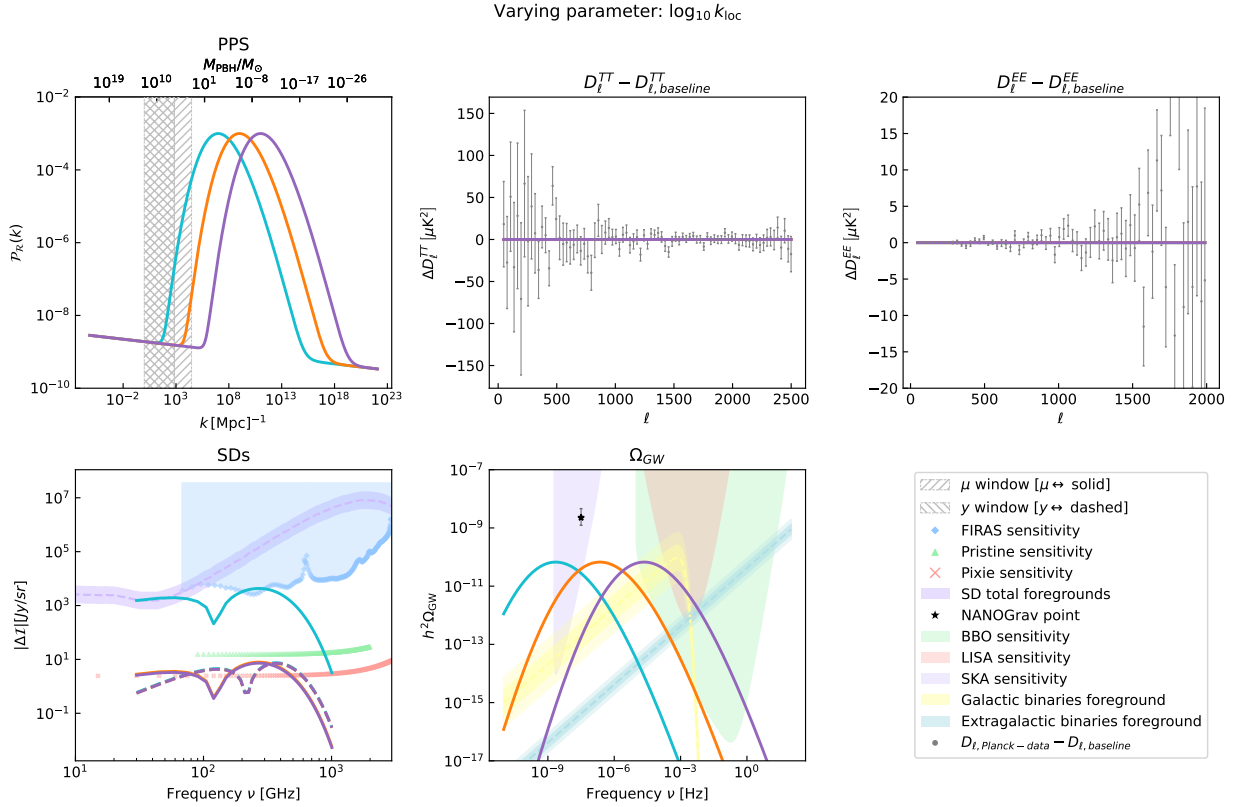


Fig. 19 – Impact of the peak location k_{loc} of the smoothly broken power law template on observables. The cyan, orange and purple curves correspond to the cases $k_{\text{loc}} = 7, 9, 11$, respectively.

Only for $\log_{10} k_{\text{loc}} = 7$ there is an interesting imprint on SDs. In the other two cases, the generated spectral distortions are the same as in the Λ CDM case.

Varying n_1 or n_2

In the original formulation of the smoothly broken power law template (14.6), the parameter α_1 represents the slope of the rising part of the bump. In our parametrization, n_1 controls mainly the slope of the left curve of the bump, as α_1 does, but it has also a slightly effect on the slope of the descending power law. Figure 20 shows this behavior. The plotted values of n_1 are $\log_{10} n_1 = 1.25, 0.75, 0.25$.

Similarly, the quantity n_2 mainly affects the slope of the power law after the peak but it has also a small effect on the slope of the power law before the bump. In figure 21 we show the impact on observables when n_2 takes the value

$$\log_{10} n_{2,1} = -0.15, \quad \log_{10} n_{2,2} = 0.10, \quad \log_{10} n_{2,3} = 1.10, \quad (15.9)$$

while other parameters are fixed to the baseline values (15.7).

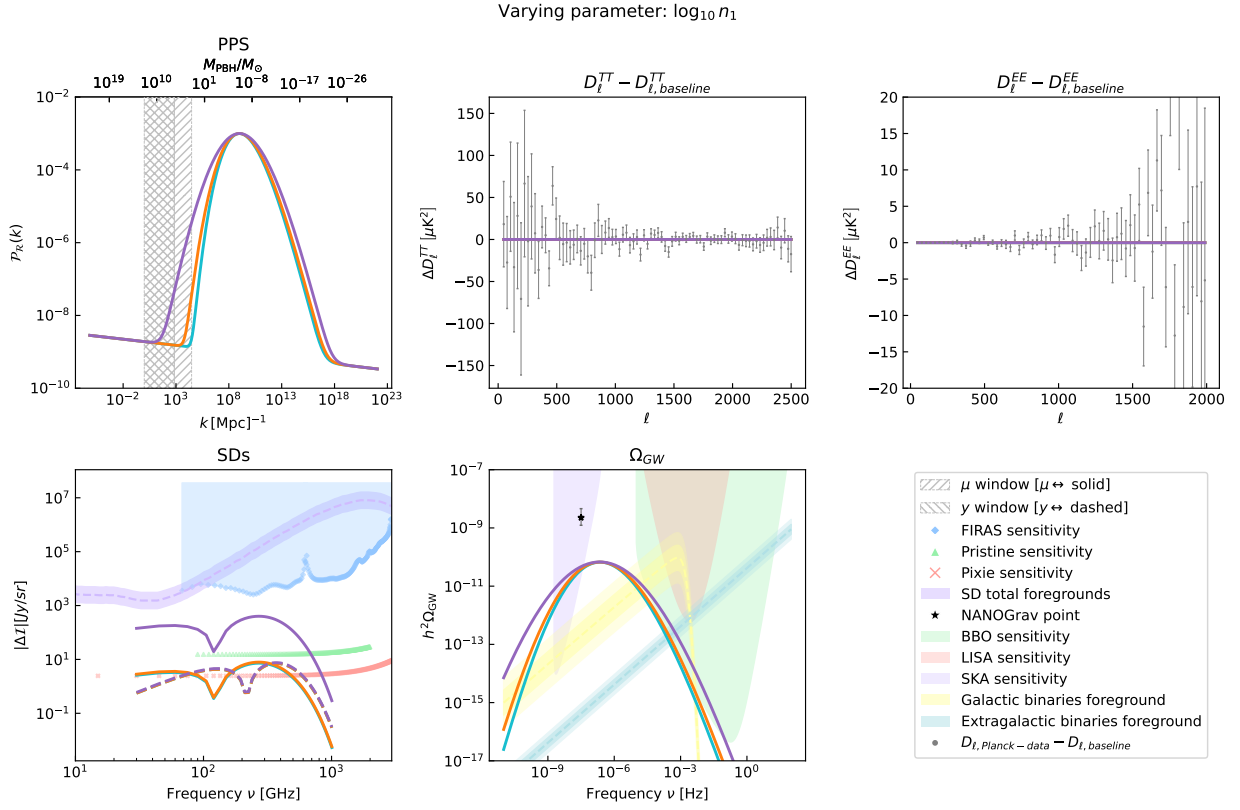


Fig. 20 – Impact of n_1 (smoothly broken power law template) on observables. The cyan, orange and purple curves correspond to the cases $\log_{10} n_1 = 1.25, 0.75, 0.25$, respectively.

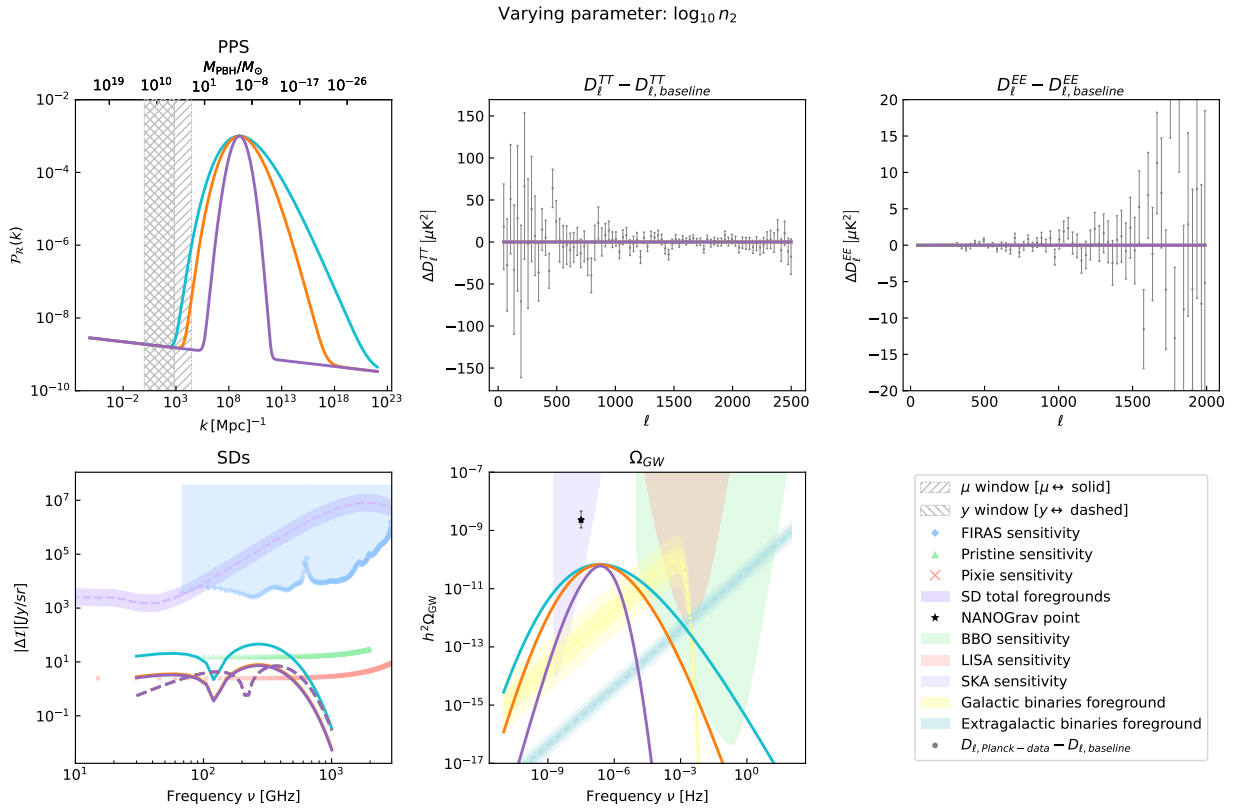


Fig. 21 – Impact of n_2 (smoothly broken power law template) on observables. The cyan, orange and purple curves correspond to the cases $\log_{10} n_2 = -0.15, 0.10, 1.10$, respectively.

Varying Δ

The smoothness parameter Δ affects both slopes. In figure 22 we show three different spectra where Δ takes the values

$$\log_{10} \Delta_1 = 0.45, \quad \log_{10} \Delta_2 = 0.85, \quad \log_{10} \Delta_3 = 1.20, \quad (15.10)$$

and the corresponding effects on observables

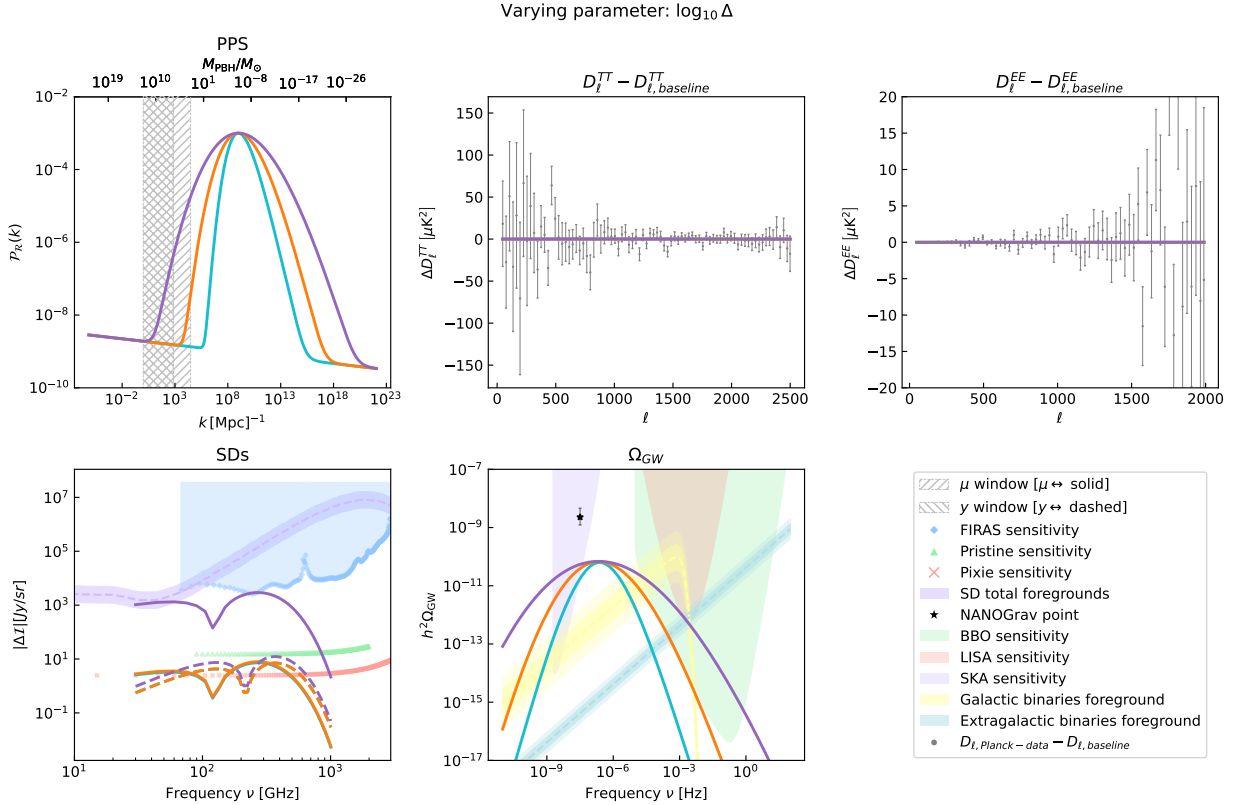


Fig. 22 – Impact of the smoothness parameter Δ (smoothly broken power law template) on observables. The cyan, orange and purple curves correspond to the cases $\log_{10} \Delta = 0.45, 0.85, 1.20$, respectively.

15.3 Oscillating bump template

The analysis of the oscillating bump is slightly different with respect to the previous templates. This is because the amplitude of the feature is not described by a simple parameter A as in the previous cases but by the combination of δN and λ_0 (14.13). Thus, we present three different spectra, each of them with different combinations of $(\delta N, \lambda_0)$ but with roughly the same amplitude. The amplitude is not affected by k_{loc} and thus we placed the three spectra at different k_{loc} in order to observe the impact of this parameter on observables. We present the results for three different amplitudes so that the overall number of spectra examined is nine.

For example, three possible combinations of $(\delta N, \lambda_0)$ - and k_{loc} - that gives an overall

amplitude of 1×10^{-3} are

$$\delta N_1^{(A)} = 0.1, \quad \lambda_{0,1}^{(A)} = 200, \quad \log_{10} k_{\text{loc},1}^{(A)} = 6, \quad (15.11a)$$

$$\delta N_2^{(A)} = 0.3, \quad \lambda_{0,2}^{(A)} = 68, \quad \log_{10} k_{\text{loc},2}^{(A)} = 2, \quad (15.11b)$$

$$\delta N_3^{(A)} = 0.6, \quad \lambda_{0,3}^{(A)} = 34, \quad \log_{10} k_{\text{loc},3}^{(A)} = 10. \quad (15.11c)$$

The effects on observables of these three spectra are given in figure 23.

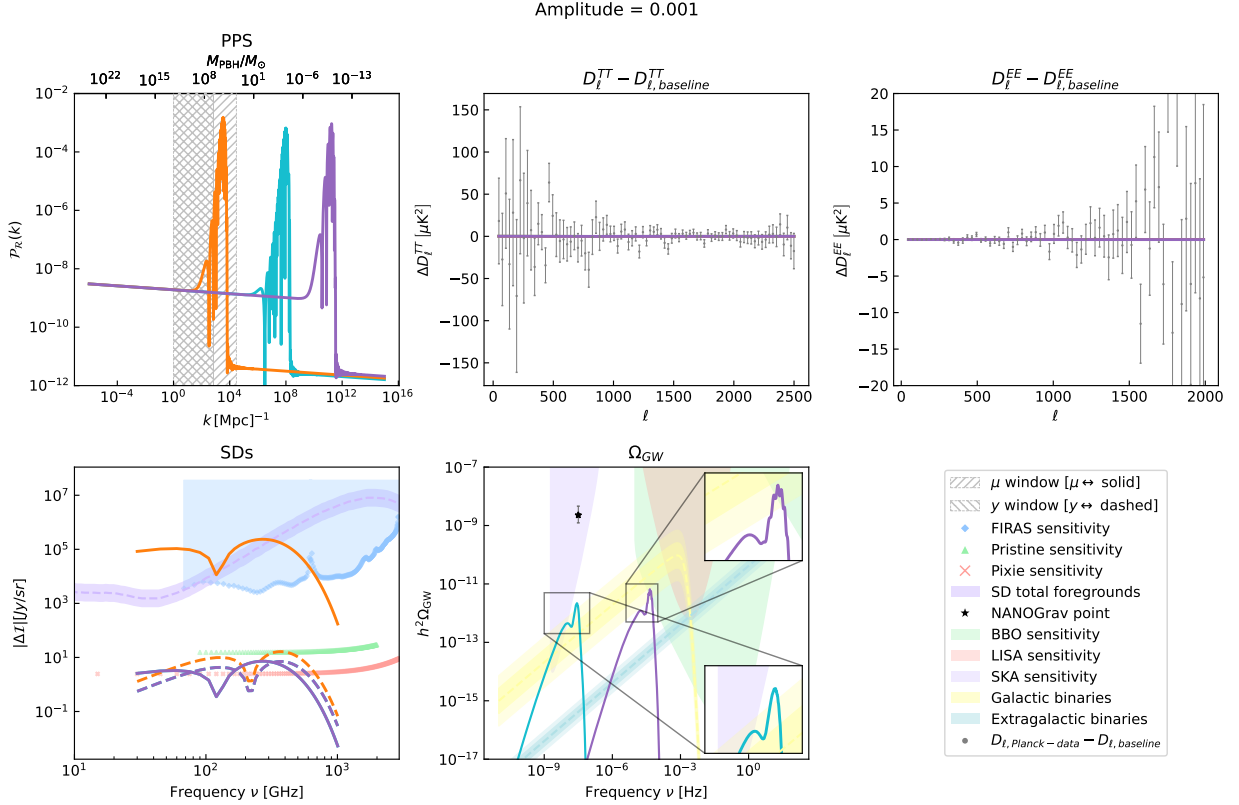


Fig. 23 – Effects on observables of three different spectra with an oscillating bump. The cyan, orange and purple curves correspond to the combinations of parameters with subscript 1, 2, 3 of the case A (15.11) respectively. The combinations of parameters are such that the overall amplitude is roughly 1×10^{-3} .

The impact of k_{loc} on observables is almost the same as the previous cases. The figure shows also how the number of oscillations is related to $(\delta N, \lambda_0)$. Notice that the power of gravitational waves Ω_{GW} depends on template parameters qualitatively in the same way as the power spectrum does. For example, both of them have a peak with oscillations and the number of the latter, as well as the shape of the peak, is similar. This is obvious because equation (11.43) suggests that $\Omega_{\text{GW}}(k) \propto \mathcal{P}_{\mathcal{R}}^2(k)$. Hence, a feature of $\mathcal{P}_{\mathcal{R}}$ located at k will be translated into a feature in Ω_{GW} at k . In this sense, gravitational waves are a unique signal because they are sensitive to the spectral shape of $\mathcal{P}_{\mathcal{R}}(k)$. In other words, they are a cumulative effect and they are not able to capture the behavior of the features in the primordial power spectrum located at k .

The other combinations of parameters that we analyzed are those giving an amplitude roughly equal to 1×10^{-4} :

$$\delta N_1^{(B)} = 1.0 \quad \lambda_{0,1}^{(B)} = 18 \quad \log_{10} k_{\text{loc},1}^{(B)} = 2, \quad (15.12a)$$

$$\delta N_2^{(B)} = 1.5 \quad \lambda_{0,2}^{(B)} = 12 \quad \log_{10} k_{\text{loc},2}^{(B)} = 10, \quad (15.12b)$$

$$\delta N_3^{(B)} = 0.5 \quad \lambda_{0,3}^{(B)} = 35 \quad \log_{10} k_{\text{loc},3}^{(B)} = 6. \quad (15.12c)$$

The results are given in figure 24.

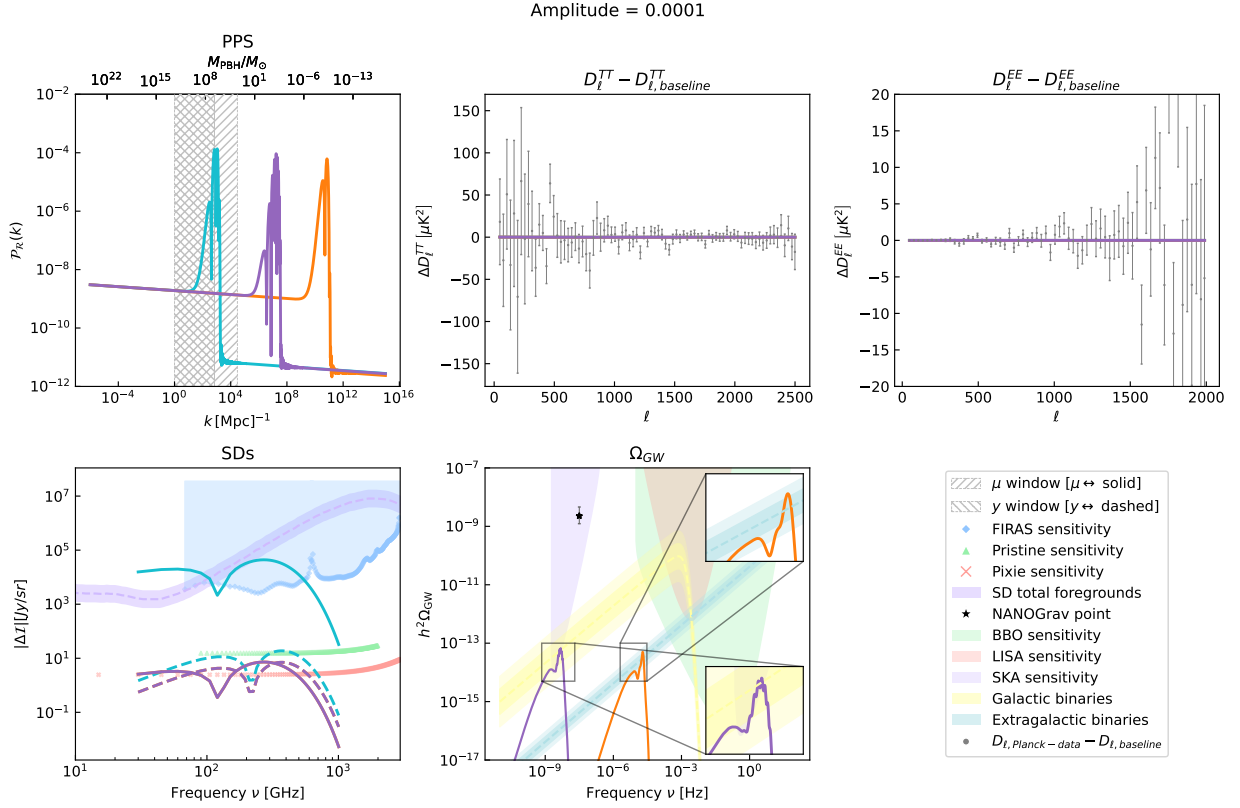


Fig. 24 – Effects on observables of three different spectra with an oscillating bump. The cyan, orange and purple curves correspond to the combinations of parameters with subscript 1, 2, 3 of the case B (15.12) respectively. The combinations of parameters are so that the overall amplitude is roughly 1×10^{-4} .

The last case we present is

$$\delta N_1^{(C)} = 0.25 \quad \lambda_{0,1}^{(C)} = 60 \quad \log_{10} k_{\text{loc},1}^{(C)} = 10, \quad (15.13a)$$

$$\delta N_2^{(C)} = 0.75 \quad \lambda_{0,2}^{(C)} = 20 \quad \log_{10} k_{\text{loc},2}^{(C)} = 2, \quad (15.13b)$$

$$\delta N_3^{(C)} = 1.25 \quad \lambda_{0,3}^{(C)} = 12 \quad \log_{10} k_{\text{loc},3}^{(C)} = 6. \quad (15.13c)$$

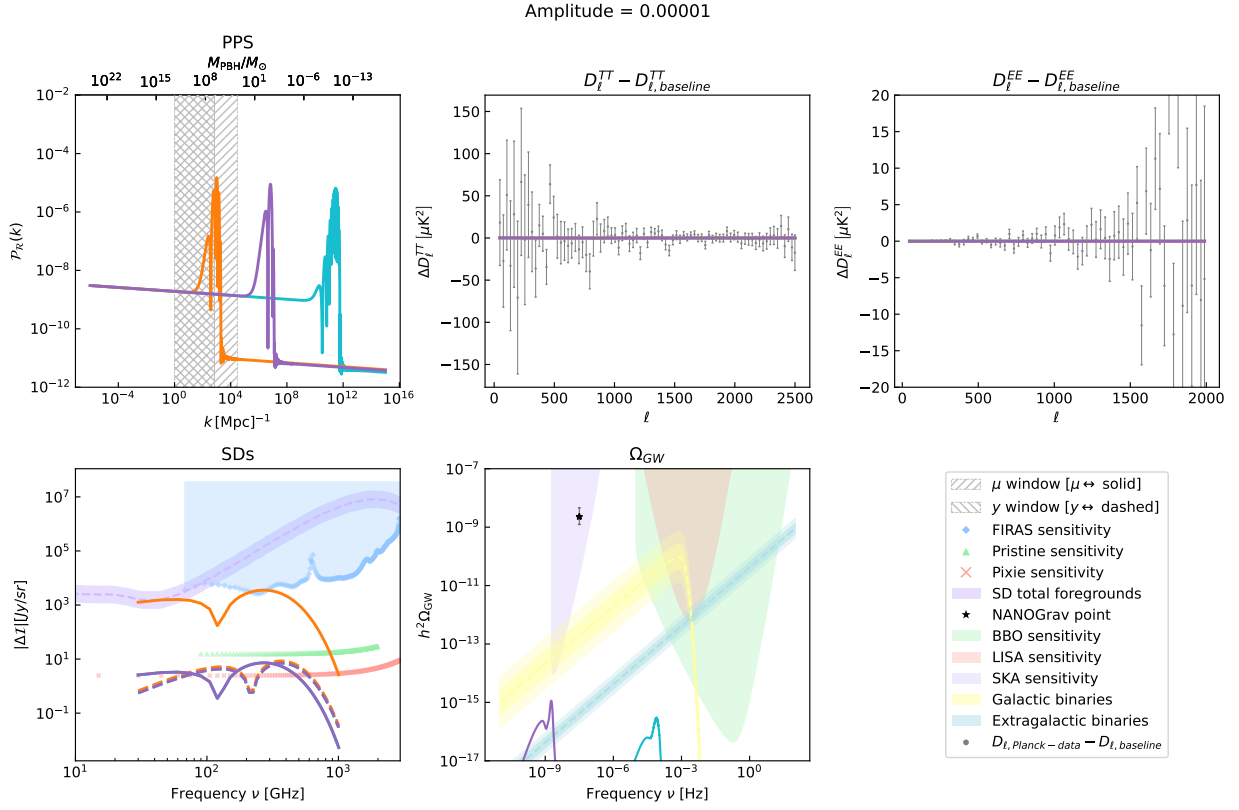


Fig. 25 – Effects on observables of three different spectra with an oscillating bump. The cyan, orange and purple curves correspond to the combinations of parameters with subscript 1, 2, 3 of the case C (15.13) respectively. The combinations of parameters are so that the overall amplitude is roughly 1×10^{-5} .

VI

CONSTRAINTS ON THE PRIMORDIAL POWER SPECTRUM FROM THE CMB

In this chapter we present current and forecast constraints on the primordial power spectrum from CMB spectral distortions alone and in combination with anisotropies data at large scales. To do so, we perform a Bayesian analysis to infer constraints on the primordial power spectrum parameters by sampling suitably built mock likelihoods with a Monte Carlo Markov Chain (MCMC) algorithm. The use of a mock likelihood for COBE/FIRAS as implemented within the MontePython code version which includes SD [Refs] instead of real data is justified because it reproduces the COBE/FIRAS constraints on μ and y (3.49).[†]

As a working example, we assume a primordial power spectrum with a bump described with the smoothly broken power law template (14.10) on top of the near scale invariant spectrum (14.2)[‡]. We derive constraints on the amplitude, width and location of the bump. For simplicity we fix $\log_{10} n_1 = 1.0$, $\log_{10} n_2 = 0.75$ so that the width of the bump depends only on Δ , which we vary in our analysis together with the overall amplitude A and the bump-location k_{loc} . Indeed, we can see from figure 22 that varying Δ while keeping fixed $n_{1,2}$ is equivalent to changing the width of the bump.

16 Methodology

Theoretical models have to be compared with observations of the phenomena they describe. Since data have always uncertainties associated with them, statistics is the necessary tool to dig out information about physical quantities from measurements. In our specific case, we are interested in statistically inferring the parameters of small-scale bumps in the PPS from current and future data.

16.1 Basics of Bayesian inference

Statistical inference proceeds in general by maximizing the probability of obtaining the observed data. Let d be such data and θ a collection of parameters parametrizing a model that tries to explain the data. The probability of getting d as a function of θ is given by the

[†] According to Jens Chluba (private communication) the use of the COBE/FIRAS publicly available measurements and errors of spectral energy density in frequency in a simple χ^2 would lead to more stringent limits on μ and y than those officials in (3.49).[‡] We set $\epsilon = 0$ in the background term since it has no effects on observables.

so-called likelihood function:

$$\mathcal{L}(\theta) \stackrel{\text{def}}{=} P(d|\theta), \quad (16.1)$$

The Bayes theorem relates the likelihood function to the posterior distribution $P(\theta|d)$

$$P(\theta|d) = \frac{P(d|\theta)P(\theta)}{P(d)}, \quad (16.2)$$

which represents what we know about the parameters after seeing the data. Suppose that the model has n parameters $\theta = \{\theta_1, \dots, \theta_n\}$. The posterior distribution for the parameter θ_1 is obtained by marginalization, that is an integration of the posterior distribution over the other parameters

$$P(\theta_1|d) \propto \int d\theta_2 \dots d\theta_n P(\theta|d) \propto \int d\theta_2 \dots d\theta_n \mathcal{L}(\theta) \pi(\theta). \quad (16.3)$$

The quantity $P(\theta) \equiv \pi(\theta)$ appearing in the Bayes theorem is called prior distribution and it represents our knowledge about the parameters before seeing the data. In this thesis we choose uniform priors, as usual, so that posterior and likelihood are simply proportional. Finally, the evidence $P(d)$ is a factor that normalizes the posterior to 1:

$$P(d) = \int d\theta \mathcal{L}(\theta) \pi(\theta). \quad (16.4)$$

Bayesian inference proceeds by updating the posterior knowledge on parameters as new data flows in. First, it is necessary to build the likelihood function, that reflects the way the data are obtained, and to specify the prior distributions of the parameters. Then, we compute the posterior distributions of the parameters through the Bayes theorem. In most cases this can be done only numerically due to the complexity of likelihood functions.

Monte Carlo Markov Chain (MCMC) is a class of algorithms used to numerically compute the posterior distribution. The general purpose of these algorithms is to construct a sequence (or chain) of points (or samples) in parameter space whose density is proportional to the posterior distribution. It can be proved that Markov Chains converge to a stationary state so that the successive elements of the chain are samples from the posterior distribution. The generation of the chain elements is probabilistic and described by the so-called transition probability T to go from the point of the parameter space $\theta^{(t)}$ to the point $\theta^{(t+1)}$. Such transition probability is obtained by imposing the detailed balance condition

$$\frac{T(\theta^{(t)}, \theta^{(t+1)})}{T(\theta^{(t+1)}, \theta^{(t)})} = \frac{P(\theta^{(t+1)}|d)}{P(\theta^{(t)}|d)}. \quad (16.5)$$

Once the posterior distribution is sampled with Markov Chains, it is possible to obtain Monte Carlo estimation of useful quantities, such as the mean E of the posterior

$$E[\theta] = \int d\theta \theta P(\theta|d) \approx \frac{1}{M} \sum_{t=0}^{M-1} \theta^{(t)}, \quad (16.6)$$

or the the marginalized posterior probability (16.3) of a single parameter, say θ_1 . This quantity can be computed directly from the Markov Chain by dividing the range of θ_1 in a series of bin and counting the number of samples falling within each bin while ignoring the other parameters $\theta_2, \dots, \theta_n$. Similarly, we compute 2-dimensional posteriors and the $\alpha\%$ credible intervals.

The Metropolis-Hastings algorithm is the simplest MCMC algorithm and it is the one we use in our analysis. The algorithm starts from a random point $\theta^{(0)}$, proposes a candidate point $\theta^{(c)}$ drawn from an arbitrarily chosen probability distribution $q(\theta^{(0)}, \theta^{(c)})$ and evaluates the quantity

$$\alpha = \min \left(\frac{P(\theta^{(c)}|d)q(\theta^{(0)}, \theta^{(c)})}{P(\theta^{(0)}|d)q(\theta^{(0)}, \theta^{(c)})}, 1 \right). \quad (16.7)$$

Then, it generates a uniform random number $\mu \in [0, 1)$ and if $\mu < \alpha$ the candidate $\theta^{(c)}$ is accepted, otherwise it is rejected. In particular, if the posterior of the candidate point is larger than the posterior at the starting point, the candidate is always accepted. If the candidate point is accepted it is added to the chain and the algorithm is repeated starting from such points. If it is rejected, the algorithm draws another candidate point.

16.2 CMB likelihoods

We perform a Bayesian analysis to infer constraints on the primordial power spectrum parameters. Our fiducial model is described by a near scale invariant PPS with

$$\ln 10^{10} A_s = 3.0448 \quad n_s = 0.96605 \quad (16.8)$$

like the plik best fit of Planck TT,TE,EE+lowE+lensing data [18]. The other remaining cosmological parameters are fixed as follows: $\Omega_b h^2 = 0.022383$, $\Omega_{\text{cdm}} h^2 = 0.12011$, $100\theta_s = 1.04091$, $\tau_{\text{reio}} = 0.0543$. Using CLASS, we generate the fiducial observables, i.e. the anisotropies angular power spectra and the spectral distortions in each frequency bin for a given detector (FIRAS or PIXIE).

Starting from these *observed* quantities, we built the SDs likelihood as follows [34, 89]

$$\ln \mathcal{L} = -\frac{1}{2} \sum_i \left(\frac{\Delta I_{\text{obs}}(\nu_i) - \Delta I_{\text{pred}}(\nu_i)}{\delta I(\nu_i)} \right)^2, \quad (16.9)$$

where $\delta I(\nu_i)$ is the detector sensitivity in the i -th frequency bin and $\Delta I_{\text{predicted}}$ are SDs computed with CLASS for a given set of parameters $(A, k_{\text{loc}}, \Delta)$. The spectral distortion term ΔI consists in the sum of the late-time reionization y -contribution (6.7), temperature shift (5.23) and foreground map:

$$\Delta I(x) = \Delta I_{\text{Silk}}(x) + \Delta I_T(x) + \Delta I_{\text{reio}}(x) + \Delta I_{\text{foregrounds}}(x), \quad (16.10)$$

where $\Delta I_{\text{Silk}}(x)$ is the distortion due to Silk damping, which is the only contribution de-

pending on the PPS. The main contribution to the foreground term $\Delta I_{\text{foregrounds}}$ comes from Galactic thermal dust and the Cosmic Infrared Background (CIB), as well as synchrotron, free-free, spinning dust, and integrated CO emissions. Expressions for these contributions can be found in [89]:

$$\Delta I_i(x) = A_i \left(\frac{x_i}{x_{i,\text{ref}}} \right)^{\beta_i+3} \frac{\exp(x_{i,\text{ref}}) - 1}{\exp(x_i) - 1}, \quad \text{and} \quad \nu_{\text{ref}} = 545 \text{ GHz} \quad (16.11a)$$

$$\Delta I_{\text{sync}}(x) = A_S \left(\frac{x_{\text{ref}}}{c} \right)^{\alpha_S+0.5\omega_S \log^2(x(x_{\text{ref}}))} \quad \text{where} \quad \nu_{\text{ref}} = 100 \text{ GHz} \quad (16.11b)$$

$$\begin{aligned} \Delta I_{\text{free-free}}(x) &= A_{ff} \mathcal{N} T_e (1 - \exp(-\tau_{ff})) \\ \tau_{ff} &\approx 0.05468 \text{EM} \left(\frac{T_e}{K} \right)^{-3/2} \left(\frac{\nu}{\text{GHz}} \right)^{-2} g_{ff} \\ g_{ff} &\approx \log \left\{ e + \exp \left[5.96 - \frac{\sqrt{3}}{\pi} \log \left(\left(\frac{\nu}{\text{GHz}} \right) \left(\frac{T_e}{10^4 K} \right)^{-3/2} \right) \right] \right\} \end{aligned} \quad (16.11c)$$

where $i \in \{\text{thermal dust, CIB}\}$. Contributions from spinning dust and integrated CO emission are modeled by using spectral templates. As can be seen, 16 nuisance parameters are needed to model foregrounds and they are

1. ΔT : temperature shift amplitude;
2. T_D : temperature of thermal dust;
3. β_D : exponent appearing in equation (16.11a);
4. A_D : amplitude of the SD due to thermal dust;
5. T_{CIB} : CIB temperature;
6. β_{CIB} : exponent appearing in equation (16.11a);
7. A_{CIB} : amplitude of the SD due to CIB;
8. α_{sync} : exponent appearing in equation (16.11b);
9. ω_{sync} : exponent appearing in equation (16.11b);
10. A_{sync} : amplitude of the SD due to synchrotron emission;
11. T_e : temperature of electron plasma;
12. EM: emission measure;
13. ν_{spin} : parameter for the shape of distortion due to spinning dust;
14. A_{spin} : amplitude of the SD due to spinning dust;
15. A_{CO} : amplitude of the SD due to CO emission;

16. y_{reio} : amplitude of y -distortion due to reionization;

All our results are obtained by marginalizing over such nuisance parameters.

Given a set of parameters $(A, k_{\text{loc}}, \Delta)$ and the rest of the cosmological parameters, we also compute the TT-TE-EE spectra of the CMB anisotropies and compare them with Planck data. In order to use the Planck data constraining power for CMB anisotropies in this work we use a mock likelihood data based on blue book sensitivity implemented in MONTEPYTHON in TT-TE-EE based on an inverse Wishart (see for instance [90]). The use of Planck DR3 likelihood in this context has been problematic, probably because of its use in combination with FIRAS-like data, and we have therefore turned to a mock likelihood for Planck data as in [34, 89]. This mock Planck likelihood covers a range of multipoles $\ell_{\text{min}} = 2$, $\ell_{\text{max}} = 2500$, use the blue book sensitivity for the nominal survey for the frequency channels 100, 143 and 217 GHz and use a fraction of the sky $f_{\text{sky}} = 0.65$. We plan to revisit the use of Planck real data in the future.

We sample the likelihood with a Metropolis-Hastings MCMC algorithm by using MONTEPYTHON [91, 92]. We assume no correlation between SDs and anisotropies and therefore likelihoods are simply multiplied. We use the Gelman-Rubin convergence criterion stopping the MCMC when the $R - 1$ coefficient of each sampled parameter is less than 0.001.

16.3 Semi-analytical constraints

Previous constraints on the PPS from SDs were derived in [93, 94, 95]. The authors of [95] derive SDs constraints by assuming a PPS growing as k^4 or with a Dirac delta function peak and by considering μ -distortions only. The constraints in the two cases are not so different. They also use an approximated equation for μ involving the window function (see e.g (10.22)) and not the quasi-exact solution obtained with the Green's function technique. We review their results in the delta Dirac case to compare them with those from our analysis. We consider a PPS given

$$\mathcal{P}_{\mathcal{R}}(k) = A \delta \left[\log \left(\frac{k}{k_*} \right) \right] \quad (16.12)$$

and we plug it into equation (10.22). The delta Dirac function allows us to analytically solve the integral

$$\mu = A \cdot W_{\mu}(\hat{k}_*). \quad (16.13)$$

The FIRAS/PIXIE upper limit on the PPS amplitude A_{upper} at a chosen k_* is computed as

$$A_{\text{upper}}(k_*) = \frac{|\mu|}{W_{\mu}(\hat{k}_*)}, \quad (16.14)$$

where $\mu_{\text{FIRAS}} = 9 \times 10^{-5}$ and $\mu_{\text{PIXIE}} = 2 \times 10^{-8}$. The FIRAS and PIXIE upper limits on A in the range of comoving wavenumbers $k \in [10^{-1}, 10^6] \text{ Mpc}^{-1}$ are shown in figure 26.

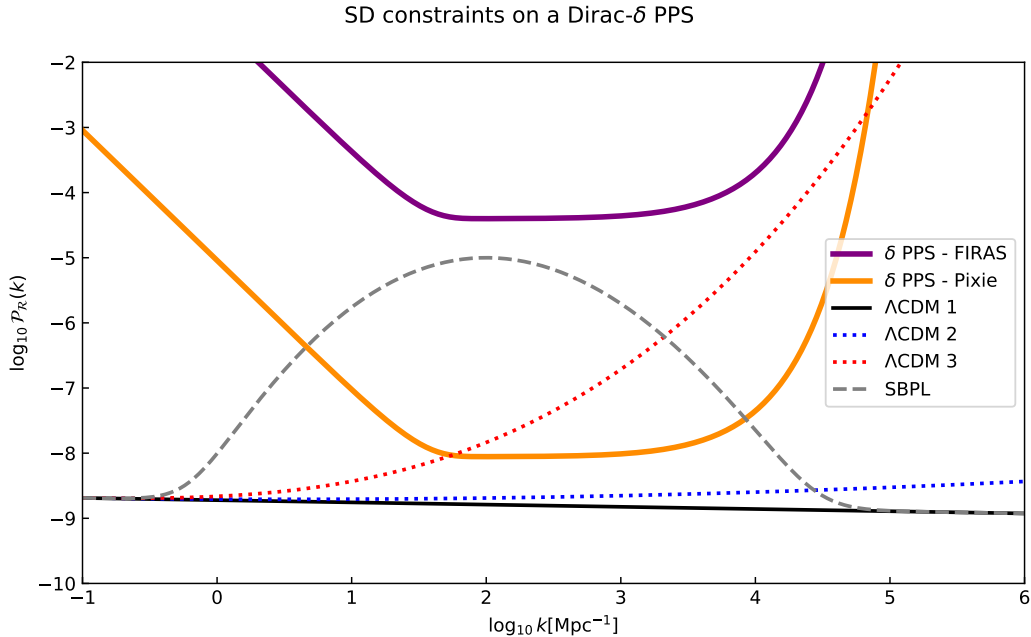


Fig. 26 – FIRAS and PIXIE upper limits on PPS amplitude using equation (10.22) and a Dirac delta PPS (see also [95]). We also plot the Λ CDM fiducial when the running of the tilt α_s and its running $d\alpha_s/d \ln k$ are zero (black), the Λ CDM fiducial when $\alpha_s = 0.008$ and $d\alpha_s/d \ln k = 0$ (blue), the Λ CDM fiducial when $\alpha_s = 0$ and $d\alpha_s/d \ln k = 0.03$ (red). The grey curve is an example of PPS with a bump described by the smoothly broken power law template (14.10).

17 Results

We now present the results obtained with our original implementation of CLASS and MONTEPYTHON in the framework described in the previous section.

17.1 FIRAS and Planck constraints

We consider first the case applied to existing data from FIRAS and Planck. To get an intuition about the typical amplitude of the PPS to which FIRAS is sensitive to, we fix $k_{\text{loc}} = 10^2 \text{Mpc}^{-1}$, and vary only the amplitude and width of the peak in the ranges

$$\log_{10} A \in [-10, -2.5], \quad \log_{10} \Delta = [0, 1.5], \quad (17.1)$$

We fix the six Λ CDM parameters to their Planck plik bestfit values: $\Omega_b h^2 = 0.022383$, $\Omega_{\text{cdm}} h^2 = 0.12011$, $100\theta_s = 1.04091$, $\tau_{\text{reio}} = 0.0543$. $\ln(10^{10} A_s) = 3.0448$, $n_s = 0.96605$. To consistently take into account the effects of foregrounds in our analysis, we vary the nuisance parameters of the FIRAS likelihood[†], and, as stated above, we marginalize over them. The resulting 1D and 2D posterior distributions are shown in figure 27.

[†] In the Planck mock likelihood there are no nuisance parameters

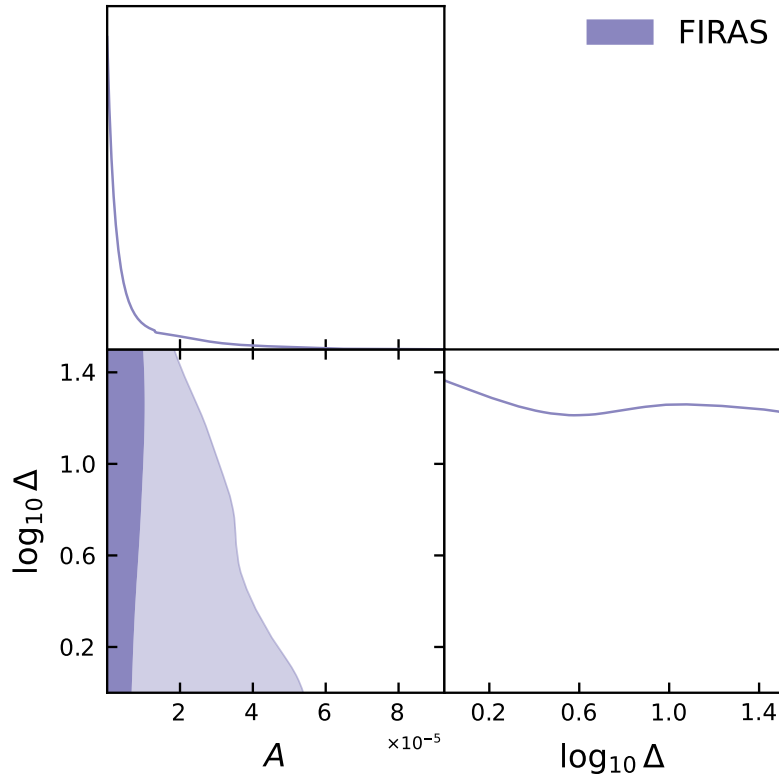


Fig. 27 – 1D and 2D (68% and 95% CL) posterior distributions of A and $\log_{10} \Delta$ obtained with FIRAS in the case of a fixed bump location $\log_{10} k_{\text{loc}}[\text{Mpc}^{-1}] = 2$.

In this case FIRAS only sets an upper limit on the amplitude, while the width of the bump is not constrained at all. The 95% CL upper limit on A is

$$A < 3.6 \times 10^{-5} \quad (\text{FIRAS}, k_{\text{loc}} = 10^2 \text{ Mpc}^{-1}, 95\% \text{ CL}). \quad (17.2)$$

Then we let also k_{loc} in the range

$$\log_{10} k_{\text{loc}}[\text{Mpc}^{-1}] = [-1, 6]. \quad (17.3)$$

FIRAS does not constrain both the width and location of the bump but sets only an upper limit on its amplitude. Therefore, if we compute the upper limit on the amplitude by marginalizing over these parameters, we would get prior-dependent results. In particular, since we vary k_{loc} in a range wider than the SDs sensitivity window[†], we would get a large value that does not represent the real constraining power of FIRAS. In this case, the best way to understand the constraints is to plot the so-called *predictive posterior distribution*, namely the constraints on the template (14.10) given the posterior distribution derived on the model parameters [96, 97]. We show the predictive posterior distribution in figure 28, where we plot 1σ (dark-shaded regions) to 3σ (light-shaded regions) constraints on the PPS. The purple color map refers to FIRAS constraints. Analogous results were obtained for other

[†] Figure 10 suggests that SDs are sensitive to the PPS in the range $k \in [1, 10^4] \text{ Mpc}^{-1}$.

phenomenological templates for $\mathcal{P}_{\mathcal{R}}(k)$ in [95]. In figure 28 we also plot the constraints from figure 26.

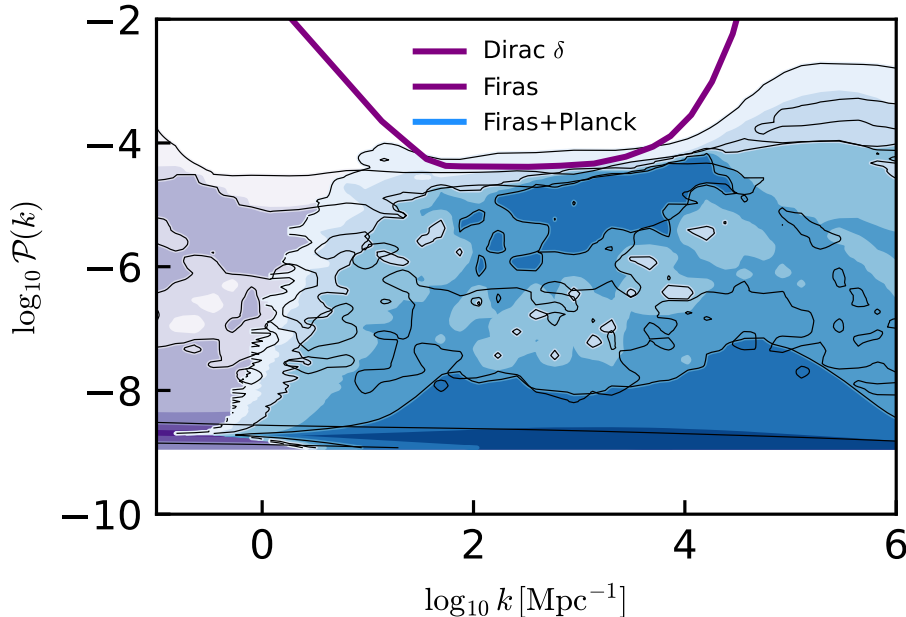


Fig. 28 – Comparison between FIRAS (purple) and FIRAS+Planck (blue) predictive posterior distributions. The solid curve is the contour obtained in literature [95] with a Dirac δ PPS and shown in figure 26.

We note that for large comoving wavenumbers $k \sim 10^4 - 10^6$ the upper bound on the amplitude is only very weak $\log_{10} \mathcal{P}_{\mathcal{R}} \sim -3$. On the other hand, we see that in the sensitivity range of SDs, FIRAS constrains the amplitude down to $\log_{10} \mathcal{P}_{\mathcal{R}} \sim -4, -5$, in agreement with the upper limit found by fixing $k_{\text{loc}} = 10^2 \text{ Mpc}^{-1}$ (17.2). Furthermore, our results are similar to figure 26, but they are extended in a wider range of comoving wavenumbers. This is due to having a broad bump that affects SDs even away from its peak at k_{loc} , as opposed to the δ function considered in Fig. 26.

We then combine Planck data with FIRAS one. In this case, we vary also the amplitude A_s and scalar tilt n_s of the nearly scale-invariant background power law (with unbounded uniform priors centered in the Planck plik best fit values aforementioned). When we consider FIRAS alone, these parameters are degenerate because they both contribute to the total SD amplitude and so we fix their values. We know that Planck constrains both A_s and n_s and therefore we choose to vary them when we add anisotropies data. We plot the 1D and 2D posterior distributions of the combination of Planck and FIRAS data and of FIRAS data only in figure 29. By looking at the 2D contours involving k_{loc} and at the 1D posterior distribution of the latter, we deduce that Planck data sets a lower bound on k_{loc} . Since k_{loc} has a lower limit, we expect that the marginalized upper limit on A improves with respect to the FIRAS-only case. Indeed, we find an upper limit to be the same order of magnitude of the Dirac δ contours 26 in the SDs sensitivity range. Notice however that our limit is obtained by marginalizing over the bump width and location, while contours 26 are not marginalized. Indeed, in the SDs sensitivity range we find an upper limit tighter than

in the Dirac δ case 26. As before, this is due to consider a broad bump in the PPS. The combination of FIRAS and Planck also sets an upper limit on the width ($\log_{10} \Delta < 0.84$), but only at the 68% CL. This is because a too-large width would affect Planck data even for a large k_{loc} .

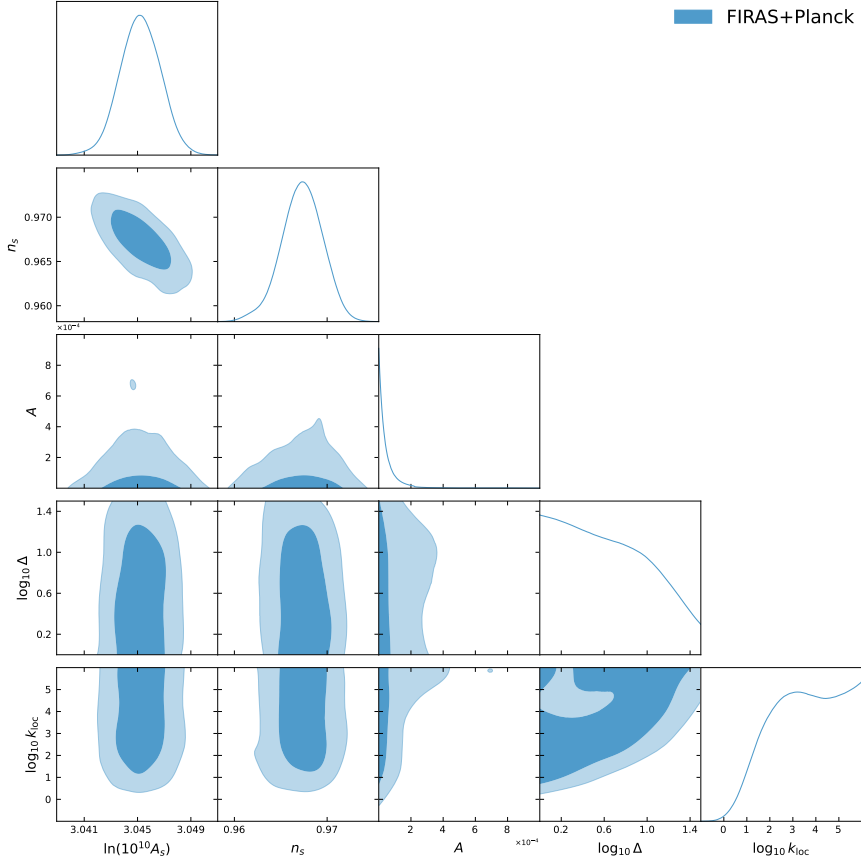


Fig. 29 – 1D and 2D (68% and 95% CL) posterior distributions of $\ln(10^{10} A_s)$, n_s , A , $\log_{10} \Delta$ and $\log_{10} k_{\text{loc}}$ obtained in FIRAS+Planck case.

To sum up, the constraints on bump parameters in the FIRAS+Planck case are

$$A < 1.5 \times 10^{-4} \quad (\text{FIRAS+Planck, 95\% CL}), \quad (17.4a)$$

$$\log_{10} k_{\text{loc}} [\text{Mpc}^{-1}] > 1.1 \quad (\text{FIRAS+Planck, 95\% CL}), \quad (17.4b)$$

$$\ln(10^{10} A_s) = 3.0452 \pm 0.0015 \quad (\text{FIRAS+Planck, 68\% CL}), \quad (17.4c)$$

$$n_s = 0.9673 \pm 0.0022 \quad (\text{FIRAS+Planck, 68\% CL}). \quad (17.4d)$$

The errors on these parameters are roughly half the ones reported in the latest analysis by Planck [18]. This is because we fix the other 4 Λ CDM parameters, while Planck results are obtained by marginalizing over them. We plan to repeat the analysis by varying all the 6 Λ CDM parameters to see the differences with respect to this case. The 2D contours in figure 29 suggest also that A_s, n_s are not degenerate with any of the bump parameters.

To help the reader understanding the constraints on the PPS, we plot the predictive posterior distribution of the FIRAS+Planck case in figure 28. The FIRAS+Planck contours

in figure 28 interpolate between the large-scale constraints on the PPS presented by the Planck collaboration in [98] and the small-scale bounds from FIRAS. From this plot, it is clear that an entire region of the parameter space for $k \lesssim 1\text{Mpc}^{-1}$ is ruled out when Planck data are combined with FIRAS one.

17.2 Forecast for PIXIE

We now go on to present our constraints from PIXIE, considered as a spectrometer and not a polarimeter [8]. We first compare the upper limit on the amplitude obtained with PIXIE and FIRAS in the case of a fixed bump location $k_{\text{loc}} = 10^2\text{Mpc}^{-1}$. We assume the priors given in equation (17.1) also in this case. We show the corresponding 1D and 2D posterior distributions of A and Δ in figure 30 and we compare them with FIRAS results.

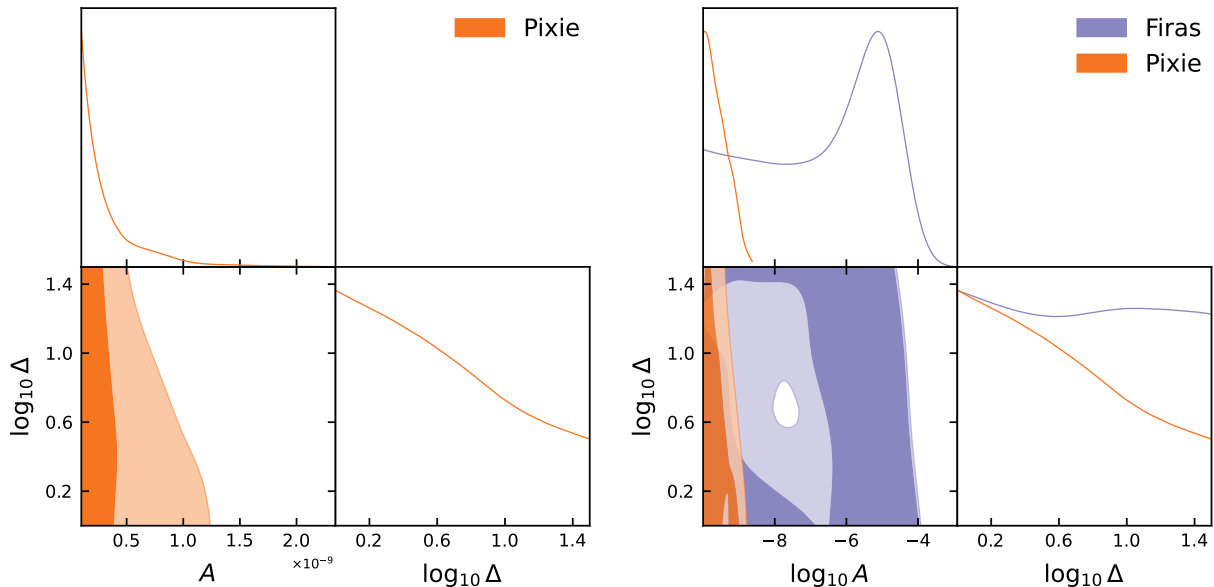


Fig. 30 – Left. 1D and 2D (68% and 95% CL) posterior distributions of A and $\log_{10} \Delta$ obtained with PIXIE in the case of a fixed bump location $\log_{10} k_{\text{loc}}[\text{Mpc}^{-1}] = 2$. Right. Comparison with FIRAS contours shown in figure 27.

The marginalized upper limit on A at 95% CL is improved by roughly four orders of magnitude with respect to FIRAS (17.2):

$$A < 9.9 \times 10^{-10} \quad (\text{PIXIE}, k_{\text{loc}} = 10^2 \text{Mpc}^{-1}, 95\% \text{ CL}). \quad (17.5)$$

We then let k_{loc} vary in the range (17.3). As before, to have an intuition on the constraints we plot the predictive posterior distribution in figure 31 in comparison with FIRAS contours. We note that PIXIE improves FIRAS constraints of about four orders of magnitude in a wider range of k and not only at the fixed bump position tested before.

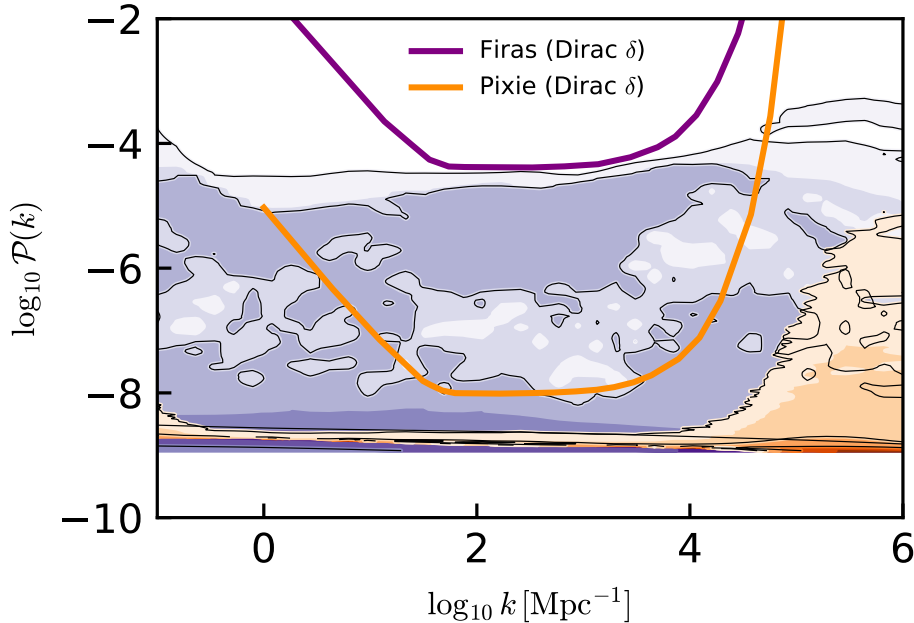


Fig. 31 – Comparison between *FIRAS* (purple) and *PIXIE* (orange) predictive posterior distributions. The solid curves are the analogous upper limits obtained in literature [95] with a Dirac δ PPS and shown in figure 26.

As in the *FIRAS*+Planck case, combining anisotropies data to SDs one sets a lower bound on the location of the bump, an upper limit on its width - though only at 68% CL - and improves the upper limit on the amplitude with respect to SDs only case. In the *PIXIE*+Planck case the limits are

$$A < 1.2 \times 10^{-9} \quad (\text{PIXIE+Planck, 95\% CL}), \quad (17.6a)$$

$$\log_{10} k_{\text{loc}} [\text{Mpc}^{-1}] > 0.72 \quad (\text{PIXIE+Planck, 95\% CL}), \quad (17.6b)$$

$$\ln(10^{10} A_s) = 3.0450^{+0.0018}_{-0.0014} \quad (\text{PIXIE + Planck, 68\% CL}), \quad (17.6c)$$

$$n_s = 0.9670^{+0.0025}_{-0.0020} \quad (\text{PIXIE + Planck, 68\% CL}). \quad (17.6d)$$

There are no significant differences between the values of A_s and n_s inferred in the *PIXIE*+Planck and *FIRAS*+Planck case (17.4c), (17.4d). This confirms that A_s and n_s are mainly determined by Planck data, while SDs play a marginal role. We plot the corresponding 1D and 2D posterior distributions in figure 32 and the predictive posterior distribution of this case in figure 33. In this case, the synergy of CMB anisotropies and SDs rules out entire regions of the parameter space both at low and high k .

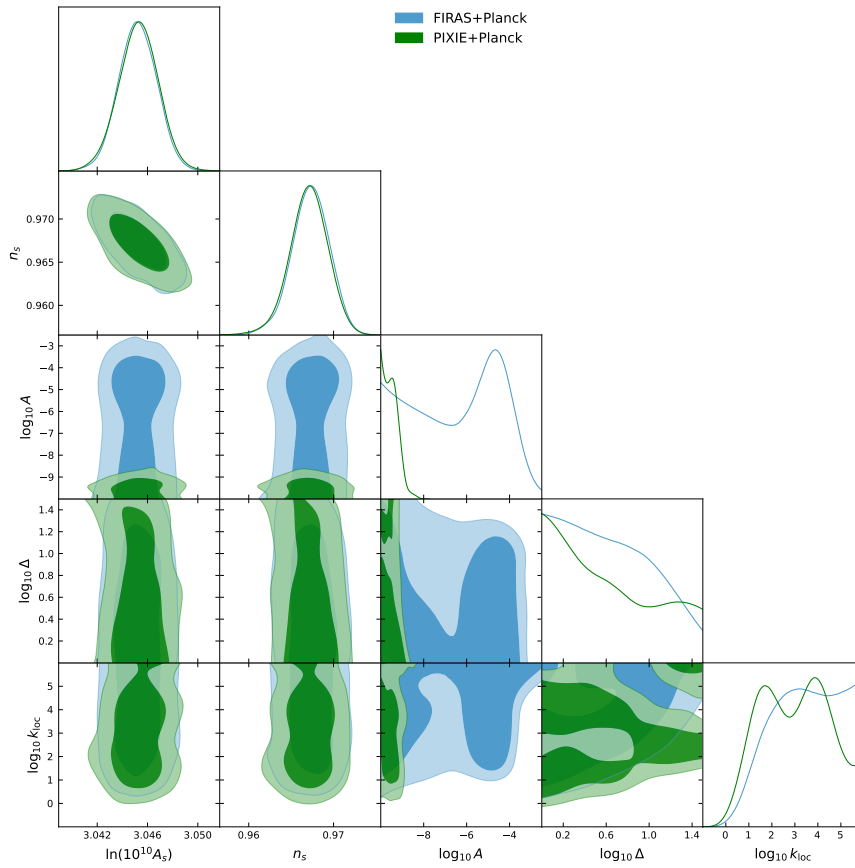


Fig. 32 – 1D and 2D (68% and 95% CL) and posterior distributions of $\ln(10^{10} A_s)$, n_s , $\log_{10} A$, $\log_{10} \Delta$ and $\log_{10} k_{\text{loc}}$ obtained with FIRAS+Planck (blue) and PIXIE+Planck (green).

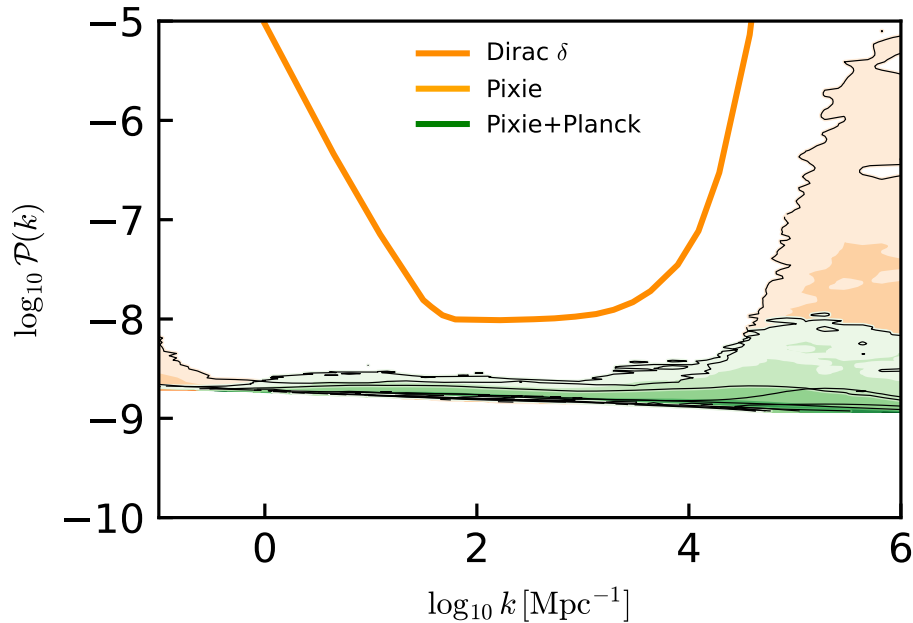


Fig. 33 – Comparison between PIXIE (orange) and PIXIE+Planck (green) predictive posterior distributions. The solid curves are the analogous contours obtained in literature [95] with a Dirac δ PPS and shown in figure 26.

18 Discussion

The main results of this thesis are shown in figures 28, 31, 33, where we plot the constraints from CMB data on the shape of a PPS with a broad bump at small scales. We derive phenomenological templates that fit different large peaks produced in multi-field models of inflation, we choose one template and we infer the constraints from CMB anisotropies (Planck) and SDs (FIRAS or PIXIE) data with an MCMC analysis performed an original modification of CLASS and MONTEPYTHON. Figure 31 suggests that FIRAS constrains the PPS amplitudes to be less than roughly 10^{-4} in the range $\log_{10} k[\text{Mpc}^{-1}] \in [-0.75, 4.5]$. PIXIE improves such upper limit by approximately four orders of magnitude. We compare our constraints with simple analytical limits shown in figure 26 and present in the literature [95]. In particular, the upper limit on the amplitude is roughly the same in the two cases, but our result is extended on a wider range of comoving wavenumbers. This is because the upper limits in figure 26 are derived considering a Dirac- δ PPS, which is characterized only by the peak amplitude and location, while we consider a broad bump that affects SDs even when the peak location is far away from the SDs sensitivity range. The authors of [95] derived similar constraints also for the case

$$\mathcal{P}_{\mathcal{R}}(k) = \begin{cases} 4A \left(\frac{k}{k_{\text{loc}}} \right)^4, & \text{for } k < k_{\text{loc}} \\ 0, & \text{otherwise} \end{cases} \quad (18.1)$$

which is motivated in the context of single-field models of inflation. The constraints obtained for such PPS are roughly the same as those for the Dirac- δ case as they depend on the same parameters. Therefore, our analysis extends previous constraints to broad bumps produced in multi-field models of inflation and we explore the effects of the width.

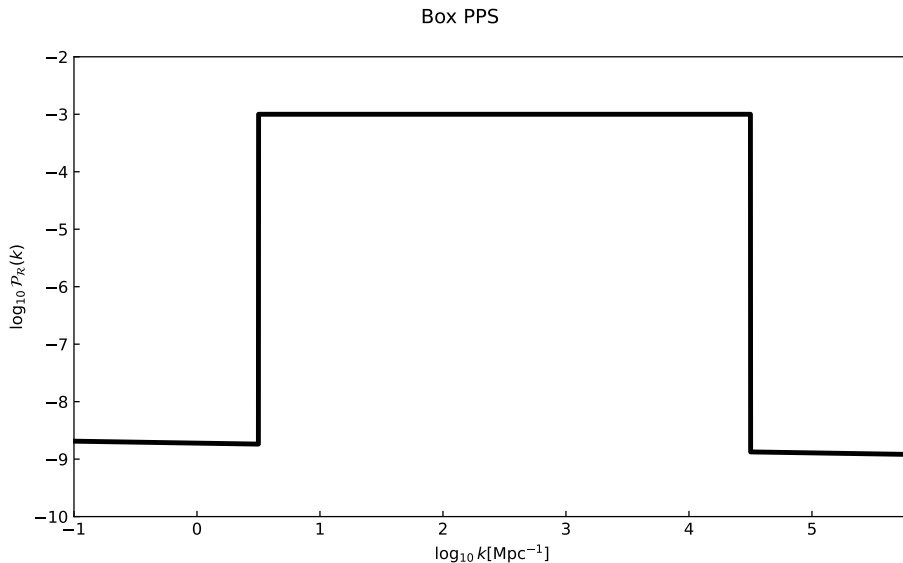


Fig. 34 – "Box" PPS given by equation (18.2) in the case of $k_a = 1 \text{ Mpc}^{-1}$, $k_b = 10^4 \text{ Mpc}^{-1}$ and $B = 10^{-3}$.

The effects of a broad bump can be naively understood by considering the following "box" PPS

$$\mathcal{P}_{\mathcal{R}}(k) = \begin{cases} B, & \text{for } k_a < k < k_b \\ A_s \left(\frac{k}{k_*}\right)^{n_s-1}, & \text{otherwise} \end{cases}, \quad (18.2)$$

We plot such PPS in figure 34 in the case $k_a = 1 \text{ Mpc}^{-1}$, $k_b = 10^4 \text{ Mpc}^{-1}$ and $B = 10^{-3}$. For a fixed value of the box width, we vary its center in the range $k \in [10^{-1}, 10^6] \text{ Mpc}^{-1}$ and we numerically integrate equation (10.22) to derive SD constraints on the box amplitude B in the range of comoving wavenumbers considered. Such constraints, shown in figure 35, extend on a wider range of k than those derived in the δ PPS case due to the broadness of the bump.

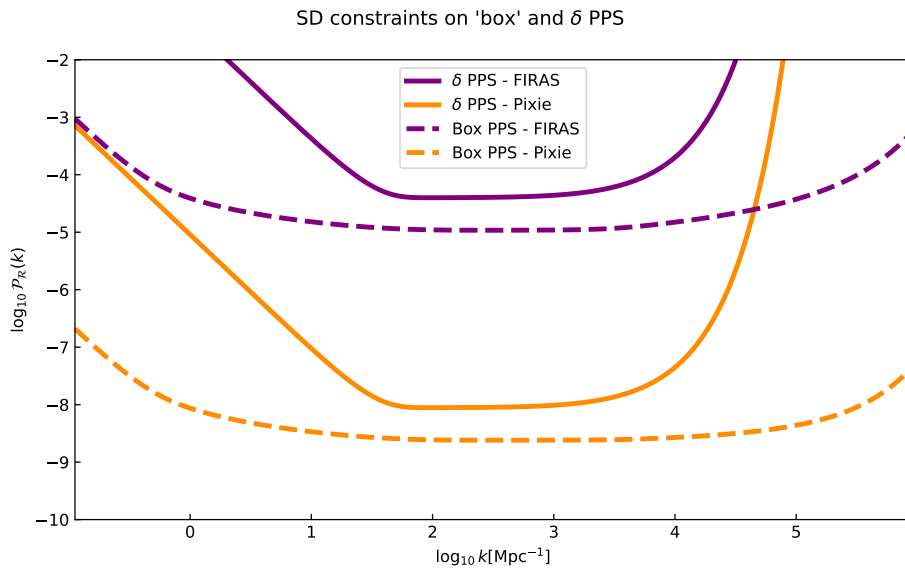


Fig. 35 – FIRAS (purple) and PIXIE (orange) upper limits on the amplitude of the "Box" (18.2) and the Dirac δ (16.12) bump. The "Box" bump has a fixed width of 10^4 Mpc^{-1} .

The contours in figure 35 are similar to the posterior predictive probability distributions 31. However, we obtain such predictive probability distributions by marginalizing over all the parameters, while we assume a fixed width to find the contours in figure 35.

We further explore the synergy between CMB anisotropies and SDs by combining Planck data with FIRAS one. We show how such combination of data improves the constraints on the PPS in figures 28 and 33. In particular, anisotropies data disfavors a bump located at $\log_{10} k_{\text{loc}}[\text{Mpc}^{-1}] < 1.1$ at 95% CL and a too broad bump when the latter is closed to SDs window. These limits, although expected, are not present in the literature yet.

CONCLUSIONS

In this thesis, we have explored constraints which can be put on large bumps in the primordial power spectrum of curvature perturbations beyond the scales probed by anisotropies of the cosmic microwave background and galaxy surveys. These large bumps in the primordial power spectrum of curvature perturbations produced during inflation is one of the standard mechanisms to seed primordial black hole formation, a topic which has drawn a great interest in the scientific community following the first detection of gravitational waves from black holes merging.

The aim of this thesis is to constrain these bumps with current and future data. For the first time we have derived phenomenological templates by employing modified lognormal, smoothly broken power-law and oscillatory shapes that match accurately the theoretical predictions obtained in multi-field models of inflation. We have also derived their imprints on anisotropies and spectral distortions of the cosmic microwave background and their contribution to the stochastic gravitational waves background induced by curvature perturbations at second order.

We have performed a Monte Carlo Markov Chain analysis to infer constraints on PPS from the latest Planck data for CMB anisotropies and FIRAS data for the CMB spectrum. In particular, we have derived the constraints on a PPS with a broad bump described by the smoothly broken power-law template. We accurately compared our results with toy models for the bump, such as the previously used Dirac δ function or a box function, the latter originally introduced in this thesis. We have found that FIRAS data sets an upper limit on the amplitude of the bump. In particular, we have found that the upper limits on the amplitude of a broad bump extends on a wider range of comoving wavenumbers than those obtained with a peak with no width, e.g a Dirac δ PPS. Indeed, the width of the bump, although not very well constrained, affects CMB SDs even when the maximum of the peak is not inside the SDs sensitivity range. When we fold in the information from CMB anisotropies, we derive a lower limit on the location of the bump. We also forecast that a future spectrometer could improve FIRAS constraints of about four orders of magnitude.

We find that FIRAS+Planck constrain the amplitude of the peak below $\times 10^{-4}$ on the whole range of comoving wavenumbers considered (see figure 28). We can then conclude that within the assumptions described in section 12 - i.e. the probability that an overdensity δ larger than some critical value δ_c collapses forming a PBH is Gaussian and $\delta_c = 0.45$ - there is no significant production of PBHs in such range of k . Indeed, the PPS threshold value required to produce a significant fraction of PBHs within these assumption is one order of magnitude larger than such upper limit. Different assumptions on δ_c and/or non-Gaussianities in the probability distribution for δ could obviously alter these conclusions.

This thesis, which contains several original results, can be extended in several directions. Beyond investigating templates different from the smoothly broken power-law studied here, a quantitative synergy with existing and future measurements on the SGWB is ongoing.

A

COSMOLOGICAL PERTURBATIONS

The full set of equations for the cosmological perturbations in Newtonian gauge is [27]:

$$\text{photons} \begin{cases} \delta'_\gamma = \frac{4}{3} \left(\frac{k}{\mathcal{H}} v_\gamma + 3\Phi' \right) \\ v'_\gamma = -\frac{k}{4\mathcal{H}} \delta_\gamma + \frac{2k}{3\mathcal{H}} \Theta_2 - \frac{k}{3\mathcal{H}} \Psi - \tau' [\Theta_1 + v_b/3] \\ \Theta'_\ell = \frac{\ell k \Theta_{\ell-1}}{(2\ell+1)\mathcal{H}} - \frac{(\ell+1)k \Theta_{\ell+1}}{(2\ell+1)\mathcal{H}} + \tau' \left[\Theta_\ell - \frac{1}{10} \Pi \delta_{\ell,2} \right], \quad \ell \geq 2 \end{cases} \quad (\text{A.1})$$

$$\gamma \text{ polarization} \begin{cases} \Theta'_{P0} = -\frac{k}{\mathcal{H}} \Theta_{P1} + \tau' \left[\Theta_{P0} - \frac{1}{2} \Pi \right] \\ \Theta'_{P\ell} = \frac{\ell k \Theta_{P\ell-1}}{(2\ell+1)\mathcal{H}} - \frac{(\ell+1)k \Theta_{P\ell+1}}{(2\ell+1)\mathcal{H}} + \tau' \left[\Theta_\ell^P - \frac{1}{10} \Pi \delta_{\ell,2} \right], \quad \ell \geq 1 \end{cases} \quad (\text{A.2})$$

$$\text{neutrinos} \begin{cases} \delta'_\nu = \frac{4}{3} \left(\frac{k}{\mathcal{H}} v_\nu + 3\Phi' \right) \\ v'_\nu = -\frac{k}{4\mathcal{H}} \delta_\nu + \frac{2k}{\mathcal{H}} \mathcal{N}_2 - \frac{k}{\mathcal{H}} \Psi \\ \mathcal{N}'_\ell = \frac{\ell k}{(2\ell+1)\mathcal{H}} \mathcal{N}_{\ell-1} - \frac{\ell+1}{2\ell+1} \frac{k}{\mathcal{H}} \mathcal{N}_{\ell+1} \quad \ell \geq 2 \end{cases} \quad (\text{A.3})$$

$$\text{cold dark matter} \begin{cases} \delta'_{\text{CDM}} = \frac{k}{\mathcal{H}} v_{\text{CDM}} + 3\Phi' \\ v'_{\text{CDM}} = -v_{\text{CDM}} - \frac{k}{\mathcal{H}} \Psi \end{cases} \quad (\text{A.4})$$

$$\text{baryons} \begin{cases} \delta'_b = \frac{k}{\mathcal{H}} v_b + 3\Phi' \\ v'_b = -v_b - \frac{k}{\mathcal{H}} \Psi + \tau' R (v_b - v_\gamma) \end{cases} \quad (\text{A.5})$$

where \mathcal{N}_ℓ is the analogous of Θ_ℓ for neutrinos $R = 4\Omega_{\gamma,0}/(3\Omega_{b,0}a)$ and $\Pi = \Theta_2 + \Theta_{P0} + \Theta_{P2}$. Notice that for massive particles it is sufficient to stop at $\ell = 1$. Einstein equations close the previous system of equations. In Newtonian gauge they are

$$\begin{aligned} -\Phi' &= \Psi + \frac{k^2}{3\mathcal{H}} \Phi + \frac{1}{2} [\Omega_{\text{CDM}}(a) \delta_{\text{CDM}} + \Omega_b(a) \delta_b + \Omega_\gamma(a) \delta_\gamma + \Omega_\nu(a) \delta_\nu] \\ \Psi &= \Phi - \frac{12\mathcal{H}^2}{k^2} [\Omega_\gamma(a) \Theta_2 + \Omega_\nu(a) \mathcal{N}_2] \end{aligned} \quad (\text{A.6})$$

To solve all these coupled differential equations it is necessary to give initial conditions.

Adiabatic initial conditions are

$$\Psi = \frac{1}{\frac{3}{2} + \frac{2f_\nu}{5}} \quad (\text{A.7})$$

$$\Phi = \left(1 + \frac{2f_\nu}{5}\right) \Psi \quad (\text{A.8})$$

$$\delta_{\text{CDM}} = \delta_{\text{b}} = -\frac{3}{2}\Psi \quad (\text{A.9})$$

$$v_{\text{CDM}} = v_{\text{b}} = -\frac{k}{2\mathcal{H}}\Psi \quad (\text{A.10})$$

$$\Theta_0 = -\frac{1}{2}\Psi \quad (\text{A.11})$$

$$\Theta_1 = +\frac{k}{6\mathcal{H}}\Psi \quad (\text{A.12})$$

$$\Theta_2 = \begin{cases} -\frac{8k}{15\mathcal{H}\tau'}\Theta_1, & (\text{with polarization}) \\ -\frac{20k}{45\mathcal{H}\tau'}\Theta_1, & (\text{without polarization}) \end{cases} \quad (\text{A.13})$$

$$\Theta_\ell = -\frac{\ell}{2\ell+1} \frac{k}{\mathcal{H}\tau'} \Theta_{\ell-1} \quad (\text{A.14})$$

$$\Theta_{0P} = \frac{5}{4}\Theta_2 \quad (\text{A.15})$$

$$\Theta_{1P} = -\frac{k}{4\mathcal{H}\tau'}\Theta_2 \quad (\text{A.16})$$

$$\Theta_{2P} = \frac{1}{4}\Theta_2 \quad (\text{A.17})$$

$$\Theta_{\ell P} = -\frac{\ell}{2\ell+1} \frac{k}{\mathcal{H}\tau'} \Theta_{\ell-1}^P \quad (\text{A.18})$$

$$\mathcal{N}_0 = -\frac{1}{2}\Psi \quad (\text{A.19})$$

$$\mathcal{N}_1 = +\frac{k}{6\mathcal{H}}\Psi \quad (\text{A.20})$$

$$\mathcal{N}_2 = -\frac{c^2 k^2 a^2 (\Psi - \Phi)}{12H_0^2 \Omega_{\nu 0}} \quad (\text{A.21})$$

$$\mathcal{N}_\ell = \frac{k}{(2\ell+1)\mathcal{H}} \mathcal{N}_{\ell-1}, \quad \ell \geq 3 \quad (\text{A.22})$$

where $f_\nu = \frac{\Omega_{\nu 0}}{\Omega_{\gamma 0} + \Omega_{\nu 0}}$.

BIBLIOGRAPHY

- [1] D. J. Fixsen et al. “The Cosmic Microwave Background Spectrum from the Full COBE/FIRAS Data Set”. In: *The Astrophysical Journal* 473.2 (Dec. 1996), pp. 576–587. DOI: [10.1086/178173](https://doi.org/10.1086/178173). URL: <https://doi.org/10.1086%2F178173>.
- [2] Planck Collaboration. “Planck 2018 results. I. Overview and the cosmological legacy of Planck”. In: *Astronomy & Astrophysics* 641 (Sept. 2020), A1. DOI: [10.1051/0004-6361/201833880](https://doi.org/10.1051/0004-6361/201833880). URL: <https://doi.org/10.1051%2F0004-6361%2F201833880>.
- [3] Peter Ade et al. “The Simons Observatory: science goals and forecasts”. In: *Journal of Cosmology and Astroparticle Physics* 2019.02 (Feb. 2019), pp. 056–056. DOI: [10.1088/1475-7516/2019/02/056](https://doi.org/10.1088/1475-7516/2019/02/056). URL: <https://doi.org/10.1088%2F1475-7516%2F2019%2F02%2F056>.
- [4] Kevork N. Abazajian et al. *CMB-S4 Science Book, First Edition*. 2016. DOI: [10.48550/ARXIV.1610.02743](https://arxiv.org/abs/1610.02743). URL: <https://arxiv.org/abs/1610.02743>.
- [5] T. Matsumura et al. “Mission Design of LiteBIRD”. In: *Journal of Low Temperature Physics* 176.5-6 (Jan. 2014), pp. 733–740. DOI: [10.1007/s10909-013-0996-1](https://doi.org/10.1007/s10909-013-0996-1). URL: <https://doi.org/10.1007%2Fs10909-013-0996-1>.
- [6] José Alberto Rubiño Martín et al. “The Tenerife Microwave Spectrometer (TMS) experiment: studying the absolute spectrum of the sky emission in the 10-20GHz range”. In: *Millimeter, Submillimeter, and Far-Infrared Detectors and Instrumentation for Astronomy X*. Vol. 11453. SPIE. 2020, pp. 155–166.
- [7] S. Masi et al. “The COSmic Monopole Observer (COSMO)”. In: *16th Marcel Grossmann Meeting on Recent Developments in Theoretical and Experimental General Relativity, Astrophysics and Relativistic Field Theories*. Oct. 2021. DOI: [10.1142/9789811269776_0131](https://doi.org/10.1142/9789811269776_0131). arXiv: [2110.12254](https://arxiv.org/abs/2110.12254) [astro-ph. IM].
- [8] A Kogut et al. “The Primordial Inflation Explorer (PIXIE): a nulling polarimeter for cosmic microwave background observations”. In: *Journal of Cosmology and Astroparticle Physics* 2011.07 (July 2011), pp. 025–025. DOI: [10.1088/1475-7516/2011/07/025](https://doi.org/10.1088/1475-7516/2011/07/025). URL: <https://doi.org/10.1088%2F1475-7516%2F2011%2F07%2F025>.
- [9] *The Polarized Radiation Interferometer for Spectral distortions and Inflation Exploration (PRISTINE)*. <https://www.ias.u-psud.fr/en/content/pristine>.
- [10] *FTS fOr CMB Spectral diStortIon expLoration (FOSSIL)*. <https://www.ias.u-psud.fr/en/content/fossil>.

- [11] J. Chluba et al. “New horizons in cosmology with spectral distortions of the cosmic microwave background”. In: *Experimental Astronomy* 51.3 (May 2021), pp. 1515–1554. DOI: [10.1007/s10686-021-09729-5](https://doi.org/10.1007/s10686-021-09729-5). URL: <https://doi.org/10.1007/s10686-021-09729-5>.
- [12] Joseph Silk. “Cosmic black body radiation and galaxy formation”. In: *Astrophys. J.* 151 (1968), pp. 459–471. DOI: [10.1086/149449](https://doi.org/10.1086/149449).
- [13] Simeon Bird et al. “Did LIGO Detect Dark Matter?” In: *Physical Review Letters* 116.20 (May 2016). DOI: [10.1103/physrevlett.116.201301](https://doi.org/10.1103/physrevlett.116.201301). URL: <https://doi.org/10.1103/physrevlett.116.201301>.
- [14] Misao Sasaki, Teruaki Suyama, Takahiro Tanaka, and Shuichiro Yokoyama. “Primordial Black Hole Scenario for the Gravitational-Wave Event GW150914”. In: *Physical Review Letters* 117.6 (Aug. 2016). DOI: [10.1103/physrevlett.117.061101](https://doi.org/10.1103/physrevlett.117.061101). URL: <https://doi.org/10.1103/physrevlett.117.061101>.
- [15] Sébastien Clesse and Juan García-Bellido. “The clustering of massive Primordial Black Holes as Dark Matter: Measuring their mass distribution with advanced LIGO”. In: *Physics of the Dark Universe* 15 (Mar. 2017), pp. 142–147. DOI: [10.1016/j.dark.2016.10.002](https://doi.org/10.1016/j.dark.2016.10.002). URL: <https://doi.org/10.1016/j.dark.2016.10.002>.
- [16] B. P. Abbott et al. “Observation of Gravitational Waves from a Binary Black Hole Merger”. In: *Phys. Rev. Lett.* 116 (6 Feb. 2016), p. 061102. DOI: [10.1103/PhysRevLett.116.061102](https://link.aps.org/doi/10.1103/PhysRevLett.116.061102). URL: <https://link.aps.org/doi/10.1103/PhysRevLett.116.061102>.
- [17] The LIGO Scientific Collaboration et al. *GWTC-3: Compact Binary Coalescences Observed by LIGO and Virgo During the Second Part of the Third Observing Run*. 2021. DOI: [10.48550/ARXIV.2111.03606](https://arxiv.org/abs/2111.03606). URL: <https://arxiv.org/abs/2111.03606>.
- [18] Planck Collaboration. “Planck 2018 results. VI. Cosmological parameters”. In: *A&A* 641 (2020), A6. DOI: [10.1051/0004-6361/201833910](https://arxiv.org/abs/1807.06209). arXiv: [1807.06209](https://arxiv.org/abs/1807.06209).
- [19] J. P. W. Verbiest et al. “The International Pulsar Timing Array: First data release”. In: *Monthly Notices of the Royal Astronomical Society* 458.2 (Feb. 2016), pp. 1267–1288. DOI: [10.1093/mnras/stw347](https://doi.org/10.1093/mnras/stw347). URL: <https://doi.org/10.1093/mnras/stw347>.
- [20] T. J. W. Lazio. “The Square Kilometre Array pulsar timing array”. In: *Classical and Quantum Gravity* 30.22, 224011 (Nov. 2013), p. 224011. DOI: [10.1088/0264-9381/30/22/224011](https://doi.org/10.1088/0264-9381/30/22/224011).
- [21] Pau Amaro-Seoane et al. *Laser Interferometer Space Antenna*. 2017. DOI: [10.48550/ARXIV.1702.00786](https://arxiv.org/abs/1702.00786). URL: <https://arxiv.org/abs/1702.00786>.
- [22] Steven Weinberg. *Gravitation and Cosmology: Principles and Applications of the General Theory of Relativity*. Wiley, 1972.

- [23] Jeremy Bernstein. *Kinetic Theory in the Expanding Universe*. Cambridge University Press, 1988. DOI: [10.1017/CB09780511564185](https://doi.org/10.1017/CB09780511564185).
- [24] Daniel Baumann. *Cosmology*. Cambridge University Press, 2022. DOI: [10.1017/9781108937092](https://doi.org/10.1017/9781108937092).
- [25] Edward W Kolb and Michael Stanley Turner. *The early universe*. Frontiers in physics. Westview Press, 1990. DOI: [10.1201/9780429492860](https://doi.org/10.1201/9780429492860).
- [26] Ruth Durrer. *The Cosmic Microwave Background*. Cambridge University Press, Dec. 2020. DOI: [10.1017/9781316471524](https://doi.org/10.1017/9781316471524).
- [27] Scott Dodelson. *Modern Cosmology*. Academic Press, 2003. ISBN: 978-0-12-219141-1.
- [28] D. J. Fixsen. “The Temperature of the Cosmic Microwave Background”. In: *The Astrophysical Journal* 707.2 (Nov. 2009), pp. 916–920. DOI: [10.1088/0004-637x/707/2/916](https://doi.org/10.1088/0004-637x/707/2/916). URL: <https://doi.org/10.1088/0004-637x/707/2/916>.
- [29] Jens Chluba. *Future Steps in Cosmology using Spectral Distortions of the Cosmic Microwave Background*. 2018. DOI: [10.48550/ARXIV.1806.02915](https://doi.org/10.48550/ARXIV.1806.02915). URL: <https://arxiv.org/abs/1806.02915>.
- [30] J. Chluba and R. A. Sunyaev. “The evolution of CMB spectral distortions in the early Universe”. In: *Monthly Notices of the Royal Astronomical Society* 419.2 (Nov. 2011), pp. 1294–1314. DOI: [10.1111/j.1365-2966.2011.19786.x](https://doi.org/10.1111/j.1365-2966.2011.19786.x). URL: <https://doi.org/10.1111/j.1365-2966.2011.19786.x>.
- [31] Jens Chluba and Donghui Jeong. “Teasing bits of information out of the CMB energy spectrum”. In: *Monthly Notices of the Royal Astronomical Society* 438.3 (Jan. 2014), pp. 2065–2082. DOI: [10.1093/mnras/stt2327](https://doi.org/10.1093/mnras/stt2327). URL: <https://doi.org/10.1093/mnras/stt2327>.
- [32] Julien Lesgourgues. *The Cosmic Linear Anisotropy Solving System (CLASS) I: Overview*. 2011. DOI: [10.48550/ARXIV.1104.2932](https://doi.org/10.48550/ARXIV.1104.2932). URL: <https://arxiv.org/abs/1104.2932>.
- [33] Diego Blas, Julien Lesgourgues, and Thomas Tram. “The Cosmic Linear Anisotropy Solving System (CLASS) II: Approximation schemes”. In: *JCAP* 07 (2011), p. 034. DOI: [10.1088/1475-7516/2011/07/034](https://doi.org/10.1088/1475-7516/2011/07/034). arXiv: [1104.2933](https://arxiv.org/abs/1104.2933) [astro-ph.CO].
- [34] Matteo Lucca, Nils Schöneberg, Deanna C. Hooper, Julien Lesgourgues, and Jens Chluba. “The synergy between CMB spectral distortions and anisotropies”. In: *JCAP* 02 (2020), p. 026. DOI: [10.1088/1475-7516/2020/02/026](https://doi.org/10.1088/1475-7516/2020/02/026). arXiv: [1910.04619](https://arxiv.org/abs/1910.04619) [astro-ph.CO].

- [35] J. Chluba and R. A. Sunyaev. “The evolution of CMB spectral distortions in the early Universe”. In: *Monthly Notices of the Royal Astronomical Society* 419.2 (Dec. 2011), pp. 1294–1314. ISSN: 0035-8711. DOI: [10.1111/j.1365-2966.2011.19786.x](https://doi.org/10.1111/j.1365-2966.2011.19786.x). eprint: <https://academic.oup.com/mnras/article-pdf/419/2/1294/3114327/mnras0419-1294.pdf>. URL: <https://doi.org/10.1111/j.1365-2966.2011.19786.x>.
- [36] Boris Bolliet, Jens Chluba, and Richard Battye. “Spectral distortion constraints on photon injection from low-mass decaying particles”. In: *Monthly Notices of the Royal Astronomical Society* 507.3 (July 2021), pp. 3148–3178. DOI: [10.1093/mnras/stab1997](https://doi.org/10.1093/mnras/stab1997). URL: <https://doi.org/10.1093/mnras/stab1997>.
- [37] Jens Chluba. “Green’s function of the cosmological thermalization problem – II. Effect of photon injection and constraints”. In: *Monthly Notices of the Royal Astronomical Society* 454.4 (Oct. 2015), pp. 4182–4196. ISSN: 0035-8711. DOI: [10.1093/mnras/stv2243](https://doi.org/10.1093/mnras/stv2243). eprint: <https://academic.oup.com/mnras/article-pdf/454/4/4182/18510110/stv2243.pdf>. URL: <https://doi.org/10.1093/mnras/stv2243>.
- [38] J. Chluba. “Refined approximations for the distortion visibility function and μ -type spectral distortions”. In: *Monthly Notices of the Royal Astronomical Society* 440.3 (Apr. 2014), pp. 2544–2563. ISSN: 0035-8711. DOI: [10.1093/mnras/stu414](https://doi.org/10.1093/mnras/stu414). eprint: <https://academic.oup.com/mnras/article-pdf/440/3/2544/23991694/stu414.pdf>. URL: <https://doi.org/10.1093/mnras/stu414>.
- [39] C. Burigana, L. Danese, and G. de Zotti. “Formation and evolution of early distortions of the microwave background spectrum - A numerical study”. In: *Astronomy and Astrophysics* 246.1 (June 1991), pp. 49–58.
- [40] J. Chluba. “Green’s function of the cosmological thermalization problem”. In: *Monthly Notices of the Royal Astronomical Society* 434.1 (June 2013), pp. 352–357. DOI: [10.1093/mnras/stt1025](https://doi.org/10.1093/mnras/stt1025). URL: <https://doi.org/10.1093/mnras/stt1025>.
- [41] Jens Chluba. “Which spectral distortions does Λ CDM actually predict?” In: *Monthly Notices of the Royal Astronomical Society* 460.1 (Apr. 2016), pp. 227–239. DOI: [10.1093/mnras/stw945](https://doi.org/10.1093/mnras/stw945). URL: <https://doi.org/10.1093/mnras/stw945>.
- [42] Hongwan Liu, Gregory W. Ridgway, and Tracy R. Slatyer. “Code package for calculating modified cosmic ionization and thermal histories with dark matter and other exotic energy injections”. In: *Physical Review D* 101.2 (Jan. 2020). DOI: [10.1103/physrevd.101.023530](https://doi.org/10.1103/physrevd.101.023530). URL: <https://doi.org/10.1103/physrevd.101.023530>.
- [43] J. Chluba and R. M. Thomas. “Towards a complete treatment of the cosmological recombination problem”. In: *Monthly Notices of the Royal Astronomical Society* (Dec. 2010), no–no. DOI: [10.1111/j.1365-2966.2010.17940.x](https://doi.org/10.1111/j.1365-2966.2010.17940.x). URL: <https://doi.org/10.1111/j.1365-2966.2010.17940.x>.

- [44] Jens Chluba and Yacine Ali-Haïmoud. “cosmospec: fast and detailed computation of the cosmological recombination radiation from hydrogen and helium”. In: *Monthly Notices of the Royal Astronomical Society* 456.4 (Jan. 2016), pp. 3494–3508. DOI: [10.1093/mnras/stv2691](https://doi.org/10.1093/mnras/stv2691). URL: <https://doi.org/10.1093%2Fmnras%2Fstv2691>.
- [45] J. Colin Hill et al. “Taking the Universe’s Temperature with Spectral Distortions of the Cosmic Microwave Background”. In: *Physical Review Letters* 115.26 (Dec. 2015). DOI: [10.1103/physrevlett.115.261301](https://doi.org/10.1103/physrevlett.115.261301). URL: <https://doi.org/10.1103%2Fphysrevlett.115.261301>.
- [46] Patrick Stöcker, Michael Krämer, Julien Lesgourgues, and Vivian Poulin. “Exotic energy injection with ExoCLASS: application to the Higgs portal model and evaporating black holes”. In: *Journal of Cosmology and Astroparticle Physics* 2018.03 (Mar. 2018), pp. 018–018. DOI: [10.1088/1475-7516/2018/03/018](https://doi.org/10.1088/1475-7516/2018/03/018). URL: <https://doi.org/10.1088%2F1475-7516%2F2018%2F03%2F018>.
- [47] Steven Weinberg. *Cosmology*. Oxford: Oxford Univ. Press, 2008.
- [48] Chung-Pei Ma and Edmund Bertschinger. “Cosmological Perturbation Theory in the Synchronous and Conformal Newtonian Gauges”. In: *The Astrophysical Journal* 455 (Dec. 1995), p. 7. DOI: [10.1086/176550](https://doi.org/10.1086/176550). URL: <https://doi.org/10.1086%2F176550>.
- [49] Daniel Baumann. *TASI Lectures on Inflation*. 2009. DOI: [10.48550/ARXIV.0907.5424](https://arxiv.org/abs/0907.5424). URL: <https://arxiv.org/abs/0907.5424>.
- [50] Fabio Finelli, Jan Hamann, Samuel M Leach, and Julien Lesgourgues. “Single-field inflation constraints from CMB and SDSS data”. In: *Journal of Cosmology and Astroparticle Physics* 2010.04 (Apr. 2010), pp. 011–011. DOI: [10.1088/1475-7516/2010/04/011](https://doi.org/10.1088/1475-7516/2010/04/011). URL: <https://doi.org/10.1088%2F1475-7516%2F2010%2F04%2F011>.
- [51] Planck Collaboration. “Planck 2013 results. XXII. Constraints on inflation”. In: *Astronomy and Astrophysics* 571 (Oct. 2014), A22. DOI: [10.1051/0004-6361/201321569](https://doi.org/10.1051/0004-6361/201321569). URL: <https://doi.org/10.1051%2F0004-6361%2F201321569>.
- [52] Daniela Paoletti, Fabio Finelli, Jussi Valiviita, and Masashi Hazumi. “Planck and BICEP/Keck Array 2018 constraints on primordial gravitational waves and perspectives for future B-mode polarization measurements”. In: *Physical Review D* 106.8 (Oct. 2022). DOI: [10.1103/physrevd.106.083528](https://doi.org/10.1103/physrevd.106.083528). URL: <https://doi.org/10.1103%2Fphysrevd.106.083528>.
- [53] Uros Seljak and Matias Zaldarriaga. “A Line-of-Sight Integration Approach to Cosmic Microwave Background Anisotropies”. In: *The Astrophysical Journal* 469 (Oct. 1996), p. 437. DOI: [10.1086/177793](https://doi.org/10.1086/177793). URL: <https://doi.org/10.1086%2F177793>.
- [54] R. Khatri, R. A. Sunyaev, and J. Chluba. “Mixing of blackbodies: entropy production and dissipation of sound waves in the early Universe”. In: *Astronomy & Astrophysics* 543 (July 2012), A136. DOI: [10.1051/0004-6361/201219590](https://doi.org/10.1051/0004-6361/201219590). URL: <https://doi.org/10.1051%2F0004-6361%2F201219590>.

- [55] J. Chluba and R. A. Sunyaev. “Superposition of blackbodies and the dipole anisotropy: A possibility to calibrate CMB experiments”. In: *Astronomy and Astrophysics* 424 (Sept. 2004), pp. 389–408. DOI: [10.1051/0004-6361:20041016](https://doi.org/10.1051/0004-6361:20041016). arXiv: [astro-ph/0404067](https://arxiv.org/abs/astro-ph/0404067) [astro-ph].
- [56] J. Chluba, R. Khatri, and R. A. Sunyaev. “CMB at 2×2 order: the dissipation of primordial acoustic waves and the observable part of the associated energy release”. In: *Monthly Notices of the Royal Astronomical Society* 425.2 (Aug. 2012), pp. 1129–1169. DOI: [10.1111/j.1365-2966.2012.21474.x](https://doi.org/10.1111/j.1365-2966.2012.21474.x). URL: <https://doi.org/10.1111%2Fj.1365-2966.2012.21474.x>.
- [57] Jens Chluba, Jan Hamann, and Subodh P. Patil. “Features and new physical scales in primordial observables: Theory and observation”. In: *International Journal of Modern Physics D* 24.10 (Aug. 2015), p. 1530023. DOI: [10.1142/s0218271815300232](https://doi.org/10.1142/s0218271815300232). URL: <https://doi.org/10.1142%2Fs0218271815300232>.
- [58] M Punturo et al. “The Einstein Telescope: a third-generation gravitational wave observatory”. In: *Classical and Quantum Gravity* 27.19 (Sept. 2010), p. 194002. DOI: [10.1088/0264-9381/27/19/194002](https://dx.doi.org/10.1088/0264-9381/27/19/194002). URL: <https://dx.doi.org/10.1088/0264-9381/27/19/194002>.
- [59] Guillem Domenech. “Scalar Induced Gravitational Waves Review”. In: *Universe* 7.11 (Oct. 2021), p. 398. DOI: [10.3390/universe7110398](https://doi.org/10.3390/universe7110398). URL: <https://doi.org/10.3390%2Funiverse7110398>.
- [60] Kishore N. Ananda, Chris Clarkson, and David Wands. “Cosmological gravitational wave background from primordial density perturbations”. In: *Physical Review D* 75.12 (June 2007). DOI: [10.1103/physrevd.75.123518](https://doi.org/10.1103/physrevd.75.123518). URL: <https://doi.org/10.1103%2Fphysrevd.75.123518>.
- [61] Jaume Garriga and V.F. Mukhanov. “Perturbations in k-inflation”. In: *Physics Letters B* 458.2-3 (July 1999), pp. 219–225. DOI: [10.1016/s0370-2693\(99\)00602-4](https://doi.org/10.1016/s0370-2693(99)00602-4). URL: <https://doi.org/10.1016%2Fs0370-2693%2899%2900602-4>.
- [62] J.R. Espinosa, D. Racco, and A. Riotto. “A cosmological signature of the SM Higgs instability: gravitational waves”. In: *Journal of Cosmology and Astroparticle Physics* 2018.09 (Sept. 2018), pp. 012–012. DOI: [10.1088/1475-7516/2018/09/012](https://doi.org/10.1088/1475-7516/2018/09/012). URL: <https://doi.org/10.1088%2F1475-7516%2F2018%2F09%2F012>.
- [63] Ya. B. Zeldovich and I.D. Novikov. “The Hypothesis of Cores Retarded during Expansion and the Hot Cosmological Model”. In: *Astronomicheskii Zhurnal* 43 (Jan. 1966), p. 758.

- [64] Stephen Hawking. “Gravitationally Collapsed Objects of Very Low Mass”. In: *Monthly Notices of the Royal Astronomical Society* 152.1 (Apr. 1971), pp. 75–78. ISSN: 0035-8711. DOI: [10.1093/mnras/152.1.75](https://doi.org/10.1093/mnras/152.1.75). eprint: <https://academic.oup.com/mnras/article-pdf/152/1/75/9360899/mnras152-0075.pdf>. URL: <https://doi.org/10.1093/mnras/152.1.75>.
- [65] B.J. Carr and S.W. Hawking. “Black holes in the early Universe”. In: *Monthly Notices of the Royal Astronomical Society* 168 (Aug. 1974), pp. 399–416. DOI: [10.1093/mnras/168.2.399](https://doi.org/10.1093/mnras/168.2.399).
- [66] B. J. Carr and M. J. Rees. “Can pregalactic objects generate galaxies?” In: *Monthly Notices of the Royal Astronomical Society* 206.4 (Feb. 1984), pp. 801–818. ISSN: 0035-8711. DOI: [10.1093/mnras/206.4.801](https://doi.org/10.1093/mnras/206.4.801). eprint: <https://academic.oup.com/mnras/article-pdf/206/4/801/2902772/mnras206-0801.pdf>. URL: <https://doi.org/10.1093/mnras/206.4.801>.
- [67] Guillermo Ballesteros and Marco Taoso. “Primordial black hole dark matter from single field inflation”. In: *Physical Review D* 97.2 (Jan. 2018). DOI: [10.1103/physrevd.97.023501](https://doi.org/10.1103/physrevd.97.023501). URL: <https://doi.org/10.1103/physrevd.97.023501>.
- [68] Juan Garcia-Bellido and Ester Ruiz Morales. “Primordial black holes from single field models of inflation”. In: *Physics of the Dark Universe* 18 (Dec. 2017), pp. 47–54. DOI: [10.1016/j.dark.2017.09.007](https://doi.org/10.1016/j.dark.2017.09.007). URL: <https://doi.org/10.1016/j.dark.2017.09.007>.
- [69] Juan Garcia-Bellido, Andrei Linde, and David Wands. “Density perturbations and black hole formation in hybrid inflation”. In: *Physical Review D* 54.10 (Nov. 1996), pp. 6040–6058. DOI: [10.1103/physrevd.54.6040](https://doi.org/10.1103/physrevd.54.6040). URL: <https://doi.org/10.1103/physrevd.54.6040>.
- [70] Sebastien Clesse and Juan Garcia-Bellido. “Massive primordial black holes from hybrid inflation as dark matter and the seeds of galaxies”. In: *Physical Review D* 92.2 (July 2015). DOI: [10.1103/physrevd.92.023524](https://doi.org/10.1103/physrevd.92.023524). URL: <https://doi.org/10.1103/physrevd.92.023524>.
- [71] Matteo Braglia et al. “Generating PBHs and small-scale GWs in two-field models of inflation”. In: *Journal of Cosmology and Astroparticle Physics* 2020.08 (Aug. 2020), pp. 001–001. DOI: [10.1088/1475-7516/2020/08/001](https://doi.org/10.1088/1475-7516/2020/08/001). URL: <https://doi.org/10.1088/1475-7516/2020/08/001>.
- [72] Matteo Braglia, Andrei Linde, Renata Kallosh, and Fabio Finelli. *Hybrid α -attractors, primordial black holes and gravitational wave backgrounds*. Nov. 2022. arXiv: [2211.14262](https://arxiv.org/abs/2211.14262) [astro-ph.CO].

- [73] Matteo Braglia, Xingang Chen, and Dhiraj Kumar Hazra. “Probing primordial features with the stochastic gravitational wave background”. In: *Journal of Cosmology and Astroparticle Physics* 2021.03 (Feb. 2021), p. 005. DOI: [10.1088/1475-7516/2021/03/005](https://doi.org/10.1088/1475-7516/2021/03/005). URL: <https://doi.org/10.1088/1475-7516/2021/03/005>.
- [74] Ogan Özsoy and Gianmassimo Tasinato. “CMB μT cross-correlations as a probe of primordial black hole scenarios”. In: *Physical Review D* 104.4 (Aug. 2021). DOI: [10.1103/physrevd.104.043526](https://doi.org/10.1103/physrevd.104.043526). URL: <https://doi.org/10.1103/physrevd.104.043526>.
- [75] Ogan Özsoy and Gianmassimo Tasinato. “Consistency conditions and primordial black holes in single field inflation”. In: *Phys. Rev. D* 105.2 (2022), p. 023524. DOI: [10.1103/PhysRevD.105.023524](https://doi.org/10.1103/PhysRevD.105.023524). arXiv: [2111.02432](https://arxiv.org/abs/2111.02432) [astro-ph.CO].
- [76] Shyam Balaji, H. V. Ragavendra, Shiv K. Sethi, Joseph Silk, and L. Sriramkumar. “Observing Nulling of Primordial Correlations via the 21-cm Signal”. In: *Phys. Rev. Lett.* 129.26 (2022), p. 261301. DOI: [10.1103/PhysRevLett.129.261301](https://doi.org/10.1103/PhysRevLett.129.261301). arXiv: [2206.06386](https://arxiv.org/abs/2206.06386) [astro-ph.CO].
- [77] Matteo Braglia, Dhiraj Kumar Hazra, L. Sriramkumar, and Fabio Finelli. “Generating primordial features at large scales in two field models of inflation”. In: *Journal of Cosmology and Astroparticle Physics* 2020.08 (Aug. 2020), pp. 025–025. DOI: [10.1088/1475-7516/2020/08/025](https://doi.org/10.1088/1475-7516/2020/08/025). URL: <https://doi.org/10.1088/1475-7516/2020/08/025>.
- [78] David Polarski and A.A. Starobinsky. “Spectra of perturbations produced by double inflation with an intermediate matter-dominated stage”. In: *Nuclear Physics B* 385.3 (1992), pp. 623–650. ISSN: 0550-3213. DOI: [https://doi.org/10.1016/0550-3213\(92\)90062-G](https://doi.org/10.1016/0550-3213(92)90062-G). URL: <https://www.sciencedirect.com/science/article/pii/055032139290062G>.
- [79] F. Di Marco, F. Finelli, and R. Brandenberger. “Adiabatic and isocurvature perturbations for multifield generalized Einstein models”. In: *Physical Review D* 67.6 (Mar. 2003). DOI: [10.1103/physrevd.67.063512](https://doi.org/10.1103/physrevd.67.063512). URL: <https://doi.org/10.1103/physrevd.67.063512>.
- [80] Fabrizio Di Marco and Fabio Finelli. “Slow-roll inflation for generalized two-field Lagrangians”. In: *Physical Review D* 71.12 (June 2005). DOI: [10.1103/physrevd.71.123502](https://doi.org/10.1103/physrevd.71.123502). URL: <https://doi.org/10.1103/physrevd.71.123502>.
- [81] Christopher Gordon, David Wands, Bruce A. Bassett, and Roy Maartens. “Adiabatic and entropy perturbations from inflation”. In: *Physical Review D* 63.2 (Dec. 2000). DOI: [10.1103/physrevd.63.023506](https://doi.org/10.1103/physrevd.63.023506). URL: <https://doi.org/10.1103/physrevd.63.023506>.

- [82] Andrei Linde. “Hybrid inflation”. In: *Physical Review D* 49.2 (Jan. 1994), pp. 748–754. DOI: [10.1103/PhysRevD.49.748](https://doi.org/10.1103/PhysRevD.49.748). URL: <https://doi.org/10.1103%2Fphysrevd.49.748>.
- [83] Jacopo Fumagalli, Sébastien Renaux-Petel, and Lukas T. Witkowski. “Oscillations in the stochastic gravitational wave background from sharp features and particle production during inflation”. In: *JCAP* 08 (2021), p. 030. DOI: [10.1088/1475-7516/2021/08/030](https://doi.org/10.1088/1475-7516/2021/08/030). arXiv: [2012.02761](https://arxiv.org/abs/2012.02761) [[astro-ph.CO](https://arxiv.org/abs/2012.02761)].
- [84] Jacopo Fumagalli, Sébastien Renaux-Petel, John W. Ronayne, and Lukas T. Witkowski. *Turning in the landscape: a new mechanism for generating Primordial Black Holes*. 2020. DOI: [10.48550/ARXIV.2004.08369](https://doi.org/10.48550/ARXIV.2004.08369). URL: <https://arxiv.org/abs/2004.08369>.
- [85] Caner Ünal, Ely D. Kovetz, and Subodh P. Patil. “Multimessenger probes of inflationary fluctuations and primordial black holes”. In: *Phys. Rev. D* 103.6 (2021), p. 063519. DOI: [10.1103/PhysRevD.103.063519](https://doi.org/10.1103/PhysRevD.103.063519). arXiv: [2008.11184](https://arxiv.org/abs/2008.11184) [[astro-ph.CO](https://arxiv.org/abs/2008.11184)].
- [86] Jeff Crowder and Neil J. Cornish. “Beyond LISA: Exploring future gravitational wave missions”. In: *Physical Review D* 72.8 (Oct. 2005). DOI: [10.1103/PhysRevD.72.083005](https://doi.org/10.1103/PhysRevD.72.083005). URL: <https://doi.org/10.1103%2Fphysrevd.72.083005>.
- [87] Ville Vaskonen and Hardi Veermäe. “Did NANOGrav See a Signal from Primordial Black Hole Formation?” In: *Physical Review Letters* 126.5 (Feb. 2021). DOI: [10.1103/PhysRevLett.126.051303](https://doi.org/10.1103/PhysRevLett.126.051303). URL: <https://doi.org/10.1103%2Fphysrevlett.126.051303>.
- [88] Pierre Auclair et al. *Cosmology with the Laser Interferometer Space Antenna*. 2022. DOI: [10.48550/ARXIV.2204.05434](https://doi.org/10.48550/ARXIV.2204.05434). URL: <https://arxiv.org/abs/2204.05434>.
- [89] Nils Schöneberg, Matteo Lucca, and Deanna C. Hooper. “Constraining the inflationary potential with spectral distortions”. In: *JCAP* 03 (2021), p. 036. DOI: [10.1088/1475-7516/2021/03/036](https://doi.org/10.1088/1475-7516/2021/03/036). arXiv: [2010.07814](https://arxiv.org/abs/2010.07814) [[astro-ph.CO](https://arxiv.org/abs/2010.07814)].
- [90] Fabio Finelli et al. “Exploring cosmic origins with CORE: Inflation”. In: *JCAP* 04 (2018), p. 016. DOI: [10.1088/1475-7516/2018/04/016](https://doi.org/10.1088/1475-7516/2018/04/016). arXiv: [1612.08270](https://arxiv.org/abs/1612.08270) [[astro-ph.CO](https://arxiv.org/abs/1612.08270)].
- [91] Benjamin Audren, Julien Lesgourgues, Karim Benabed, and Simon Prunet. “Conservative Constraints on Early Cosmology: an illustration of the Monte Python cosmological parameter inference code”. In: *JCAP* 1302 (2013), p. 001. DOI: [10.1088/1475-7516/2013/02/001](https://doi.org/10.1088/1475-7516/2013/02/001). arXiv: [1210.7183](https://arxiv.org/abs/1210.7183) [[astro-ph.CO](https://arxiv.org/abs/1210.7183)].
- [92] Thejs Brinckmann and Julien Lesgourgues. “MontePython 3: boosted MCMC sampler and other features”. In: (2018). arXiv: [1804.07261](https://arxiv.org/abs/1804.07261) [[astro-ph.CO](https://arxiv.org/abs/1804.07261)].

- [93] Jens Chluba, Adrienne L. Erickcek, and Ido Ben-Dayan. “Probing the inflaton: small-scale power spectrum constraints from measurements of the cosmic microwave background energy spectrum”. In: *The Astrophysical Journal* 758.2 (Sept. 2012), p. 76. DOI: [10.1088/0004-637x/758/2/76](https://doi.org/10.1088/0004-637x/758/2/76). URL: <https://doi.org/10.1088/0004-637x/758/2/76>.
- [94] Sebastien Clesse, Björn Garbrecht, and Yi Zhu. “Testing Inflation and Curvaton Scenarios with CMB Distortions”. In: *JCAP* 10 (2014), p. 046. DOI: [10.1088/1475-7516/2014/10/046](https://doi.org/10.1088/1475-7516/2014/10/046). arXiv: [1402.2257](https://arxiv.org/abs/1402.2257) [astro-ph.CO].
- [95] Christian T. Byrnes, Philippa S. Cole, and Subodh P. Patil. “Steepest growth of the power spectrum and primordial black holes”. In: *Journal of Cosmology and Astroparticle Physics* 2019.06 (June 2019), pp. 028–028. DOI: [10.1088/1475-7516/2019/06/028](https://doi.org/10.1088/1475-7516/2019/06/028). URL: <https://doi.org/10.1088/1475-7516/2019/06/028>.
- [96] Will Handley. “fgivenx: A Python package for functional posterior plotting”. In: *Journal of Open Source Software* 3.28 (Aug. 2018), p. 849. DOI: [10.21105/joss.00849](https://doi.org/10.21105/joss.00849). URL: <https://doi.org/10.21105/joss.00849>.
- [97] Will J. Handley, Anthony N. Lasenby, Hiranya V. Peiris, and Michael P. Hobson. “Bayesian inflationary reconstructions from Planck 2018 data”. In: *Physical Review D* 100.10 (Nov. 2019). DOI: [10.1103/physrevd.100.103511](https://doi.org/10.1103/physrevd.100.103511). URL: <https://doi.org/10.1103/physrevd.100.103511>.
- [98] Planck Collaboration. “Planck 2018 results. X. Constraints on inflation”. In: *Astronomy & Astrophysics* 641 (Sept. 2020), A10. DOI: [10.1051/0004-6361/201833887](https://doi.org/10.1051/0004-6361/201833887). URL: <https://doi.org/10.1051/0004-6361/201833887>.